MARIA CURIE-SKŁODOWSKA UNIVERSITY
LUBLIN, REPUBLIC OF POLAND

Doctoral School of Quantitative and Natural Sciences

Scientific field: Physics
Discipline: Solar Physics

Mayank Kumar
Album number: 311076

A Global Magnetohydrodynamic Coronal Model

Doctoral dissertation prepared under the scientific supervision of
Prof. Dr. hab. Krzysztof Murawski
Prof. Emilia K J Kilpua
Dr. Błażej Kuźma

KATEDRA FIZYKI TEORETYCZNEJ
$|\Psi|^2$
UMCS LUBLIN

Lublin, October 20, 2025

Dedicated to my family, whose support and encouragement made this journey possible

I am among those who think that science has great beauty

······ *Marie Curie*

Preface from the Author

This thesis is a compilation of research that I have brought together over the past four years. I am pleased to present it as my contribution to the field of solar physics. During my doctoral studies, I encountered numerous challenges and breakthroughs. Navigating the intricacies of my Ph.D., along with my academic commitments, taught me valuable lessons in perseverance and critical thinking at every step. As I embarked on this challenging journey, I discovered that the deeper I delved into the vast ocean of knowledge, the more I recognized my limitations. The work included in this thesis represents just a small fraction of my arduous pursuit of my Ph.D. Despite the considerable effort put forth, the thesis may contain typographical errors, inaccuracies, and passages that are challenging to understand.

Acknowledgments

A four-year study odyssey would have been impossible to complete without the help of innumerable individuals. The number of people is indeed large, and mentioning each with at least a brief description of their assistance would require a text comparable in length to a chapter of the thesis. Therefore, I will unfortunately limit myself to expressing my gratitude.

First and foremost, I would like to express my heartfelt gratitude to Almighty God, whose blessings have made this endeavor possible. I am grateful to my family, especially my parents, **Parmila Devi** and **Yogesh Kumar**, for their unconditional love and support during my academic journey. Their faith in me has been an unwavering source of strength, and I will always be grateful for their sacrifices. I would like to offer my heartfelt gratitude to my dearest friend **Priyal**. Her unwavering support and presence have been instrumental in my successful completion of this significant task and project. She has always been my support and stronghold throughout this journey, and I feel indebted to her for the rest of my life. Special gratitude to my younger sister, **Aanchal**, who stands by and encourages me in this challenging quest. I would like to express my sincere thanks to the supervisors who guided this work:

- **Prof. Dr. hab. Krzysztof Murawski**
- **Prof. Emilia K. J. Kilpua**
- **Dr. Błażej Kuźma**

The work in this thesis was carried out as part of the Space Weather Awareness Training (**SWATNet**) project, which was funded by the European Union's Horizon 2020 research and innovation program under grant agreement No. 955620. I would like to thank **Prof. Krzysztof Murawski** for the opportunity to participate in the international **SWATNet** project as a Ph.D. student and for providing me with his esteemed guidance and support in my Ph.D. work. Throughout my association with SWATNet, no group member, directly or indirectly, has ever declined assistance or advice. I would like to thank **Prof. Emilia Kilpua** for hosting my Ph.D. studies at the University of Helsinki, Finland. My special thanks must go to **Prof. Ryszard Zdyb**, Director of the Institute of Physics, UMCS, for his cooperation in this project. I am also grateful to the other members of the Department of Theoretical Physics at UMCS for their friendly demeanor and warm welcome to the team at KFT. In particular, I want to thank **Prof. Tadeusz Domański**, **Prof. Jerzy Matyjasek**, and **Prof. Karol Izydor Wysokiński** for enhancing my applied skills during their seminars. I extend my sincere gratitude to **Prof. Stefaan Poedts** for teaching and expanding my knowledge of the basics of solar physics. Many thanks to **Dr. Błażej Kuźma** for encouraging me to be an independent researcher and for always lending a helping hand whenever I got stuck. I would also like to thank **Robert Niedziela** and **Maria Pelekhata**, who graduated with Ph.D.s from the department, for their initial help in settling down in Lublin.

I am very grateful to **Anna Wielgus**, the secretary of the KFT, for her constant support and patience. She has been a blessing in helping me navigate the often challenging administrative tasks at UMCS and the complex bureaucracy of residence in Poland. From handling official documents to assisting me with procedural formalities, she has always been approachable, gracious, and responsive. Her assistance not only saved me a significant amount of time and stress but also allowed me to focus more intensely on my academic pursuits. My special word of thanks to **Magdalena Pokrzycka Walczak**—the international project manager—for dealing with the complexity of the SWATNet project. Her presence and consistent effort ensured the project's administrative success. In addition, I would like to mention my friend **Mr. Piotr Mendel** for helping me deal with IT issues and cheering up my stay in Lublin. I am deeply grateful for his friendship and kindness. Special thanks to the members of the UMCS doctoral school—**Magdalena M. Wątróbka** and **Anna Jędrzejewska**—and the highly respected director of the doctoral school—**Prof. Aleksandara Szczęś**—for making all the obligatory doctoral studies successful. I am grateful to my mentor, **Prof. Pradeep Kashyap**, for his blessings and assistance in my career pursuits.

Last but not least, my kind gratitude to my elder brother, **Dr. Smarak Bandoupadhaya**, and his wife **Payal Mitra**, for brightening my stay in Lublin. I sincerely acknowledge their positive influence, acts of kindness, and the special bond we share. I cherish my friendship with **Sainul Abidh, Abhita, Mohsin Ali**, and **Tianjing Ren**. I am lucky to have such great friends in my life.

Declaration

I hereby certify that the contents of this dissertation are original and have not, in whole or in part, been submitted to this or any other university for consideration for any other degree or qualification, except for any apparent references to the work of others. Except as noted in the text and acknowledgments, this dissertation is my work and does not contain any results of work done in conjunction with others.

UMCS, Lublin, Poland

Mayank Kumar

Abstract

The sharp increase in plasma temperature, from approximately 5700 Kelvin in the photosphere to several million degrees Kelvin in the corona, along with the origin of the solar wind, remains one of the most enduring problems in space physics. Among the proposed mechanisms, Magnetohydrodynamic (MHD) waves are widely considered a potential mechanism for transporting energy from the lower to the upper solar atmosphere. MHD waves are thought to originate from convective motions beneath the solar surface, which perturb the plasma and magnetic field lines extending into the chromosphere and higher solar atmosphere. These waves, along with other processes such as jets and spicules, can potentially transport energy, mass, and momentum across the solar atmosphere by converting kinetic energy into thermal energy through dissipative mechanisms, such as ion–neutral collisions.

The present Ph.D. thesis project, *A Global MHD Coronal Model*, investigates these processes by integrating local and global approaches to solar atmospheric modeling, utilizing existing cutting-edge multi-fluid chromospheric models in the context of plasma heating and outflows. This project utilizes the Joint Analytical Numerical Approach (JOANNA) code for local modeling and the COolfluid COronal uNstrUcTured (COCONUT) code for global modeling of the solar atmosphere. The localized high-resolution two-fluid simulations focus on the dissipation of MHD waves excited by impulsive perturbations and solar granulation. The obtained results provide detailed insights into wave propagation, their dissipation, and the accompanying plasma heating and outflows. The results reveal that the MHD waves, whether generated by impulsive events or sustained granulation, can contribute to chromospheric heating via ion–neutral collisions. This supports the broader perspective that the cumulative effect of numerous small-scale, intermittent energy-release events may sustain the solar corona. These local insights were extended to global scales by incorporating parameterized source–sink terms into the energy equation of the multi-fluid polytropic COCONUT model. The results highlight the influence of such terms on the plasma dynamics of the solar atmosphere, including plasma heating and outflows, and their potential applications to space weather predictions.

Together, the local and global models presented here offer a consistent framework that connects small-scale dissipation processes with their influence on the large scale. The presented study strengthens the case for MHD wave dissipation as a potential candidate for coronal heating and for driving plasma outflows, thereby advancing our understanding of plasma heating in the upper solar atmosphere.

Keywords: Sun, Photosphere, Chromosphere, Corona, MHD waves, Numerical simulation.

Streszczenie

Gwałtowny wzrost temperatury plazmy od około 5700 kelwinów w fotosferze do kilku milionów kelwinów w koronie, wraz z pochodzeniem wiatru słonecznego, pozostają jednymi z najdłużej istniejących problemów fizyki kosmicznej. Wśród proponowanych mechanizmów, fale magnetohydrodynamiczne (MHD) są powszechnie uznawane za potencjalny mechanizm transportu energii z dolnych do górnych warstw atmosfery Słońca. Uważa się, że fale MHD powstają w wyniku ruchów konwekcyjnych pod powierzchnią Słońca, które zaburzają plazmę oraz linie pola magnetycznego rozciągające się do chromosfery i wyższych warstw atmosfery słonecznej. Fale te, wraz z innymi procesami, takimi jak dżety i spikule, mogą potencjalnie transportować energię, masę i pęd przez atmosferę Słońca, przekształcając energię kinetyczną w energię cieplną za pomocą mechanizmów dyssypatywnych, takich jak zderzenia jonów i cząstek neutralnych.

Niniejszy projekt *Global MHD Coronal Model* ma na celu zbadanie tych procesów poprzez połączenie lokalnych i globalnych podejść do modelowania atmosfery słonecznej, wykorzystując istniejące, najnowocześniejsze wielopłynowe modele chromosferyczne w kontekście ogrzewania plazmy i jej wypływów. W projekcie wykorzystano kod Joint Analytical Numerical Approach (JOANNA) do modelowania lokalnego oraz kod COolfluid COronal uNstrUcTured (COCONUT) do globalnego modelowania atmosfery słonecznej. Lokalizowane symulacje dwupłynowe o wysokiej rozdzielczości koncentrują się na dyssypacji fal MHD wzbudzanych przez zaburzenia impulsowe i granulację słoneczną. Uzyskane wyniki dostarczają szczegółowych informacji na temat propagacji fal, ich dyssypacji oraz towarzyszącego im ogrzewania i wypływów plazmy. Wyniki wskazują, że fale MHD, niezależnie od tego, czy generowane przez zdarzenia impulsowe, czy przez granulację, mogą przyczyniać się do ogrzewania chromosfery poprzez zderzenia jonowo-neutralne. Wspiera to szerszą perspektywę, że skumulowany efekt licznych, małoskalowych, okresowych procesów uwalniania energii może podtrzymywać temperaturę korony słonecznej. Te lokalne spostrzeżenia zostały rozszerzone na skalę globalną poprzez wprowadzenie sparametryzowanych członów źródłowo-ujęciowych do równania energii wielopłynowego, politropowego modelu COCONUT. Wyniki podkreślają wpływ tych członów na dynamikę plazmy w atmosferze Słońca, w tym na ogrzewanie i wypływy plazmy, oraz ich potencjalne zastosowanie w prognozowaniu pogody kosmicznej.

Przedstawione tutaj modele lokalne i globalne wiążą procesy dyssypacji w małej skali z ich wpływem na skalę dużą. Przeprowadzone badania przemawiają za tym, że dyssypacja fal MHD jest potencjalnym czynnikiem ogrzewania korony i generacji wypływów plazmy, pogłębiając tym samym naszą wiedzę na temat ogrzewania plazmy w górnych warstwach atmosfery słonecznej.

Słowa kluczowe: Słońce, fotosfera, chromosfera, korona, fale MHD, symulacja numeryczna

List of Publications

The research presented in this thesis has been documented in peer-reviewed articles. The content of this thesis is based on the following research articles:

1. **Paper I**

   - **Authors: M. Kumar**, K. Murawski, L. Kadowaki, B. Kuźma, and E. K. J. Kilpua
   - **Title:** Impulsively generated waves in two-fluid plasma in the solar chromosphere: heating and generation of plasma outflows
   - **Journal:** Astronomy & Astrophysics
   - **Volume, article number, year:** 681, A60, 2024
   - **DOI:** 10.1051/0004-6361/202245638

   Summary: Kumar et al. (2024a) studies how a launched Gaussian velocity pulse, mimicking an impulsive perturbation, excites and couples MHD wave modes in a partially ionized plasma using a two-fluid (ions + neutrals) model. The authors conduct a comparative analysis of two magnetic-field configurations: a purely vertical field and an inclined field with a small horizontal component. The strictly vertical setup excites magnetoacoustic waves (MAWs), while the inclined field allows for linear coupling of Alfvén and MAWs. The results show that ion–neutral collisions dissipate part of the wave energy, resulting in local plasma heating and outflows. Further studies reveal that coupled Alfvén–MAWs are considerably more effective in heating the solar chromosphere than MAWs alone. The transported energy and mass flux obtained remain insufficient to compensate for radiative losses or to supply the entire solar wind in the upper solar atmosphere.

   The author's contribution: I carried out all the necessary numerical simulations; obtained the numerical data, results, and visualizations; and performed the associated analyses. I authored the entire manuscript and prepared it for submission. Prof. Krzysztof Murawski assisted in setting up and refining the numerical code, as well as providing comments and guidance on improving the manuscript. The remaining co-authors further provided their comments and suggestions to improve the manuscript.

2. **Paper II**

    - **Authors: M. Kumar**, K. Murawski, B. Kuźma, E. K. J. Kilpua, S. Poedts, and R. Erdélyi
    - **Title:** Numerical experiment on the influence of granulation-induced waves on solar chromosphere heating and plasma outflows in a magnetic arcade
    - **Journal:** The Astrophysical Journal
    - **Volume, article number, year:** 975, 3, 2024
    - **DOI:** 10.3847/1538-4357/ad746

    Summary: Kumar et al. (2024b) investigates how granulation-induced motions beneath the photosphere excite a broad spectrum of waves, such as Alfvén, magnetoacoustic–gravity, and neutral acoustic–gravity waves. These excited waves dissipate some of their energy due to ion–neutral collisions, which cause localized heating in the solar chromosphere and drive associated plasma outflows. The paper reports that realistic photospheric drivers (granulation) can power heating and plasma outflows in the solar atmosphere, supporting the coronal heating and solar wind origin problem.

    The author's contribution: I performed all the required numerical simulations; obtained the numerical data, results, and visualizations; and carried out the analysis. I wrote the entire manuscript and prepared it for submission. Prof. Krzysztof Murawski assisted in setting up the numerical code and its subsequent adjustment and provided comments and guidance on writing the manuscript. The remaining co-authors provided comments and suggestions to enhance the manuscript.

3. **Paper III**

    - **Authors: M. Kumar**, B. Kuźma, S. Poedts, K. Murawski, and E. K. J. Kilpua
    - **Title:** Investigating the Influence of the Source–Sink Terms in a Two-Fluid Global Coronal Model
    - **Journal:** Astronomy & Astrophysics
    - **Status:** Submitted

    Summary: Kumar et al. (2025) extend global MHD modeling into a two-fluid model for space weather applications. The authors investigate the influence of source–sink terms on coronal dynamics and test steady-state solutions using magnetograms from solar minimum and maximum. The paper reports that the inclusion of such source–sink terms is crucial to reproduce realistic density, temperature, and flow profiles and has potential applications in space weather forecasting. The obtained results reveal that the solver robustly handles global scales, reproducing large-scale coronal structures.

The author's contribution: I performed all the numerical simulations; obtained numerical data; and visualized and analyzed them for the manuscript. I implemented a new source–sink term in the COCONUT model within the framework of a two-fluid model. Furthermore, I authored the manuscript and prepared it for final submission. Dr. Błażej Kuźma helped in setting up the numerical code and its operations. Prof. Stefaan Poedts proposed implementing new source–sink terms. All co-authors provided further comments to improve the manuscript.

Additional review paper not included in this thesis:

- **Authors:** T. Barata, D. Del Moro, R. Erdélyi, J. Fernandes, R. Gafeira, M. K. Georgoulis, K. Murawski, A. Nindos, O. Oliveira, S. Patsourakos, K. Petrovay, S. Poedts, R. Vanio, A. Afanasiev, M. B. Korsós, A. Boiko, L. Annie John, S. Biswal, S. Bourgeois, S. Chierichini, G. Francisco, A. André-Hoffmann, E. Husidic, S. Koya, **M. Kumar**, R. Mugatwala, G. Nogueira, A. Wagner, and E. Kilpua
- **Title:** The Space Weather Awareness Training Network SWATNet
- **Journal:** Journal of Space Weather and Space Climate
- **Status:** Submitted

Conferences and Activities

During my Ph.D. work, I participated in the following programs:

- International conferences
  - **Conference name:** Space Weather Awareness Training Network (SWATNet) final conference (9 – 14 February 2025)
  - **Place:** Helsinki, Finland
  - **Task:** Oral presentation
  - **Title:** Numerical experiment on the influence of granulation-induced waves on solar chromosphere heating and plasma outflows in a magnetic arcade

  - **Conference name:** European Geosciences Union (EGU) (14 – 19 April 2024)
  - **Place:** Vienna, Austria
  - **Task:** Oral presentation
  - **Title:** Solar granulation-generated chromosphere heating and plasma outflows in the two-fluid magnetic arcade

  - **Conference name:** European Space Weather Week (ESWW) (20 – 24 November 2023)
  - **Place:** Toulouse, France
  - **Task:** Poster presentation
  - **Poster title:** Impulsively generated waves in two-fluid plasma in the solar chromosphere: heating and generation of plasma outflows

  - **Conference name:** UK Space Weather and Space Environment Meeting, Cardiff, Wales, United Kingdom (12 – 15 September 2023)
  - **Place:** Cardiff, Wales, United Kingdom
  - **Task:** Oral presentation
  - **Title:** Impulsively generated waves in two-fluid plasma in the solar chromosphere: heating and generation of plasma outflows

  - **Conference name:** Physics Day (29 – 31 March 2023)
  - **Place:** Tampere University, Tampere, Finland
  - **Task:** Poster presentation
  - **Poster title:** Impulsively generated waves in two-fluid plasma in the solar chromosphere: heating and generation of plasma outflows

- Activities
  - **Industrial internship**
  - **Institute:** Space Applications Services, Brussels, Belgium
  - **Duration:** 24 June – 24 September 2024

  - **Solar observations**
  - **Institute:** Gyula Bay Zoltán Solar Observatory, Gyula, Hungary
  - **Duration:** 1 – 31 July 2022

  - **Summer school title:** Space Weather Simulation Summer School (SWSSS) (24 July – 4 August 2023)
  - **Conducted by:** University of Michigan and Massachusetts Institute of Technology, USA

  - **Workshop title:** SWATNet workshop 6: Entrepreneurship in Space Physics (15 –16 June 2023)
  - **Conducted by:** Eötvös Loránd University, Budapest, Hungary

  - **School title:** SWATNet summer school 3: Space weather and our technology-based society (12 – 14 June 2023)
  - **Conducted by:** Eötvös Loránd University, Budapest, Hungary

  - **Workshop title:** SWATNet workshop 5: Mini MBA (23 – 24 March 2023)
  - **Conducted by:** University of Sheffield, Sheffield, United Kingdom

  - **Workshop title:** SWATNet workshop 3: Solar activity and space weather: Physics behind the process (29 – 30 September 2022)
  - **Conducted by:** Academy of Athens and University of Ioannina, Athens, Greece

  - **Summer school title:** SWATNet summer school 2: Sun–Earth interactions (26 – 28 September 2022)
  - **Conducted by:** Academy of Athens and University of Ioannina, Athens, Greece

  - **Workshop title:** SWATNet workshop 4: Communication and outreach (20 – 22 June 2022)
  - **Conducted by:** University of Coimbra, Coimbra, Portugal

  - **Workshop title:** SWATNet workshop 2: Managing research projects (Online, 15 – 16 March 2022)

- **Conducted by:** KU Leuven, Leuven, Belgium, and UMCS, Lublin, Poland

- **Workshop title:** SWATNet workshop 1: Communicating science (Online, 10 – 11 January 2022)
- **Conducted by:** University of Rome Tor Vergata, Rome, Italy

- **Summer school title:** SWATNet summer school 1: Introduction to space weather (Online, 8 – 12 November 2021)
- **Conducted by:** University of Helsinki, Helsinki, and University of Turku, Turku, Finland

The publications and the present thesis are part of the **Space Weather Awareness Training Network (SWATNet)**, which has received funding from the European Union's Horizon 2020 research and innovation programme under the Marie Skłodowska-Curie Innovative Training Networks, Grant Agreement No. 955620. The thesis's content solely expresses the author's viewpoint. It does not reflect that of the European Commission (EC), which also disclaims any liability for any potential uses of the information and data.

Dissertation structure and content overview

The content of this thesis is structured as follows. Chapter 1 introduces the basics of plasma, the Sun, and its atmosphere, as well as basic mathematical frameworks and modeling techniques for describing plasma. Chapter 2 describes the motivation and aims of the dissertation. Chapter 3 derives the multi-fluid and magnetohydrodynamic (MHD) equations from the kinetic equations in the context of this thesis. Chapter 4 discusses dispersion relations for linear MHD waves propagating in a homogeneous medium. Chapter 5 presents numerical approaches and methods for solving multi-fluid equations, including a brief note on the adopted model and numerical code. Chapters 6 and 7 discuss the numerical results. Chapter 8 concludes the thesis and addresses possible future work.

List of Abbreviations

- **SWATNet** – Space Weather Awareness Training Network
- **ISRO** – Indian Space Research Organisation
- **NASA** – National Aeronautics and Space Administration
- **ESA** – European Space Agency
- **EST** – European Solar Telescope
- **SDO** – Solar Dynamics Observatory
- **HMI** – Helioseismic and Magnetic Imager
- **DKIST** – Daniel K. Inouye Solar Telescope
- **AIA** – Atmospheric Imaging Assembly
- **EUV** – Extreme UltraViolet
- **MHD** – Magnetohydrodynamics
- **LHS** – Left - Hand Side
- **RHS** – Right - Hand Side
- **MAWs** – Magnetoacoustic Waves
- **RTI** – Rayleigh – Taylor Instability
- **PDE** – Partial Differential Equation
- **ODE** – Ordinary Differential Equation
- **ParaView** – Parallel Visualization
- **CFL** – Courant – Friedrichs–Lewy
- **PIL** – Polarity Inversion Line
- **IRIS** – Interface Region Imaging Spectrograph
- **PSP** – Parker Solar Probe
- **EUHFORIA** – EUropean Heliospheric FORcasting Information Asset
- **JOANNA** - JOint ANalytical Numerical Approach
- **COCONUT** - COolfluid COronal uNstrUcTured

Contents

List of Figures

List of Tables

Chapter 1

Introduction

1.1 Understanding plasma: definition and properties

In physics, matter refers to everything in the visible universe that has non-zero mass and occupies some space. Matter exists in one of four distinct states: solid, liquid, gas, and plasma. The state of matter is primarily determined by the force acting between the constituent particles (e.g., ions, atoms, or molecules). In a *solid* state of matter, the force between neighboring particles keeps the particles close together, rendering the particles immobile and only able to vibrate. Consequently, a solid has a finite shape and volume. When the temperature of a solid rises above its melting point, the force binding the constituent particles together weakens, causing it to transition to another fundamental state of matter called a *liquid*. Unlike in solids, the particles in the liquid state are not tightly bound, resulting in limited particle mobility. This limited mobility allows liquids to flow and assume the shape of the container into which they are poured. As the temperature of liquids is raised to their boiling point, the effective force binding the particles is weakened further; consequently, it transitions to another fundamental state of matter called *gas*. In a gas, the separation between particles is much greater than the size of the constituent particles themselves. As a result, gas has low density and viscosity, and its constituent particles spread out across the container they fill. When a neutral gas is heated enough to free some of its electrons from the atoms or molecules, it transforms into another fundamental state of matter known as *plasma*—a partially ionized gas composed of ions, electrons, and remaining neutral atoms. The content in this thesis primarily deals with plasma.

Plasma is the most ubiquitous of the four states of matter, accounting for almost 99 % of the visible universe. The word plasma originates from Ancient Greek (plásma), meaning *moldable substance*. In broad terms, plasma is commonly defined as an electrically quasi-neutral gas comprising unbound positively and negatively charged particles that can be influenced by electric and magnetic fields. Unlike solid, liquid, and gas, plasma is relatively rare on Earth, thus limiting our everyday encounters. Examples of plasma on Earth include lightning, welding arcs, neon and fluorescent tubes, among others. Beyond Earth, however, plasma is abundant—stars, nebulae, and even interstellar space. The solar wind permeates the solar system, and the Earth itself is surrounded by plasma trapped in its magnetic field.

However, not all ionized gas qualifies as plasma. Therefore, to differentiate plasma from other states of matter, specific critical parameters must be satisfied. In nature, non-zero temperatures generally lead to a small degree of ionization in gas; for hydrogen gas in equilibrium, Saha's equation gives,

$$\boxed{\frac{I^2}{1-I} = 2.4 \times 10^{21} \times \frac{T^{3/2}}{n_i} \exp\left(-\frac{U_i}{k_B T}\right)} \tag{1.1}$$

Here $I = n_i/n_{tot}$ is the degree of ionization and $n_{tot} = n_i + n_n$ is the total number density with $n_{i,n}$ denoting the number density of ions and neutrals in m^{-3}. The symbol T is the temperature of the gas in K, U_i is the ionization energy, and k_B is the Boltzmann constant. Physically, Eq. 1.1 states how the degree of ionization in a gas at finite temperature depends on both temperature and density. As T rises, I increases (especially when $U_i \ll k_B T$), and decreases with higher n_{tot} due to the likelihood of recombination. This is why highly ionized plasmas are favored by high temperature and low density. This combination of conditions is easily met in astrophysical environments, but not on Earth.

So far, we have given only a general description of plasma. A more precise definition provided by Chen et al. (1984) states that *a plasma is a quasi-neutral gas of charged and neutral particles that exhibit collective behavior*. Quasi-neutrality and collective effects drive the constraints on characteristic length, time scale, and particle number density. These criteria are essential for distinguishing plasma from other states of matter, which are described in detail in the following subsections.

1.1.1 Quasi-neutrality and collective behavior

Plasma primarily consists of positively and negatively charged particles, making it electrically neutral on a large scale. However, on a small scale or under certain conditions (e.g., the presence of an electric field), a local imbalance between positive and negative charges can arise. This charge separation leads to a phenomenon known as *Debye shielding*, where plasma rearranges its charges to screen the rest of the plasma from the electric field, effectively restoring quasi-neutrality (Martínez-Fuentes et al., 2017). Debye shielding is a fundamental characteristic of plasma that provides insight into plasma quasi-neutrality and establishes a minimum length scale below which a fluid cannot be treated as plasma.

Let ψ be the electric potential of a plasma grid embedded in the plasma system. If n_i and n_e, respectively, are the number densities of ions and electrons, from the Poisson equation we have (Linhart et al., 1961, Chen et al., 1984)

$$\nabla^2 \psi = q\left(\frac{n_i - n_e}{\epsilon_0}\right) \tag{1.2}$$

Here ϵ_0 is the electric permittivity of free space and q is the electric charge taken here equal to $-e$. Assuming plasma is cold ($T \to 0$) and in thermal equilibrium (Pathare et al., 2015), the statistical distribution of the velocity of a particle (v) can be described by the Maxwell–Boltzmann distribution function $g(v)$, which is given by

$$g(v) = U_0 \, \exp\left(\frac{-(mv^2/2 + q\psi)}{k_B T_e}\right) \tag{1.3}$$

The notion U_0 is constant, T_e is the electron temperature, m is the mass of the particle, and $q\psi$ is the electrical potential energy. Now, by integrating Eq. 1.3 over the entire velocity space, we can determine n_e as

$$n_e = \int_{-\infty}^{\infty}\int_{-\infty}^{\infty}\int_{-\infty}^{\infty} U_0 \exp\left(\frac{-(mv^2/2 + q\psi)}{k_B\, T_e}\right) \, d^3v \tag{1.4}$$

Here, the term $q\psi$ is independent of v; therefore, it can be taken out of the integral. The remaining part can be integrated over v using spherical coordinates, where $v^2 = v_x^2 + v_y^2 + v_z^2$ and the volume element $d^3v = v^2 \, \sin\theta \, dv \, d\theta \, d\phi$. Setting the limits $0 \leq v \leq \infty$, $0 \leq \theta \leq \pi$ and $0 \leq \phi \leq 2\pi$, we get

$$n_e = U_0 \, \exp\left(-\frac{q\psi}{k_B T_e}\right) \int_0^{\infty}\int_0^{\pi}\int_0^{2\pi} \exp\left(\frac{-mv^2/2}{k_B T_e}\right) v^2 \, \sin\theta \, dv \, d\theta \, d\phi \tag{1.5}$$

Using the standard Gaussian integral,

$$\int_0^{\infty} v^2 \, \exp\left(-\frac{mv^2/2}{k_B T_e}\right) \, dv = \left(\frac{2k_B T_e}{m}\right)^{3/2} \frac{\sqrt{\pi}}{2} \tag{1.6}$$

we obtain

$$n_e = U_0 \left(\frac{2\pi k_B T_e}{m}\right)^{3/2} \, \exp\left(-\frac{q\psi}{k_B\, T_e}\right) \tag{1.7}$$

Setting $q = -e$ and noting $n_e = n_\infty \equiv U_0 \, (2\pi k_B T_e/m)^{3/2}$ for $\psi \to 0$ at ∞, we get

$$n_e = n_\infty \, \exp\left(\frac{e\psi}{k_B T_e}\right) \tag{1.8}$$

The above expression is derived for electrons. Now, for n_i, we assume the whole background is filled with ions of number density n_i; therefore, the density far away ($\psi \to 0$) is n_∞. We have

$$n_i \approx n_\infty \tag{1.9}$$

Substituting Eqs. 1.8 & 1.9 for n_i and n_e in Eq. 1.2, for the one-dimensional case (1-D), we have

$$\frac{d^2\psi}{dx^2} = \frac{e\,n_\infty}{\epsilon_0}\left\{\exp\left(\frac{e\psi}{k_B\,T_e}\right) - 1\right\} \tag{1.10}$$

In the region where $k_B T_e \gg e\psi$, the term $\exp(e\psi/k_B T_e)$ can be expanded in a Taylor series:

$$\frac{d^2\psi}{dx^2} = \frac{e\,n_\infty}{\epsilon_0}\left\{1 + \frac{\left(\frac{e\psi}{k_B T_e}\right)}{1!} + \frac{\left(\frac{e\psi}{k_B T_e}\right)^2}{2!} + \cdots - 1\right\} \tag{1.11}$$

Keeping only the linear term, Eq. 1.11 reduces to

$$\frac{d^2\psi}{dx^2} - \frac{1}{\lambda_D^2}\psi = 0 \tag{1.12}$$

Here, λ_D denotes the Debye length defined as:

$$\boxed{\lambda_D^2 = \frac{\epsilon_0 k_B T_e}{e^2\,n_\infty}} \tag{1.13}$$

Now, the general solution of Eq. 1.12 can be written in the form

$$\psi = A\,\exp\left(-\frac{x}{\lambda_D}\right) + B\,\exp\left(\frac{x}{\lambda_D}\right) \tag{1.14}$$

Here, A and B are constants. Since $x \to \infty$ implies $\psi \to 0$, B must be zero. This simplifies the solution to

$$\psi = A\,\exp\left(-\frac{x}{\lambda_D}\right) \tag{1.15}$$

Physically, λ_D is the measure of the shielding thickness. Predictably, as n_∞ increases, λ_D decreases (Eq. 1.13), since each layer now will hold more charges. On the other hand, as thermal agitation ($k_B T_e$) increases, λ_D also increases. Without it, the cloud would collapse into an infinitely thin layer. With the Debye length, we are at the stage of defining quasi-neutrality. *Quasi-neutrality is the fundamental property of plasma, which occurs when the densities of oppositely charged particles are approximately equal, i.e., $n_i \simeq n_e$, but not so exactly equal as to eliminate key features of the electromagnetic field.* Quasi-neutrality imposes a condition on the characteristic length: to maintain quasi-neutrality, we must have $\lambda_D \ll L$, where L represents the characteristic size of the plasma system. This physical condition shields the bulk of the plasma from the electric field arising from the local concentration of charge or from external potentials introduced in the plasma medium at a very short distance compared to L. The Debye shielding described here leads to the generation of a charged cloud known as the *Debye sphere*. The number of charged particles in the Debye sphere is given by

$$\boxed{n_D = \frac{4}{3}\lambda_D^3 n_e} \tag{1.16}$$

For the shielding to be effective, we must have a large number of particles within the Debye sphere, i.e., $n_D \gg 1$.

Besides quasi-neutrality, *collective behavior* is another crucial physical trait that qualifies ionized gas as plasma. In plasma, *collective behavior refers to how charged particles behave as a group rather than as individual particles.* This occurs when long-range electromagnetic (EM) forces are far more robust than any particular force among the particles (e.g., drag forces in collisional plasma). As a result, the constituent particles in plasma are influenced not only by the local state but also by the overall electric and magnetic fields generated by the collective motions of plasma elements in other, far regions.

In addition to quasi-neutrality, the characteristic time scale is another crucial factor in defining plasma. In ionized gas, the dynamics are primarily controlled by hydrodynamic forces resulting from frequent collisions between particle species. However, when the EM forces from the Coulomb interaction between charged particles outweigh the ordinary collisional forces, the ionized gas starts behaving like a plasma. If Ω is the plasma oscillation frequency and ω_c is the mean collision frequency between ions and neutrals, the condition on the time scale for ionized gas to qualify as plasma requires

$$\boxed{\Omega \gg \omega_c} \tag{1.17}$$

In this condition, the plasma is often referred to as a collisionless plasma. It is worth mentioning that the condition given by Eq. 1.17 is necessary only for the fluid model of plasma.

1.1.2 Criterion of plasma formation

The preceding section explains critical physical parameters that must be considered for an ionized gas to be classified as plasma. To summarize, three conditions must be met for ionized gas to qualify as plasma (Chen et al., 1984).

1. The dimension of the plasma system L must be much greater than the Debye length λ_{D}, i.e., $L \gg \lambda_{\mathrm{D}}$.

2. The number of particles in the Debye sphere N_D must be large to shield the potential or electric field effectively, i.e., $N_D \gg 1$.

3. The frequency of plasma oscillation Ω must be much greater than the mean collision frequency ω_c between ions and neutrals, i.e., $\Omega\tau_c \gg \omega_c$.

The closest star to the Earth — the Sun — is a natural plasma laboratory, where plasma is abundant. The Sun, with a diameter (L) of approximately 1.39×10^9 km, is enormous compared to the Debye length (λ_D), which is of the order of millimeters or less in the solar atmosphere. The number density of plasma in the Sun is approximately $10 \times 10^{25}\,\mathrm{m}^{-3}$, resulting in a Debye sphere containing a large number of particles, exceeding the minimum requirement for Debye shielding ($N_D \gg 1$). The large dimension of the plasma system and the high particle count in the Debye sphere ensure effective Debye shielding, allowing the solar plasma to shield itself from locally generated electric fields and maintain stability on the large scale. Additionally, due to high density and strong magnetic field, $\Omega \gg \omega_c$, meaning that charged particles complete many gyro-orbits before experiencing significant collisions with neutrals. As a result, collisions are rare compared to the frequency of plasma oscillations, reinforcing the collective, collisionless nature of the solar plasma.

Similar characteristics, such as large physical size, high temperatures, and high-density environments, are commonly found in other astrophysical objects, including stars, neutron stars, the interstellar medium, and accretion disks around black holes. The absence of such extreme conditions on Earth explains why plasma is rare under terrestrial conditions but becomes ubiquitous beyond our planet.

1.2 Mathematical frameworks for plasma modeling

Due to the high particle density and strong collective behavior of plasma, its physical and mathematical description is far more complex than that of the other states of matter (solid, liquid, gas). A complete description of plasma requires information on critical physical quantities, both electromagnetic and thermodynamic, such as position (r), velocity (V), density (ρ), and temperature (T). Together, these quantities provide a comprehensive view of the plasma's behavior and its response to external fields and forces, enabling the analysis of critical physical phenomena such as wave propagation, plasma stability, and magnetic reconnection, etc.

With this, plasma modeling can be defined as *the process of solving equations of motion that characterize the state of plasma in space and time.* Various mathematical approaches exist for modeling plasma, including single-particle, kinetic, fluid, hybrid, and gyrokinetic models, etc., each offering different levels of detail and computational complexity. These models are typically coupled with Maxwell's equations for EM fields or the Poisson equation for electrostatic fields. The following subsections provide a brief overview of widely used mathematical methods for describing the plasma state (Inan et al., 2010).

1.2.1 Particle model

Single-particle orbit theory describes the motion of individual particles in a plasma (comprising electrons and ions) in the presence of an applied electromagnetic field by solving their equation of motion. The trajectory of each particle is governed by Newton's second law with the Lorentz force law:

$$\boxed{m_s \frac{d^2\mathbf{r}_s}{dt^2} = q_s\Big(\mathbf{E} + \mathbf{v}_s \times \mathbf{B}\Big)} \tag{1.18}$$

Here, $\mathbf{r}_s$, $\mathbf{v}_s = d\mathbf{r}_s/dt$, m_s, and q_s respectively denote the position, velocity, mass, and charge of the constituent species. The notations $\mathbf{E}$ and $\mathbf{B}$ are the electric and magnetic fields, respectively (Dendy, 1995). Unfortunately, the description of plasma is not as straightforward as it appears from Eq. 1.18. The single-orbit theory is practical only for plasmas of relatively low densities where particle interactions can be neglected. An example is the interstellar medium, which has a particle number density of order $1\,\mathrm{cm}^{-3}$. In contrast, many plasmas are far denser; e.g., the core of our Sun has densities exceeding $10^{26}\,\mathrm{cm}^{-3}$, while fusion reactors operate at densities of approximately $10^{13}\,\mathrm{cm}^{-3}$. In such a dense plasma environment, tracking the intricate journey of each particle becomes computationally impractical, and alternative modeling approaches are required.

The single-orbit theory overlooks the self-consistent electromagnetic fields (EM fields hereafter) that arise from the collective behavior of the plasma. The assumption of an externally applied EM field rather than one generated by the particles themselves ignores the realistic treatment of plasma. In such a situation, the constituent particles generate and influence EM fields through their charges and currents, which requires a self-consistent treatment. Furthermore, the single-particle orbit theory fails to predict characteristic parameters such as gas pressure, mass density, temperature, and bulk flow, which are macroscopic averages over many particles, thereby limiting its application to predicting plasma behavior on a large scale (Boyd et al., 2003; Zita, 2006). Due to these limitations, more sophisticated models, such as kinetic theory, magnetohydrodynamics (MHD), or multi-fluid models (the primary focus of this thesis), are typically employed to represent the plasma state more accurately, especially in systems where self-consistent fields and collective effects cannot be neglected.

1.2.2 Kinetic theory of plasma

Kinetic theory describes plasma statistically, replacing the detailed motion of microscopic particles with measurable macroscopic parameters that characterize the plasma as a whole. The kinetic theory serves as the foundation for most plasma models, which disregard the identity of individual particles and focus on the statistical behavior of species, treating them as a continuous medium. Central to this framework is the *distribution function*, $f_s(\mathbf{r}_s, \mathbf{v}_s, t)$, which defines how plasma particles are distributed throughout phase space. This six-dimensional phase space contains both the position and momentum (or velocity) information for each particle. The time evolution of the distribution function in a collisionless plasma is governed by the *Vlasov equation (collisionless Boltzmann equation)* (Koskinen, 2011; Chaudhary et al., 2018):

$$\boxed{\frac{\partial f_s}{\partial t} + \mathbf{v}_s \cdot \frac{\partial f_s}{\partial \mathbf{r}_s} + \frac{q_s}{m_s}\left(\mathbf{E} + \mathbf{v}_s \times \mathbf{B} + \frac{m_s}{q_s}\mathbf{g}\right) \cdot \frac{\partial f_s}{\partial \mathbf{v}_s} = 0} \tag{1.19}$$

Here, the symbols m_s, $\mathbf{v}_s$, and q_s respectively denote the particle mass, velocity, and charge of plasma species s. The notions $\mathbf{E}$ and $\mathbf{B}$ are the self-consistent electric and magnetic fields, respectively. The term $\mathbf{g}$ represents external body forces such as gravity. More precisely, the *Vlasov equation* describes the evolution of the distribution function in 6-D phase space for plasma in which charged particles primarily interact through long-range Coulomb forces mediated by self-consistent $\mathbf{E}$ and $\mathbf{B}$ fields. The motion of electric charges modifies currents and their distributions, which in turn alter the fields, making the problem inherently self-consistent. In many astrophysical and laboratory plasma systems, the most dominant interactions are due to long-range Coulomb encounters whose averaged effect is taken into account by the Lorentz force term, $q(\mathbf{E} + \mathbf{v} \times \mathbf{B})$.

When collisional and other interaction effects cannot be neglected, the *Boltzmann equation* provides the more general form:

$$\boxed{\frac{\partial f_s}{\partial t} + \mathbf{v}_s \cdot \frac{\partial f_s}{\partial \mathbf{r}_s} + \frac{q_s}{m_s}\left(\mathbf{E} + \mathbf{v}_s \times \mathbf{B} + \frac{m_s}{q_s}\mathbf{g}\right) \cdot \frac{\partial f_s}{\partial \mathbf{v}_s} = \left(\frac{\partial f_s}{\partial t}\right)_c + \left(\frac{\partial f_s}{\partial t}\right)_{other}} \tag{1.20}$$

The terms on the right-hand side account for binary-collision effects $\left(\frac{\partial f_s}{\partial t}\right)_c$ and $\left(\frac{\partial f_s}{\partial t}\right)_{other}$ for other processes such as charge-exchange collisions, ionization, chemical reactions, and wave scattering. The *Vlasov equation* is thus a special case of the *Boltzmann equation*, with collisions and other interaction terms set to zero. Kinetic theory models plasma at the level of individual particle dynamics; therefore, it retains information about velocity-space structure and non-equilibrium effects. This enables the study of phenomena requiring detailed information on velocity distribution, such as *Landau damping*. It is also suitable for studying plasmas with strong temperature gradients or velocity anisotropies, common in Earth's magnetosphere. The kinetic framework presented here serves as the theoretical foundation for most plasma fluid models, which are discussed in the following subsection.

1.2.3 Fluid approximation in plasmas

The kinetic model described in the previous subsection provides the most complete representation of plasma physics, retaining all relevant microscopic details. However, this accuracy comes at the cost of high mathematical complexity and computationally expensive numerical simulation. This often makes fully kinetic simulations challenging for many practical problems. Therefore, alternative approaches are frequently employed. *Fluid theory* simplifies kinetic theory by averaging the distribution function over velocity, effectively smoothing out velocity-space details, and focuses on the macroscopic picture of plasma. Instead of tracking individual particles, fluid theory offers a simpler alternative by describing only the bulk quantities of plasma—such as mass density, average velocity, and temperature—for each plasma species. This treatment models plasma as a continuous medium with macroscopic variables obtained by taking the velocity moments of the particle distribution function $f(\mathbf{r}_s, \mathbf{v}_s, t)$ introduced in kinetic theory (Koskinen, 2011; Inan et al., 2010).

This approach reduces mathematical complexity and computational cost; however, it does so at the expense of sacrificing information on small-scale kinetic effects and non-Maxwellian features of the distribution. Unlike kinetic theory, which derives quantities such as mass density, momentum, and energy self-consistently from a single distribution function, fluid theory describes plasma behavior using equations such as mass conservation, momentum, and energy, obtained by taking the velocity moments of the Boltzmann equation. This approach leads to an infinite hierarchy of equations, since each moment depends on the next higher one. In practice, the chain of equations is typically closed by making assumptions about these higher-order moments, often through the equation of state (see chapter 3).

Fluid theory assumes that collisions and interactions occur frequently enough to establish local thermodynamic equilibrium and sustain a Maxwellian velocity distribution function. Furthermore, it also requires that the characteristic length scale of the system be much larger than the Debye length and particle gyroradii. These assumptions introduce approximations that limit the model's applicability and the range of phenomena it can accurately describe. For example, fluid theory loses validity in plasmas with large temperature gradients, shocks, or velocity-space instabilities, as well as in regimes where the Maxwellian assumption breaks down. Another notable example is *Landau damping*—a purely kinetic phenomenon in which waves exchange energy with particles in the absence of collisions. Such an effect cannot be captured by fluid models. MHD and multi-fluid theory are two widely used frameworks in fluid dynamics. Chapter 3 of this thesis provides an in-depth discussion of the multi-fluid approach.

1.2.4 Hybrid kinetic-fluid approach

The hybrid kinetic–fluid theory models ions kinetically to capture their non-Maxwellian distributions, while electrons are treated as a fluid. This simplification for electrons reduces computational costs while preserving essential physics governing magnetic and electric field dynamics. Such a formulation enables a more accurate description of plasma dynamics in cases where different species exhibit divergent physical behaviors. Hybrid models are particularly effective at capturing plasma systems such as the solar wind and Earth's magnetosphere. Examples of hybrid simulation techniques include *Hybrid Particle-in-Cell (PIC)* and *Hybrid Vlasov* (Von Alfthan et al., 2014; Yang et al., 2023). This approach strikes a balance between computational efficiency and physical accuracy, albeit with implementation challenges. Coupling methods involving interactions between fluid and kinetic components must be handled carefully to ensure proper matching of boundary conditions and temporal characteristics. Hybrid simulations can also suffer from numerical instabilities due to the differing temporal and spatial resolution requirements of ions and electrons.

In many plasma problems, neither fluid nor kinetic theory alone can provide an adequate description of plasma behavior. In such cases, tracking the individual trajectories of particles using orbital theory may be necessary—a complex task again. Fortunately, modern computers are advanced enough to simulate the intricate behavior of a considerably large number of particles in the system, although limitations remain. High-performance computing plays a key role in bridging the gap between theoretical predictions and regimes where conventional models fail to explain observed phenomena.

1.3 The Sun and its solar atmosphere: General overview

The Sun, our nearest star, is a massive sphere of plasma that accounts for approximately 99.86 % of the total mass of the solar system. Like other stars, it serves as a spectacular laboratory for plasma physics, offering valuable insights into the behavior of hot, ionized matter. The Sun is not only a primary source of energy for Earth but also a dynamic star whose activity influences all life on our planet, both directly and indirectly. Studying the Sun, therefore, is essential for both understanding its physics and assessing its influence on Earth's atmosphere and space weather events throughout the solar system (Fig. 1.1a). Space weather phenomena driven by solar activity include the solar wind and embedded interplanetary transients, solar energetic particles (SEPs), auroras, dramatic variations in the radiation belts, geomagnetic storms, and geomagnetically induced currents. As a G-type main-sequence star, the Sun serves as an excellent example of stellar evolution. By studying its structure and dynamics, we gain a comprehensive understanding of how stars are typically formed, evolve, and ultimately die. Tab. 1.1 summarizes the fundamental physical parameters of the Sun.

1.3.1 Composition of the Sun

The Sun is primarily composed of hydrogen (H) and Helium (He), respectively accounting for approximately 73 % and 25 % of the its matter (Payne, 1925). Other heavier elements, such

Table 1.1: The physical parameters of the Sun (*Credit: NASA*).

Physical parameters	Numerical values
Mass	1.98×10^{30} kg
Age	4.5×10^{9} years
Radius	6.96×10^{5} km
Mass density	$1.408 \times 10^{3}\,\mathrm{kg\,m^{-3}}$
Gravity on surface	$274\,\mathrm{m\,s^{-2}}$
Luminosity	$3.82 \times 10^{26}\,\mathrm{J\,s^{-1}}$
Mean distance from planet Earth	1AU (1.496×10^{11} m)
Mass conversion rate	$4.260 \times 10^{10}\,\mathrm{kg\,s^{-1}}$
Mean energy production	$1.925 \times 10^{-4}\,\mathrm{J\,kg^{-1}\,s^{-1}}$
Surface emission	$6.294 \times 10^{7}\,\mathrm{J\,m^{2}\,s^{-1}}$
Escape velocity	$617.6\,\mathrm{km\,s^{-1}}$
Effective temperature	5772 K
Surface gas pressure (top of photosphere)	0.868 mb
Sun-spot cycle	11.4 years
Typical polar field	1-2 Gs
Typical sunspots field	3000 Gs

Table 1.2: Composition of the Sun in terms of mass and number of atoms percentage (*Credit: NASA*).

Element	Mass (%)	Number of atom (%)
H	73.4	92
He	25	7.8
Nitrogen	0.09	0.008
Carbon	0.20	0.20
Neon	0.16	0.01
Oxygen	0.80	0.06
Magnesium	0.06	0.003
Sulfur	0.05	0.002
Silicon	0.09	0.004
Iron	0.14	0.003

as Carbon (C), Oxygen (O), Nitrogen (N), and Iron (Fe), make up roughly 2 % of the mass of our star. Tab. 1.2 briefly summarizes the main elements, corresponding mass, and number percentage.

1.3.2 Internal structure of the Sun

The Sun is not a homogeneous ball of gas but rather comprises several layers. Its internal structure mainly consists of the *core*, *radiative zone*, *tachocline*, and *convective zone*. Each

(a) (b)

Figure 1.1: (a)A Coronal Mass Ejection (CME), a gigantic bubble of coronal plasma filled with magnetic field lines, shoots off the surface of the Sun towards the Earth, followed by its subsequent impact on the magnetosphere of the Earth. (b) The northern lights (aurora borealis) illuminating the night sky due to the perturbations in the Earth's magnetosphere caused by the CME. These phenomena are connected with space weather, which deals with varying conditions of the solar system and its heliosphere (*Credit: NASA*).

layer differs from the others in terms of distinct physical properties, such as temperature, thickness, gas pressure, and composition of matter. The following subsections provide a brief description of each layer.

The core

The *core* is the innermost and central layer of the Sun. This layer is also known as the engine of the Sun, where hydrogen nuclei undergo the proton-proton chain, producing helium and releasing vast amounts of energy. The core is responsible for 99 % of the total energy output, with the remaining 1 % of the energy generated from another sequence of fusion reactions, known as the Carbon-Nitrogen-Oxygen (CNO) cycle. It extends to roughly $0.25\,R_\odot$, where $R_\odot$ denotes the solar radius. The conditions in the core are extreme: the temperature reaches approximately 15 million K, the pressure exceeds 250 billion atmospheres, and the mass density is around $150\,\mathrm{g\ cm^{-3}}$.

The radiative zone

The *radiative zone* caps the core, spanning around $0.25 - 0.70\,R_\odot$, making it the thickest layer of the Sun. It is named for its dominant mode of energy transport—radiative diffusion—where energy is carried outward by radiation rather than the bulk motion of plasma (convection). The density falls from $20\ \mathrm{g\,cm^{-3}}$ at the base to only $0.2\,\mathrm{g\,cm^{-3}}$ near the top. The relatively

(a) (b)

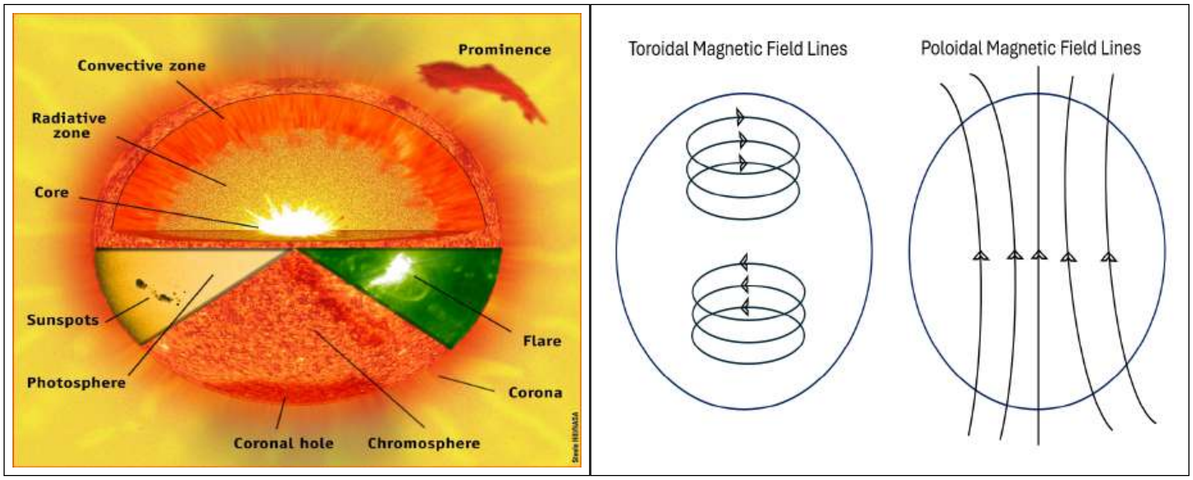

Figure 1.2: The anatomy of the Sun reveals its internal structure, which ranges from the core to the outer corona. The figure illustrates the dynamic and complex nature of activity in the Sun's atmosphere (*Credit: NASA*). (b) The two possible constituents of the solar magnetic field are the toroidal component (left) and the poloidal component (right). The poloidal field resembles a dipole field with lines of force passing from pole to pole, while the toroidal field is oriented east–west, resembling loops around the Sun.

high mass density in the lower region stabilizes the plasma against convection, allowing radiation to remain the primary mode of energy transport. The same high mass density also causes photons to undergo more frequent collisions with other particles, which significantly change their propagation direction and delay their escape. The temperature gradient is also steep, ranging from approximately 7×10^6 K at the bottom to 2×10^6 K at the top.

The tachocline

The *tachocline* is a thin transition layer with a thickness of approximately $0.03\,R_\odot$ located near $0.7\,R_\odot$ that separates the radiative zone from the convection zone. This layer is characterized by a sharp transition in rotation behavior: the radiative zone lying below it rotates as a rigid body, while the convective zone above rotates differentially. The tachocline plays a crucial role in the *solar dynamo*, the primary mechanism responsible for generating the magnetic field of the Sun. In this region, the magnetic field is amplified by the so-called ω-*effect*, which converts poloidal magnetic fields into toroidal ones (Krüger et al., 2005). The poloidal magnetic field resembles the Earth's dipole field, where the magnetic field runs from the north to the south pole. In contrast, the toroidal magnetic field lines are a ring-shaped magnetic field that is produced when differential rotation in the Sun stretches and twists the Sun's poloidal field lines (Fig. 1.2 b). The solar dynamo operates through continuous conversion between toroidal and poloidal fields and vice versa, a process that underlies the 11-year sunspot cycle of the

(a) (b)

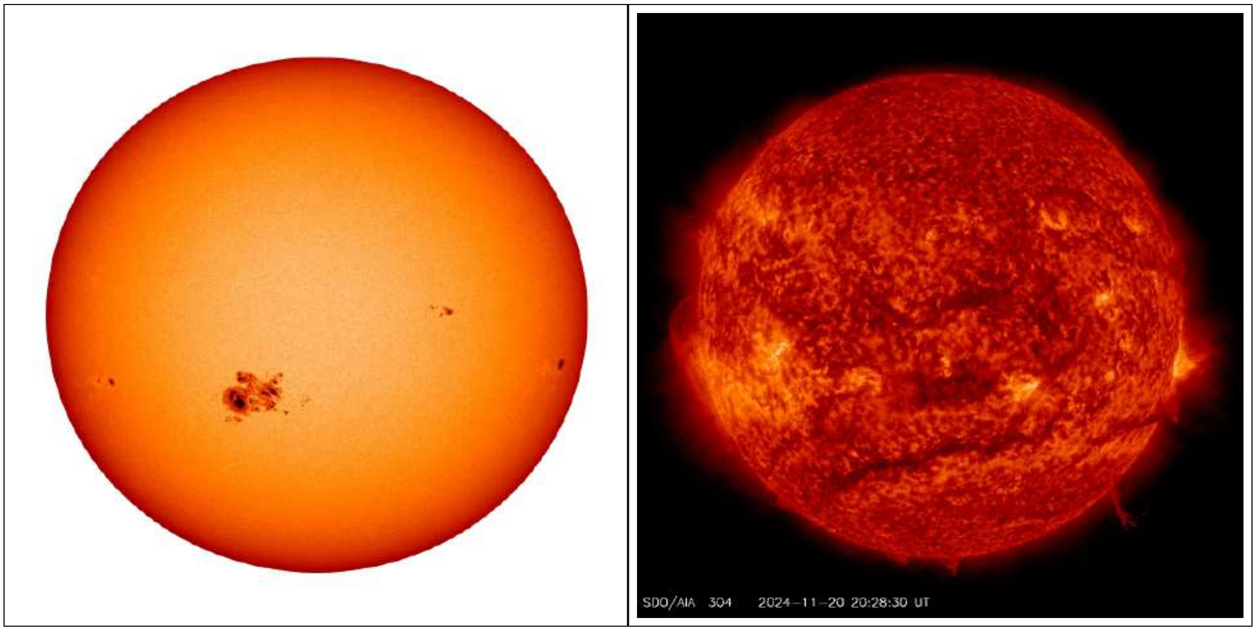

Figure 1.3: (a) The photosphere with large sunspots from SDO. (b) The upper chromosphere of the Sun, observed through He II 304 Å by AIA/SDO, reveals the regions above the photosphere where colder, denser plasma plumes known as filaments and prominences are located (*Credit: NASA*).

Sun.

The convection zone

The *convection zone* follows the tachocline and radiative zone, extending from about $0.7R_\odot$ to $R_\odot$ (the solar surface, i.e., the photosphere). In this region, the mass density and gas pressure are significantly lower than in the radiative zone, thus allowing convective motion to develop and transport energy outward. At the base of the convection zone, the plasma is heated by the lower layers, causing it to expand and rise as plasma with a relatively lower density. This buoyant motion forms convection cells that transport heat energy toward the solar surface. Upon reaching the top, these convection cells form a granular appearance on the photosphere known as *solar granulation*, typically with a size of $\sim 1000 - 2000$ km, and *super-granulation*, typically with a size of $\sim 20000 - 30000$ km. Some of the quantitative results in this thesis include the analysis of solar granulation and the waves it generates (see chapter 6).

The plasma near the photosphere loses thermal energy due to radiative cooling, becoming dense. Consequently, it sinks toward the base of the convection zone, where it gathers thermal energy and prepares for the next cycle. At the upper boundary of the convection zone, both temperature and density drop significantly, reaching $6000\,\mathrm{K}$ and $2 \times 10^{-7}\mathrm{g\ cm^{-3}}$, respectively.

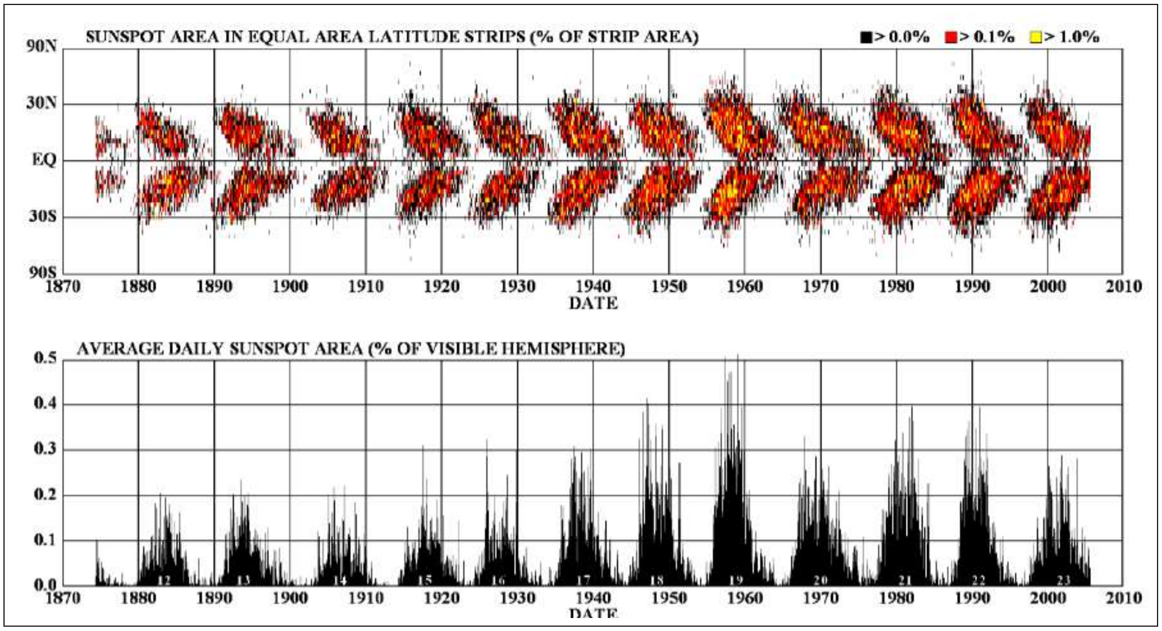

Figure 1.4: The upper panel features a butterfly diagram that portrays the latitudinal distribution and its corresponding migration from the year 1874 to 2010. This illustrates how the solar dynamo effect causes the migration of sunspots across the surface of the Sun. The lower panel shows the average daily sunspot area for each solar cycle since May 1874, plotted against time (*Image courtesy: D.H. Hathaway*).

1.3.3 Anatomy of the solar atmosphere

The solar atmosphere refers to the outermost region of the Sun. It is primarily composed of four layers: *photosphere*, *chromosphere*, *transition region*, and *solar corona*. These layers exhibit a vast range of temperatures and densities, rising from the relatively cooler solar surface through the chromosphere and transition region to the extremely hot solar corona. Many prominent features, such as *sunspots*, *coronal holes*, *coronal mass ejections* (CMEs), *coronal loops*, *solar prominences*, and *solar flares*, are observed in this atmospheric region. The following subsections provide a brief description of each layer of the outer solar atmosphere.

The photosphere

The word *photosphere* means *light sphere*. Although not a solid layer, it marks the outer boundary of the visible disk of the Sun, below which it becomes opaque to visible light. The sunlight reaching the Earth originates from the photons escaping this layer after passing through the solar atmosphere above it. The photosphere is about 500 km thick, with the temperature approximately 6600 K (at the top) and 4300 K (at the bottom). It hosts relatively dark, cooler regions known as *sunspots*, one of the most crucial features characterizing the solar cycle (Fig. 1.3 a). Sunspots follow an approximately 11-year solar cycle, during which their number increases (solar maximum) and decreases (solar minimum) periodically. Sunspots at the beginning of each cycle emerge at mid-latitudes. As the cycle advances, the active zones appear at progressively lower latitudes over each hemisphere before drifting toward the equator. Around the cycle maximum, the activity bands from each hemisphere approach but rarely cross the equator. Older cycles are often observed near the equator, whereas newer cycles arise in the mid-latitudes. Strong cycles typically begin at higher latitudes and extend farther toward the lower latitudes, often with faster drift rates. The meridional circulation of the Sun is incorporated into many dynamo models to explain the migration of the sunspot cycle, with drift rates linked to the speed of the circulation.

All successful dynamo models proposed must reproduce the butterfly diagram (Fig. 1.4), first introduced by E.W. Maunder in 1904. Sunspots are typically associated with intense magnetic field lines, which range from several thousand to tens of thousands of gauss. These strong magnetic fields temporarily suppress convection, leading to cooler regions ($3000 \sim 4500\,\mathrm{K}$). They often appear in pairs, featuring a central dark region known as the *umbra*, surrounded by a lighter region known as the *penumbra*. For further details, readers are referred to the review by Hathaway (2015). Some parts of the numerical results in this thesis explore the scenarios of solar maximum and solar minimum within the broader framework of the multi-fluid global model of the solar corona (see chapter 7).

The chromosphere

The word *chromosphere* is derived from the term *colored sphere*. It is a roughly 1500 km thick layer of the solar atmosphere where the temperature begins at a minimum of about 4000 K and rises steadily outward, reaching approximately 2×10^4 K near the upper boundary. This unusual temperature rise indicates that the chromosphere is relatively hotter than the photosphere beneath it. This relatively higher temperature produces H-alpha emission, giving the chromosphere a crimson tint. During total solar eclipses, this vivid red glow is visible in prominences that arch above the limb of the Sun. The name *chromosphere* itself originates from this red crimson hue (Fig. 1.3 b).

Due to local temperature minima, along with a fall in gas pressure with height, the plasma in the photosphere and chromosphere is partially ionised (Zaqarashvili et al., 2011), retaining a non-negligible amount of neutral particles. The degree of ionization in the photosphere is approximately 10^{-4}, but in the chromosphere and above, this ratio increases with height due to the aforementioned temperature increase (Khomenko et al., 2014). The presence of partially ionized plasma enables dissipation mechanisms, such as ion-neutral collisions, which can efficiently damp the MHD waves originating in the underlying layers. This damping facilitates the transport of wave energy into the outer layers of the solar atmosphere. The local model developed in this thesis examines the dissipation of MHD waves in the chromosphere

(a) (b)

Figure 1.5: (a) The solar corona during a solar eclipse, which is usually hidden under the intense light originating from the lower layers of the Sun (*Credit: NASA/Aubrey Gemignani*). (b) Illustration of the termination shock, heliosheath, and heliopause—three essential elements of the heliosphere—along with *NASA's Voyager 1 and Voyager 2* probes visible in the outer heliosphere (*Credit: NASA*).

and investigates their role in heating the upper solar atmosphere (chapter 6).

Transition region

Above the chromosphere, a thin layer known as the *transition region*, with a thickness of roughly 100 km, separates the chromosphere from the solar corona. This layer marks the beginning of a sharp temperature jump from the top of the chromosphere to nearly a million K in the solar corona. Moreover, the transition layer separates the lower solar atmosphere, characterized by partially ionized plasma, from the almost fully ionized plasma of the corona. These sharp changes in the temperature and mass density profiles are visible in Fig. 1.6 (adopted from Song et al. 2023).

The solar corona

Following the transition region, the solar corona is the outermost layer of the solar atmosphere, emitting energy primarily at EUV and X-ray wavelengths. With a particle number density of approximately $10^{15} - 10^{16}\,\mathrm{m}^{-3}$ near the solar surface, the solar corona can extend into space by about $2 - 3\,R_\odot$. Despite its extended reach, the solar corona appears dim due to intense light emitted from the layer beneath it; therefore, it is best visible during total solar eclipses, where it appears as a pearly white crown (named after) encircling the Sun (Fig. 1.5 a). The temperature of plasma in the solar corona is exceptionally high, reaching an

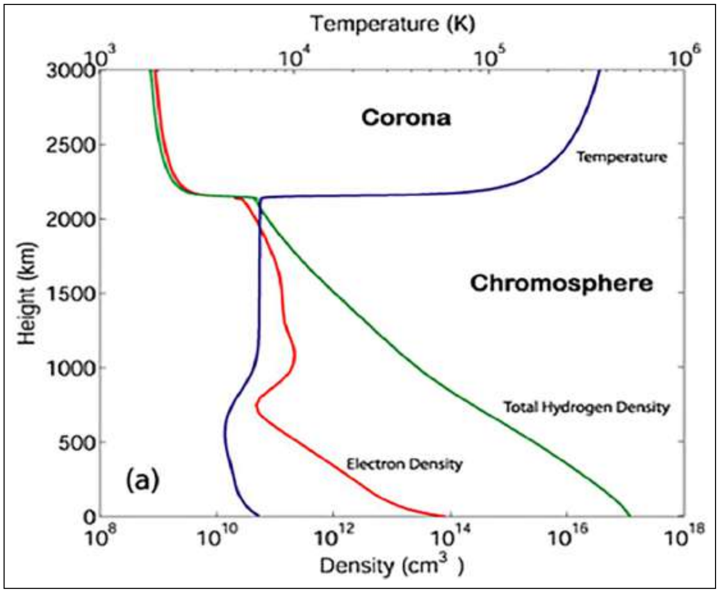

Figure 1.6: The variation of the electron density (red), total hydrogen number density (green), and temperature (blue) with height in the solar atmosphere (*Image courtesy: Song et al., 2023*).

average of $1-3$ M K, with localized regions reaching $8-20$ M K (Fig. 1.6). At such extreme temperatures, the matter in the solar corona is essentially fully ionized, with the exception of prominences, where the plasma is weakly ionized. In contrast, a non-negligible fraction of neutrals is present in the photosphere and chromosphere. This rapid temperature rise with height is a long-standing mystery in solar physics, widely known as the *coronal heating problem*. Historically, unexplained bright emission lines in the visible spectrum from the corona prompted scientists to speculate about a new element, *coronium*, that did not match any known element at the time. However, it was later discovered that the lines originate from familiar elements such as iron and calcium, made possible by the extreme temperature of the corona. The hot and tenuous plasma expands supersonically, discharging high-conductivity material into interplanetary space as the *solar wind*. The solar wind consists of protons and electrons that flow outward from the Sun, shaping the heliosphere and interacting with the planetary magnetospheres (see Sec. 1.3.5).

1.3.4 Central problems in heliophysics

The heliosphere

The *heliosphere* refers to the region influenced by the Sun. The solar magnetic field and solar wind essentially dictate its edge and shape, resulting in a rough teardrop cavity with a tail extending behind it (Fig. 1.5 b). The solar wind originating from the Sun extends beyond the orbits of the planets in the solar system, creating a giant bubble that surrounds the Sun and its planetary system. The *termination shock* occurs when the outward-flowing solar wind slows down due to the influence of the interstellar medium. Beyond the termination shock lies the *heliopause*, a boundary where the pressure of the solar wind balances with the pressure of interstellar space. As a natural barrier, the heliosphere shields the planets inside it from interstellar particles and high-energy cosmic rays.

The study of the Sun and its extended space environment, which treats the Sun and its planetary system as a single, cohesive system, is known as *heliophysics*. Despite considerable research, heliophysics faces some critical unsolved problems, including:

- Modeling the properties and dynamics of hot plasma in the solar atmosphere, particularly in the active photosphere and chromosphere.
- Explaining the unusual and unexpected sharp growth in temperature above the transition region (the solar corona heating problem).
- Understanding how energy is transported to the upper layers of the solar atmosphere (chromosphere, corona) to compensate for radiation losses.
- Understanding the mechanism that generates and accelerates the solar wind, as well as how mass flux from the solar upper atmosphere balances the steady mass loss due to the solar wind.
- Determining the exact mechanism behind the magnetic reconnection process and how magnetic energy is efficiently converted to kinetic and thermal energy during solar flares and CMEs.
- Explaining the origin and dynamics of the solar cycle, including the 11-year solar cycle, and the mechanism of the magnetic field reversal.

Among the issues mentioned above, the *coronal heating problem* and the *origin and acceleration of the solar wind* remain critical and unresolved problems in heliophysics. Many mechanisms have been proposed to understand these problems (see, e.g., Viall et al. (2021)). Earlier studies, such as Bierman (1946), proposed that MHD waves were a potential source and mechanism for non-radiative energy transportation and plasma outflows in the upper solar atmosphere. This idea was later extended by Schwarzschild (1948) and Schatzman (1949), who explained that waves generated in the convection zone would propagate through the solar atmosphere, offering a possible energy source for heating both the chromosphere and the solar corona. See earlier reviews such as those by Stein et al. (1974); Narain et al. (1990); Narain et al. (1996); Ulmschneider (1997).

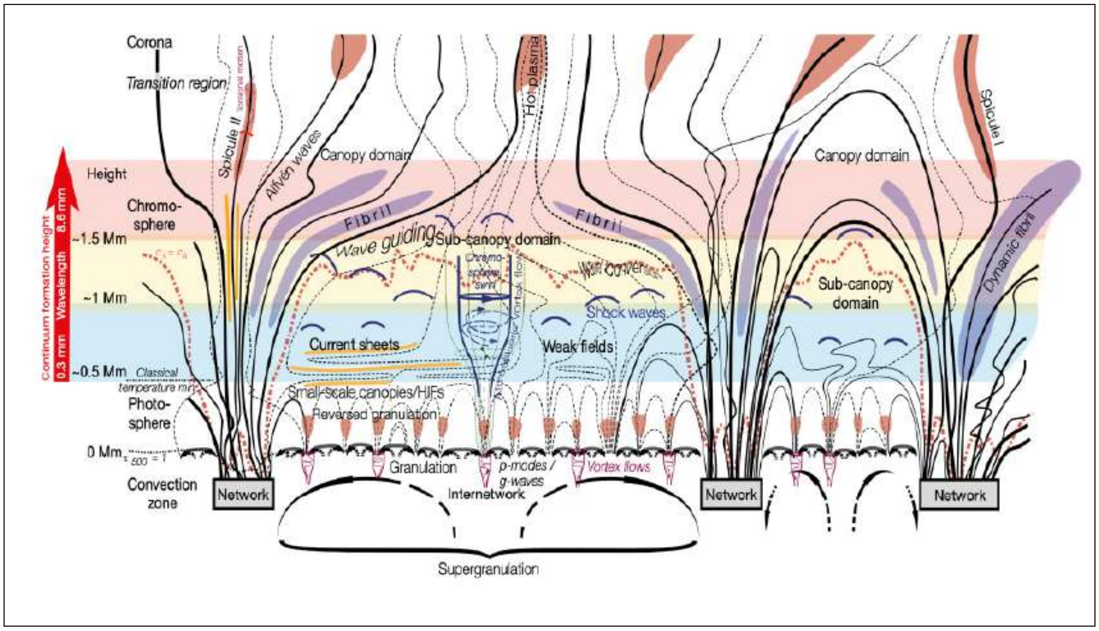

Figure 1.7: (a)The multilayered structure of the solar atmosphere, highlighting the propagation of waves, dynamic features, and their interaction with the magnetic field and plasma (Wedemeyer et al., 2016).

Despite significant theoretical work, the underlying physical mechanism remains fundamentally unclear. Nevertheless, the advancement in large-scale observations and high-resolution numerical models has led to substantial progress toward comprehending the heating of the upper layers of the solar atmosphere and the origin of the solar wind (Cranmer et al., 2017; Cranmer et al., 2019; Van Doorsselaere et al., 2020).

1.3.5 Dynamic and transient features of the Sun

The Sun is far from a bland and homogeneous star. Its dynamic character hosts many interesting phenomena, ranging from minor bright points to large-scale solar flare events, leading to an intriguing structure that undergoes dynamic processes. Figure 1.7 illustrates the complex processes ongoing in the solar atmosphere, such as waves, spicules, and fibrils, which govern its dynamics. The following subsection summarizes the transient and dynamic features of the Sun.

Prominences and filaments

A *prominence* is a giant, bright, anchored structure extending from the photosphere (Fig. 1.8 a). Although prominences extend outward into the solar corona, they exhibit intriguing characteristics compared to the surroundings, such as a temperature about a hundred times lower and densities about a hundred or even a thousand times greater than those in the solar

(a) (b)

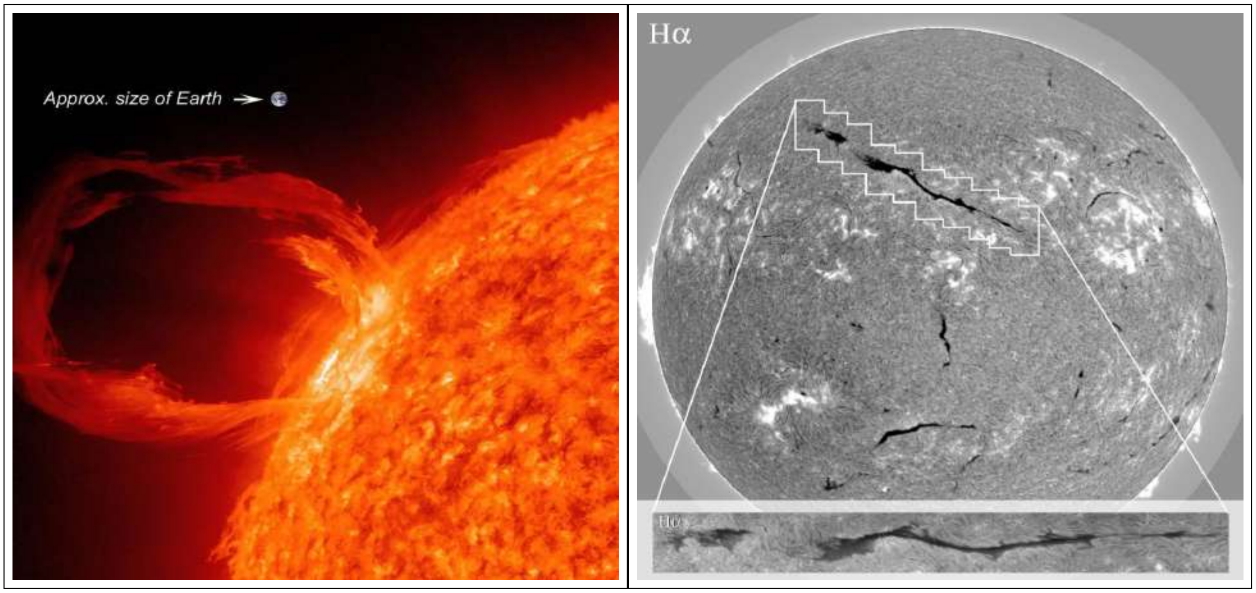

Figure 1.8: (a)This image shows a prominence — a solar eruptive event observed in EUV. It showcases hot plasma erupting from the surface of the Sun, with Earth overlaid for scale, demonstrating the vast magnitude of these solar structures (*Credit: NASA/SDO*). (b) H_α image of a filament, a cold and dense region of plasma suspended above the solar surface by magnetic fields. The strip below shows a detailed zoomed-in view of the filament's black, elongated structure (*Credit: EST*).

corona. Typical dimensions include heights and widths of the order of 10^3 km, and lengths reaching up to 10^5 km. They generally form along polarity inversion lines (PILs) of the magnetic field in the photosphere. Despite extensive research, the precise mechanisms behind their formation remain an open question (Yeates et al., 2009). Prominences are classified into two categories based on their lifetime and stability: (a) quiescent prominences and (b) active prominences. Quiescent prominences are relatively stable structures that persist for several months. They are typically associated with active regions, filaments with temperatures reaching 7000 K, and a magnetic field strength of $5 - 10$ G. In contrast, active prominences are dynamic and short-lived, with lifetimes ranging from a few minutes to a few hours. They are frequently associated with solar flares and exhibit significantly higher temperatures than quiescent prominences. A detailed review of the physical properties and environments of these structures is provided by Parenti (2014).

The *filament* is another way to visualize prominences. When prominences are observed on the disk, for example, in H_α 6562.8 Å & He II 304 Å, they appear darker than the surrounding quiet Sun due to absorption processes in the plasma. Presently, prominence and filament can be used interchangeably to indicate these features. Figure 1.8 (b) illustrates a typical example of a filament.

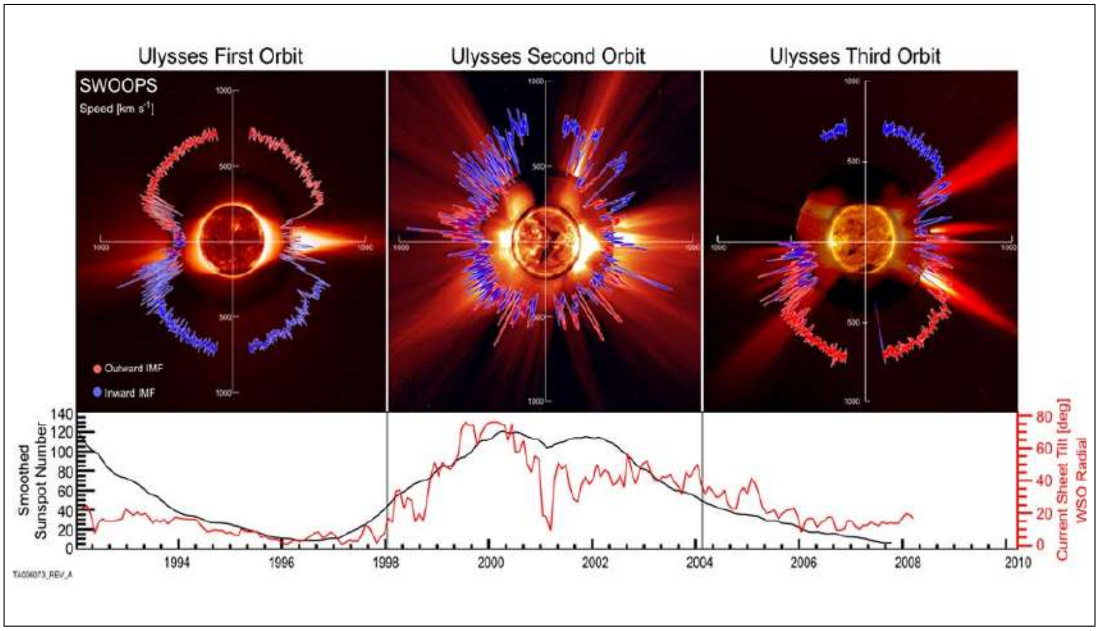

Figure 1.9: Top: Speed of the solar wind (in $\mathrm{km\,s^{-1}}$) vs. heliocentric latitude during solar minima (left), solar maxima (middle), and solar minima (flipped magnetic field) as observed by the *Ulysses* space probe, launched jointly by *ESA* and *NASA* in 1990. During solar minima, the slow solar wind is confined to the equatorial region, and fast solar wind can be observed at higher latitudes. During solar maxima, both fast and slow winds can be witnessed at all latitudes. Bottom: The plot represents the variation of sunspot number (left) and the current sheet tilt (right) with time (*Credit: ESA*).

The solar wind

The *solar wind* is a stream of charged particles that emerges from the upper solar atmosphere. It blows outward in all directions, filling interplanetary space and transporting the Sun's magnetic field. The solar wind mainly comprises electrons, protons, and α particles, with traces of some heavy ions and atomic nuclei of elements such as carbon, nitrogen, oxygen, and iron (Eddington, 1910; Parker, 1958). The extreme temperature of the solar corona fuels this tremendous kinetic energy, typically in the range of $0.5-10$ keV, which helps the particles to escape the intense gravity of the Sun.

Based on their fundamental states, the solar wind is classified into two categories: slow and fast. The top (left) panel of Fig. 1.9 shows the variation of the solar wind speed with the latitude of the Sun during the solar minimum. The slow solar wind, with speeds lying in the range of $300-500\ \mathrm{km\,s^{-1}}$, usually originates from a region around the equatorial belt ($30-35^{\circ}$) of the Sun. This releasing equatorial belt may expand toward the poles as the solar cycle approaches solar maximum (middle panel), where the polar region appears to produce fast solar wind. In contrast, the fast solar wind, with speeds spanning $700-800\ \mathrm{km\,s^{-1}}$, originates primarily from the coronal holes found near the polar region of the Sun. During the solar maxima, the fast and slow winds can be observed at all latitudes (Fig. 1.9 middle). It is worth mentioning that the distinction between slow and fast solar wind is not just limited to their speeds, but also depends on other parameters, including composition, flow state, and temperature. Refer to Meyer-Vernet (2007) for more in-depth details.

Solar physicists still debate the physical mechanism responsible for compensating for the mass flux lost from the solar atmosphere due to the continuous solar wind flow. *Plasma outflow*, which refers to the localized escape of plasma from the solar atmosphere, is often confined to specific regions such as coronal holes or magnetic reconnection sites. Such outflows have been proposed as a potential candidate to compensate for the mass loss flux and to play a role in generating the solar wind. Biermann (1951) and Parker (1965) performed the earliest studies of the solar wind. In recent years, some studies have emphasized the significance of plasma outflows from specific solar regions in mitigating mass loss and their vital role in solar wind production (Niedziela et al., 2021; Pelekhata et al., 2021). Tu et al. (2005) argued that the solar wind may originate from a magnetic funnel in the solar corona above a height of $5-20$ Mm. Recently, Bale et al. (2023) concluded that interchange reconnection is a primary driver of the fast solar wind in coronal holes. Moreover, Uritsky et al. (2023) conducted a structured examination of plasma outflows above coronal holes and determined that impulsive reconnection events can contribute to the fast solar wind's mass and energy fluxes. MHD waves can also accelerate plasma outflows by transferring momentum via interactions with magnetic fields and plasma. A review by Ofman (2005) provided a comprehensive view of single-fluid 2.5-D and multi-fluid 2.5-D MHD models of waves in coronal holes and their role in both heating and accelerating the plasma outflows.

Waves in the solar atmosphere

In physics, a *wave* is a dynamic disturbance that propagates through space and time, transporting energy while maintaining the equilibrium of the system. In classical physics, waves are typically classified into two categories: mechanical waves (e.g., acoustic, seismic, and gravity waves) and electromagnetic (EM) waves (e.g., light waves). Mechanical waves arise from the oscillations of the stress and strain about a mechanical equilibrium. For instance, the energy of sound waves, due to local variations in pressure, propagates through the medium. In contrast, EM waves involve coupled electric and magnetic fields governed by Maxwell's equations. The solar atmosphere is a rich source of waves due to its dynamic nature over a wide range of spatial and temporal scales. Among them, MHD waves are frequently observed in plasma systems, including the solar atmosphere. These waves result from the combined action of mechanical stresses — such as pressure gradients, the Coriolis force, and gravity — and electromagnetic interactions involving perturbations and Lorentz forces. They are therefore considered a hybrid phenomenon, blending fluid dynamics and electromagnetism.

Table 1.3: MHD wave modes in the plasma system of the solar atmosphere and their associated restoring forces.

Wave mode	Restoring force
Sound waves	Plasma pressure
Alfvén waves	Magnetic tension
Magneto-acoustic waves	Magnetic tension + plasma pressure
Internal gravity waves	Force of gravity
Magneto-acoustic gravity waves	Magnetic tension + plasma pressure + gravity

In other words, *MHD waves* are disturbances in an electrically conducting fluid, such as the plasma of the solar atmosphere, that are permeated by magnetic field lines. The magnetic field lines and Coriolis forces provide the necessary tension for the restoring force when the plasma is displaced across the field lines.

Depending on the dominant restoring forces in the plasma, different MHD wave modes can arise, as described in Tab. 1.3. For MHD waves to play a dominant role in coronal heating, an efficient dissipation mechanism is required. In recent years, ion-neutral collisions and ohmic diffusion have gained attention for their strong influence on the dissipation of MHD waves in the solar atmosphere (Wójcik et al., 2020; Murawski et al., 2020). Figure 1.7 highlights how magnetic fields, waves, and plasma outflows act together to alter the dynamics of the solar atmospheric layers—driving both heating and plasma outflows.

1.4 Summary

In this chapter, we described the four states of matter: solid, liquid, gas, and plasma, with a particular focus on plasma. We provided the precise definition of plasma, its core properties, and fundamental characteristics. For an ionized gas to be classified as a plasma, it must meet specific and essential physical characteristics, such as quasi-neutrality, collective behavior, and plasma oscillation. We then discussed various mathematical frameworks and modeling approaches for studying the spatial and temporal characteristics of plasma. These include single-particle orbit theory, plasma kinetics, fluid theory, and hybrid theory, each differing in terms of complexity and limits on the level of available information. Later, we discussed the Sun and its atmospheric layer structure, as well as the significance of studying its dynamic features. The Sun is not a single solid sphere but rather is composed of many layers, each with distinct physical properties, varying in terms of composition, temperature, pressure, and density. Furthermore, the Sun is non-stationary and therefore home to various intricate dynamics, such as spicules, fibrils, MHD waves, prominences, filaments, solar wind, CMEs, and solar flares. One of the central problems in heliophysics is the transportation of energy and mass flux from the lower to the upper layers of the solar atmosphere. The generation of the solar wind and the mechanism by which plasma outflows compensate for the lost mass flux remain unsolved problems. MHD waves and plasma outflows are proposed as possible physical mechanisms for energy and mass transfer between the solar layers, thereby compensating for radiative and mass flux losses.

Chapter 2

Objectives of the dissertation

The main goal of this thesis is to investigate plasma heating and outflow mechanisms in the solar atmosphere by developing and utilizing a multi-scale numerical model framework. The thesis specifically seeks to

- Investigate the local excitation, propagation, and dissipation of MHD waves in a partially ionized plasma, with a focus on the role of ion-neutral collisions in chromospheric heating and plasma outflows, using high-resolution two-fluid simulations with the JOANNA code.
- Extend these local insights to large scales by parameterizing the effects of such small-scale dissipation processes and incorporating them into the energy equation of the multi-fluid COCONUT model, to study their influence on large-scale plasma dynamics and associated coronal heating and plasma outflows.

With this, the thesis aims to enhance our understanding of solar atmosphere heating and the subsequent generation of plasma outflows, while bridging the gap between wave dissipation on the local scale and its influence on coronal dynamics on the global scale.

Chapter 3

Mathematical description of multi-fluid plasma

3.1 Introduction

This chapter presents the detailed derivation of the general multi-fluid plasma equations from the *Boltzmann equation* (Eq.;1.20), following the kinetic theory of plasma (Sec. 1.2.2). The *macroscopic equations*, also called *transport equations*, are derived by taking the velocity moments of the Boltzmann equation. Each velocity moment corresponds to an equation in the multi-fluid theory. The zeroth velocity moment gives the *equation of mass conservation*. The first velocity moment yields the *momentum transport equation, also known as the macroscopic equation of motion*. The second velocity moment leads to the *energy equation*. The third-order velocity moment gives the *heat flux*. The chain of equations is usually closed by taking the thermodynamic equations of state for each species. Additionally, we will briefly introduce Maxwell's equations in the context of plasma physics and discuss the cases of resistive and ideal MHD.

3.2 Motivation of a multi-fluid theory

In this thesis, we adopted the two-fluid theory to model the solar atmosphere. Numerous earlier studies have acknowledged the superiority of the two-fluid MHD model over the traditional single-fluid model (MHD) (Andretta et al., 1997; Braileanu et al., 2019; Khomenko et al., 2021). Despite high temperatures, the plasma in the solar atmosphere remains partially ionized. Both analytical and numerical studies have underscored the importance of considering neutrals when modeling solar atmospheric events. According to Khomenko et al. (2014), the ratio of ions to neutrals rises with height in the chromosphere, while the degree of ionization in the photosphere remains as low as 10^{-4}. Similarly, Zaqarashvili et al. (2011) argued that the relatively low temperature in the chromosphere and photosphere leads to the presence of a non-negligible neutral population. The authors concluded that the single-fluid approximation fails for time scales comparable to the ion-neutral collision time scale in a partially ionized plasma; therefore, the single-fluid model is unable to fully capture the evolution of partially ionized plasmas. Further studies have shown that neutral fractions in the solar atmosphere can affect both large-scale activity and small-scale dynamics, altering wave propagation, damping, and shock formation (Judge, 2020; Melis et al., 2021). Brchnelova et al. (2023), in the context of global multi-fluid simulations, showed that even a tiny percentage of neutrals can locally influence the ion temperature and velocity via the momentum and energy source terms. Moreover, Martínez-Gómez et al. (2022) incorporated two-fluid effects in solar corona simulations and challenged the traditional assumption that neutrals do not significantly impact solar corona dynamics (Martínez-Sykora et al., 2015). These studies underscore the importance of considering neutrals when modeling solar atmospheric events, both analytically and numerically.

Motivated by the above literature review, we conclude that a more comprehensive approach, utilizing multi-fluid MHD, is necessary to fully capture the complexity of partially ionized plasma in the solar atmosphere. The two-fluid model presented in this thesis captures the rich physics of momentum and energy exchange between neutrals and ions in partially ionized solar plasma by solving these equations explicitly. This approach not only enhances our understanding of the processes underlying phenomena such as wave heating and plasma outflows, but also contributes to the development of improved predictive models for space weather.

3.3 Multi-fluid equations of plasma

The macroscopic quantities — particle number density n_s, mass density ϱ_s, bulk velocity $\mathbf{V}_s$, temperature T_s, and internal energy U_s — provide the bridge between the kinetic and fluid (macroscopic) descriptions of a plasma. These variables are obtained by taking velocity-space moments of the distribution function f_s for species s. Below, we define the local macroscopic variables as follows:

- Number density
$$n_s(\mathbf{r}, t) = \int f_s(\mathbf{r}, \mathbf{v}, t)\, d^3\mathbf{v}_s \tag{3.1}$$

- Mass density
$$\varrho_s(\mathbf{r}, t) = m_s n_s = m_s \int f_s(\mathbf{r}, \mathbf{v}, t)\, d^3\mathbf{v}_s \tag{3.2}$$

- Bulk velocity
$$\mathbf{V}_s(\mathbf{r}, t) = \frac{1}{n_s} \int f_s \mathbf{v}_s(\mathbf{r}, \mathbf{v}, t)\, d^3\mathbf{v}_s \tag{3.3}$$

- Internal energy
$$U_s = \frac{m_s}{2} \int (\mathbf{v}_s - \mathbf{V}_s)^2 f_s(\mathbf{r}, \mathbf{v}, t)\, d^3\mathbf{v}_s \tag{3.4}$$

- Random (thermal) velocity
$$\mathbf{c} = \mathbf{v}_s - \mathbf{V}_s \tag{3.5}$$

Here, $\mathbf{v}_s$ denotes the microscopic velocity for species s. The transport equations governing the evolution of these macroscopic variables can be derived by taking the velocity moment of the *Boltzmann equation* (Khomenko et al., 2014)

$$\boxed{\frac{\partial f_s}{\partial t} + \mathbf{v}_s \cdot \nabla_r f_s + \frac{q_s}{m_s}(\mathbf{E} + \mathbf{v}_s \times \mathbf{B} + \frac{m_s}{q_s}\,\mathbf{g}) \cdot \nabla_{v_s} f_s = \left(\frac{\partial f_s}{\partial t}\right)_c + \left(\frac{\partial f_s}{\partial t}\right)_{other}} \tag{3.6}$$

3.3.1 Zeroth moment: mass conservation equation

The mass continuity equation is derived by taking the integral over the entire $\mathbf{v}_s$ space, denoting $\int(\dots)d^3\mathbf{v}_s$ as the velocity space integral. From Eq. 3.6, we have

$$\begin{aligned}\int \frac{\partial f_s}{\partial t}\, d^3\mathbf{v}_s + \int \mathbf{v}_s \cdot \nabla_r\, f_s\, d^3\mathbf{v}_s + \int \frac{q_s}{m_s}(\mathbf{E} + \mathbf{v}_s \times \mathbf{B} + \frac{m_s}{q_s}\mathbf{g}) \cdot \nabla_{v_s} f_s\, d^3\mathbf{v}_s = \int \left(\frac{\partial f_s}{\partial t}\right)_c d^3\mathbf{v}_s \\ + \int \left(\frac{\partial f_s}{\partial t}\right)_{other} d^3\mathbf{v}_s\end{aligned} \tag{3.7}$$

We simplify each sub-term on the LHS:

1. **Time-derivative term:**

$$\int \frac{\partial f_s}{\partial t}\, d^3\mathbf{v}_s = \frac{\partial}{\partial t}\int f_s\, d^3\mathbf{v}_s = \frac{\partial n_s}{\partial t} \qquad \text{[using Eq. 3.1]} \tag{3.8}$$

2. **Spatial advection term:**

$$\int \mathbf{v}_s \cdot \nabla_r f_s\, d^3\mathbf{v}_s = \nabla_r \cdot \int \mathbf{v}_s f_s\, d^3\mathbf{v}_s = \nabla_r \cdot (n_s \mathbf{V}_s) \qquad \text{[using Eq. 3.2]} \tag{3.9}$$

3. **Force term:**

$$\int \frac{q_s}{m_s}(\mathbf{E} + \mathbf{v}_s \times \mathbf{B} + \frac{m_s}{q_s}\mathbf{g}) \cdot \nabla_{v_s}\, f_s\, d^3\mathbf{v}_s \tag{3.10}$$

Denoting $\frac{q_s}{m_s}(\mathbf{E}+\mathbf{v}_s\times\mathbf{B}+\frac{m_s}{q_s}\mathbf{g})$ as $\mathbf{A}_s$ and using the identity $\nabla_{v_s}\cdot(\mathbf{A}_s f_s) = \mathbf{A}_s\cdot\nabla_{v_s} f_s + f_s\,\nabla_{v_s}\cdot\mathbf{A}_s$, we get

$$\int \mathbf{A}_s \cdot (\nabla_{v_s}\, f_s)\, d^3\mathbf{v}_s = \int \nabla_{v_s} \cdot (\mathbf{A}_s\, f_s)\, d^3\mathbf{v}_s - \int f_s(\nabla_{v_s} \cdot \mathbf{A}_s)\, d^3\mathbf{v}_s \tag{3.11}$$

We note that $\mathbf{A}_s$ is a constant vector in velocity space; therefore, the term $\nabla_{v_s} \cdot \mathbf{A}_s$ is zero. The above equation becomes

$$\int \mathbf{A}_s \cdot (\nabla_{v_s} f_s)\, d^3\mathbf{v}_s = \int \nabla_{v_s} \cdot (\mathbf{A}_s f_s)\, d^3\mathbf{v}_s \tag{3.12}$$

Upon applying the Gauss divergence theorem

$$\int \nabla_{v_s} \cdot (\mathbf{A}_s f_s)\, d^3\mathbf{v}_s = \oint (\mathbf{A}_s f_s) \cdot d\mathbf{S}_{v_s} \tag{3.13}$$

Here, $\mathbf{S}_{v_s}$ is the surface element in velocity space. Since the distribution function f_s vanishes as $|\mathbf{V}_s| \to \infty$, the surface integral evaluates to zero, i.e.,

$$\int \nabla_{v_s} \cdot (\mathbf{A}_s f_s)\, d^3\mathbf{v}_s = \oint (\mathbf{A}_s f_s) \cdot d\mathbf{S}_{v_s} = 0 \tag{3.14}$$

Therefore,

$$\int \frac{q_s}{m_s}(\mathbf{E} + \mathbf{v}_s \times \mathbf{B} + \frac{m_s}{q_s}\mathbf{g}) \cdot \nabla_{v_s} f_s\, d^3\mathbf{v}_s = 0 \tag{3.15}$$

Similarly, we simplify each sub-term on the RHS:

1. **Collision and source/sink terms** Defining

$$\int \left(\frac{\partial f_s}{\partial t}\right)_c d^3\mathbf{v}_s = \Gamma_{c_s}, \quad \int \left(\frac{\partial f_s}{\partial t}\right)_{other} d^3\mathbf{v}_s = \Gamma_{other_s} \tag{3.16}$$

Here, Γ_{c_s} is the net particle gain/loss due to collisions and Γ_{other_s} is the net particle gain/loss due to processes such as ionization and recombination. Finally, the most general form of the continuity equation is

$$\frac{\partial n_s}{\partial t} + \nabla \cdot (n_s \mathbf{V}_s) = \Gamma_{c_s} + \Gamma_{other_s} \tag{3.17}$$

We multiply the above equation on both sides by the particle mass m_s, yields the continuity equation in terms of mass density $\varrho_s = m_s n_s$

$$\boxed{\frac{\partial \varrho_s}{\partial t} + \nabla \cdot (\varrho_s \mathbf{V}_s) = m_s\,\Gamma_{c_s} + m_s\,\Gamma_{other_s}} \tag{3.18}$$

This equation represents the standard form of the conservation equation which includes source and sink terms resulting from physical phenomena such as collisions, ionization, recombination, etc. In the case of purely elastic collisions, the total number of particles for a given species remains conserved; thus, Γ_{c_s} is zero. However, in the presence of processes such as ionization and recombination of species, the term Γ_{other_s} is non-zero.

3.3.2 First moment: momentum equation

Multiplying Eq. 3.6 on both sides by $m_s\mathbf{v}_s$ and integrating over $\mathbf{v}_s$, we obtain

$$\int m_s\mathbf{v}_s\frac{\partial f_s}{\partial t}\,d^3\mathbf{v}_s+\int m_s\mathbf{v}_s[\mathbf{v}_s\cdot\nabla_r\,f_s]\,d^3\mathbf{v}_s+\int m_s\mathbf{v}_s\frac{q_s}{m_s}(\mathbf{E}+\mathbf{v}_s\times\mathbf{B}+\frac{m_s}{q_s}\mathbf{g})\cdot\nabla_{v_s}f_s\,d^3\mathbf{v}_s=\int m_s\mathbf{v}_s\left(\frac{\partial f_s}{\partial t}\right)_c d^3\mathbf{v}_s+\int m_s\mathbf{v}_s\left(\frac{\partial f_s}{\partial t}\right)_{other} d^3\mathbf{v}_s \tag{3.19}$$

We simplify each sub-term on the LHS:

1. **Time-derivative term:**

$$\int m_s\mathbf{v}_s\frac{\partial f_s}{\partial t}\,d^3\mathbf{v}_s=\frac{\partial}{\partial t}\int m_s\mathbf{v}_s f_s\,d^3\mathbf{v}_s=\frac{\partial}{\partial t}(\rho_s\mathbf{V}_s)\qquad\text{[using Eq. 3.3]} \tag{3.20}$$

2. **Spatial advection term:**

$$\int m_s\mathbf{v}_s[\mathbf{v}_s\cdot\nabla_r f_s]\,d^3\mathbf{v}_s=\nabla_r\cdot\int m_s\mathbf{v}_s\mathbf{v}_s f_s\,d^3\mathbf{v}_s \tag{3.21}$$

Splitting, $\mathbf{v}_s$ as the sum of bulk velocity $\mathbf{V}_s$, and thermal velocity $\mathbf{c}$, that is, $\mathbf{v}_s=\mathbf{V}_s+\mathbf{c}$ and understanding that $\mathbf{c}$ evaluates to zero when integrated over the distribution function f_s, we define the momentum flux tensor $\mathbf{M}_s$ as follows:

$$\mathbf{M}_s=\int m_s(\mathbf{V}_s+\mathbf{c})(\mathbf{V}_s+\mathbf{c})f_s\,d^3\mathbf{v}_s=\rho_s\mathbf{V}_s\mathbf{V}_s+\int m_s\,\mathbf{c}\,\mathbf{c}\,f_s\,d^3\mathbf{v}_s \tag{3.22}$$

The second term in the equation above is called the pressure tensor $\mathbf{P}_s$; therefore, $\mathbf{M}_s=\rho_s\mathbf{V}_s\mathbf{V}_s+\mathbf{P}_s$. Hence we rewrite the Eq. 3.21 as

$$\int m_s\mathbf{v}_s[\mathbf{v}_s\cdot\nabla_{\mathbf{r}}f_s]\,d^3\mathbf{v_s}=\nabla\cdot(\rho_s\mathbf{V}_s\mathbf{V}_s+\mathbf{P}_s) \tag{3.23}$$

3. **Force term:**

$$\begin{aligned}\int m_s\mathbf{v}_s\frac{q_s}{m_s}\left(\mathbf{E}+\mathbf{v}_s\times\mathbf{B}+\frac{m_s}{q_s}\mathbf{g}\right)\cdot\nabla_{v_s}f_s\,d^3\mathbf{v}_s&=q_s\int\mathbf{v}_s\left(\mathbf{E}\cdot\nabla_{v_s}f_s\right)\,d^3\mathbf{v}_s\\&+q_s\int\mathbf{v}_s\left[(\mathbf{v}_s\times\mathbf{B})\cdot\nabla_{v_s}f_s\right]\,d^3\mathbf{v}_s\\&+m_s\int\mathbf{v}_s\left(\mathbf{g}\cdot\nabla_{v_s}f_s\right)\,d^3\mathbf{v}_s\end{aligned} \tag{3.24}$$

- Electric sub-term: Noting as $\mathbf{v}_s \to \infty$, $f_s \to 0$

$$q_s \int \mathbf{v}_s \left(\mathbf{E} \cdot \nabla_{v_s} f_s\right)\, d^3\mathbf{v}_s = -\, q_s \int f_s \, \nabla_{\mathbf{v}_s} \cdot \Big(\mathbf{v}_s \, \mathbf{E}\Big)\, d^3\mathbf{v}_s$$
$$= -\, q_s \int f_s \, \mathbf{E}\, d^3\mathbf{v}_s \tag{3.25}$$
$$= -\, q_s n_s \mathbf{E}$$

- Magnetic sub-term: Applying $\nabla_{v_s} \cdot [\mathbf{v}_s(\mathbf{v}_s \times \mathbf{B})] = (\mathbf{v}_s \times \mathbf{B})$

$$q_s \int \mathbf{v}_s \left[(\mathbf{v}_s \times \mathbf{B}) \cdot \nabla_{v_s} f_s\right]\, d^3\mathbf{v}_s = -\, q_s \int f_s \, \nabla_{\mathbf{v}_s} \cdot \Big[v_s(\mathbf{v}_s \times \mathbf{B})\Big]\, d^3\mathbf{v}_s$$
$$= -\, q_s \int f_s \, (\mathbf{v}_s \times \mathbf{B})\, d^3\mathbf{v}_s$$
$$= -\, q_s \Big(\int \mathbf{v}_s f_s \, d^3\mathbf{v}_s \Big) \times \mathbf{B} \tag{3.26}$$
$$= -\, q_s \, n_s \, (\mathbf{V}_s \times \mathbf{B})$$

- Gravitational sub-term:

$$m_s \int \mathbf{v}_s \left(\mathbf{g} \cdot \nabla_{\mathbf{v}_s} f_s\right)\, d^3\mathbf{v}_s = -\, m_s \int f_s \, \nabla_{v_s} \cdot \Big(\mathbf{v}_s \, \mathbf{g}\Big)\, d^3\mathbf{v}_s$$
$$= -\, m_s \int f_s \, \mathbf{g}\, d^3\mathbf{v}_s \tag{3.27}$$
$$= -\, m_s n_s \mathbf{g}$$
$$= -\, \rho_s \mathbf{g}$$

Similarly, we simplify each sub-term on the RHS:

1. **Momentum exchange with other species:**

$$\int m_s \mathbf{v}_s \left(\frac{\partial f_s}{\partial t}\right)_c d^3\mathbf{v}_s = \mathbf{R}_s \tag{3.28}$$

   Here, $\mathbf{R}_s$ denotes the net collisional momentum transfer between the species.

2. **Momentum exchange due to other physical processes:**

$$\int m_s \mathbf{v}_s \left(\frac{\partial f_s}{\partial t}\right)_{other} d^3\mathbf{v}_s = \mathbf{S}_{p_s} \tag{3.29}$$

   The term $\mathbf{S}_{p_s}$ refers to the momentum transfer due to processes such as ionization, recombination, etc.

Finally, plugging all the simplified integrals into Eq. 3.19 and rearranging the terms, we get the general form of the momentum equation

$$\boxed{\frac{\partial}{\partial t}(\rho_s \mathbf{V}_s) + \nabla \cdot (\rho_s \mathbf{V}_s \mathbf{V}_s + \mathbf{P}_s) = q_s n_s [\mathbf{E} + (\mathbf{V}_s \times \mathbf{B})] + \rho_s \mathbf{g} + \mathbf{R}_s + \mathbf{S}_{p_s}} \tag{3.30}$$

3.3.3 Second moment: energy equation

Multiplying both sides of Eq. 3.6 by $\frac{1}{2}m_s|\mathbf{v}_s|^2$ and integrating over $\mathbf{v}_s$, we get

$$\begin{aligned} \int \tfrac{1}{2}m_s|\mathbf{v}_s|^2 \frac{\partial f_s}{\partial t}\, d^3\mathbf{v}_s + \int \tfrac{1}{2}m_s|\mathbf{v}_s|^2 \left[\mathbf{v}_s \cdot \nabla_r f_s\right] d^3\mathbf{v}_s + \int \tfrac{1}{2}m_s|\mathbf{v}_s|^2 \tfrac{q_s}{m_s}\left(\mathbf{E} + \mathbf{v}_s \times \mathbf{B} + \tfrac{m_s}{q_s}\mathbf{g}\right) \cdot \frac{\partial f_s}{\partial \mathbf{v}_s}\, d^3\mathbf{v}_s \\ = \int \tfrac{1}{2}m_s|\mathbf{v}_s|^2 \left(\frac{\partial f_s}{\partial t}\right)_c d^3\mathbf{v}_s \quad + \int \tfrac{1}{2}m_s|\mathbf{v}_s|^2 \left(\frac{\partial f_s}{\partial t}\right)_{other} d^3\mathbf{v}_s \end{aligned} \tag{3.31}$$

We simplify each sub-term on the LHS:

1. **Time-derivative term:** The term $\frac{1}{2}m_s|\mathbf{v}_s|^2$ is independent of time explicitly (it is a function of $|\mathbf{v}_s|^2$ only). Therefore, after the differentiation can be taken under the integral sign, we arrive at

$$\int \frac{1}{2}m_s|\mathbf{v}_s|^2 \frac{\partial f_s}{\partial t}\, d^3\mathbf{v}_s = \frac{\partial}{\partial t}\int \frac{1}{2}m_s|\mathbf{v}_s|^2 f_s\, d^3\mathbf{v}_s = \frac{\partial E_s}{\partial t} \tag{3.32}$$

   Here, $E_s = \int \frac{1}{2}m_s|\mathbf{v}_s|^2 f_s d^3\mathbf{v}_s$ is the total kinetic energy density of species s.

2. **Spatial term:** Using the identity $\nabla_r \cdot (\mathbf{v}_s f_s) = \mathbf{v}_s \cdot \nabla_r f_s + f_s(\nabla_r \cdot \mathbf{v}_s)$ and noting that $\nabla_r \cdot \mathbf{v}_s = 0$, we get

$$\int \frac{1}{2}m_s|\mathbf{v}_s|^2 \left(\mathbf{v}_s \cdot \nabla_r f_s\right) d^3\mathbf{v}_s = \nabla_r \cdot \int \frac{1}{2}m_s|\mathbf{v}_s|^2\, \mathbf{v}_s f_s\, d^3\mathbf{v}_s \tag{3.33}$$

   Defining the energy flux $\mathbf{q}_s$ as

$$\mathbf{q}_s(x,t) = \int \frac{1}{2}m_s|\mathbf{v}_s|^2\, \mathbf{v}_s f_s\, d^3\mathbf{v}_s \tag{3.34}$$

   The Eq. 3.33 becomes

$$\int \frac{1}{2}m_s|\mathbf{v}_s|^2(\mathbf{v}_s \cdot \nabla_r f_s)\, d^3\mathbf{v}_s = \nabla_r \cdot \mathbf{q}_s \tag{3.35}$$

3. **Force term:** Let

$$\int \frac{1}{2}m_s|\mathbf{v}_s|^2 \frac{q_s}{m_s}\left(\mathbf{E} + \mathbf{v}_s \times \mathbf{B} + \frac{m_s}{q_s}\mathbf{g}\right) \cdot \frac{\partial f_s}{\partial \mathbf{v}_s}\, d^3\mathbf{v}_s = \int \phi(\mathbf{v}_s)(\mathbf{A}_s \cdot \nabla_{v_s} f_s)\, d^3\mathbf{v}_s \tag{3.36}$$

where

$$\mathbf{A}_s = \frac{q_s}{m_s}(\mathbf{E} + \mathbf{v}_s \times \mathbf{B}) + \mathbf{g}, \qquad \phi(\mathbf{v}_s) = \frac{1}{2}m_s|\mathbf{v}_s|^2 \tag{3.37}$$

Using the vector calculus identity $\nabla_{v_s} \cdot (\phi\, f_s\, \mathbf{A}_s) = \phi\,(\mathbf{A}_s \cdot \nabla_{v_s} f_s) + f_s\,(\mathbf{A}_s \cdot \nabla_{v_s}\phi) + \phi f_s\,(\nabla_{v_s} \cdot \mathbf{A}_s)$. Since $\phi f_s(\nabla_{v_s} \cdot \mathbf{A}_s) = 0$, Eq. 3.36 gives

$$\begin{aligned}
\int \phi(\mathbf{v}_s)(\mathbf{A}_s \cdot \nabla_{v_s} f_s)\, d^3v_s &= \int \nabla_{v_s} \cdot (\phi\, f_s\, \mathbf{A}_s)\, d^3\mathbf{v}_s - \int f_s\,(\mathbf{A}_s \cdot \nabla_{v_s}\phi)\, d^3\mathbf{v}_s \\
&= -\int f_s\,(\mathbf{A}_s \cdot \nabla_{v_s}\phi)\, d^3\mathbf{v}_s \\
&= -\int f_s \left(\mathbf{A}_s \cdot \frac{\partial}{\partial \mathbf{v}_s}\frac{1}{2}m_s|\mathbf{v}_s|^2\right) d^3\mathbf{v}_s \\
&= -\int f_s\, m_s\,(\mathbf{A}_s \cdot \mathbf{v}_s)\, d^3\mathbf{v}_s
\end{aligned} \tag{3.38}$$

Substituting $\mathbf{A}_s \cdot \mathbf{v}_s = (q_s/m_s)\,\mathbf{E} \cdot \mathbf{v}_s + \mathbf{g} \cdot \mathbf{v}_s$ above, we get

$$\begin{aligned}
\int \phi(\mathbf{v}_s)(\mathbf{A}_s \cdot \nabla_{v_s} f_s)\, d^3v_s &= -m_s \int f_s\mathbf{v}_s \cdot \left[\frac{q_s}{m_s}\mathbf{E} + \mathbf{g}\right] d^3\mathbf{v}_s \\
&= -\left(\frac{q_s}{m_s}\right)\left[\mathbf{E} \cdot \left(m_s \int \mathbf{v}_s f_s\, d^3\mathbf{v}_s\right)\right] - m_s\left[\mathbf{g} \cdot \int \mathbf{v}_s\, f_s\, d^3\mathbf{v}_s\right] \\
&= -(q_s\,\mathbf{E} + m_s\mathbf{g}) \cdot \left(\int \mathbf{v}_s\, f_s\, d^3\mathbf{v}_s\right) \\
&= -(q_s\,\mathbf{E} + m_s\mathbf{g}) \cdot n_s\mathbf{V}_s \qquad \because \int \mathbf{v}_s\, f_s\, d^3\mathbf{v}_s = n_s\mathbf{V}_s
\end{aligned} \tag{3.39}$$

Collecting all terms, Eq. 3.36 becomes

$$\int \frac{1}{2}m_s|\mathbf{v}_s|^2\,\frac{q_s}{m_s}\left(\mathbf{E} + \mathbf{v}_s \times \mathbf{B} + \frac{m_s}{q_s}g\right) \cdot \frac{\partial f_s}{\partial \mathbf{v}_s}\, d^3\mathbf{v}_s = -\left[q_s n_s(\mathbf{V}_s \cdot \mathbf{E}) \;+\; n_s m_s(\mathbf{V}_s \cdot \mathbf{g})\right] \tag{3.40}$$

Now simplifying each sub-term on the RHS:

1. **Collisional friction heating term:**

$$\int \frac{1}{2}m_s|\mathbf{v}_s|^2 \left(\frac{\partial f_s}{\partial t}\right)_c d^3\mathbf{v}_s = Q_{ss'}^{coll} \tag{3.41}$$

Here, $Q_{ss'}^{coll}$ denotes the collisional energy transfer term. This term arises when the frictional force acts on the fluid due to relative velocity between species s and s' in a multi-species plasma. For example, collisions between ions and neutrals can produce this effect.

2. **Heating and cooling from other processes:**

$$\int \frac{1}{2} m_s |\mathbf{v}_s|^2 \left(\frac{\partial f_s}{\partial t}\right)_{other} d^3\mathbf{v}_s = S \tag{3.42}$$

Here, S accounts for the source and sink terms due to other physical processes, such as ionization, recombination, charge exchange, and various heating and cooling processes, as described briefly below.

- **Ionization and recombination terms:** In a partially ionized plasma, processes such as ionization and recombination occur at different rates, directly affecting the energy density of the constituent fluid. Ionization processes typically require energy input, while recombination releases energy into the fluid. Accordingly, we modify the energy equation for species s as

$$Q_s^{ion} + Q_s^{rec} \tag{3.43}$$

- **Charge-exchange terms:** Charge exchange is a process in which ions and neutrals exchange electrons while maintaining the total number of ions and neutrals in the fluid system. This process can lead to the exchange of energy between the participating species, thereby transferring both momentum and energy between the fluids. Therefore, we modify the energy equation for species s as

$$+S_{ss'}^{ex} \tag{3.44}$$

Putting all the simplified integrals together in Eq. 3.31, we obtain the general form of the energy equation:

$$\boxed{\frac{\partial E_s}{\partial t} + \nabla \cdot \mathbf{q}_s = [q_s n_s (\mathbf{V}_s \cdot \mathbf{E}) + n_s m_s (\mathbf{V}_s \cdot \mathbf{g})] + Q_{ss'}^{coll} + Q_s^{ion} + Q_s^{rec} + S_{ss'}^{ex}} \tag{3.45}$$

Finally, the equations derived in this section are obtained in their most general form. The exact form of these equations in the adopted model is covered in chapter 6 and chapter 7 of this thesis.

3.3.4 Maxwell equations

In modeling the plasma of the solar atmosphere, the macroscopic equations derived above are coupled to Maxwell's equations, which govern the electric field ($\mathbf{E}$) and magnetic field ($\mathbf{B}$) in space and time. A brief overview of these equations is provided below.

- Magnetic monopole

$$\nabla \cdot \mathbf{B} = 0 \tag{3.46}$$

This equation is also known as the *solenoidal equation*, emphasizing the nonexistence of magnetic monopoles and the fact that magnetic field lines are always closed.

- Gauss's law

$$\nabla \cdot \mathbf{E} = \frac{\varrho_s}{\epsilon_0} \tag{3.47}$$

Gauss's law states that the divergence of the electric field $\mathbf{E}$ is proportional to the local charge density ϱ_s.

- Faraday's law

$$\nabla \times \mathbf{E} = -\frac{\partial \mathbf{B}}{\partial t} \tag{3.48}$$

Faraday's law of induction states that a time-varying magnetic field induces an electric field.

- Ampère–Maxwell law

$$\nabla \times \mathbf{B} = \mu_0 \mathbf{j}_s + \mu_0 \epsilon_0 \frac{\partial \mathbf{E}}{\partial t} \tag{3.49}$$

The Ampère–Maxwell law states that a varying electric field and current induce a magnetic field.

In the equations above, ϵ_0 and μ_0 denote, respectively, the electrical permittivity and the magnetic permeability of free space. The current density $\mathbf{j}_s$ and charge density ϱ_s for the species s in the multi-fluid plasma are defined as

$$\mathbf{j}_s = \sum q_s n_s \mathbf{V}_s, \quad \text{and} \quad \varrho_s = \sum q_s n_s \tag{3.50}$$

Note that the principles of electromagnetic phenomena in plasma are valid under the assumption of non-relativistic variations, i.e., $v_0 \ll c$, where $c = 1/\sqrt{\mu_0 \epsilon_0}$ is the speed of light in vacuum. In this limit, the displacement current term $\mu_0 \epsilon_0 \, \partial \mathbf{E}/\partial t$ in Eq. 3.49 can be neglected. This can be shown as follows. Let $v_0 = l_0/t_0$ be the characteristic speed of plasma, where l_0 and t_0 denote, respectively, the characteristic length and time scales of the plasma. To keep the magnitudes on both sides of Eq. 3.48 comparable for a typical plasma system, we assume that

$$\begin{aligned} \frac{E_0}{B_0} &\approx \frac{l_0}{t_0} = v_0 \\ \Rightarrow \frac{1}{c^2}\frac{E_0}{t_0} &\approx \frac{1}{c^2}\frac{B_0}{l_0}\frac{l_0^2}{t_0^2} \\ \Rightarrow \frac{1}{c^2}\frac{E_0}{t_0} &\approx \left|\nabla \times \mathbf{B}\right| \frac{v_0^2}{c^2} \end{aligned} \tag{3.51}$$

The displacement current term $E_0/(t_0c^2)$ is smaller than $\nabla \times \mathbf{B}$ by a factor of v_0^2/c^2 and therefore can be neglected in the non-relativistic limit.

3.3.5 General Ohm's law

The general form of Ohm's law can be derived by using the momentum conservation equation (Eq. 3.34). The essence of the derivation is to combine the ion and electron momentum equations to solve for $\mathbf{E}$. The momentum conservation equations for ions and electrons can be written as (replacing s by i, e, and substituting $|q_e| = |q_i| = e$)

$$\frac{\partial}{\partial t}(n_i m_i \mathbf{V}_i) + \nabla \cdot (n_i m_i \mathbf{V}_i \mathbf{V}_i + \mathbf{P}_i) = e n_i(\mathbf{E} + (V_i \times \mathbf{B})) + n_i m_i \mathbf{g} + \mathbf{R}_i + \mathbf{S}_{p_i} \tag{3.52}$$

$$\frac{\partial}{\partial t}(n_e m_e \mathbf{V}_e) + \nabla \cdot (n_e m_e \mathbf{V}_e \mathbf{V}_e + \mathbf{P}_e) = -e n_e(\mathbf{E} + (V_e \times \mathbf{B})) + n_e m_e \mathbf{g} + \mathbf{R}_e \tag{3.53}$$

Multiplying Eq. 3.52 by m_e/m_i, and subtracting Eq. 3.53 yields

$$\begin{aligned} m_e \frac{\partial}{\partial t}(n_i \mathbf{V}_i - n_e \mathbf{V}_e) + m_e \nabla \cdot (n_i \mathbf{V}_i \mathbf{V}_i - n_e \mathbf{V}_e \mathbf{V}_e) + \nabla \cdot \left(\frac{m_e}{m_i}\mathbf{P}_i - \mathbf{P}_e\right) \\ = e\left[\left(\frac{m_e}{m_i} n_i + n_e\right)\mathbf{E} + \left(\frac{m_e}{m_i} n_i \mathbf{V}_i + n_e \mathbf{V}_e\right) \times \mathbf{B}\right] \quad + \; m_e\, \mathbf{g}(n_i - n_e) \\ + \left(\frac{m_e}{m_i}\mathbf{R}_i - \mathbf{R}_e\right) + \left(\frac{m_e}{m_i}\mathbf{S}_{p_i}\right) \end{aligned} \tag{3.54}$$

Now, from quasi-neutrality in the MHD regime, we have $n_i \approx n_e \equiv n$, neglecting all $\mathcal{O}\left(m_e/m_i\right)$ terms, since $m_e \ll m_i$:

$$\frac{m_e}{e}\frac{\partial \mathbf{j}}{\partial t} + m_e \nabla \cdot [n(\mathbf{V}_i \mathbf{V}_i - \mathbf{V}_e \mathbf{V}_e)] - \nabla \cdot \mathbf{P}_e = en(\mathbf{E} + \mathbf{V}_e \times \mathbf{B}) - \mathbf{R}_e \tag{3.55}$$

Here, $\mathbf{j} = ne(\mathbf{V}_i - \mathbf{V}_e)$ is the current density. The bulk velocity of the plasma is defined as

$$\mathbf{V} = \frac{m_i \mathbf{V}_i + m_e \mathbf{V}_e}{m_i + m_e} = \frac{\mathbf{V}_i + (m_e/m_i)\mathbf{V}_e}{1 + m_e/m_i} \approx \mathbf{V}_i \tag{3.56}$$

$$\Rightarrow \mathbf{V}_e = \mathbf{V} - \frac{\mathbf{j}}{ne} \tag{3.57}$$

Substituting $\mathbf{V}_e$ in Eq. 3.55 and rearranging the terms, we get

$$\mathbf{E} + \mathbf{V} \times \mathbf{B} = \frac{\mathbf{R}_e}{ne} - \frac{\nabla \cdot \mathbf{P}_e}{ne} + \frac{\mathbf{j} \times \mathbf{B}}{ne} + \frac{m_e}{ne^2}\left[\frac{\partial \mathbf{j}}{\partial t} + \nabla \cdot \left(\mathbf{V}\,\mathbf{j} + \mathbf{j}\,\mathbf{V} - \frac{\mathbf{j}\,\mathbf{j}}{ne}\right)\right] \tag{3.58}$$

The term $\mathbf{R}_e$ here denotes the rate of change of the electron momentum due to collisions with ions,

$$\mathbf{R}_e = n\,e\,\lambda\,\mathbf{j} \tag{3.59}$$

where λ is the electrical resistivity, and

$$\nu_c = \frac{n\,e^2}{\lambda\,m_e} \tag{3.60}$$

Here, ν_c is the electron–ion collision frequency. Substituting $\mathbf{R}_e = n\,e\,\lambda\,\mathbf{j}$ into Eq. 3.58, we obtain the most general form of Ohm's law

$$\boxed{\mathbf{E} + \mathbf{V} \times \mathbf{B} = \lambda\,\mathbf{j} - \frac{1}{ne}\nabla \cdot \mathbf{P}_e + \frac{\mathbf{j} \times \mathbf{B}}{ne} + \frac{m_e}{ne^2}\left[\frac{\partial \mathbf{j}}{\partial t} + \nabla \cdot \left(\mathbf{V}\mathbf{j} + \mathbf{j}\mathbf{V} - \frac{\mathbf{j}\mathbf{j}}{ne}\right)\right]} \tag{3.61}$$

Usually, in collisional (resistive) MHD, we neglect Hall, electron-pressure, and electron-inertia terms, retaining a finite resistivity. This yields the Ohmic relation as

$$\boxed{\mathbf{j} = \sigma(\mathbf{E} + \mathbf{V} \times \mathbf{B})} \tag{3.62}$$

Here, $\sigma = 1/\lambda$ is the electrical conductivity of the plasma.

3.3.6 Induction equation and Reynolds number

From Ohm's law (Eq. 3.62) and Ampére-Maxwell's law (Eq. 3.49), we get

$$\mathbf{j} = \sigma(\mathbf{E} + \mathbf{V} \times \mathbf{B}), \qquad \nabla \times \mathbf{B} = \mu_0 \mathbf{j} \tag{3.63}$$

Eliminating $\mathbf{j}$ to express $\mathbf{E}$ in terms of $\mathbf{V}$ and $\mathbf{B}$:

$$\mathbf{E} = \frac{1}{\mu_0 \sigma}\nabla \times \mathbf{B} - \mathbf{V} \times \mathbf{B} \tag{3.64}$$

From Faraday's law:

$$\nabla \times \mathbf{E} = -\frac{\partial \mathbf{B}}{\partial t} \tag{3.65}$$

Substituting $\mathbf{E}$ from Eq. 3.64 into Eq. 3.65 gives

$$\frac{\partial \mathbf{B}}{\partial t} = \nabla \times (\mathbf{V} \times \mathbf{B}) - \frac{1}{\mu_0 \sigma} \nabla \times (\nabla \times \mathbf{B}) \tag{3.66}$$

Using the vector identity $\nabla \times (\nabla \times \mathbf{B}) = \nabla (\nabla \cdot \mathbf{B}) - \nabla^2 \mathbf{B}$ and noting that $\nabla \cdot \mathbf{B} = 0$, we obtain the well-known magnetic induction equation of resistive MHD

$$\boxed{\frac{\partial \mathbf{B}}{\partial t} = \nabla \times (\mathbf{V} \times \mathbf{B}) + \eta \nabla^2 \mathbf{B}} \tag{3.67}$$

Here, $\eta = 1/\mu_0 \sigma$ is the magnetic diffusivity.

Alfvén theorem of flux freezing

Before explaining the Alfvén theorem of flux freezing, we first introduce the dimensionless quantity called the magnetic *Reynolds number* R_M. It is defined as the ratio of the magnitude of the advection term $\nabla \times (\mathbf{V} \times \mathbf{B})$ to the magnitude of the diffusion term $\eta \nabla^2 \mathbf{B}$ (Eq. 3.67).

If B, V, and L denote, respectively, the characteristic scales of the magnetic field strength, velocity, and length for a plasma, then

$$R_M \approx \frac{VB/L}{\eta B/L^2} \approx \frac{VL}{\eta} \tag{3.68}$$

Note that $R_M \propto L$, therefore $R_M \gg 1$ for astrophysical plasma systems where L is large, whereas $R_M \ll 1$ for most laboratory plasma systems.

- **Laboratory plasmas ($R_M \ll 1$):** In this limit, Eq. 3.67 reduces to

$$\frac{\partial \mathbf{B}}{\partial t} \approx \eta \nabla^2 \mathbf{B} \tag{3.69}$$

  This equation indicates that the magnetic field undergoes resistive diffusion, with η acting as the diffusion coefficient. The current density $\mathbf{j}$ decays due to plasma resistivity, and consequently, the magnetic field generated by those currents also decays over time.

- **Astrophysical plasmas ($R_M \gg 1$):** For large-scale systems such as the Sun, Eq. 3.67 becomes

$$\frac{\partial \mathbf{B}}{\partial t} \approx \nabla \times (\mathbf{V} \times \mathbf{B}) \tag{3.70}$$

  From the equation above, we arrive at the well-known *Alfvén theorem of flux freezing*, which states that in the limit of $R_M \gg 1$, the magnetic flux is frozen into the plasma and follows the plasma flow. Large-scale astrophysical plasma systems, such as stellar interiors with $L \gg 1$, therefore satisfy $R_M \gg 1$ and provide the ideal conditions for this flux-freezing behavior.

3.3.7 Ideal gas law

Finally, the chain of the above equations is closed by the equation of state for an ideal gas. For each species s, the ideal gas law is defined as

$$p_s = n_s k_B T_s \tag{3.71}$$

Here, p_s, T_s, and n_s denote, respectively, the pressure, temperature, and number density of species s. The above relation can be derived from the kinetic theory of gases; see, e.g., Rapp-Kindner et al. (2024) for a detailed discussion.

3.4 Magnetohydrodynamics

Magnetohydrodynamics treats the plasma as a continuum medium of an electrically conducting fluid (Sec. 1.2.3). The key assumptions of MHD are

- Quasi-neutrality ($n_i \approx n_e \equiv n$).
- Electron inertia is negligible since $m_e \ll m_i (\equiv m)$, and therefore $\rho = m_i\, n_i + m_e\, n_e \approx m\, n$.
- Gyro-period and mean free path time $\ll$ characteristic time.
- Gyro-radius and mean free path length $\ll$ characteristic scale.
- Plasma bulk velocities $\mathbf{V} \approx \mathbf{V}_i$ (Eq. 3.56) are non-relativistic ($V \ll c$).
- For a singly ionized plasma system, the current is defined as $\mathbf{j} \approx ne(\mathbf{V}_i - \mathbf{V}_e)$.
- The total pressure p is defined as the sum of the ion and electron pressures, i.e., $p = p_i + p_e$.

Considering all the critical assumptions, we can transition from the system of two-fluid equations to the MHD equations as follows.

1. **Mass conservation equation:**

$$\boxed{\frac{\partial \varrho}{\partial t} + \nabla \cdot (\varrho \mathbf{V}) = 0} \tag{3.72}$$

2. **Momentum equation:** The single-fluid momentum equation can be obtained by combining the ion and electron momentum equations. Adding Eqs. 3.52 & 3.53, and observing that Coulomb collisions satisfy $\mathbf{R}_i + \mathbf{R}_e = 0$ and $\mathbf{S}_{p_i} = 0$, we arrive at

$$\frac{\partial}{\partial t}(\varrho_i \mathbf{V}_i + \varrho_e \mathbf{V}_e) + \nabla \cdot (\varrho_i \mathbf{V}_i \mathbf{V}_i + \mathbf{P}_i + \varrho_e \mathbf{V}_e \mathbf{V}_e + \mathbf{P}_e) = e(n_i - n_e)\,\mathbf{E} + (\varrho_i + \varrho_e)\mathbf{g} \\ + \; e[n_i \mathbf{V}_i - n_e \mathbf{V}_e] \times \mathbf{B}) \tag{3.73}$$

Since $\varrho_i \mathbf{V}_i \gg \varrho_e \mathbf{V}_e,\ \varrho_i \mathbf{g} \gg \varrho_e \mathbf{g}$, and $n_i \approx n_e \equiv n$, we obtain the single-fluid momentum equation

$$\boxed{\frac{\partial}{\partial t}(\varrho \mathbf{V}) + \nabla \cdot (\varrho \mathbf{V}\mathbf{V} + p\mathbf{I}) = \mathbf{j} \times \mathbf{B} + \varrho \mathbf{g}} \tag{3.74}$$

Here $\mathbf{P}_i + \mathbf{P}_e = p\mathbf{I}$, and $\mathbf{I}$ is the identity dyadic.

3. **Energy equation:** The single-fluid standard MHD energy equation can be derived by combining the energy equations for the ions and electrons (Eq. 3.45). The energy equation for the ions and electrons in the single-fluid MHD regime is

$$\frac{\partial E_i}{\partial t} + \nabla \cdot \mathbf{q}_i = e n_i (\mathbf{V}_i \cdot \mathbf{E}) + n_i m_i (\mathbf{V}_i \cdot \mathbf{g}) + Q_{ie}^{coll} \tag{3.75}$$

$$\frac{\partial E_e}{\partial t} + \nabla \cdot \mathbf{q}_e = -e n_e (\mathbf{V}_e \cdot \mathbf{E}) + n_e m_e (\mathbf{V}_e \cdot \mathbf{g}) + Q_{ei}^{coll} \tag{3.76}$$

Adding Eqs. 3.75 & 3.76, and noting that $Q_{ie}^{coll} + Q_{ei}^{coll} = 0$, with $n_i \approx n_e \equiv n$, we get

$$\frac{\partial (E_i + E_e)}{\partial t} + \nabla \cdot (\mathbf{q}_i + \mathbf{q}_e) = en(\mathbf{V}_i - \mathbf{V}_e) \cdot \mathbf{E} + n m_i (\mathbf{V}_i \cdot \mathbf{g}) + n m_e (\mathbf{V}_e \cdot \mathbf{g}) \tag{3.77}$$

- Defining $E_i + E_e = E$ as the total energy density.
- Similarly, $\mathbf{q}_i + \mathbf{q}_e = \mathbf{q}$ as the total energy flux.
- $n_i m_i (\mathbf{V}_i \cdot \mathbf{g}) + n_e m_e (\mathbf{V}_e \cdot \mathbf{g}) \approx nm(\mathbf{V} \cdot \mathbf{g})$.

Putting it all together, we get the general form of the single-fluid MHD energy equation:

$$\boxed{\frac{\partial E}{\partial t} + \nabla \cdot \mathbf{q} = \mathbf{j} \cdot \mathbf{E} + nm\mathbf{V} \cdot \mathbf{g}} \tag{3.78}$$

The rest of the equations, namely Ohm's law (Eq. 3.62), the induction equation (Eq. 3.67), and the equation of state (Eq. 3.71), remain the same here.

3.4.1 Ideal magnetohydrodynamics

The ideal MHD is the special case of MHD where all dissipation-related terms, such as resistivity and viscosity, are zero in the set of MHD equations. This assumption holds in the limit of $R_M \gg 1$ (Sec. 3.3.6). Without dissipation terms, Ohm's law and the induction equation respectively read as

$$\boxed{\mathbf{E} + \mathbf{V} \times \mathbf{B} = 0} \qquad \boxed{\frac{\partial \mathbf{B}}{\partial t} = \nabla \times (\mathbf{V} \times \mathbf{B})} \tag{3.79}$$

It is worth mentioning that in full MHD, we typically use the ideal gas law to close the chain of equations. In ideal adiabatic MHD, we can replace the energy equation with the adiabatic closure, which comes from assuming the energy equation contains no heating or cooling terms:

$$\boxed{\left[\frac{\partial}{\partial t} + \mathbf{V} \cdot \nabla\right] \left(\frac{p}{\varrho^\gamma}\right) = 0} \tag{3.80}$$

Here, $p\,,\varrho\,,\gamma$ respectively denote the pressure, density, and adiabatic index.

3.5 Summary

In this chapter, we derived the multi-fluid and single-fluid MHD equations from the Boltzmann equation. The zeroth moment of the Boltzmann equation yields the mass continuity equation, which expresses the conservation of mass. The first moment yields the momentum equation, which describes the balance of the forces and pressures exerted on the plasma. The second moment leads to the energy equation governing the evolution of internal, kinetic, and EM energy. We briefly discussed Maxwell's equations and their coupling to the multi-fluid MHD equations. We derived a general form of Ohm's law that incorporates all non-ideal terms, such as Ohmic heating and the Hall effect. Later, we discussed the induction equation, a key equation in plasma dynamics that explains the Reynolds number and Alfvén theorem of flux freezing. Subsequently, we reduced the MF-MHD equations to the single-fluid MHD equations and highlighted their fundamental assumptions. Finally, we briefly examined the ideal MHD limit.

The next chapter will elaborate on MHD waves and their implications in the stratified solar atmosphere.

Chapter 4

Magnetohydrodynamic waves in plasma

4.1 Introduction

In physics, waves are defined as a type of disturbance that propagates through a medium, primarily carrying energy away from the source (Russell, 2014). The plasma in the solar atmosphere serves as an excellent medium for hosting MHD waves (Sec. 1.3.5). These waves are a natural response of a restoring force to an introduced perturbation, and different restoring forces lead to different wave modes with distinct properties (Tab. 1.3). Both empirical observations and theoretical models acknowledge the importance of MHD waves in the seismic study of the solar atmosphere (Nakariakov et al., 2020). In this chapter, we will discuss basic linear MHD waves in plasma, derive their dispersion relations for the different modes, and examine their characteristics.

4.2 Dispersion relation

MHD waves are often studied using the linear theory of wave motions. The mathematical derivations of the dispersion relations presented here follow a standard pattern. We begin with the plasma in an equilibrium state, introduce small-amplitude perturbations to a static and homogeneous background, linearize the ideal MHD equations to obtain the dispersion relations, and analyze the corresponding characteristics. The derivation presented here broadly follows standard plasma physics books (Priest, 2014; Roberts, 2019).

4.2.1 General dispersion relation for a still medium

We consider an ideal MHD case, where the plasma is frozen to the magnetic field and thermally isolated from its surroundings, with an equilibrium temperature T. The analysis is carried out in a frame of reference rotating with instantaneous angular velocity $\mathbf{\Omega}$ relative to an inertial frame. Assuming the z axis is aligned with the outward normal to the solar surface, the gravitational force per unit volume can be written as $\varrho\, g\, \hat{\mathbf{z}}$, with g assumed constant. The fundamental ideal MHD equations governing the analysis are given below (Sec. 3.4.1).

- Mass conservation equation
$$\frac{\partial \varrho}{\partial t} + \nabla \cdot (\varrho \mathbf{V}) = 0 \tag{4.1}$$

- Momentum equation

$$\frac{\partial}{\partial t}(\varrho \mathbf{V}) + \varrho\,(\mathbf{V}\cdot\nabla)\,\mathbf{V} + \nabla p = \frac{1}{mu_0}(\nabla \times \mathbf{B}) \times \mathbf{B} - \rho\, g\, \hat{\mathbf{z}} - 2\varrho\,(\boldsymbol{\Omega} \times \mathbf{V}) \tag{4.2}$$

- Energy equation
$$\left[\frac{\partial}{\partial t} + \mathbf{V} \cdot \nabla\right]\left(\frac{p}{\varrho^{\gamma}}\right) = 0 \tag{4.3}$$

- Induction equation
$$\frac{\partial \mathbf{B}}{\partial t} = \nabla \times (\mathbf{V} \times \mathbf{B}) \tag{4.4}$$

- Magnetic monopole
$$\nabla \cdot \mathbf{B} = 0 \tag{4.5}$$

Here, $|(\boldsymbol{\Omega}\times\mathbf{r})+\mathbf{V}| \ll c$, where $\mathbf{r}$ is the position vector from the axis of rotation. We assumed a gravitationally stratified infinite stationary plasma ($\mathbf{V}_0 = 0$) at equilibrium, permeated by the constant magnetic field $\mathbf{B}_0$, under pressure p_0, and mass density ϱ_0 (Eq. 4.16). Introducing small perturbations to this equilibrium — in mass density, velocity, and magnetic field — we write each physical quantity as the sum of its equilibrium value, denoted by subscript 0, and a first-order disturbance, denoted by subscript 1.

$$\varrho = \varrho_0(z) + \varrho_1(x, y, z, t), \;\; \mathbf{B} = \mathbf{B_0} + \mathbf{B_1}, \;\; p = p_0 + p_1, \;\; \mathbf{V} = \mathbf{V}_1 \tag{4.6}$$

The amplitude of the perturbation here is much smaller than the equilibrium amplitude; therefore, when linearizing the system of equations, the terms containing higher powers can be neglected. It is crucial to note that perturbation is a localized phenomenon where variations in the background occur on a timescale much larger than the wave motion of interest; therefore, it overlooks the broader gradients of macroscopic variables. Substituting the perturbation ansatz of Eq. 4.6 into Eqs. 4.1 – 4.5, we obtain

-
$$\frac{\partial \varrho_1}{\partial t} + \mathbf{V}_1 \cdot (\nabla \varrho_0) + \varrho_0(\nabla \cdot \mathbf{V}_1) = 0 \tag{4.7}$$

-

$$\frac{\partial}{\partial t}(\varrho_0 \mathbf{V}_1) + \nabla p_1 = \frac{1}{\mu_0}(\nabla \times \mathbf{B}_1) \times \mathbf{B}_0 - \varrho_1\, g\, \hat{\mathbf{z}} - 2\varrho_0(\boldsymbol{\Omega} \times \mathbf{V}_1) \tag{4.8}$$

- $$\frac{\partial p_1}{\partial t} + (\mathbf{V}_1 \cdot \nabla) p_0 - C_s^2 \left[\frac{\partial \varrho_1}{\partial t} + (\mathbf{V}_1 \cdot \nabla) \varrho_0 \right] = 0 \tag{4.9}$$

- $$\frac{\partial \mathbf{B}_1}{\partial t} = \nabla \times (\mathbf{V}_1 \times \mathbf{B}_0) \tag{4.10}$$

- $$\nabla \cdot \mathbf{B}_1 = 0 \tag{4.11}$$

Here $C_s^2 = \gamma p_0 / \varrho_0$ denotes the sound speed. Differentiating Eq. 4.8 with respect to t, we get

$$\frac{\partial^2}{\partial t^2}(\varrho_0 \mathbf{V}_1) + \nabla \left(\frac{\partial p_1}{\partial t} \right) = \frac{\partial}{\partial t} \left(\frac{(\nabla \times \mathbf{B}_1) \times \mathbf{B}_0}{\mu_0} \right) - g \, \frac{\partial \varrho_1}{\partial t} \, \hat{\mathbf{z}} - 2 \, \varrho_0 \, \mathbf{\Omega} \times \frac{\partial \mathbf{V}_1}{\partial t} \tag{4.12}$$

To obtain the general wave equation, we will use a couple of substitutions. Substituting $\partial \varrho_1 / \partial t$ from Eq. 4.7 into Eq. 4.9,

$$\frac{\partial p_1}{\partial t} = -(\mathbf{V}_1 \cdot \nabla) \, p_0 - C_s^2 \, \varrho_0 \, \nabla \cdot \mathbf{V}_1 \tag{4.13}$$

From Eq. 4.7, we have

$$g \, \hat{\mathbf{z}} \, \frac{\partial \varrho_1}{\partial t} = -g \, \hat{\mathbf{z}} \, [(\mathbf{V}_1 \cdot \nabla) \varrho_0 + \varrho_0 \nabla \cdot \mathbf{V}_1] \tag{4.14}$$

Also,

$$\begin{aligned} \frac{\partial}{\partial t} \left(\frac{(\nabla \times \mathbf{B}_1) \times \mathbf{B}_0}{\mu_0} \right) &= \frac{1}{\mu_0} \left(\nabla \times \frac{\partial \mathbf{B}_1}{\partial t} \right) \times \mathbf{B}_0 \\ &= \frac{1}{\mu_0} \left[\nabla \times (\nabla \times (\mathbf{V}_1 \times \mathbf{B}_0)) \right] \times \mathbf{B}_0 \quad \text{(using Eq. 4.10)} \end{aligned} \tag{4.15}$$

Plugging Eqs. 4.13, 4.14, and 4.15 into Eq. 4.12 and assuming an exponentially stratified background with

$$p_0(z) = k_p e^{-z/\Lambda}, \quad \varrho_0(z) = k_\varrho e^{-z/\Lambda} \tag{4.16}$$

where k_p and k_ϱ are constants, and $\Lambda = p_0 / \varrho_0 g$ is the pressure scale height. We finally get

$$\begin{aligned} \frac{\partial^2 \mathbf{V}_1}{\partial t^2} = C_s^2 \nabla(\nabla \cdot \mathbf{V}_1) - g(\nabla \mathrm{V}_{1z}) - g(\gamma - 1)(\nabla \cdot \mathbf{V}_1) \, \hat{\mathbf{z}} - 2\mathbf{\Omega} \times \frac{\partial \mathbf{V}_1}{\partial t} \\ + \frac{1}{\mu_0 \varrho_0} \left[\nabla \times (\nabla \times (\mathbf{V}_1 \times \mathbf{B}_0)) \right] \times \mathbf{B}_0 \end{aligned} \tag{4.17}$$

This is the generalized wave equation for the disturbance $\mathbf{V}_1$. To obtain the plane wave solution, we assume that $\mathbf{V}_1$ varies sinusoidally in space and time. Note that this mathematical assumption does not lead to a loss of generality, since any physically realizable wave motion can, in principle, be represented as a superposition of plane waves.

$$\therefore \quad \mathbf{V}_1 = \mathrm{V}_1 \exp\left[\,\mathrm{i}\,(\mathbf{k}\cdot\mathbf{r} - \omega \mathrm{t})\right] \tag{4.18}$$

Here, ω and $\mathbf{k}$ denote, respectively, the angular frequency and wave vector of the plane wave. Substituting $\mathbf{V}_1$ from Eq. 4.18 into Eq. 4.17, and reconciling the time derivative $\partial/\partial t$ with $i\omega$, and the gradient ∇ with $i\mathbf{k}$, we obtain

$$\begin{aligned}\omega^2\mathbf{V}_1 = C_s^2(\mathbf{V}_1\cdot\mathbf{k})\,\mathbf{k} + i\,g\,k\,\mathrm{V}_1\,\hat{\mathbf{z}} + i\,g\,(\gamma-1)\,(\mathbf{V}_1\cdot\mathbf{k})\,\hat{\mathbf{z}} - i\,2\,\omega\,\boldsymbol{\Omega}\times\mathbf{V}_1 + \\ \frac{1}{\mu_0\varrho_0}\left[\mathbf{k}\times(\mathbf{k}\times(\mathbf{V}_1\times\mathbf{B}_0))\right]\times\mathbf{B}_0\end{aligned} \tag{4.19}$$

This equation serves as the starting point for deriving the dispersion relation, which expresses ω as a function of $\mathbf{k}$. In the following subsections, we will examine the dispersion relations of fundamental MHD modes and discuss their key properties.

4.2.2 Acoustic waves

Acoustic waves are a kind of mechanical wave (longitudinal wave) in which pressure acts as the restoring force. In these waves, pressure variations propagate through the medium, while other restoring forces, such as magnetic tension, gravity, and the Coriolis force, are typically negligible. Consequently, setting $\mathbf{B}_0 = 0$ and $g = \Omega = \mathcal{O}(0)$, Eq. 4.19 simplifies to

$$\omega^2\mathbf{V}_1 = C_s^2\,\mathbf{k}\,(\mathbf{V}_1\cdot\mathbf{k}) \tag{4.20}$$

Taking the scalar product with $\mathbf{k}$ on both sides, we finally get the dispersion relation for acoustic waves:

$$\boxed{\omega^2 = C_s^2\,k^2} \tag{4.21}$$

This relation indicates that sound waves are longitudinal and compressional, as the velocity perturbation $\mathbf{V}_1$ lies in the direction of the wave vector ($\mathbf{V}_1\cdot\mathbf{k} \neq 0$). Both the phase velocity $v_p = \Omega/k$ and the group velocity $v_g = d\omega/dk$ are equal to the sound speed C_s, which is independent of the wave number k. Therefore, acoustic waves are non-dispersive and isotropic.

4.2.3 Magnetoacoustic waves

Magnetoacoustic waves (MAWs) are low-frequency compressional waves driven by the mutual interaction between an electrically conducting fluid and a magnetic field, which propagate in a plasma where both gas pressure and the magnetic field provide the restoring forces.

Therefore, by assigning $\omega = g = 0$, recognizing $\mathbf{B}_0 = B_0\,\hat{\mathbf{z}}$, and defining the Alfvén speed V_A as $B_0/\sqrt{\mu\rho_0}$, we simplify Eq. 4.19 to

$$\frac{\omega^2 \mathbf{V}_1}{V_A^2} = \frac{C_s^2}{V_A^2}\,(\mathbf{V}_1 \cdot \mathbf{k})\,\mathbf{k} + [\mathbf{k} \times (\mathbf{k} \times (\mathbf{V}_1 \times \hat{\mathbf{z}}))] \times \hat{\mathbf{z}} \tag{4.22}$$

Using the identity $\mathbf{A} \times (\mathbf{B} \times \mathbf{C}) = \mathbf{B}(\mathbf{A} \cdot \mathbf{C}) - \mathbf{C}(\mathbf{A} \cdot \mathbf{B})$ here, we get

$$\frac{\omega^2 \mathbf{V}_1}{V_A^2} = \frac{C_s^2}{V_A^2}\,(\mathbf{V}_1 \cdot \mathbf{k})\,\mathbf{k} + (\mathbf{k} \cdot \hat{\mathbf{z}})^2\,\mathbf{V}_1 - (\mathbf{V}_1 \cdot \hat{\mathbf{z}})(\mathbf{k} \cdot \hat{\mathbf{z}})\,\mathbf{k} + (\mathbf{V}_1 \cdot \mathbf{k})\,\mathbf{k} - (\mathbf{k} \cdot \hat{\mathbf{z}})(\mathbf{V}_1 \cdot \mathbf{k})\,\hat{\mathbf{z}} \tag{4.23}$$

Hence,

$$\frac{\omega^2 \mathbf{V}_1}{V_A^2} = (k\cos\theta)^2\,\mathbf{V}_1 - (\mathbf{V}_1 \cdot \hat{\mathbf{z}})(k\cos\theta)\,\mathbf{k} + \left(1 + \frac{C_s^2}{V_A^2}\right)(\mathbf{V}_1 \cdot \mathbf{k})\,\mathbf{k} - (k\cos\theta)(\mathbf{V}_1 \cdot \mathbf{k})\,\hat{\mathbf{z}} \tag{4.24}$$

Here, $0 \le \theta \le \pi/2$ is the angle between $\mathbf{B}_0$ and $\mathbf{k}$. By taking the scalar product with $\mathbf{k}$ and $\hat{\mathbf{z}}$ on both sides and rearranging the equations, we arrive at

$$\frac{\omega^2}{V_A^2} - k^2\left(1 + \frac{C_s^2}{V_A^2}\right)(\mathbf{V}_1 \cdot \mathbf{k}) = -k^3\cos\theta\,(\mathbf{V}_1 \cdot \hat{\mathbf{z}}) \tag{4.25}$$

and

$$\omega^2(\mathbf{V}_1 \cdot \hat{\mathbf{z}}) = k\cos\theta\; C_s^2(\mathbf{V}_1 \cdot \mathbf{k}) \tag{4.26}$$

Eliminating $\mathbf{V}_1 \cdot \hat{\mathbf{z}}$ and $\mathbf{V}_1 \cdot \mathbf{k}$ between Eqs. 4.25 and 4.26, we derive the dispersion relation for the MAWs:

$$\boxed{\omega^4 - \omega^2\,k^2(V_A^2 + C_s^2) + C_s^2 V_A^2 k^4 \cos^2\theta = 0} \tag{4.27}$$

The dispersion relation above has two distinct solutions:

$$\boxed{\frac{\omega^2}{k^2} = \frac{1}{2}\left((V_A^2 + C_s^2) \pm \sqrt{(V_A^2 + C_s^2)^2 - 4\cos^2\theta\,V_A^2 C_s^2}\right)} \tag{4.28}$$

The solution associated with the higher-frequency mode ($'+'$) corresponds to the fast MAWs, while the solution related to the lower-frequency mode ($'-'$) refers to the slow MAWs (Ofman et al., 1999). Unlike acoustic waves, the dispersion relation reveals that the phase speed of MAWs depends explicitly on the propagation angle θ; therefore, these waves are dispersive and anisotropic. For the fast-frequency mode, at $\theta = 0$ (aligned with magnetic field lines), the fast MAWs propagate with a phase speed equal to V_A. However, when $\theta = \pi/2$ (perpendicular to magnetic field lines), the waves propagate with a phase speed of $\sqrt{V_A^2 + C_s^2}$, indicating that fast MAWs propagate fastest across the magnetic field lines.

For the slow MAWs, at $\theta = 0$, the dispersion relation yields $\omega^2 = k^2 C_T^2$, where $C_T^2 =$

$C_s^2 V_A^2/(C_s^2 + V_A^2)$ is the tube (cusp) speed. This means that the tube speed is the phase speed at which the slow MAWs travel along the magnetic field lines. On the other hand, for $\theta = \pi/2$, the dispersion relation reduces to $\omega/k = 0$, indicating that slow MAWs are unable to propagate perpendicular to the magnetic field lines.

4.2.4 Alfvén waves

The Alfvén waves, named after Hannes Alfvén (Alfvén, 1942), are elastic transverse waves that propagate along magnetic field lines, with magnetic tension as the main restoring force (Cramer, 2011). In this context, Eq. 4.24 becomes

$$\left(\frac{\omega^2}{V_A^2}\right)\mathbf{V}_1 = (\mathbf{k}\cdot\hat{\mathbf{z}})^2\,\mathbf{V}_1 - (\mathbf{V}_1\cdot\hat{\mathbf{z}})(\mathbf{k}\cdot\hat{\mathbf{z}})\,\mathbf{k} + (\mathbf{V}_1\cdot\mathbf{k})\,\mathbf{k} - (\mathbf{k}\cdot\hat{\mathbf{z}})(\mathbf{V}_1\cdot\mathbf{k})\,\hat{\mathbf{z}} \tag{4.29}$$

Taking the dot product with $\hat{\mathbf{z}}$ and $\mathbf{k}$ respectively gives

$$\left(\frac{\omega^2}{V_A^2}\right)\mathbf{V}_1\cdot\hat{\mathbf{z}} = \Big((\mathbf{k}\cdot\hat{\mathbf{z}})^2\,\mathbf{V}_1 - (\mathbf{V}_1\cdot\hat{\mathbf{z}})(\mathbf{k}\cdot\hat{\mathbf{z}})\,\mathbf{k} + (\mathbf{V}_1\cdot\mathbf{k})\,\mathbf{k} - (\mathbf{k}\cdot\hat{\mathbf{z}})(\mathbf{V}_1\cdot\mathbf{k})\,\hat{\mathbf{z}}\Big)\cdot\hat{\mathbf{z}} \tag{4.30}$$

$$\left(\frac{\omega^2}{V_A^2}\right)\mathbf{V}_1\cdot\hat{\mathbf{z}} = (\mathbf{V}_1\cdot\hat{\mathbf{z}})\Big((\mathbf{k}\cdot\hat{\mathbf{z}})^2 - (\mathbf{k}\cdot\hat{\mathbf{z}})^2\Big) + (\mathbf{k}\cdot\hat{\mathbf{z}})\Big((\mathbf{V}_1\cdot\mathbf{k}) - (\mathbf{V}_1\cdot\mathbf{k})\Big) \tag{4.31}$$

$$\Longrightarrow \mathbf{V}_1\cdot\hat{\mathbf{z}} = 0 \tag{4.32}$$

and

$$\left(\frac{\omega^2}{V_A^2}\right)\mathbf{V}_1\cdot\mathbf{k} = \Big((\mathbf{k}\cdot\hat{\mathbf{z}})^2\,\mathbf{V}_1 - (\mathbf{V}_1\cdot\hat{\mathbf{z}})(\mathbf{k}\cdot\hat{\mathbf{z}})\,\mathbf{k} + (\mathbf{V}_1\cdot\mathbf{k})\,\mathbf{k} - (\mathbf{k}\cdot\hat{\mathbf{z}})(\mathbf{V}_1\cdot\mathbf{k})\,\hat{\mathbf{z}}\Big)\cdot\mathbf{k} \tag{4.33}$$

$$\left(\frac{\omega^2}{V_A^2}\right)\mathbf{V}_1\cdot\mathbf{k} = \Big(\cancel{(\mathbf{k}\cdot\hat{\mathbf{z}})^2(\mathbf{V}_1\cdot\mathbf{k})} - k^2(\mathbf{V}_1\cdot\hat{\mathbf{z}})(\mathbf{k}\cdot\hat{\mathbf{z}}) + k^2\,(\mathbf{V}_1\cdot\mathbf{k}) - \cancel{(\mathbf{k}\cdot\hat{\mathbf{z}})^2(\mathbf{V}_1\cdot\mathbf{k})}\Big) \tag{4.34}$$

$$\Longrightarrow (\mathbf{V}_1\cdot\mathbf{k})\,(\omega^2 - k^2V_A^2) = 0 \tag{4.35}$$

If the perturbation is incompressible, i.e., $\nabla\cdot\mathbf{V}_1 = 0$, then $\mathbf{V}_1\cdot\mathbf{k} = 0$. This indicates an incompressible disturbance, characterized by a velocity perturbation that is perpendicular to the propagation vector. This leads to incompressible Alfvén waves; conversely, substituting $\mathbf{V}_1\cdot\mathbf{k} = 0$ and $\mathbf{V}_1\cdot\hat{\mathbf{z}} = 0$ in Eq. 4.29 gives the dispersion relation for the incompressible Alfvén waves:

$$\boxed{\frac{\omega}{k} = V_A\cos\theta} \tag{4.36}$$

These waves are characterized as transverse and non-dispersive because the phase speed $V_A\cos\theta$ is determined by the field-aligned component of k. When $\theta = 0$, which is aligned with the magnetic field lines, the phase speed reaches its maximum value, V_A. Conversely, for $\theta = \pi/2$, the phase speed becomes zero, indicating that the incompressible Alfvén wave cannot travel perpendicular to the magnetic field lines.

Finally, the derived dispersion relations indicate the role different restoring forces play in shaping the wave properties. When the magnetic field is absent ($V_A = 0$), the slow MAWs vanish, while the fast MAWs convert into sound waves. In contrast, in the absence of gas pressure ($C_s = 0$), the slow MAWs disappear, and the fast MAWs transform into compressible Alfvén waves.

4.2.5 Internal gravity waves in gravitationally stratified plasma

Understanding gravity waves requires familiarity with convection, the related concept of *convective instability*, and the *Schwarzschild's criterion* (Schatten et al., 1981) in a stratified solar atmosphere. In the convection zone of the Sun, solar convection is the primary means of energy transport, typically forming a circular convection current where warm plasma rises and cool plasma sinks (Sec. 1.3.2). Schwarzschild's criterion indicates when a stellar medium is stable against convection.

In this context, consider a blob (parcel) with mass m and volume V of a fluid in hydrostatic equilibrium inside the Sun. Suppose the parcel is initially located at position z with internal (inside the parcel) mass density ϱ_i and pressure p_i. Initially, the external mass density and pressure are the same as inside the blob, i.e., (ϱ_i, p_i). Let this parcel be displaced slightly by a force F. The internal mass density and pressure of the blob at the new position are, respectively, ϱ_f^* and p_f. Assuming an adiabatic process and that the fluid remains in pressure equilibrium with its surroundings, the external mass density and pressure at the new position $(z+\Delta z)$ are, respectively, ϱ_f and p_f (Fig. 4.1). If $\varrho_f^* < \varrho_f$, the blob will continue to rise under the influence of the buoyant force, resulting in convective instabilities. On the other hand, for $\varrho_f^* > \varrho_f$, the blob attempts to return to its original position z, driving the system to stability and preventing convective instabilities (Choudhuri, 2010). From Eq. 4.3, we obtain

$$p_i \varrho_i^{-\gamma} = p_f \varrho_f^{*-\gamma} \Rightarrow \varrho_f^* = \varrho_i \left(\frac{p_f}{p_i}\right)^{\frac{1}{\gamma}} \tag{4.37}$$

Let $d\varrho_i/dz$ and dp_i/dz denote the density and pressure gradients in the solar stratified atmosphere, respectively, then

$$\varrho_f \approx \varrho_i + \frac{d\varrho_i}{dz}\Delta z\,, \qquad p_f \approx p_i + \frac{dp_i}{dz}\Delta z \tag{4.38}$$

Inserting ϱ_f from Eq. 4.38 into Eq. 4.37, expanding binomially, and keeping only the linear

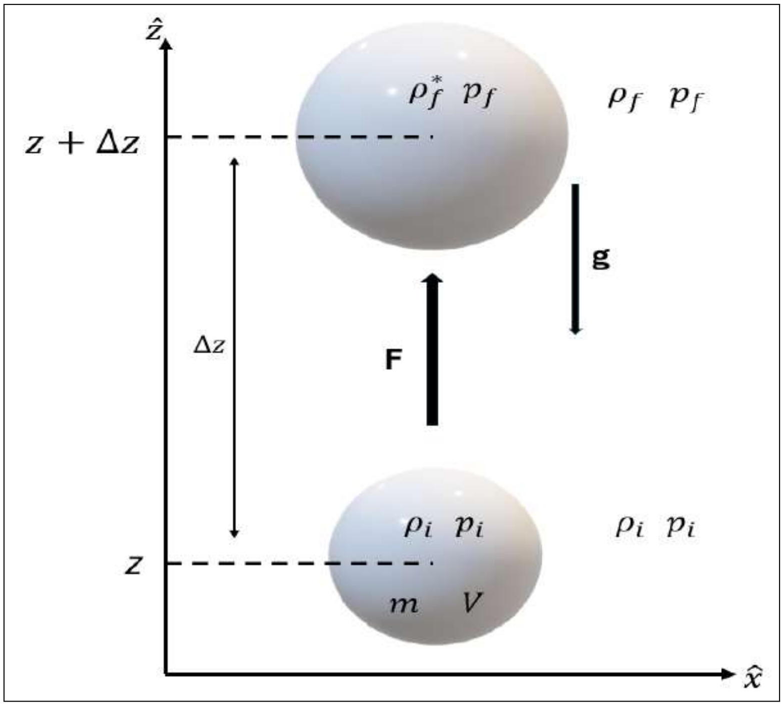

Figure 4.1: A blob of plasma moving vertically from the height z to the height $z + \Delta z$ in the stratified solar atmosphere.

term in Δz, we get

$$\varrho_f^* = \varrho_i \left(1 + \frac{1}{p_i}\frac{dp_i}{dz}\Delta z\right)^{\frac{1}{\gamma}} \Longrightarrow \varrho_f^* \approx \varrho_i \left(1 + \frac{1}{\gamma p_i}\frac{dp_i}{dz}\Delta z\right) \tag{4.39}$$

From the ideal gas law, we have

$$\varrho_i = \frac{p_i}{RT} \Longrightarrow \frac{d\varrho_i}{dz} = \frac{1}{RT}\frac{dp_i}{dz} - \frac{p_i}{RT^2}\frac{dT}{dz} \tag{4.40}$$

$$\Rightarrow \frac{d\varrho_i}{dz} = \frac{\varrho_i}{p_i}\frac{dp_i}{dz} - \frac{\varrho_i}{T}\frac{dT}{dz} \tag{4.41}$$

Substituting $d\varrho_i/dz$ in Eq. 4.38, we obtain

$$\varrho_f = \varrho_i + \left(\frac{\varrho_i}{p_i}\frac{dp_i}{dz} - \frac{\varrho_i}{T}\frac{dT}{dz}\right)\Delta z \tag{4.42}$$

Now subtracting Eq. 4.42 from Eq. 4.40

$$\varrho_f^* - \varrho_f = \left[-\left(1 - \frac{1}{\gamma}\right)\frac{\varrho_i}{p_i}\frac{dp_i}{dz} + \frac{\varrho_i}{T}\frac{dT}{dz}\right]\Delta z \tag{4.43}$$

Since T and p fall with height; therefore dT/dz and dp_i/dz are both negative, Eq. 4.43 can be rewritten as

$$\varrho_f^* - \varrho_f = \left[\left(1 - \frac{1}{\gamma}\right)\frac{\varrho_i}{p_i}\left|\frac{dp_i}{dz}\right| - \frac{\varrho_i}{T}\left|\frac{dT}{dz}\right|\right]\Delta z \tag{4.44}$$

The system is stable only if the blob can return to its original position after the initial displacement; i.e., $\varrho_f^* - \varrho_f > 0$. Therefore, from Eq. 4.44, we have

$$\boxed{\left|\frac{dT}{dz}\right| < \left(1 - \frac{1}{\gamma}\right)\frac{T}{p_i}\left|\frac{dp_i}{dz}\right|} \tag{4.45}$$

This condition is commonly referred to as the *Schwarzschild criterion for convective stability*, which states that for convection to occur, $\left|\frac{dT}{dz}\right| > \left(1 - \frac{1}{\gamma}\right)\frac{T}{p_i}\left|\frac{dp_i}{dz}\right|$. The layer of the solar atmosphere where this criterion is fulfilled is the convection zone.

If F is the buoyant force experienced by the plasma blob, then

$$F = (\varrho_f^* - \varrho_f)gV \tag{4.46}$$

Hence,

$$m_i\frac{d^2\Delta z}{dt^2} = (\varrho_f^* - \varrho_f)\, g\, V_i \tag{4.47}$$

Using Eq. 4.45 and $m_i = \varrho_i V_i$, we get

$$\varrho_i\frac{d^2\Delta z}{dt^2} = \left[\left(1 - \frac{1}{\gamma}\right)\frac{\varrho_i}{p_i}\left|\frac{dp_i}{dz}\right| - \frac{\varrho_i}{T}\left|\frac{dT}{dz}\right|\right] g\Delta z \tag{4.48}$$

The above equation indicates that the plasma blob executes simple harmonic motion (SHM) at the *Brunt-*Väisälä *frequency* K, where

$$K^2 = g\left[\left(1 - \frac{1}{\gamma}\right)\frac{1}{p_i}\left|\frac{dp_i}{dz}\right| - \frac{1}{T}\left|\frac{dT}{dz}\right|\right] \tag{4.49}$$

From Eq. 4.38, we infer the existence of gravity waves due to the SHM of the fluid blob. If the buoyant force is the sole force F acting on the blob, then Eq. 4.19 simplifies to

$$\omega^2\,\mathbf{V}_1 = C_s^2\,\mathbf{k}\,(\mathbf{V}_1\cdot\mathbf{k}) + i\,g\,V_{1z}\,\mathbf{k} + i\,g\,(\gamma-1)\,(\mathbf{V}_1\cdot\mathbf{k})\,\hat{\mathbf{z}} \tag{4.50}$$

Taking the scalar product with $\mathbf{k}$ and $\hat{\mathbf{z}}$, we get

$$\Big(\omega^2 - C_s^2\,k^2 - i\,g\,(\gamma-1)(\mathbf{k}\cdot\hat{\mathbf{z}})\Big)\mathbf{V}_1\cdot\mathbf{k} = i\,g\,k^2\,V_{1z}\,, \tag{4.51}$$

and

$$\Big(C_s^2\,(\mathbf{k}\cdot\hat{\mathbf{z}}) + i\,g\,(\gamma-1)\Big)\mathbf{V}_1\cdot\mathbf{k} = \Big(\omega^2 - i\,g\,(\mathbf{k}\cdot\hat{\mathbf{z}})\Big)V_{1z} \tag{4.52}$$

Dividing Eq. 4.51 by Eq. 4.52 and noting that $k_z = \mathbf{k}\cdot\hat{\mathbf{z}} = k\cos\theta$,

$$\frac{\Big(\omega^2 - C_s^2\,k^2 - i\,g\,(\gamma-1)(\mathbf{k}\cdot\hat{\mathbf{z}})\Big)\mathbf{V}_1\cdot\mathbf{k}}{\Big(C_s^2\,(\mathbf{k}\cdot\hat{\mathbf{z}}) + i\,g\,(\gamma-1)\Big)\mathbf{V}_1\cdot\mathbf{k}} = \frac{i\,g\,k^2\,V_{1z}}{\Big(\omega^2 - i\,g\,(\mathbf{k}\cdot\hat{\mathbf{z}})\Big)\,V_{1z}} \tag{4.53}$$

Hence,

$$(\omega^2 - C_s^2\,k^2 - i\,g\,(\gamma-1)(\mathbf{k}\cdot\hat{\mathbf{z}}))(\omega^2 - i\,g\,(\mathbf{k}\cdot\hat{\mathbf{z}})) = (C_s^2\,(\mathbf{k}\cdot\hat{\mathbf{z}}) + i\,g\,(\gamma-1))(i\,g\,k^2) \tag{4.54}$$

or

$$\omega^4 - i\,\omega^2 g\,k\cos\theta - \omega^2 C_s^2\,k^2 + i\,g\,C_s^2\,k^3\cos\theta - g^2k^2(\gamma-1)\cos^2\theta = i\,g\,C_s^2\,k^3\cos\theta - g^2\,k^2\,(\gamma-1) \tag{4.55}$$

In the limit of $\omega/k \ll C_s$, ω^4 is negligible compared to $C_s^2\,k^2\,\omega^2$, so we reduce the above equation to the following form:

$$-i\,\omega^2\,g\,k\cos\theta - \omega^2\,C_s^2\,k^2 - g^2\,k^2\,(\gamma-1)\cos^2\theta = -g^2\,k^2\,(\gamma-1) \tag{4.56}$$

Equating only the real part, we obtain

$$\boxed{\omega^2 = \frac{g^2(\gamma-1)\sin^2\theta}{C_s^2}} \tag{4.57}$$

Here, for $\theta = 0$, $\omega = 0$, indicating pure vertical propagation is forbidden; this means internal gravity waves must have at least a horizontal propagation component. Consequently, internal gravity waves exhibit anisotropy, unlike acoustic waves, which are fundamentally isotropic.

4.3 Waves in inhomogeneous plasma

In the previous section, we found that a fully homogeneous plasma can host a wide range of wave modes. In real plasma, the background parameters, such as mass density, pressure, and magnetic field, exhibit inhomogeneity due to spatio-temporal variations, or regions exist where the linear approximation is no longer valid. These inhomogeneities or nonlinear behaviors alter the local wave characteristics and cause effects such as phase mixing, reflection, and coupling, etc., at interfaces with varying physical characteristics.

Phase mixing occurs when Alfvén waves, propagating along magnetic field lines with varying Alfvén speeds, gradually become out of phase and develop smaller spatial scales, resulting in enhanced wave dissipation (Nakariakov et al., 1998). Consider Alfvén waves traveling along the z-axis with $V_A = V_A(x)$. In this case, different parts of the wavefront travel at different velocities so that adjacent field lines oscillate out of phase. This gives rise to steep gradients in wave properties, effectively damping the waves and generating MAWs, thus coupling Alfvén and MAWs. Such phase-mixed Alfvén waves have been proposed as a potential contributing mechanism for compensating chromospheric radiative losses (Howson et al., 2019).

Plasma inhomogeneity may result in sharp density or temperature gradients, leading to interfaces. At such a boundary, wave refraction or reflection can occur depending on the incidence angle and boundary conditions. In earlier studies, Petrukhin (1981) reported the refraction of acoustic gravity waves (AGWs) across a boundary between two isothermal media with different temperatures, in the context of energy transfer into the solar corona. Krogulec et al. (1994) analyzed Alfvén wave reflection efficiencies using reflection coefficients, identifying regions of enhanced reflection across various wave models. Along similar lines, Murawski et al. (2015) performed 2.5-D numerical simulations with geometry-dependent reflection and reported that only about 5% of the wave amplitude is reflected in the transition region, while the remaining is transmitted and partially mode-converted into magnetoacoustic jets. A model with upward- and downward-propagating waves, recently proposed by Chaturmutha et al. (2024), provides strong evidence for reflection in the solar atmosphere.

Nonlinearities in the MHD equations can lead to coupling between wave modes. One example is the *ponderomotive force*, a nonlinear effect stemming from spatio-temporal variations in the magnetic tension. This nonlinear effect enables Alfvén waves to drive both slow and fast MAWs. Detailed discussions of Alfvén-wave–driven mode coupling in different wavelength regimes are presented in Murawski (1992). Similarly, Ohtani et al. (1989) examined wave coupling in an inhomogeneous two-fluid plasma characterized by varying plasma β, which is equal to the ratio of thermal to magnetic pressure. See also studies by Misra et al. (2025), Wright et al. (2020), Ballester et al. (2020), Ballester (2023), and Terradas et al. (2011). Chapter 6 discusses several results regarding the coupling of Alfvén-MAWs in the context of the heating of the solar chromosphere and associated plasma outflows.

Rayleigh-Taylor instability (RTI) is a prominent energy-mixing mechanism due to plasma inhomogeneities (e.g., a heavy fluid lying on top of a light fluid) under the influence of magnetic and gravitational fields. Comprehending RTI requires the orbital theory (Chen et al., 1984), where the drift velocity V_D of a particle with charge q and mass m subjected to a magnetic $\mathbf{B}$ and force field $\mathbf{F} = m\mathbf{g}$, assuming $F/qB \ll c$,

$$\boxed{\mathbf{V}_D = \frac{m\mathbf{g} \times \mathbf{B}}{qB^2}} \tag{4.58}$$

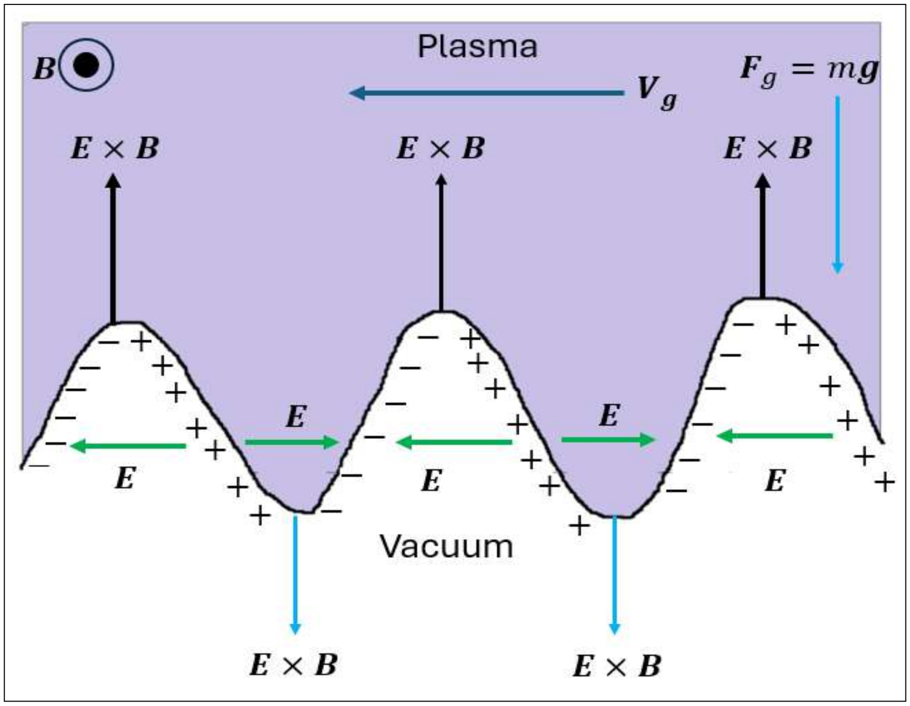

Figure 4.2: A demonstration of how Rayleigh–Taylor instabilities are caused by the interaction of electric and gravitational drifts at the interface between the plasma and the vacuum.

To understand RTI, envision a wave-like structure growing on the interface of the vacuum and plasma (Fig. 4.2). According to Eq. 4.58, gravitational drift causes the ion and electron to migrate apart in opposing directions, producing a weak local electric field. This locally generated electric $\mathbf{E}$ and externally applied magnetic field $\mathbf{B}$ result in the equivalent $\mathbf{E}\times\mathbf{B}$ drift perpendicular to $\mathbf{E}$ and $\mathbf{B}$, which acts upward if the layer is shifted upward, and downward if the layer is already down. This effect causes the ripple to spread farther, resulting in a phenomenon known as the *Rayleigh-Taylor instability.*

4.4 Dissipation of waves

The convective instabilities in the convection zone (Sec. 1.3.2) generate highly turbulent plasma motions, which, when coupled with magnetic fields, drive a broad spectrum of wave modes in the solar atmosphere (Musielak et al., 2001). The ubiquitous solar magnetic flux tubes serve as natural waveguides for channeling wave motion from the solar surface into the upper layer of the solar atmosphere. High-resolution observations have confirmed the widespread presence of such wave modes, some of which transport sufficient energy flux to heat the atmospheric plasma (Erdelyi et al., 2007; Jess et al., 2009; Morton et al., 2015). Traditionally, MHD waves have been studied under the simplifying assumption of a single-fluid, fully ionized plasma with ideal conditions, such as the magnetic field being frozen into it. The dispersion relation derived from these simplified assumptions often overlooks non-ideal effects, including resistivity, viscosity, Ohmic dissipation, electrical resistivity, and non-adiabatic effects such as thermal conductivity and radiative losses. However, in a real solar plasma, especially in the lower layers, these neglected non-ideal effects often act as key dissipation mechanisms. They must therefore be considered to accurately model the wave dynamics.

In the local aspect of this thesis, we consider ion-neutral collisions as the primary dissipation mechanism in modeling local wave dynamics in the solar atmosphere. Due to relatively low temperatures in the lower solar atmosphere, the presence of the neutral population leads to frictional coupling between the ions and neutrals through ion-neutral collisions (Sec. 3.2). This interaction alters the wave propagation and introduces frictional heating caused by the relative motion between ions (tied to magnetic field lines) and neutrals (primarily unresponsive to magnetic forces) in a partially ionized plasma. In numerical simulations, modeling and capturing this dissipation are challenging; nevertheless, considerable research has been conducted in this direction, with many studies proposing ion-neutral friction as a potential mechanism for addressing the coronal heating problem and the origin of the solar wind through the dissipation of MHD waves. For example, Carbonell et al., 2010 discussed how partial ionization under prominence-like conditions influences the damping of MHD waves. The author showed that the damping lengths of adiabatic fast and slow waves are strongly modified by the degree of ionization (Courant et al., 1928; Whang, 1997). In a similar context, Hahn (2013) provided observational evidence that Alfvén waves experience significant damping in the lower solar atmosphere. Further, Arregui (2015) reviewed wave-based energy transport and dissipation, highlighting the roles of Alfvén waves, resonant damping, and phase mixing processes.

Numerical modeling has also shed light on chromospheric heating via MHD waves. Wang et al., 2021 performed a 2-D radiative MHD simulation of wave propagation in the quiet solar chromosphere and found that fast MAWs generated via mode conversion from high-β fast sonic waves play a crucial role in heating the low-β chromosphere. Similarly, Kuźma et al. (2019) demonstrated that short-period ion and neutral acoustic waves are strongly damped by ion-neutral collisions, leading to localized chromospheric heating. More recently, Niedziela et al. (2021) modeled the chromospheric heating caused by the dissipation of MAWs triggered by impulsive photospheric perturbations. Several studies also identify Alfvén waves as an essential heating mechanism. For example, a parametric study by Pelekhata et al. (2021) showed that large-amplitude Alfvén waves generate more efficient heating and drive more substantial plasma outflows than small-amplitude Alfvén waves. Similarly, Maneva et al. (2017) simulated MAWs driven by the photospheric velocity driver at the magnetic field footpoint. The author found that wave-induced plasma heating dominates outside the flux tube in the upper chromosphere. In this case, the heating is primarily a result of the conversion of kinetic energy into thermal energy as the wavefront of fast MAWs steepens.

Coupled wave modes have also received significant attention in recent studies, which report that they play a significant role in heating the solar atmosphere. For instance, De Moortel et al. (2004) reported that horizontal density inhomogeneity induces coupling of the slow and fast MAWs, thereby enhancing the damping of the wave. Morton et al. (2019) provided evidence that the Sun's internal acoustic modes contribute to the basal flux of Alfvénic waves. A recent comparative study by Niedziela et al. (2022) showed that MAWs are more effective in heating and generating plasma outflows than the coupled magnetoacoustic-gravity waves. Similarly, Wójcik et al. (2020) investigated the dissipation of various wave modes generated by granulation-driven convection and found good agreement with an observationally based semi-empirical model without including shock heating. Along similar lines, Murawski et al. (2022) incorporated additional non-ideal effects, including magnetic diffusivity and viscosity, and concluded that dissipated wave energy effectively heats the plasma, compensating for radiative and thermal energy losses. More recently, Niedziela et al. (2024) performed a numerical experiment using a magnetic carpet model and showed that higher values of the magnetic field enhanced ion-neutral velocity drift, leading to more substantial heating and plasma flows.

Inspired by the studies mentioned above, the local aspect of this thesis investigates heating and plasma outflows in the upper chromosphere, focusing on MHD waves triggered by granulation and convective instabilities in the lower solar atmosphere.

4.5 Summary

This chapter focused on the MHD waves in a stratified equilibrium plasma. We begin with the ideal MHD equations and follow the conventional path by introducing a small perturbation and linearizing them about the equilibrium to obtain the generalized wave equation for the disturbance $\mathbf{V}_1$. We then studied the principal wave families: Acoustic waves, where plasma pressure is the sole restoring force, leading to an isotropic, non-dispersive dispersion relation. MAWs, where magnetic tension and plasma pressure act as restoring forces, yield dispersive and anisotropic dispersion relations. These waves are classified into two modes: slow and fast. For the fast mode, the Alfvén speed V_A is the phase speed along magnetic-field lines, while $\sqrt{V_A^2 + C_s^2}$ is the phase speed across them. On the other hand, for the slow mode, the phase speed is the tube speed $C_T^2 = C_s^2 V_A^2/(C_s^2 + V_A^2)$ along the magnetic field lines; however, these waves cannot propagate perpendicular to the field. The resulting dispersion relation indicates that these waves can be incompressible, where $\mathbf{V}_1 \cdot \mathbf{k} = 0$, or compressible, where $\mathbf{V}_1 \cdot \mathbf{k} \neq 0$. Next, we discuss convective stability in a stratified solar atmosphere via the Schwarzschild criterion and derive the dispersion relation for gravity waves that emerge due to convective instability. The dispersion confirms that gravity waves do not propagate in the vertical direction, emphasizing their anisotropic nature. The physical phenomena responsible for driving the coupling of the pure modes are discussed, along with a brief treatment of Rayleigh–Taylor instabilities in vacuum and plasma.

In the following chapter, we discuss the numerical techniques and methods often used to solve the two-fluid equations.

Chapter 5

A note on numerical schemes

5.1 Introduction

The multi-fluid MHD equations derived in chapter 3 are often too complex to solve analytically and seldom admit closed-form solutions; therefore, we must rely on numerical methods. Numerical methods are a set of algorithms designed to solve complex mathematical problems when optimal analytical solutions are not available. The process of employing these methods to model and analyze a system over time is called *numerical simulation*. It utilizes computer software to model known mathematical equations of physical systems, generating approximate results. The standard numerical simulation process involves developing a mathematical model, typically composed of a set of differential equations, followed by transforming it into a discrete form for numerical processing. The numerical simulation involves the following basic steps.

1. **Problem definition:** The very first step of the numerical simulation requires us to define the objective of the physical problem. This includes the physical process to be simulated, the relevant input and output parameters, and the required performance criteria for evaluating the simulation output.

2. **Model design:** The model design involves establishing the set of mathematical equations capturing the behavior of the system. Once the mathematical model is established, validation, such as setting a benchmark or conducting an experimental comparison, is needed to verify whether it accurately represents the real system.

3. **Boundary conditions and input parameters:** The physical system must be clearly defined by its boundary conditions along with a set of input parameters to reproduce the system's behavior under various conditions.

4. **Simulation phase:** Upon establishing the input parameters and boundary conditions, the primary phase of numerical simulation can now be executed. The numerical code is the most critical element required to perform the numerical simulation. In this thesis, we employed two advanced numerical codes: the **JO**int **AN**alytical **N**umerical **A**pproach (JOANNA) and the **C**omputational **O**bject-**O**riented **L**ibraries for **Flui**d **D**ynamics

(COOLFluiD) to perform the numerical simulation (Sec. 5.10).

5. **Analysis of the results:** Once the simulation run is over and the output data is collected, visualization tools, such as *VisIt* (Data, 2012) and *Paraview* (Squillacote et al., 2007), can be used to analyze simulation output data. Both of these tools were employed in the analysis and visualization of the numerical results presented in this thesis.

6. **Model refinement:** Since no model is perfect, it is necessary to compare the obtained results with real data to guide further improvements. If significant inconsistencies are found between the simulation output and the actual data, the model parameters can be adjusted and the model rerun until the results are satisfactory.

Numerical methods and simulations are potent tools for evaluating solutions to complex problems. The primary advantage of numerical simulation over traditional tests is that the physical effect can be readily controlled by turning it on or off, varying its strength, modifying its functional shape, or setting the virtual boundary conditions, which can be controlled systematically. This is not always the case in nature. Furthermore, non-linear and inhomogeneous physical processes can be regulated in a manner comparable to homogeneous and linear systems. Numerical simulations also aid in model optimization by revealing possible flaws and opportunities for improvement before the model is physically developed or manufactured. In other words, numerical simulations enable us to create a model of a system, conduct virtual experiments, and gain a deeper understanding of how it behaves under various circumstances and hypotheses, serving as a bridge between experiment and theory. This approach overcomes the mutual shortcomings of pure experimentation and pure theory.

Despite several perks, numerical methods have limitations. The equations derived in chapter 3 form a complex system of partial differential equations (PDEs). To represent a continuous system of equations in the finite memory of a computer, the equations must be discretized. This discretization often results in truncation and rounding errors (Chapra et al., 2011). Furthermore, numerical simulations can be computationally expensive, demanding significant processing power or time to achieve high-precision results. As a result, the findings may not be as precise as those obtained from exact analytical solutions. Nonetheless, numerical methods can provide essential insight into the behavior of the system and allow us to arrive at solutions that are relatively closer to the optimal one. In solar physics, numerical simulations are particularly valuable for modeling large spatial-scale systems (e.g., the magnetosphere and solar atmosphere) or when limited observational data and network facilities are available. Our goal in this chapter is not to provide an exhaustive treatment of numerical methods, as a large body of literature already exists on the subject, e.g., Sastry (2012). Instead, we aim to present some essential numerical methods often employed in the chosen numerical codes without going into too much depth.

5.2 Some basics of numerical methods

Differentiation discretizations

- Consider a function $f(x)$, with values $f_0, f_1, f_2 \cdots f_n$ defined at $x_0, x_1, x_2 \cdots x_n$ discrete points in space. The Taylor series expansion of f centered at the point x_n is

$$f_{n+1} = f_n + \Delta x \frac{\partial f}{\partial x}\bigg|_n + \frac{1}{2\,!}(\Delta x)^2 \frac{\partial^2 f}{\partial x^2}\bigg|_n + \frac{1}{3\,!}(\Delta x)^3 \frac{\partial^3 f}{\partial x^3}\bigg|_n + \cdots \tag{5.1}$$

Here, $\Delta x = x_n - x_{n-1}$, and the higher powers of Δx are the leading terms. For the first-order accurate solution in $\frac{\partial f}{\partial x}\big|_n$, we can omit the higher-order terms if Δx is small. Therefore, the derivative of the function f at the point n is

$$\boxed{\frac{\partial f}{\partial x}\bigg|_n = \frac{f_{n+1} - f_n}{\Delta x}} \tag{5.2}$$

This differential approximation is known as the *right-sided first-order difference (forward Euler scheme)*. Similarly, the *left-sided first-order difference (Backward Euler scheme)* is

$$\boxed{\frac{\partial f}{\partial x}\bigg|_n = \frac{f_n - f_{n-1}}{\Delta x}} \tag{5.3}$$

Adding Eqs. 4.2 & 4.3, we get the *first-order centered difference (centered Euler scheme)*

$$\boxed{\frac{\partial f}{\partial x}\bigg|_n = \frac{f_{n+1} - f_{n-1}}{2\Delta x}} \tag{5.4}$$

Integration discretizations

- **Rectangle rule:** Perhaps the simplest method for approximating an integral is the *rectangle rule*, also known as the *midpoint rule*. According to this rule, the approximate integral I of the function sampled at n evenly spaced points, $x_0 \equiv a, x_1, \cdots, x_n \equiv b$, is given by

$$\boxed{I \equiv \int_a^b f(x)\,dx \approx \Delta x \sum_{n=0}^{n-1} f(x_n)} \tag{5.5}$$

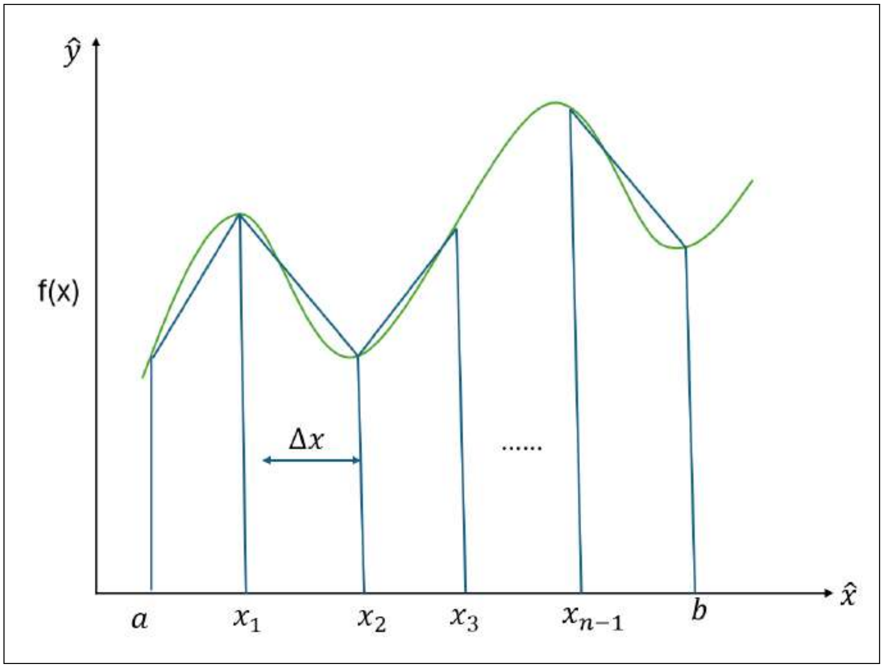

Figure 5.1: The trapezoidal rule is a common method for numerically estimating definite integrals, represented by $\int_a^b f(x)\,dx$, which are approximated by summing the areas of the resulting n trapezoids.

Here, $\Delta x = (b-a)/n$. Note that in the limit $\Delta x \to 0$, we end up with our typical definition of integration we learn in Calculus. In Eq. 5.5 above, we sum the area of the collection of rectangles lying between the points $n=0$ and $n-1$, each with width Δx and height $f(x_n)$.

- **Trapezoidal rule:** The *trapezoidal rule* is another method for calculating an approximate integral. In this method, the total area is determined by summing the areas of n trapezoids beneath the curve. The trapezoid is a more accurate shape than a rectangle, which improves accuracy. Suppose the curve bounded between a and b is divided into n trapeziums; therefore, the area of the first trapezium A_1 can be written as the sum of the area of a rectangle and a triangle (Fig. 5.1)

$$A_1 = \Delta x\, f(a) + \frac{\Delta x}{2}[f(x_1) - f(a)] \Longrightarrow A_1 = \frac{\Delta x}{2}[f(x_1) + f(a)] \tag{5.6}$$

Similarly,

$$A_2 = \frac{\Delta x}{2}[f(x_2) + f(x_1)],\ \cdots A_{n-1} = \frac{\Delta x}{2}[f(x_{n-1}) + f(x_{n-2})],\ A_n = \frac{\Delta x}{2}[f(x_n) + f(b)] \tag{5.7}$$

The approximate integral I, therefore, is the sum of the areas of all n trapeziums.

$$\boxed{I = \frac{\Delta x}{2}\{f(a) + 2[f(x_1) + f(x_2) + f(x_3) + \cdots + f(x_{n-1})] + f(b)\}} \tag{5.8}$$

- **Simpson's 1/3 rule:** Rectangle and trapezoidal rules rely respectively on piecewise constant and linear approximations, which can lead to significant errors. *Simpson's rule*, in contrast, employs a piecewise quadratic approximation. The key idea is to fit a parabola passing through three arbitrary consecutive points n, i.e., $(x_{n-1},\, y_{n-1})$, $(x_n,\, y_n)$, $(x_{n+1},\, y_{n+1})$ To apply Simpson's rule, we first divide the interval of interest (a, b) into an n even number of sub-intervals, each with width $\Delta x = (b - a)/n$. This approach yields the approximation

$$\boxed{\int_a^b f(x)\, dx = \frac{\Delta x}{3}[f_0 + 4(f_1 + f_3 + f_5 + \cdots + f_{n-1}) + 2(f_2 + f_4 + f_6 + \cdots + f_{n-2}) + f_n]} \tag{5.9}$$

The truncation error in Simpson's 1/3 formula is given by (Sahoo, 2025)

$$\boxed{\epsilon \leq -\frac{b-a}{180}(\Delta x)^4 f^4(\bar{x})} \tag{5.10}$$

Here, $f^4(\bar{x})$ is the largest value of the fourth derivative.

- **Simpson's 3/8 rule:** Unlike Simpson's 1/3 rule based on quadratic approximations, *Simpson's 3/8 rule* provides a more accurate approximation by using cubic interpolation. The rule is applied when the number of intervals n is a multiple of 3. The approximate integral can be calculated as

$$\boxed{\int_a^b f(x)\, dx = \frac{3\Delta x}{8}[f_0 + f_n + 3(y_3 + y_6 + y_9 + y_{12} + \cdots) + 2(y_1 + y_2 + y_4 + y_5 + \cdots)]} \tag{5.11}$$

The truncation error in Simpson's 3/8 formula is given by

$$\boxed{\epsilon \leq -\frac{3}{80}(\Delta x)^5 f^4(\bar{x})} \tag{5.12}$$

and it is smaller than for the Simpson's 1/3 rule (Eq. 5.10).

Root finding

In numerical methods, root finding refers to the computational algorithms used to identify the values at which a particular function equals zero. Various methods are available to find the roots; however, we will only discuss some of the most popular and frequently used ones here.

- **Bisection method:** Consider a function $f(x)$ continuous in $[a, b]$, where $f(a)$ and $f(b)$ have opposite signs. According to the *bisection method*, a root x_0 must lie between points a and b, where the estimated root is given by $x_0 = (a+b)/2$. If $f(x_0) = 0$, then x_0 is the root of $f(x)$. On the other hand, if $f(x_0) \neq 0$, then the new approximate root either lies in $[a, x_0]$ if $f(x_0) > 0$, or in $[x_0, b]$ if $f(x_0) < 0$. Consequently, we get two new intervals $[a, x_0]$ and $[x_0, b]$ that are exactly half the length of the original interval $[a, b]$. We repeatedly apply the same method to the newly obtained intervals until the final interval reaches the desired small size, denoted as ϵ. Note that the length of the interval is halved after each iteration. Therefore, we must limit the number of iterations required to attain the precision ϵ at the end of the n^{th} iteration.

$$\therefore \quad \frac{|b-a|}{2^n} \leq \epsilon \implies \boxed{n \geq \frac{\ln(|b-a|/\epsilon)}{\ln 2}} \tag{5.13}$$

- **Regula falsi method:** The *regula falsi method* is similar to the bisection method above; however, here, instead of bisecting the interval $[a, b]$, this method employs a straight line passing through the endpoints to estimate the root. The equation of the line joining points $(a, f(a))$ and $(b, f(b))$ is

$$\frac{x-a}{y-f(a)} = \frac{b-a}{f(b)-f(a)} \tag{5.14}$$

  Let $(x_0, 0)$ denote the point of intersection at the x-axis. Substituting $(x_0, 0)$ and solving for x_0, we obtain the initial approximation for the root of the equation $f(x) = 0$, that is

$$x_0 = \frac{af(b) - bf(a)}{f(b) - f(a)} \tag{5.15}$$

  The new approximate root is located either in the interval $[a, x_0]$ or $[x_0, b]$, depending on whether $f(a)$ and $f(b)$ have opposite signs, respectively. This method is repeated until the roots are achieved with the desired accuracy.

- **Newton-Raphson method:** The *Newton-Raphson method* is based on the initial guess value of the root. If x_0 is the initial guessed root for the function $f(x)$ continuous in $[a, b]$, let $x_1 = x_0 + \lambda$ be the actual root. By using the Taylor series expansion centered at x_0,

$$f(x_0+\lambda) = \frac{\lambda^0}{0!} f(x_0) + \frac{\lambda^1}{1!} f^{'}(x_0) + \frac{\lambda^2}{2!} f^{''}(x_0) + \frac{\lambda^3}{3!} f^{'''}(x_0) + \cdots \tag{5.16}$$

Neglecting the second and higher-order derivatives if λ is small,

$$f(x_0 + \lambda) \approx f(x_0) + \lambda f^{'}(x_0) = 0 \tag{5.17}$$

$$\Rightarrow \lambda = -\frac{f(x_0)}{f'(x_0)} \tag{5.18}$$

Therefore, a more accurate initial guess than x_0 is given by

$$x_1 = x_0 - \frac{f(x_0)}{f'(x_0)} \tag{5.19}$$

Similarly

$$x_2 = x_1 - \frac{f(x_1)}{f'(x_1)}, \quad x_3 = x_2 - \frac{f(x_2)}{f'(x_2)}, \; \cdots, \; x_{n+1} = x_n - \frac{f(x_n)}{f'(x_n)} \tag{5.20}$$

This formula is known as the *Newton-Raphson formula*. It is important to note that this method typically converges rapidly to the target root if the initial guessed root is sufficiently close to the actual root and $f'(x)$ is not too close to zero. However, this method struggles to converge if the initial guess root is too far away from the actual root, the first derivative is close to zero, or the function is not differentiable.

- **The Secant method:** The Secant method is a derivative-free *Newton-Raphson formula*. In this method, the derivative of $f(x)$ is calculated as (Eq. 5.3)

$$f'(x_n) \approx \frac{f(x_n) - f(x_{n-1})}{x_n - x_{n-1}} \tag{5.21}$$

Plugging $f'(x_n)$ into Eq. 5.20, we get

$$\boxed{x_{n+1} = \frac{x_{n-1}\, f(x_n) - x_n\, f(x_{n-1})}{f(x_n) - f(x_{n-1})}} \tag{5.22}$$

The method for evaluating the root of the function is not limited to the layout presented here. Other advanced methods, such as the *Ramanujan* and *Muller methods*, are also available depending on the complexity of the equation. For further details, potential readers may refer to standard textbooks on numerical analysis and methods (Kiusalaas, 2010; Epperson, 2013).

5.3 Classification of the partial differential equations

The set of complex partial differential equations (PDEs) derived in chapter 3 primarily governs plasma dynamics. Mathematically, PDEs involve an unknown function of two or more independent variables and their partial derivatives. In this subsection, we focus our discussion on the second-order PDEs of the form

$$A\,\frac{\partial^2 u}{\partial x^2} + B\,\frac{\partial^2 u}{\partial x \partial y} + C\,\frac{\partial^2 u}{\partial y^2} + D\,\frac{\partial u}{\partial x} + E\,\frac{\partial u}{\partial y} + F\,u = S \tag{5.23}$$

Here, the symbols A, B, C, D, E, F, u are functions of (x, y), and S is the source term. PDEs are primarily categorized according to the sign of the discriminant D, defined as

$$D = B^2 - 4AC$$

Hyperbolic partial differential equations

When $D > 0$, a second-order linear PDE is *hyperbolic*; the canonical example is the *wave equation*. In one spatial dimension, it is written as

$$c^2 \frac{\partial^2 u}{\partial x^2} = \frac{\partial^2 u}{\partial t^2} \tag{5.24}$$

Here, c denotes the speed of the waves traveling in either direction. Another example is the *linear advection equation*

$$c\,\frac{\partial u}{\partial x} + \frac{\partial u}{\partial t} = 0 \tag{5.25}$$

Physically, it transports the initial profile $u(x, 0)$ rigidly to the right with speed $c > 0$. The linear advection equation will be discussed in further detail in a subsequent section on numerical approaches.

Elliptic partial differential equations

When $D < 0$, a second-order linear PDE is of *elliptic* type. *Poisson's equation* is a good example of an elliptic partial differential equation, written as

$$\Delta^2 \psi = \phi \tag{5.26}$$

Here, ϕ is the source term. The *Laplace equation* is another example, where $\phi = 0$. This equation is a pure boundary value problem without a time variable. Therefore, the solution ψ is fully determined by the source term ϕ and the corresponding boundary condition.

Parabolic partial differential equations

When $D = 0$, a second-order linear PDE is *parabolic*. The canonical example is the *heat conduction equation*

$$\frac{\partial u}{\partial t} = \lambda \frac{\partial^2 u}{\partial x^2} \tag{5.27}$$

Here, λ is the diffusion coefficient. The heat equation indicates that no wave propagation occurs, since it incorporates elements of both hyperbolic and elliptic PDEs.

5.4 Grid in numerical simulation

The system of equations obtained in chapter 3 is a continuous function of space and time, making it almost impossible to write them in finite computer memory. As a result, it is critical to discretize these equations onto a numerical grid. This *grid* is typically generated by dividing the domain into small subregions, each referred to as a *cell*. The purpose of dividing the domain into small cells is to approximate PDEs with algebraic equations. The numerical grid remains a critical component of numerical simulation since a very coarse or low-quality grid often leads to non-physical or inaccurate simulation results.

The numerical grid is broadly classified into two main categories: structured (e.g., aligned with the coordinate system) and unstructured (e.g., irregularly shaped). The decision on whether to use a structured or unstructured mesh is highly problem-specific. When dealing with PDEs supplemented by initial and boundary conditions, we can approximate the equations on a mesh using finite difference, finite volume, and finite element methods. Such discretized PDEs are usually solved using popular programming languages (e.g., FORTRAN, C++, and Python). The following subsection provides a brief overview of how meshes are classified based on their style.

5.4.1 Structured grid

Structured grids provide a regular and predictable arrangement of grid points, following a simple, logical pattern based on a Cartesian, cylindrical, or spherical coordinate system. In the structured grid, points are placed in a predictable, often rectangular or cubic pattern, and the location of any such subdivision in the domain of interest is identified via an integer index i in each spatial dimension. *Finite difference methods (FDM)* and *finite volume methods (FVM)* often rely on structured grids. They offer better convergence, high-quality control, reduced computational cost, and improved time resolution. The following sub-points classify the grid based on how data are represented on the mesh.

- **Finite difference method:** The *finite difference method* only enforces the discrete

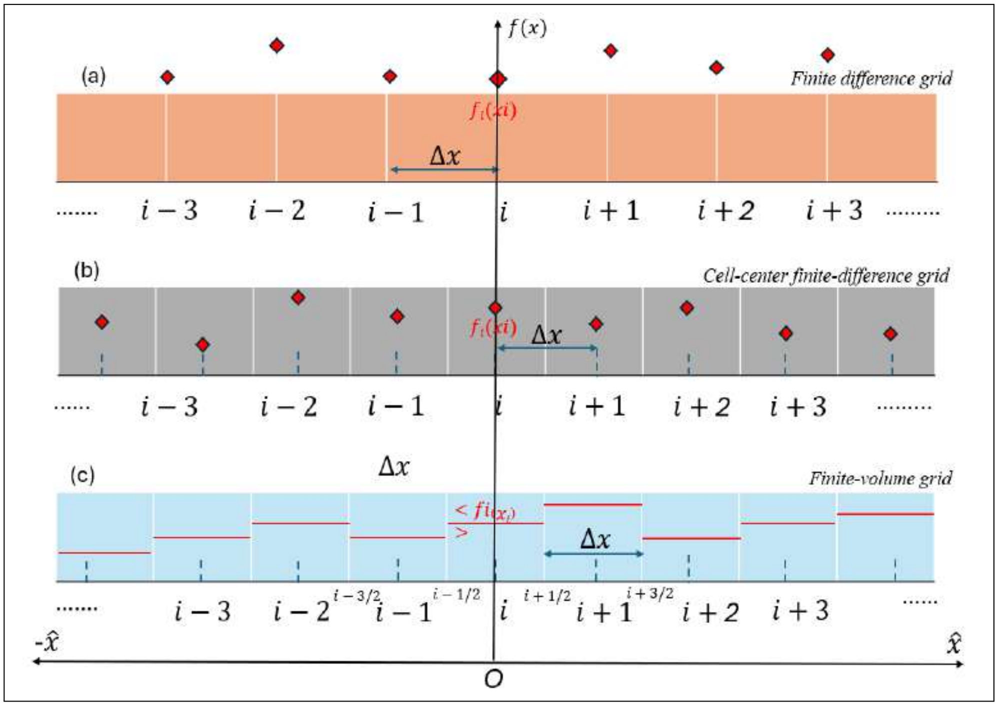

Figure 5.2: The structured grid (Cartesian) demonstrates multiple ways of displaying the function $f_i(x_i)$. (a) Finite difference grid: the data are placed precisely on the grid points. (b) Cell-centered finite difference grid: similar to the finite difference grid, but with the data placed at the center. (c) Finite volume grid: the average data value is recorded in each sub-region, represented by a horizontal line.

form of the equation at a finite number of points, where we only concentrate on the nodes in space. Let $f(x)$ be a continuous function and $f_i(x_i)$ denote a discrete value at mesh point i, where $x_i = i\,\Delta x$, and $i = 0, 1, 2, \cdots N-1$, so the nodes are evenly spaced by $\Delta\, x$. In FDM, each datum $f_i(x_i)$ is associated with a specific point in the mesh (Fig. 5.2 a).

- **Cell-centered finite difference method:** In a *cell-centered method*, the data value $f_i(x_i)$ is stored at the center of the cell i with $x_i = (i + 1/2)\Delta x$. Therefore, the center of the cell lies at $\Delta x/2$. The left edge of the cell coincides with the left physical boundary, while the rightmost cell is arranged symmetrically at the opposite boundary (Fig. 5.2 b).

- **Finite volume method:** In the *finite-volume method*, the average data value $\langle f_i(x_i)\rangle$ is stored at each mesh point. This average value is defined as

$$\langle f_i(x_i)\rangle = \frac{1}{\Delta x}\int_{x_i-1/2}^{x_i+1/2} f(x)\,dx \tag{5.28}$$

Here, $x_{i\pm1/2} = x_i \pm \Delta x/2$ denotes the left and right edges of the i^{th} cell. Unlike the cell-centered finite difference method, where each data point refers to the function value at a single node, the FVM associates each data point with the average value over an entire cell. This is visually represented by the horizontal line spanning the entire sub-zone in panel (c) of Fig. 5.2.

5.4.2 Unstructured grid

Unstructured grids allow grid points to be placed arbitrarily within the domain. These grids are composed of elements that can take a variety of shapes, including triangular or tetrahedral (2D/3D), quadrilateral or hexahedral (2D/3D), and polygonal or polyhedral (2D/3D). Hybrid meshes are also extensively used, which blend different element types to achieve a more efficient solution. Unstructured meshes offer the advantage of being adaptive to complex, arbitrary shapes, sharp boundaries, and localized features. They are commonly applied in finite element methods, especially for irregular or complex domains (Hansen et al., 2004). Unlike structured grids, which follow a set pattern, unstructured meshes are defined by explicit connection information that specifies the interactions between elements. This offers geometric versatility but at the expense of increased memory usage and computational complexity for assembling and solving numerical systems. Unstructured meshes avoid the strict alignment and indexing requirements imposed by structured grids; consequently, numerical solutions using unstructured meshes can be obtained much faster, especially when dealing with complex domains. The detailed description of the grid and its method of generation, etc., is beyond the scope of this thesis. Interested readers may consult the recent book by Sadrehaghighi (2022) for more information.

5.5 Advection equation

The *linear advection equation* is one of the simplest examples of first-order hyperbolic PDEs that govern the motion of a conserved scalar field $\psi(x, t)$ advected by a velocity V. Such advection processes represent how fluid currents transport conserved quantities through bulk motion. Mathematically, the scalar advection equation in its conservative form can be expressed as

$$\boxed{\frac{\partial \psi}{\partial t} + \frac{\partial}{\partial x}(V\psi) = 0} \tag{5.29}$$

with $\psi(x, 0) = \psi_o(x)$ The general solution of the linear advection equation is

$$\psi(x, t) = \psi_0(x - Vt) \tag{5.30}$$

This demonstrates that the scalar field flows through space with a constant velocity V without losing shape, regardless of the nature of ψ. Geometrically, the solution is constant along the characteristic line $x = Vt$ in the $x - t$ plane, the so-called *characteristic line*. Physically, the solution of the given equation moves the initial scalar field ψ with the constant velocity V. Here, the scalar advection equation assumes V to be constant, but if V depends on the scalar field or varies spatially and temporally, then the equation becomes nonlinear, that is

$$\frac{\partial \psi}{\partial t} + \frac{\partial f(\psi)}{\partial x} = 0 \tag{5.31}$$

For Burgers' equation, with flux function $f(\psi) = \psi^2/2$, the characteristic in $x - t$ is governed by $dx/dt = V(x,t)$. Unlike in the linear case, such characteristic lines are not parallel and therefore can intersect with each other, which generates multi-valued solutions. The region, where such characteristic lines merge, forms the *shock*. These shocks can generate instability and non-physical oscillations. Therefore, accurate numerical methods, such as *Godunov* or *Roe-type flux splitters*, typically employ flux limiters (Venkatakrishnan, 1993) to handle nonlinearities and shocks, ensuring stability and preventing non-physical oscillations. In multiple dimensions, the advection equation generalizes to

$$\frac{\partial \psi}{\partial t} + \nabla \cdot (\mathbf{V}\psi) = 0 \tag{5.32}$$

Here, the characteristics are transformed into curves, and shocks are observed as surfaces rather than lines. These characteristic curves are critical for studying propagation and shock waves in time-distance plots. In chapter 6 of this thesis, we investigate these distinctive curves in detail to infer wave propagation in the solar atmosphere.

5.6 Numerical solutions for advection equation

Let $f(x,t)$ be a continuous function. We discretize f on a uniform grid in both space and time as follows:

$$f_i^n \equiv f(x_i, t^n)\,, \;\; x_i = i\Delta x, \;\; t^n = n\Delta t, \;\; n = 0, 1, \cdots, N-1, \;\; \text{with} \;\; i = 1, 2, \cdots, N \tag{5.33}$$

Here, Δx and Δt denote the uniform spatial and temporal step sizes, respectively. Applying the forward Euler scheme (Eq. 5.2) to represent the spatial derivative and the backward Euler scheme (Eq. 5.3) for the temporal derivative to the advection equation (Eq. 5.29) with $f \equiv \psi$, we obtain the upwind (Godunov) scheme

$$\frac{f_i^{n+1} - f_i^n}{\Delta t} = -V \frac{f_i^n - f_{i-1}^n}{\Delta x} \tag{5.34}$$

$$\boxed{f_i^{n+1} = f_i^n - C(f_i^n - f_{i-1}^n)} \tag{5.35}$$

Here, $C = V\Delta t/\Delta x$ is the *Courant-Friedrichs-Lewy (CFL) number* (Courant et al., 1928). The discretized nature is evident from the above equation, where the updated solution f_i^{n+1} depends only on the past solutions f_i^n and f_{i-1}^n. Furthermore, the utilization of the derivative forward Euler scheme is referred to as upwinding since the solution information flows from the LHS to the RHS. The dimensionless CFL number plays a crucial role in ensuring the numerical stability of the solution by imposing restrictions on Δt in relation to Δx (Deriaz et al., 2020). Numerical stability requires $C \leq 1$, that is

$$\boxed{\frac{V\Delta t}{\Delta x} \leq 1} \tag{5.36}$$

Physically, for the solution to be stable, Δt must be smaller than the time it takes for information to flow across a single cell in the mesh. Also, the corresponding local truncation error is

$$L_{TE} = \left[\frac{\Delta t}{2}\frac{\partial^2 f}{\partial t^2} - \frac{V\Delta x}{2}\frac{\partial^2 f}{\partial x^2} + \mathcal{O}((\Delta t)^2) + \mathcal{O}((\Delta x)^2)\right]_i^n \tag{5.37}$$

Now, instead of using the backward Euler scheme to represent the spatial derivative, we can also apply the centered difference for the spatial derivative (Eq. 5.4), resulting in

$$\boxed{f_i^{n+1} = f_i^n - \frac{C}{2}(f_{i+1}^n - f_{i-1}^n)} \tag{5.38}$$

This method is known as *forward in time, centered in space* (FTCS). One may have the impression that the FTCS scheme is relatively stable. However, *Von Neumann stability analysis* (Sec. 5.6.1) reveals that this scheme is, in fact, unconditionally unstable (Dubey, 2015), which limits its practical applicability. Ultimately, we seek higher-order accurate methods. The most apparent change from our initial discretization is to try a higher-order spatial derivative, for example, using the *Lax-Friedrichs* and *Lax-Wendroff schemes*. The Lax-Friedrichs scheme and the Lax-Wendroff scheme using FTCS, respectively, are ((Murawski, 2002)):

$$\boxed{f_i^{n+1} = \frac{f_{i+1}^n + f_{i-1}^n}{2} - \frac{C}{2}(f_{i+1}^n - f_{i-1}^n)} \tag{5.39}$$

$$\boxed{f_i^{n+1} = \frac{C(1+C)}{2}f_{i-1}^n + (1-C^2)f_i^n - \frac{C(1-C)}{2}f_{i+1}^n} \tag{5.40}$$

Both schemes are conditionally stable for $0 < |C| < 1$.

5.6.1 Von Neumann stability analysis

Von Neumann stability analysis is a method used to assess the stability of numerical schemes for solving PDEs. The analysis is particularly important for ensuring the reliability of numerical simulations. The fundamental concept behind this approach is to decompose the solution into Fourier modes. Mathematically, the *Fourier analysis* allows us to quantify the frequency content of a signal by decomposing a function f into a sum of sine and cosine functions (or complex exponentials) of different frequencies. As argued earlier, numerical computation involves discretizing a continuous function f by sampling it at specific times and spaces; in return, the frequency components of the signal are described by a finite number of discrete samples, which results in solution errors.

To assess the stability of the numerical scheme, it is essential to understand how these errors propagate throughout the solution and recognize how to prevent such instability. Fourier stability is the classical method of assessing stability in terms of the growth of a single Fourier mode, or how the amplitude of a given frequency component changes as the discretization system evolves in space.

Here, we introduce a mode by substituting f_i^n with $A^n \exp(Ii\phi)$, where $I = \sqrt{-1}$ is the imaginary number and ϕ is the phase. Inserting into Eq. 5.35, we obtain

$$A^{n+1} \exp(Ii\phi) = A^n \exp(Ii\phi) - C[A^n \exp(Ii\phi) - A^n \exp(I(i-1)\phi)] \tag{5.41}$$

$$\frac{A^{n+1}}{A^n} = (1 - C[1 - \exp(-I\phi)]) \tag{5.42}$$

The corresponding complex conjugate is

$$\frac{A^{*\,n+1}}{A^{*n}} = (1 - C[1 - \exp(I\phi)]) \tag{5.43}$$

Therefore

$$\boxed{\left|\frac{A^{n+1}}{A^n}\right|^2 = 1 - 2C(1-C)(1-\cos\phi)} \tag{5.44}$$

The method ensures stability only if

$$\left|\frac{A^{n+1}}{A^n}\right| \leq 1 \tag{5.45}$$

Since $-1 \leq \cos\phi \leq 1$, stability requires $0 \leq C \leq 1$ or $2C(1-C) \geq 0$. This means that errors do not grow unbounded for the Godunov (upwind) scheme.

Similarly, for the FTCS scheme (Eq. 5.38), we have

$$A^{n+1}\exp(Ii\phi) = A^n\exp(Ii\phi) - \frac{C}{2}\left[A^n\exp(I(i+1)\phi) - A^n\exp(I(i-1)\phi)\right] \tag{5.46}$$

$$\frac{A^{n+1}}{A^n} = (1 - IC\sin\phi) \tag{5.47}$$

The corresponding complex conjugate is

$$\frac{A^{*\,n+1}}{A^{*\,n}} = (1 + IC\sin\phi) \tag{5.48}$$

Therefore

$$\boxed{\left|\frac{A^{n+1}}{A^n}\right|^2 = 1 + C^2\sin^2\phi} \tag{5.49}$$

Since $C^2\sin^2\phi \geq 0$, there exists no value of C that can stabilize the solution. From this, we conclude that the FTCS scheme remains unconditionally unstable.

5.7 Riemann problem

In physics, we frequently encounter problems, where the system of equations undergoes a rapid change (discontinuity) in its initial conditions. The *Riemann problem* aims to investigate how this discontinuity evolves. This problem represents an initial value problem consisting of a conservation equation and piecewise constant initial data, with a single discontinuity in the domain of interest. In computational fluid dynamics (CFD), due to the discretization of the computational domain, the Riemann problem naturally arises for solving conservation law equations using finite volume methods. The Riemann problem is a crucial building block in numerical approaches for studying complex wave propagation phenomena such as shock and rarefaction waves. The rupture of a dam is a perfect example of a Riemann problem, where the dam initially separates water from the shallower side, akin to a cell boundary dividing the two states in the Riemann problem, with one to the left and the other to the right. For the linear advection equation from Eq. 5.29, with initial data of the form

$$\psi(x,0) = \left\{\begin{array}{ll} \psi_L\,, & x_0 < 0 \\ \psi_R\,, & x_0 \geq 0 \end{array}\right\} \tag{5.50}$$

Here ψ_L and ψ_R are the constant states on the left and right, respectively. With this, the Riemann problem is simple to analyze. The discontinuity here moves at the constant speed V. For $V > 0$, the wave travels to the right at speed V. Thus $\psi(x,t) = \psi_L$ for $x < Vt$ (behind the discontinuity) and $\psi(x,t) = \psi_R$ for $x > Vt$ (ahead of the discontinuity). On

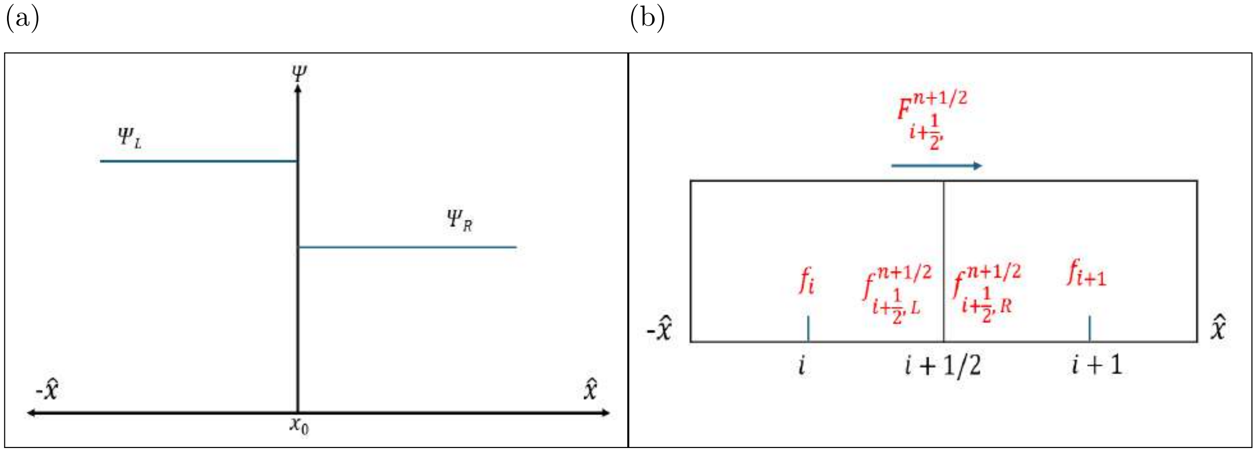

Figure 5.3: (a) The Riemann problem comprises a left ψ_L and right ψ_R state separated by an interface located at x_0. (b) The picture depicts the left and right states divided by the interface at $i + 1/2$. The arrow represents the flux through the interface, estimated by the Riemann solver using these input states.

the other hand, for $V < 0$, the wave travels to the left at speed V, where $\psi(x,t) = \psi_L$ for $x < Vt$ and $\psi(x,t) = \psi_R$ for $x > Vt$. No formation of a shock takes place here since all the characteristics travel at the speed of V, carrying the left state in the direction of propagation. For the Burgers equation of the form (Eq. 5.31), we have

$$\frac{\partial \psi}{\partial t} + \frac{\partial}{\partial x}\left(\frac{1}{2}\psi^2\right) = 0 \tag{5.51}$$

Since this equation is nonlinear, the wave speed here depends on the state ψ; therefore, the form of the solution to the Riemann problem now depends on the ordering of the left and right states.

- **The case of rarefaction ($\psi_L < \psi_R$):** The solution is given as (LeVeque et al., 1992)

$$\psi(x,t) = \left\{ \begin{array}{ll} \psi_L, & x < V_L\, t \\ \frac{x}{t}, & x \in [V_L\, t, \;\; V_R\, t] \\ \psi_R, & x > V_R\, t \end{array} \right\} \tag{5.52}$$

  In this case, the characteristic speeds V increase from left to right, preventing the formation of a shock. Instead, each value with $\psi_L < V < \psi_R$ moves with its characteristic speed V, so the discontinuity spreads out into a fan of characteristics that do not intersect.

- **The case of shock ($\psi_L > \psi_R$):** This condition results in the formation of a shock since characteristic speeds fall from left to right, causing characteristics to intersect.

The solution of the related shock moving at the speed V is given as

$$\psi(x,t) = \left\{ \begin{array}{ll} \psi_L\,, & x < Vt \\ \psi_R\,, & x \geq Vt \end{array} \right\} \tag{5.53}$$

The corresponding shock propagates with a speed given by the *Rankine–Hugoniot jump condition* (Krehl, 2015)

$$V = \frac{f(\psi_L) - f(\psi_R)}{\psi_L - \psi_R} \tag{5.54}$$

In summary, Burgers' Riemann solution consists of either a rarefaction wave or a shock wave. The Riemann solution highlights not only the analytical evolution of discontinuities for both the advection and Burgers equations, but also how to calculate interfacial fluxes based on the states on the left and right sides of the discontinuity. Further details related to the Riemann problem will not be discussed here, as they remain outside the scope of the present thesis. The potential reader may refer to standard textbooks on numerical methods (Ketcheson et al., 2020).

5.8 Runge-Kutta and Euler methods

The *Runge-Kutta method* is a collection of numerical methods that find approximate solutions to ordinary differential equations (ODEs). The method is primarily appreciated for its good balance of accuracy and efficiency, particularly when compared with other, more basic methods, such as the Euler method (Murawski, 2002). *Euler's method* is a first-order numerical method to approximate solutions of ODEs with an initial value. It utilizes only the slope at the start of the interval to integrate the initial value problem. Consider the general first-order ODE:

$$\frac{\partial y}{\partial x} = f(x,y) \quad \text{with} \quad y(x=0) = y_0 \tag{5.55}$$

The Euler method approximates the solution by discretizing the domain using Eq. 4.3:

$$\frac{y_{i+1} - y_i}{\Delta x} = f(x_i, y_i) \;\Rightarrow y_{i+1} = y_i + \Delta x\, f(x_i, y_i) \tag{5.56}$$

Here, Δx is the step size. This numerical method can be easily applied to solve ODEs. However, it lacks accuracy due to large truncation errors, particularly for large step sizes, because it has only one slope estimate per step. The local truncation error of Euler's method is $\mathcal{O}(\Delta x^2)$, which makes it a first-order method.

The *Runge-Kutta method* provides a more accurate solution by computing intermediate slopes. The most widely employed formula is the fourth-order Runge-Kutta (RK4) scheme, which averages four slope approximations to advance the solution from (x_i, y_i) to (x_{i+1}, y_{i+1})

$$y_{i+1} = y_i + \frac{\Delta x}{6}(k_1 + 2k_2 + 2k_3 + k_4) \tag{5.57}$$

where

$$k_1 = f(x_i, y_i), \quad k_2 = f\left(x_i + \frac{\Delta x}{2}, y_i + \frac{k_1\,\Delta x}{2}\right) \tag{5.58}$$

$$k_3 = f\left(x_i + \frac{\Delta x}{2}, y_i + \frac{k_2\,\Delta x}{2}\right), \quad k_4 = f(x_i + \Delta x, y_i + k_3\,\Delta x) \tag{5.59}$$

The local truncation error of the RK4 method is $\mathcal{O}(\Delta x^5)$, making it a fourth-order method. See Murawski (2002) for more details.

5.9 Godunov schemes

The *Godunov scheme* is a first-order, conservative numerical method for solving hyperbolic partial differential equations. The core idea of the Godunov scheme involves evolving the solution using piecewise-constant approximations within each cell and solving Riemann problems at each cell interface, that is (Fig. 5.3 b)

$$f^n(x_i) = f_i^n \quad \text{for} \quad x \in [x_{i-1/2},\, x_{i+1/2}] \tag{5.60}$$

Here, f_i^n is the initial condition for the Riemann problem at each cell interface located at $i + 1/2$, given by the neighboring cell averages. The scheme computes the numerical flux at cell interfaces by solving the Riemann problem between adjacent cells and updates the cell average using a finite-volume formulation as

$$f_i^{n+1} = f_i^n - \frac{1}{\lambda}(F_{i+1/2}^{n+1/2} - F_{i-1/2}^{n+1/2}) \tag{5.61}$$

Here, $\lambda = \Delta x/\Delta t$ and $F_{i+1/2}$ is the flux obtained from the Riemann problem solution. The stability of the numerical scheme requires $\Delta t \leq \Delta x/\lambda_{\max}$. The Godunov scheme accurately and efficiently captures shocks and discontinuities, making it a suitable approach for MHD equations. However, it suffers from some limitations.

The above scheme does not consider how the state f evolves within the cell, thus making it first-order accurate. The Godunov approach offers a well-behaved shock treatment in the Riemann problem; however, its first-order accuracy leads to numerical dissipation and the spreading of discontinuities due to piecewise constant reconstruction. Additionally, it requires a Riemann solver, which can be computationally expensive. To address these limitations, higher-order Godunov-type schemes are available to reconstruct the interface state, such as linear MUSCL (Monotonic Upstream-Centered Scheme for Conservation Laws), which achieves second-order spatial accuracy (Van Leer, 1979). Higher-order reconstruction methods involve parabolic reconstruction in each cell. This scheme is known as the piecewise parabolic method (PPM; Colella et al., 1984). Once the interface states are created, the Riemann solver is called, which returns the solution at every interface in the numerical grid.

It is worth mentioning that exact Riemann solvers are often computationally expensive; therefore, approximate solvers, such as the Harten-Lax-van Leer-Discontinuities (HLLD) Riemann solver, are utilized to solve the Riemann problem, which builds upon the HLL (Harten-Lax-van Leer) solver. For further details on the HLLD Riemann solver, refer to the papers by Miyoshi et al. (2005), Miyoshi et al. (2007), Mignone et al. (2009), and Minoshima et al. (2021).

5.10 A brief note on adopted codes

The most critical element required for performing numerical simulations is the computer program. The research work in this thesis has adopted two advanced numerical codes, namely the **JO**int **AN**alytical **N**umerical **A**pproach (JOANNA) code and the **C**omputational **O**bject-**O**riented **L**ibraries for **Flui**d **D**ynamics (COOLFluiD). The following subsections provide a brief overview of the employed codes.

5.10.1 JOANNA code

JOANNA is a numerical code for computational heliophysics developed by Dr. D. Wójcik at the University of Marie Curie-Skłodowska, Lublin, Poland. The code has been designed to solve common solar physics problems, including the heating of the solar corona, the study of wave propagation, understanding the origin of the solar wind, and energy transportation from the lower to the upper layers of the solar atmosphere. The JOANNA code adopted in this thesis is based on the second-order Godunov-type approach and the Harten-Lax-van Leer-Discontinuities (HLLD) Riemann solver. The code solves the set of MHD equations described in chapter 3 by employing Godunov-type schemes, Harten-Lax-Van-Leer solvers, and reconstructors such as linear methods, the piecewise parabolic method (PPM), Weighted Essentially Non-Oscillatory 3 (WENO, third-order accurate), and WENO5 (fifth-order accurate) (Liu et al., 1994; Jiang et al., 1996; Wang et al., 2007). The code has passed standard tests for the accuracy of computational fluid dynamics by demonstrating the stability of solutions for problems such as the SOD shock tube (Sod, 1978), the Brio-Wu MHD shock tube (Brio et al., 1988), the Kelvin-Helmholtz instability (McNally et al., 2012), and the Orszag-Tang vortex (Orszag et al., 1979; Dai et al., 1998). In this thesis, the code is employed to study the behavior of MHD waves in two-fluid plasma systems and their role in heating plasma and generating plasma outflows in the upper atmosphere. The prime motivation for adopting this code is that JOANNA's results have shown good consistency with observational data (Wójcik et al., 2018; Wójcik et al., 2019; Wójcik et al., 2020). Additionally, the code is modular, user-friendly, and optimized to run on a large number of CPUs. Chapter 6 covers the exact numerical setup of the code.

5.10.2 COOLFluiD code

COOLFluiD is an open-source, modular, and extensible framework developed initially at the Von Karman Institute for Fluid Dynamics and the KU Leuven Center for Mathematical Plasma Astrophysics (CmPA), KU Leuven, Belgium. The code can be employed for simulating space physics (e.g., solar wind modeling, coronal heating), space weather problems, aeroacoustics, turbulence, chemistry, and aerothermodynamics for aerospace problems ranging from the incompressible regime to hypersonics, including steady and unsteady flows, MHD, multi-fluid, and plasma flows. The adopted COCONUT global coronal modeling code is one of many setups that can be run within the framework of COOLFluiD. This code supports a range of numerical schemes, such as finite volume methods (FVM), finite difference (Sec. 5.4.1), discontinuous Galerkin (DG), including high-resolution limiters (Venkatakrishnan, 1993), and HLL and HLLC solvers for Riemann problems (Sec. 5.7). This wide range of available schemes enables user customization based on the specific problem and desired accuracy in resolving various solar coronal models within the context of MHD and multi-fluid plasma equations. The motivation behind adopting this code is its flexible simulation environment for computational fluid dynamics (CFD) and plasma physics, including MHD and multi-fluid modeling (Lani et al., 2013; Perri et al., 2022; Kuźma et al., 2023; Baratashvili et al., 2024; Brchnelova et al., 2024; Linan et al., 2025; Wang et al., 2025). The COCONUT setup resolves the dynamics of plasma flow in the solar corona up to 0.1 AU, where it can be integrated with heliospheric models.

In the present thesis, COCONUT is utilized to model the solar corona by accounting for the impact of source and sink terms on a two-fluid model of the partially ionized solar atmosphere and its implications for the dynamics of the solar corona, particularly in the context of space weather forecasting. Chapter 7 will provide detailed information on the actual numerical setup for the adopted problem.

5.11 Summary

This chapter summarizes the main numerical schemes used in the adopted numerical codes and simulations. Numerical simulation is a process that uses mathematical models to simulate and predict the behavior of a system under various conditions. It has an advantage over traditional experiments as it allows for the exploration of more scenarios, the quick adjustment of parameters, and the optimization of designs without the need for a physical prototype. There are several numerical methods for discretization, such as the left-sided first-order difference, right-sided first-order difference, central difference, and others. Often, an analytical solution to the physical problem is not available. Consequently, numerical techniques such as the Newton-Raphson method, the Regula Falsi method, and the bisection method are used to determine approximate roots of the equations. Later, we discussed second-order partial differential equations (PDEs) and their classifications based on the sign of the discriminant D. The equation is said to be of hyperbolic, elliptic, or parabolic type when $D > 0$, $D < 0$, or $D = 0$, respectively. Numerical grids are an integral part of the numerical process, where continuous functions are represented on them. The grid is categorized as either structured or unstructured based on its style. The finite difference method, the cell-centered finite difference method, and the finite volume approach are among the most important methods for presenting data on a mesh. Later, we expanded on the advection equation, a first-order hyperbolic PDE that represents how a physical quantity is advected through space by the bulk motion of a fluid. It is one of the most fundamental equations in fluid dynamics, appearing in plasma physics, weather modeling, oceanography, and astrophysics. A standard numerical solution to the advection equation was discussed. We defined the Riemann problem as a special initial value problem composed of a conservation equation and a piecewise constant initial condition, with a single discontinuity in the domain of interest. Godunov schemes, along with reconstruction schemes such as the Monotonic Upstream-Centered Scheme (linear reconstruction) and the piecewise parabolic method (parabolic reconstruction), were outlined. Finally, some brief observations were made on the adopted numerical codes: JOANNA and COOLFluiD.

Chapter 6

Numerical Results: The Local Aspects

6.1 Introduction

Section 1.3.5 of chapter 1 highlights the coronal heating problem and the origin of the solar wind among the long-standing questions in solar physics that have baffled astronomers for more than a century. The high mass density in the chromosphere causes it to emit energy more rapidly compared to the solar corona. As a result, the energy flux from the lower layer of the solar atmosphere is insufficient to offset this loss. To address the issue, solar physicists have proposed several theories in recent times, including magnetic reconnection, MHD waves, and nano-flare heating (Sakurai, 2017; Srivastava et al., 2025). Both spaceborne and ground-based observational data support such theories (Cheng et al., 2023; Mondal et al., 2024; Meringolo et al., 2024). However, the wave theory has gained significant attention (Srivastava et al., 2021). It suggests that convective energy from the photosphere is transported into the diffuse corona, potentially heating it to millions of degrees (Sec. 4.4).

This chapter presents numerical results based on papers by Kumar et al. (2024a) and Kumar et al. (2024b), focusing on impulsively and granulation-generated wave dynamics in the chromosphere, and establishing their role in local energy transfer and the generation of plasma outflows. The subsequent analysis is extended to the global corona, where we finally implement empirically derived source and sink terms to model the upper solar atmosphere (Kumar et al., 2025, in preparation). The present chapter establishes MHD waves as a viable local heating mechanism in the chromosphere, followed by extending these principles to global scales (chapter 7) by unifying the three key elements: (1) wave-driven energy injection from the dissipation of MHD waves in the two-fluid plasma, (2) empirical coronal heating, as a collective proxy for wave dissipation and unresolved small-scale processes, and (3) sink terms such as thermal conduction and radiative loss, governing energy distribution and loss. This supports the idea that impulsive and granular events can contribute to sustaining the coronal temperature and driving plasma outflows.

It is crucial to note that the results presented here are limited to local spatial domains, typically tens of megametres (Mm) in maximum size, and short dynamical timescales on the order of seconds to minutes. On this restricted scale, the numerical model can afford high spatial resolution, allowing us to track individual ion-neutral fluids of distinct character and to follow individual Alfvén and MAW packets with accuracy. These local simulations therefore capture the small-scale processes, such as ion–neutral drift, shock formation, viscosity, and resistivity, that govern how wave energy is transferred into heat and drives associated plasma outflows. However, the presented numerical model also holds two inherent limitations: (a) it is unable to capture the cumulative, long-term impact of countless such events occurring all over the entire solar surface, and (b) it does not deal with global magnetic-field geometry or large-scale mass and energy balance. To bridge this gap, the physical parameterizations derived from these high-resolution simulations, such as heating rates, momentum exchange terms, and empirical source-sink functions, are used to inform and constrain the steady-state, multi-fluid equations in our global COCONUT-MF model, introduced in chapter 7. To put it another way, the presented local solutions provide us with essential quantitative foundations—specific heating efficiencies, profiles of wave-energy flux, and ion-neutral coupling—that are incorporated as parameterized energy source and sink terms. This approach enables us to seamlessly continue our analysis from the upper chromosphere out to several solar radii without compromising the fundamental small-scale physics.

6.2 Impulsively-generated waves in two-fluid plasma

6.2.1 Objective

This study focuses on impulsively generated MAWs and coupled Alfvén-MAWs in the context of chromospheric heating and associated plasma outflows. The study presented here examines the effects of two fluids, which can alter wave propagation, leading to dissipation and plasma heating through ion-neutral collisions.

6.2.2 Model of the solar atmosphere

As outlined in Sec. 3.2, it is crucial to consider the behavior of neutrals when modeling the solar chromosphere. Therefore, the gravitationally stratified and magnetically confined solar atmosphere is represented by a two-fluid plasma model. The model considers ions + electrons as one fluid and neutrals as another. Each fluid has its own physical characteristics, such as flow velocity, mass density, and viscosity, among others. Other species are not considered here for the sake of simplicity. We assume that ions are protons and neutrals are hydrogen atoms. This model does not include ionization or recombination. Additionally, the influence of electrons on ions, charge exchange, heat conduction, and radiative losses is omitted to keep the model simple. While the general form of the two-fluid equations is thoroughly derived in chapter 3, the following subsection provides the exact form of the adopted two-fluid equations and the corresponding numerical setup.

(a) Mass conservation equations

$$\frac{\partial \varrho_i}{\partial t} + \nabla \cdot (\varrho_i \mathbf{V}_i) = 0 \tag{6.1}$$
$$\frac{\partial \varrho_n}{\partial t} + \nabla \cdot (\varrho_n \mathbf{V}_n) = 0 \tag{6.2}$$

(b) Momentum equations

$$\frac{\partial (\varrho_i \mathbf{V}_i)}{\partial t} + \nabla \cdot (\varrho_i \mathbf{V}_i \mathbf{V}_i + p_{ie}\mathbf{I}) = \varrho_i \mathbf{g} + \frac{1}{\mu}(\nabla \times \mathbf{B}) \times \mathbf{B} + \mathbf{S}_i \tag{6.3}$$
$$\frac{\partial (\varrho_n \mathbf{V}_n)}{\partial t} + \nabla \cdot (\varrho_n \mathbf{V}_n \mathbf{V}_n + p_n\mathbf{I}) = \varrho_n \mathbf{g} + \mathbf{S}_n \tag{6.4}$$

(c) Energy equations

$$\frac{\partial E_i}{\partial t} + \nabla \cdot \left[\left(E_i + p_{ie} + \frac{\mathbf{B}^2}{2\mu}\right)\mathbf{V} - \frac{\mathbf{B}}{\mu}(V_i \cdot \mathbf{B})\right] = (\varrho_i \mathbf{g} + \mathbf{S}_i) \cdot \mathbf{V}_i + Q_i \tag{6.5}$$
$$\frac{\partial E_n}{\partial t} + \nabla \cdot [(E_n + p_n)\mathbf{V}_n] = (\varrho_n \mathbf{g} - \mathbf{S}_n) \cdot \mathbf{V}_n + Q_n \tag{6.6}$$

with energy densities, $E_{i,n}$ given as

$$E_i = \frac{\varrho_i \mathbf{V}_i^2}{2} + \frac{p_{ie}}{\gamma - 1} + \frac{\mathbf{B}^2}{2\mu}\,, \qquad E_n = \frac{\varrho_n \mathbf{V}_n^2}{2} + \frac{p_n}{\gamma - 1} \tag{6.7}$$

Induction and solenoidal constraints supplement the above equations, expressed as

$$\frac{\partial \mathbf{B}}{\partial t} = \nabla \times (\mathbf{V}_i \times \mathbf{B})\,, \qquad \nabla \cdot \mathbf{B} = 0 \tag{6.8}$$

The notations in Eqs. 6.1 – 6.8 are defined as follows: the ion and neutral components are represented by subscripts i and n, respectively. The corresponding velocities of these species are given by $\mathbf{V}_{i,n}$, while their associated mass densities are denoted by $\varrho_{i,n}$. The energy densities are $E_{i,n}$, and their temperatures are $T_{i,n}$. The total pressure for the ionized component, including electrons, is represented by $p_{ie} = p_i + p_e = 2\,p_i$, while the neutral gas pressure is denoted by p_n (Eq. 6.13). The magnetic field is denoted by $\mathbf{B}$, the magnetic permeability by μ, and $\mathbf{I}$ refers to the identity matrix. The gravitational acceleration vector, $\mathbf{g}$, acts in the negative $\mathbf{y}$-direction, with a magnitude of $274.78\,\mathrm{m\,s^{-2}}$. The adiabatic index γ, defined as the ratio of specific heats at constant pressure to that at constant volume, is taken to be equal to 5/3 here. The collisional momentum transfer term is $\mathbf{S}_{i,n}$. The collisional energy exchange terms for ions and neutrals, respectively, are $Q_{i,n}$, following the definitions provided by Oliver et al. (2016) and Meier et al. (2012a). These terms are specified as

$$\mathbf{S}_i = \varrho_i \nu_{in} (\mathbf{V}_n - \mathbf{V}_i), \quad \mathbf{S}_n = \varrho_i \nu_{in} (\mathbf{V}_i - \mathbf{V}_n) \tag{6.9}$$

$$Q_i = \frac{1}{2} \nu_{in} \varrho_i (\mathbf{V}_i - \mathbf{V}_n)^2 + \frac{3 k_B \nu_{in} \varrho_i}{m_n + m_i} (T_n - T_i) \tag{6.10}$$

$$Q_n = \frac{1}{2} \nu_{in} \varrho_i (\mathbf{V}_i - \mathbf{V}_n)^2 + \frac{3 k_B \nu_{in} \varrho_i}{m_n + m_i} (T_i - T_n) \tag{6.11}$$

In the formulation above, ν_{in} is the ion-neutral collision frequency adopted from Braginskii (1965), defined as

$$\nu_{in} = \frac{4}{3} \frac{\sigma_{in} \varrho_n}{m_i + m_n} \sqrt{\frac{8 k_B}{\pi} \left(\frac{T_i}{m_i} + \frac{T_n}{m_n} \right)} \tag{6.12}$$

Here, $m_i = m_H \mu_i$ and $m_n = m_H \mu_n$ are the masses of ions and neutrals, respectively, taken to be equal to the hydrogen mass m_H. The parameters $\mu_i = 1$ and $\mu_n = 1$ represent the mean masses of ions and neutrals, respectively. The collision cross section σ_{in} is taken as $1.4 \times 10^{-19}\,\mathrm{m}^2$ (Chapman et al., 1970; Vranjes et al., 2013). We note that the current model does not consider charge transfer collisions, which have not yet been implemented in the JOANNA code. The ideal gas law defines the ion and neutral temperature as follows:

$$p_i = \frac{k_B \varrho_i T_i}{m_i}, \quad p_n = \frac{k_B \varrho_n T_n}{m_n} \tag{6.13}$$

Here, the symbol k_B denotes the Boltzmann constant. The remaining symbols retain their conventional physical meanings. Note that the adopted two-fluid model provides a detailed description of the chromosphere and low corona, which are the main focuses of the present study. However, it still has limitations in accurately representing the photosphere (Khomenko et al. 2014). MHD models (Sec. 3.4) can simulate the fluids individually, thus allowing the assumptions of quasi-neutrality, small Larmor radius, and small Debye length to be dropped (Sec. 1.1.1).

6.2.3 Magnetohydrostatic equilibrium of the solar atmosphere

In the present model, the plasma system of the solar atmosphere is initially (i.e., at $t = 0$ s) considered to be in a state of magnetohydrostatic equilibrium (MHE) before conducting any numerical simulations, that is, $\partial f / \partial t = 0$, where f stands for any equilibrium plasma quantity. Magnetohydrostatic equilibrium is the state for stationary fluids ($\mathbf{V}_{i,n} = \mathbf{0}$) in which the inward gravitational force balances the radially outward pressure gradient force. The corresponding mathematical expression can be obtained by setting $\mathbf{V}_{i,n} = \mathbf{0}$ and $\mathbf{B} = \mathbf{0}$

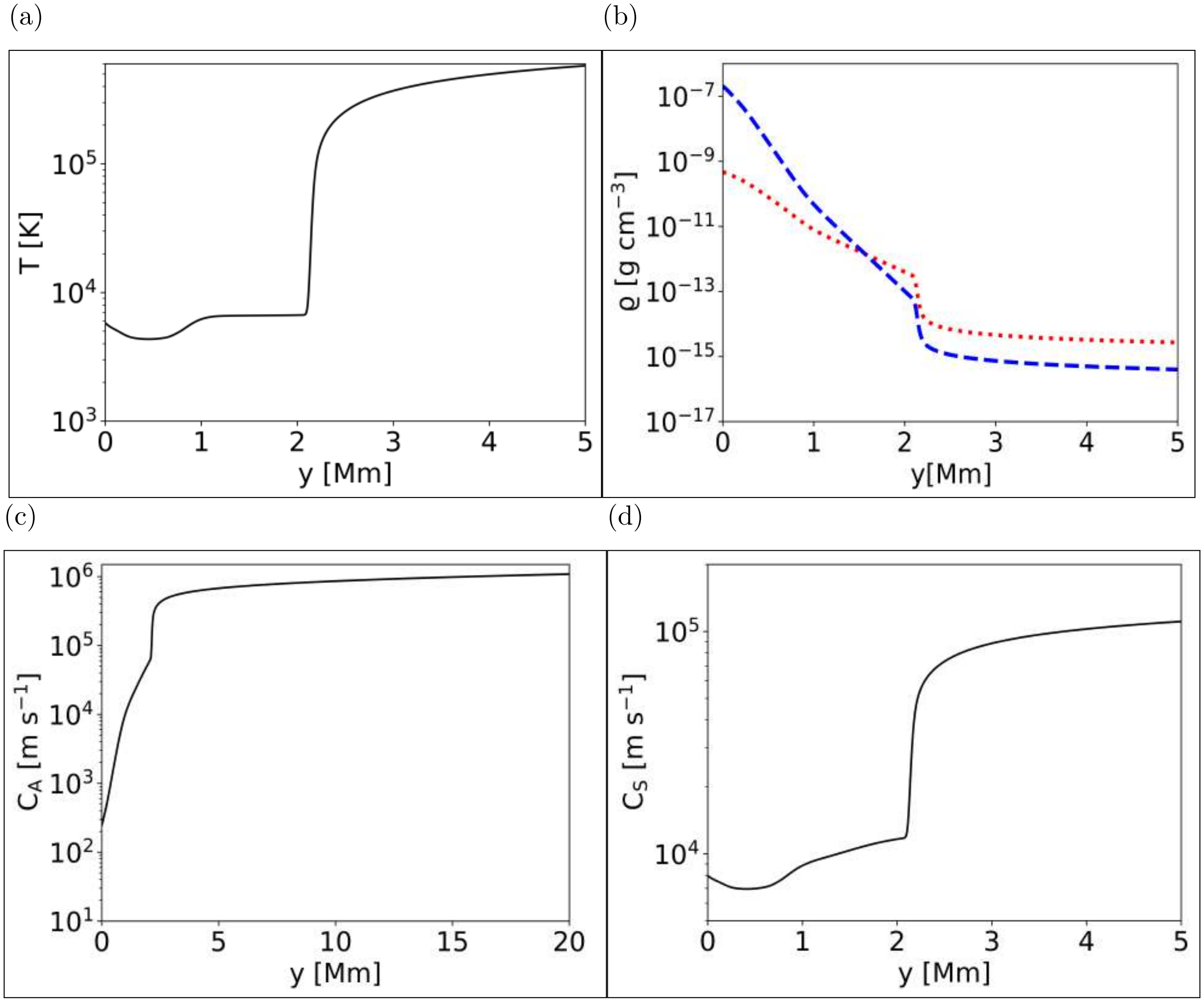

Figure 6.1: Vertical profiles displaying (a) the equilibrium temperature, (b) the mass densities of ions (dotted line) and neutrals (dashed line), (c) the bulk Alfvén speed, and (d) the sound speed in the two-fluid model of the solar atmosphere for the initial configuration of magnetohydrostatic equilibrium. It is assumed that initially $T_i = T_n$; however, this assumption is later relaxed, allowing for variations between T_i and T_n.

in the momentum equations (Eqs. 6.3 - 6.4), resulting in the expression

$$\nabla p_{ie,n} = \varrho_{ie,n}\,\mathbf{g} \tag{6.14}$$

Here, the hydrostatic gas pressure $p_{ie,n}$ and mass densities $\varrho_{ie,n}$ are defined respectively as

$$p_{ie,n}(y) = p_{0ie,n}\,\exp\left(-\int_{y_r}^{y}\frac{dy}{\Lambda_{ie,n}(y)}\right), \qquad \varrho_{ie,n}(y) = \frac{p_{ie,n}(y)}{g\Lambda_{ie,n}(y)} \tag{6.15}$$

Here, $\Lambda_{ie,n} = k_B T/\mu_{ie,n} g$ denotes the pressure scale heights for ions and neutrals, and $T(y)$ is the temperature adopted from the semi-empirical model of Avrett et al. (2008a). The pressure scale height is defined as the distance in an isothermal atmosphere (not discussed here) at which the pressure decreases by a factor of e. The reference height is set to $y = y_r = 50$ Mm. The symbols $p_{0ie,n}$ represent the equilibrium pressures of ions and neutrals at the selected reference height, which are taken here to be $p_{0n} = 0.05$ Pa and $p_{0ie} = 0.1$ Pa, respectively. Figure 6.1 shows the profiles of the temperature (a) and mass density (b) of ions (ϱ_i, dashed) and neutrals (ϱ_n, dotted) with height, adapted from the model of Avrett et al. (2008a). In the temperature profile, we observe a drop in temperature from 5600 K in the lower photosphere ($y = 0$ Mm) to 4300 K at its upper limit ($y = 0.5$ Mm). The temperature rises in the chromosphere, but the most significant change occurs in the transition region ($y = 2.1$ Mm), where a substantial temperature spike is observed. The temperature reaches approximately 10^6 K at around $y \approx 10$ Mm, attaining the values expected in the solar corona (not shown here). The profile of $\varrho_{i,n}(y)$ indicates that ϱ_i is less than ϱ_n in the photosphere and lower chromosphere, owing to relatively lower temperatures in these regions. Furthermore, the ratio ϱ_i/ϱ_n reaches its minimum value of 10^{-2} in the lower photosphere. In the transition region, as expected, a substantial fall in ϱ_n occurs. These characteristics of $\varrho_{i,n}(y)$ indicate the variation of the ratio ϱ_i/ϱ_n with height in the solar atmosphere.

In solar physics, understanding variations in bulk Alfvén speed C_A and sound speed C_s with height is crucial for investigating the propagation of MHD waves in the solar atmosphere. The plot in Fig. 6.1 shows the profiles of $C_A(y)$ (c) and the sound speed $C_S(y)$ (d). These parameters are defined as follows:

$$C_A = \sqrt{\frac{{B_y}^2 + {B_z}^2}{\mu_0(\varrho_i + \varrho_n)}}, \qquad C_S = \sqrt{\frac{\gamma(p_i + p_n)}{\varrho_i + \varrho_n}} \tag{6.16}$$

In the lower solar atmosphere ($y \approx 1$ Mm), the mean Alfvén speed is about $10\,\mathrm{km\,s^{-1}}$. It rises with a steep jump in the transition region and subsequently plateaus at a relatively constant value. This steep jump is due to a decrease in ϱ_i, as indicated by Fig. 6.1(b). The profile of $C_S(y)$ follows the trend of $T(y)$ near the transition region. C_S attains a minimum value of about $10\,\mathrm{km\,s^{-1}}$ in the photospheric ($0 \le y \le 0.5$ Mm).

6.2.4 Adopted magnetic field configuration and impulsive perturbations

The topology of the magnetic field can influence the behavior and propagation of MHD waves (Bogdan et al., 2003). The hydrostatic equilibrium, characterized by Eqs. 6.14 - 6.15, is overlaid by a homogeneous and unidirectional magnetic field with $\mathbf{B} = [0,\, B_y,\, B_z]$, where the vertical component is kept constant at $B_y = 10$ Gs. The magnetic field here is current-free and hence force-free, i.e., $(\nabla \times \mathbf{B}) \times \mathbf{B}/\mu = \mathbf{0}$. This value of B_y corresponds to the typical quiet Sun magnetic field strength under such circumstances (see Fig. 1 in Shelyag et al. (2012)). Here, we compare and contrast two values for B_z: (a) $B_z = 0$ Gs (Case 1) and (b) $B_z = 2$ Gs (Case 2). The latter adopted value lies in the range $1 - 4$ Gs, a typical value of B in the solar corona, for $1.05 - 1.35\, R_\odot$ (Yang et al., 2020). Since our model assumes a uniform magnetic field $\mathbf{B}$ remains constant in the lower regions of the solar atmosphere, specifically in the photosphere and chromosphere. Therefore, the resultant magnetic field adopted and discussed above is within observational limits and physically justified.

The central theme of the present work revolves around Alfvén and MAWs. To excite these waves, we launched *Gaussian pulse* in the horizontal components of the ion and neutral velocities, perturbing the initially assumed MHE. This Gaussian pulse is defined as follows:

$$V_{ix}(x, y, t = 0) = V_{nx}(x, y, t = 0) = A \exp\left(-\frac{x^2 + (y - y_0)^2}{w^2}\right) \tag{6.17}$$

Here, the notation A, w, and y_0 respectively denote the pulse's amplitude, width, and launching height. It is worth mentioning that the actual perturbations in the solar atmosphere are significantly more complex than what is presented in Eq. 6.19. Still, this relatively straightforward approach can improve our understanding of the underlying physics of solar atmosphere heating and plasma outflows. The adopted values for the parameters here are: $A = 6$ km s^{-1}, $w = 0.25$ Mm, and $y_0 = 0.5$ Mm, unless otherwise specified. The physical intuition behind these parameters can be explained as follows. The adopted width, $w = 0.25$ Mm, aligns with the spatial scale of solar granules, which typically range in diameter from 200 to 1000 km (Cloutman, 1980). The chosen height, $y_0 = 0.5$ Mm, corresponds to the top of the photosphere in the solar atmosphere. We note that $A = 6$ km s^{-1} is significantly greater than the horizontal flow amplitude within a solar granule (Stein et al., 1998), although such magnitudes can occur sporadically due to magnetic reconnection, transient strong convective plumes, or vortex motions. Thus, while not typical of the global solar atmosphere, this value serves as a physically driven proxy for investigating the excitation of MHD waves under impulsive driving. Therefore, the adopted parameter values are scientifically valid and physically justified. The following subsection explains the basic physical mechanism by which the introduced Gaussian pulse perturbs the system to excite MHD waves.

6.2.5 Impulsively excited MHD waves in a uniform plasma: A qualitative description

The implemented Gaussian pulses (Eq. 6.19) excite MHD waves in two-fluid plasma depending on the adopted background magnetic field configuration $[B_x, B_y, B_z]$, in our case [0, 10, 0] Gs

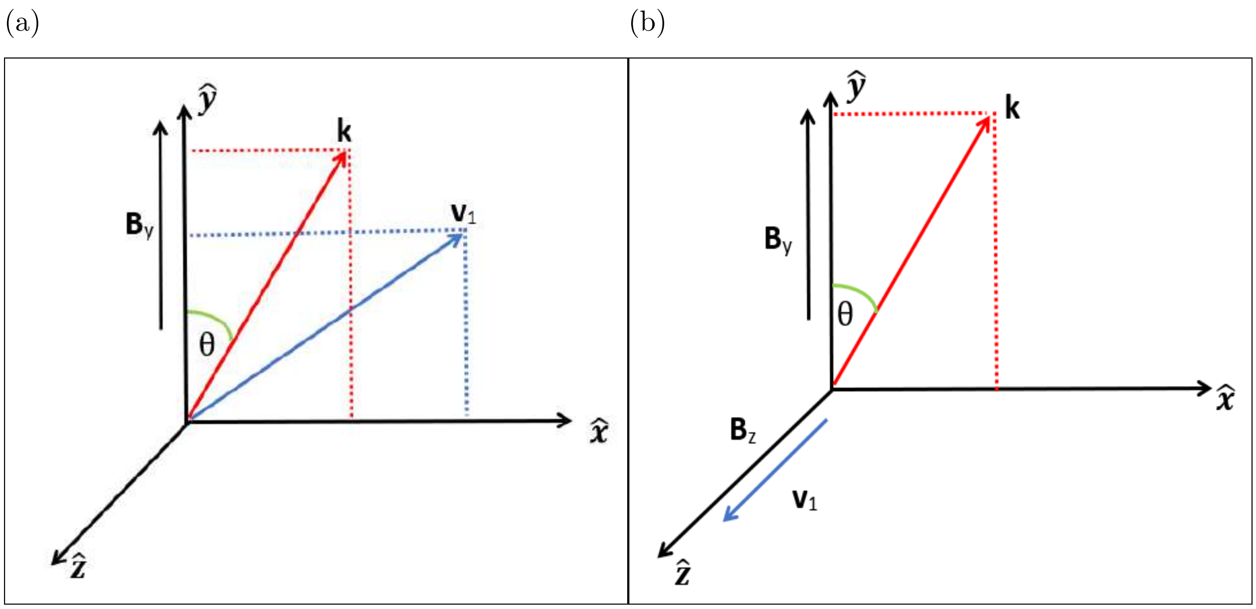

Figure 6.2: Figures showing the orientation of the velocity perturbation $\mathbf{V}_1$ and the wave vector $\mathbf{k}$ for magnetic field configurations represented as (a) $\mathbf{B} = [0, B_y, 0]$ Gs and (b) $\mathbf{B} = [0, B_y, B_z]$ Gs.

and [0, 10, 2] Gs. In the solar atmosphere, the presence of large-scale varying dynamics is capable of continuously transmitting kinetic energy — such as disturbances caused by granular motion in the photosphere, blast waves generated by high-altitude flares, and shocks resulting from magnetic reconnection. In this context, the Gaussian pulse simulates a rapid disturbance of magnetic field lines by granular cells, which in turn influences the plasma in the local region. The interaction between the perturbed magnetic field and the plasma generates waves that carry energy and momentum into the upper solar atmosphere. Here, we will briefly describe the physical picture behind the generation of MHD waves in the context of the present work; a more detailed discussion is provided in chapter 4.

Let $\mathbf{b}_1$ and $\mathbf{V}_1$ respectively denote the small perturbations in the magnetic field $\mathbf{B}$ and velocity, such that ($|\mathbf{b}_1| \ll |\mathbf{B}|$). Figure 6.2 shows the direction of $\mathbf{B}$, $\mathbf{k}$, and $\mathbf{V}_1$ in a homogeneous plasma for Case 1 (a) and Case 2 (b). Panel (a) illustrates the case with $\mathbf{V}_1 \cdot \mathbf{k} \neq 0$ (Eq. 4.25 - 4.28). Recognizing that $\mathbf{V}_1$ is induced by the Gaussian pulse, we infer that this setup led to the generation of MAWs, neutral acoustic waves that are compressive and longitudinal, as well as internal gravity waves. Consequently, we can analyze their overall progression in ion velocity, $V_{i_{x,y}}$ (Figs. 6.4 - 6.5). Similarly, panel (b) displays a case of $B_z \neq 0$ with $\mathbf{V}_1 \cdot \mathbf{k} = 0$ (Battaglia et al., 2021). This configuration leads to the generation of linearly coupled Alfvén and MAWs (Sec. 4.2.4). The Alfvén waves are incompressible and transverse (Eq. 4.36); therefore, we can trace their evolution in V_{iz} (Figs. 6.7 & 6.8). We note that fast and slow MAWs exhibit strong coupling in the low chromosphere; in the upper regions, where plasma-$\beta < 1$, the coupling between these waves weakens (Murawski, 2002; Pandey et al., 2010). The next subsection details the specific numerical configuration and boundary conditions adopted for performing the simulation.

6.2.6 Numerical setup and boundary conditions

The preliminary information regarding JOANNA is discussed in Sec. 5.10.1. In the present model, the code employs an accurate third-order Runge-Kutta method for the discretization of temporal derivatives (Durran, 2010) with the Courant-Friedrichs-Lewy (CFL) number set equal to 0.9 (Courant et al. 1928). The divergence of $\mathbf{B}$ (Eq. 6.8) is not naturally achieved by the solution of the two-fluid equations. Therefore, magnetic monopoles are cleaned using the method described by Dedner et al. (2002). The grid configuration extends from -2.56 Mm to 2.56 Mm in the x direction and from 0 to 40 Mm in the y direction. In the x direction, the grid is divided into 2048 cells, resulting in a cell size of $\Delta x = 2.5$ km. For $y < 5.12$ Mm, each cell in the numerical grid measures $\Delta y = 2.5$ km, while for $y > 5.12$ Mm, the grid is stretched and remapped into 32 cells, leading to an approximate cell size of $\Delta y \approx 1090$ km at the upper boundary. A stretched grid behaves like an absorber, damping the incident signal and reducing unwanted reflections from the top boundary. Initially ($t = 0$), all the plasma parameters at the bottom and top boundaries are maintained at their equilibrium values (Eqs. 6.14 - 6.15). The left and right edges of the simulation box are implemented with open boundary conditions, which are achieved by copying data from the closest neighboring physical cells into the boundary cells.

Physically, this setting gives a small, high-resolution box to follow the initial impulsive pulse and subsequent wavefront with minimal numerical diffusion. The numerical simulation is performed for 3000 s. We adopted the Cartesian coordinate system where $[x, y, z]$ denotes the horizontal, vertical, and transversal directions, respectively. In the present model, the positions of the various layers in the solar atmosphere are initially as follows: the top and bottom of the photosphere are located at $y = 0.5$ Mm and $y = 0$ Mm, respectively. Similarly, the top and bottom of the chromosphere are located at $y = 2$ Mm and $y = 0.5$ Mm. The transition layer is located in 2 Mm $\leq y \leq$ 2.1 Mm.

6.2.7 Numerical test

Several interlinked parameters, including magnetic fields, plasma density, temperature, and collisional interactions, influence wave propagation and behavior in the solar atmosphere. These complexities make it difficult to distinguish actual physical effects, such as ion–neutral coupling and collisional energy losses, from minor errors introduced by the adopted numerical methods. To address this, we perform numerical tests before running the simulations. In this

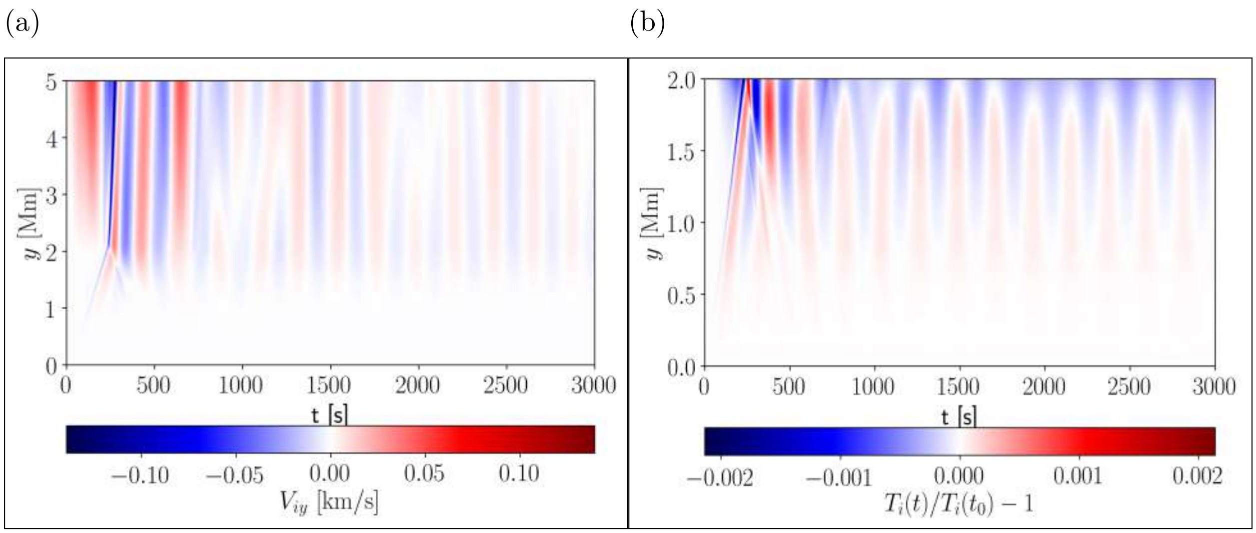

Figure 6.3: Time-distance plot for V_{iy} (a) and the relative perturbation of ion temperature $\delta T_i(x = 0, y, t)/T(y) = (T_i(x = 0, y, t) - T(y))/T(y)$ (b) in the case of no pulse for $B_z = 2$ Gs.

test, we run a baseline simulation with no initial perturbation by setting the amplitude $A = 0$ in Eq. 6.17, to ensure that our code does not produce any spurious signals. If the system remains quiet, we can confidently attribute the observed waves to our launched Gaussian pulse rather than to hidden numerical artifacts. Figure 6.3 (a) shows the time–distance plot of the vertical component of the ion velocity, V_{iy}. The observed signals reveal weak numerical noise, likely resulting from numerical approximations in modeling the MHD waves. The deep red and deep blue bands are most prominent during the first 500 seconds but quickly fade away thereafter. The maximum value of $|V_{iy}| \approx 0.075$ km s^{-1} is observed above the transition region ($y \approx 2.1$ Mm), which is significantly less than the sound speed (Fig. 6.1 d). Panel (b) of Fig. 6.3 displays the time–distance plot of the relative perturbed temperature, given by $\delta T_i(x = 0, y, t)/T(y) = [T_i(x = 0, y, t) - T(y)]/T(y)$. Here $T_i(x = 0, y, t)$ is the ion temperature and $T(y)$ is the background temperature profile adopted from the model of Avrett et al. (2008a) (Fig. 6.1 a). The maximum perturbation $\delta T_i/T(y)$ reaches approximately 2×10^{-3} near the transition region, which is negligible compared to the background temperature. The presence of oblique red–blue stripes with respect to the y-axis indicates wave reflection from the transition zone. This reflection is caused by the sudden jump in sound speed (Fig. 6.1 d), which alters the refractive index of the plasma. As waves propagate from the chromosphere to the transition region, the sudden change in the sound speed modifies their velocity and direction, leading to partial reflection (Wentzel, 1978).

In summary, the numerical test confirms that in the region of interest ($0.5 < y < 2$ Mm), the numerical noise is negligible compared to typical physical values. This indicates that the adopted numerical scheme and grid resolution have a negligible influence on the numerical results.

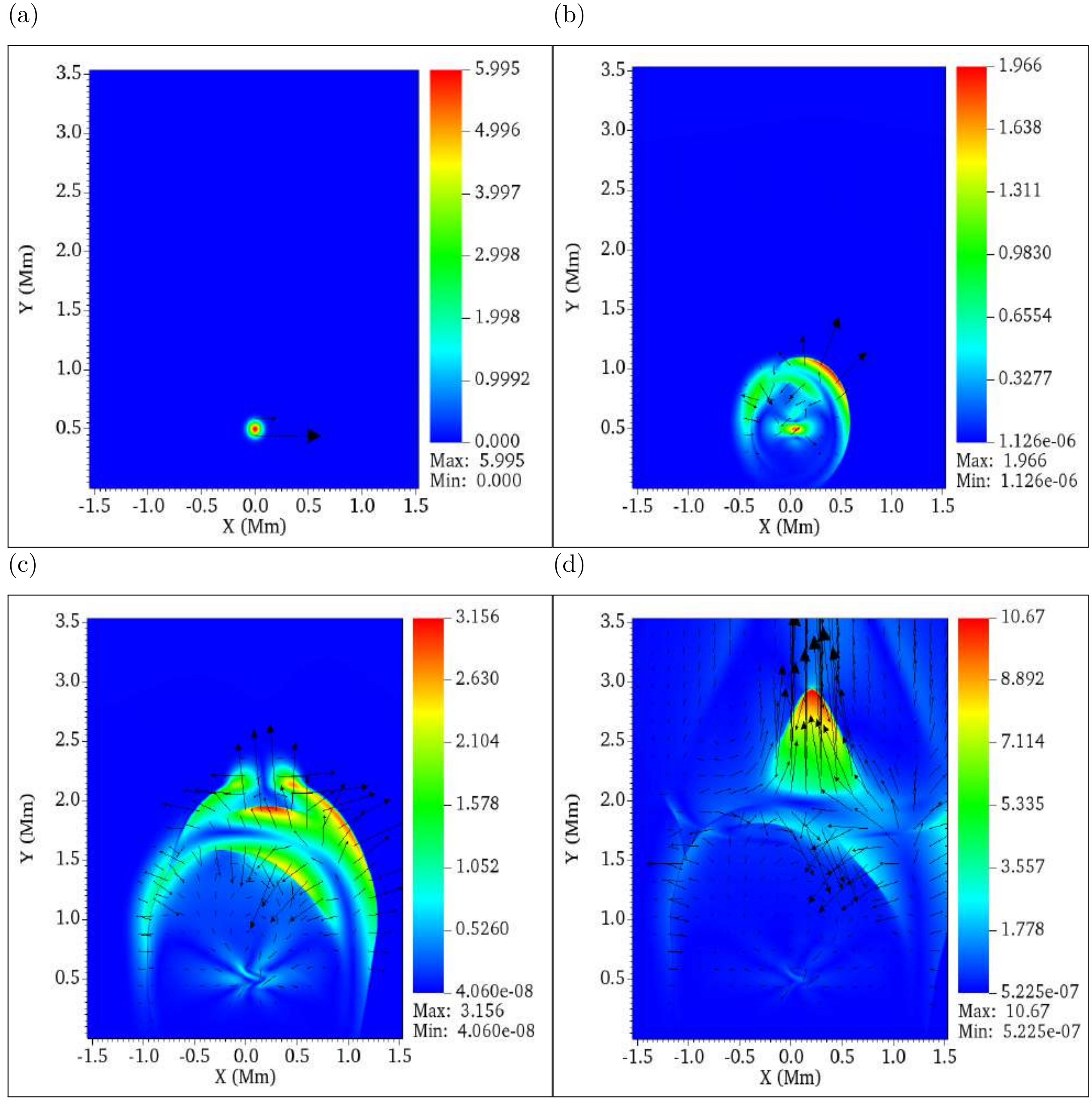

Figure 6.4: Snapshots of spatial profiles of the total velocity V_i (color map) expressed in units of $\mathrm{km\,s^{-1}}$, overlaid by $\mathbf{V}_i$ (arrows) at $t = 0$ s (a), $t = 60$ s (b), $t = 135$ s (c), and $t = 160$ s (d) for the initial $\mathbf{B} = [0, 10, 0]$ Gs. This configuration led to the generation of MAWs. The spatial profiles here represent the propagation of the perturbations in the chromosphere and upper layers of the solar atmosphere.

6.2.8 Numerical results

In this subsection, we present numerical results for both cases mentioned above, i.e., $B_z = 0$ Gs (Case 1) and $B_z = 2$ Gs (Case 2), in the context of plasma heating and associated outflows.

Magnetoacoustic waves — the case of $\mathbf{B}_z = 0$ Gs

The horizontal Gaussian pulse in V_{ix}, V_{nx} excites both slow and fast MAWs, which can be traced through the total ion velocity, defined as $V_i = \sqrt{V_{ix}^2 + V_{iy}^2}$. Figure 6.4 presents the spatial profiles of V_i, overlaid by $\mathbf{V}_i$ (represented by arrows), at key moments. At $t = 0$, a symmetric, localized peak with $V_i \approx 6\,\mathrm{km\,s^{-1}}$ observed at the top of the photosphere indicates the impulsive energy injection. This perturbation launches the fast MAWs, which propagate quasi-isotropically across magnetic field lines, and slow MAWs propagating along field lines. Comparing the snapshots at $t = 0$ s (a) and $t = 160$ s (d) reveals how the pure horizontal perturbation (x-direction) is diverted along the vertical direction (y-direction). The absence of vertical velocity asymmetry in the initial state further supports the notion that vertical motion arises solely from the coupling of slow–fast MAWs, rather than from initial conditions.

As the Gaussian pulse expands into space, the amplitude of V_i initially decreases to $A = 1.96$ km s^{-1} at $t \approx 60$ s (b), indicating energy loss from ion–neutral friction, which is consistent with heating in the chromosphere. Subsequently, the amplitude increases to $A = 3.15$ km s^{-1} at $t \approx 135$ s (c) due to a fall in background plasma mass density with height (Fig. 6.1 b).

Fast and slow MAWs predominantly propagate along the x and y directions, respectively. The elongated patterns along the y-axis (close to $x = 0$) demonstrate field-aligned slow MAWs, while the diffuse horizontal spreading indicates fast MAWs. Ion–neutral collisions dissipate part of the wave energy as thermal energy. The strongest signals remain elongated along the central axis ($x = 0$), further supporting the slow MAWs, which are primarily guided by the vertical magnetic field. Around $t \approx 135 - 160$ s, the perturbation reaches the transition region ($y \approx 2.1$ Mm), leaving the convective instabilities (Sec. 4.2.5) near the source location ($y = 0.5$ Mm) behind. By $t \approx 160$ s, the signal amplitude has nearly doubled from its initial value at $t = 0$. As the waves cross the transition region, a sharply defined front emerges, with a large region of red hue indicating enhanced velocity. This steep wavefront denotes the emergence of a shock wave. In the upper chromosphere ($y > 2.5$ Mm), the amplified vertical component of ion velocity $V_{iy} \approx 10.7$ km s^{-1} indicates the presence of plasma outflows. To visualize wave propagation in the solar atmosphere, we present time–distance plots of the driven MAWs. Figure 6.5 shows the time–distance plots for V_{ix} (a) and V_{iy} (b), both measured at $x = 0$. In both panels, the alternating red and blue stripes indicate the propagation of waves through different layers of the solar atmosphere over time. The plot for V_{ix} corresponds to the fast MAWs (for $\beta \ll 1$) with a peak value of $|V_{ix}| \approx 4$ km s^{-1} observed near the top of the photosphere. This is followed by very weak oscillations, indicating that fast MAWs are damped within a very short time. Notably, the lack of any remaining transverse oscillations suggests that Alfvén waves are absent. In contrast, the trend observed in the time–distance plot for V_{iy} reveals that strong upward-propagating ridges are characteristic of slow MAWs. The maximum value $|V_{iy}| \approx 8$ km s^{-1} occurs at the top of the chromosphere. However, the signal

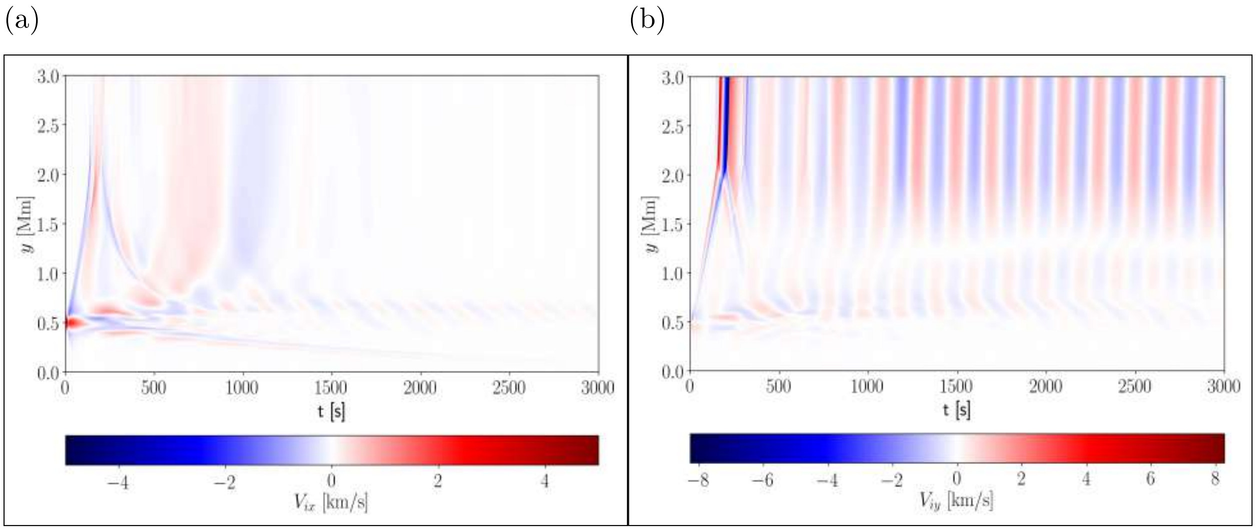

Figure 6.5: The time-distance plot for V_{ix} (a) and V_{iy} (b) corresponding to MAWs for $\mathbf{B} = [0, 10, 0]$ Gs. These maps correspond to the slices taken at $x = 0$ along y in Fig. 6.4. The red and blue bands in both panels represent the propagation of waves over time.

gradually fades with time, though not as strongly as observed for V_{ix}. This suggests that slow MAWs play a primary role in plasma heating and driving the outflows in the chromosphere, while fast MAWs tend to dissipate in the x-direction. Additionally, we observe that a narrow dark band appears in the early phase of the simulation, indicating the occurrence of shock waves that rapidly release their energy.

The kinetic energy flux carried by slow MAWs, as they propagate through the system, is expressed as

$$F_E(x = 0, y, t) \approx \frac{1}{2}\varrho_i \mathbf{V}_i^2 C_s \tag{6.18}$$

Figure 6.6 (a) represents a time–distance plot of the kinetic energy flux (F_E) transported by slow MAWs. A direct correlation with V_{iy} (Fig. 6.5 b) indicates that the majority of the kinetic energy flux is carried by the slow MAWs along the magnetic field lines in the y direction. Initially, at the top of the photosphere ($y \approx 0.5$ Mm), the kinetic energy flux reaches a value of $\approx 10^6\,\mathrm{erg\,cm^{-2}s^{-1}}$. This large kinetic energy flux at the launching site suggests efficient energy transfer from the original perturbation to the ambient plasma via MAWs. The wavefront, seen as a diagonal structure with negative slope, represents upward-propagating waves with a propagation speed of $\approx 7\,\mathrm{km\,s^{-1}}$. This matches the typical sound speed C_s in the solar chromosphere, further supporting that these are slow-mode MAWs traveling along the magnetic field lines. Moreover, the time–distance plot reveals that the energy flux exhibits its most intense characteristics during the first 200 s as the MAWs travel from the photosphere to the transition region. Upon reaching the transition zone, part of the wave energy is reflected, primarily due to the steep rise in the sound speed C_s with height (Fig. 6.1 d). This causes

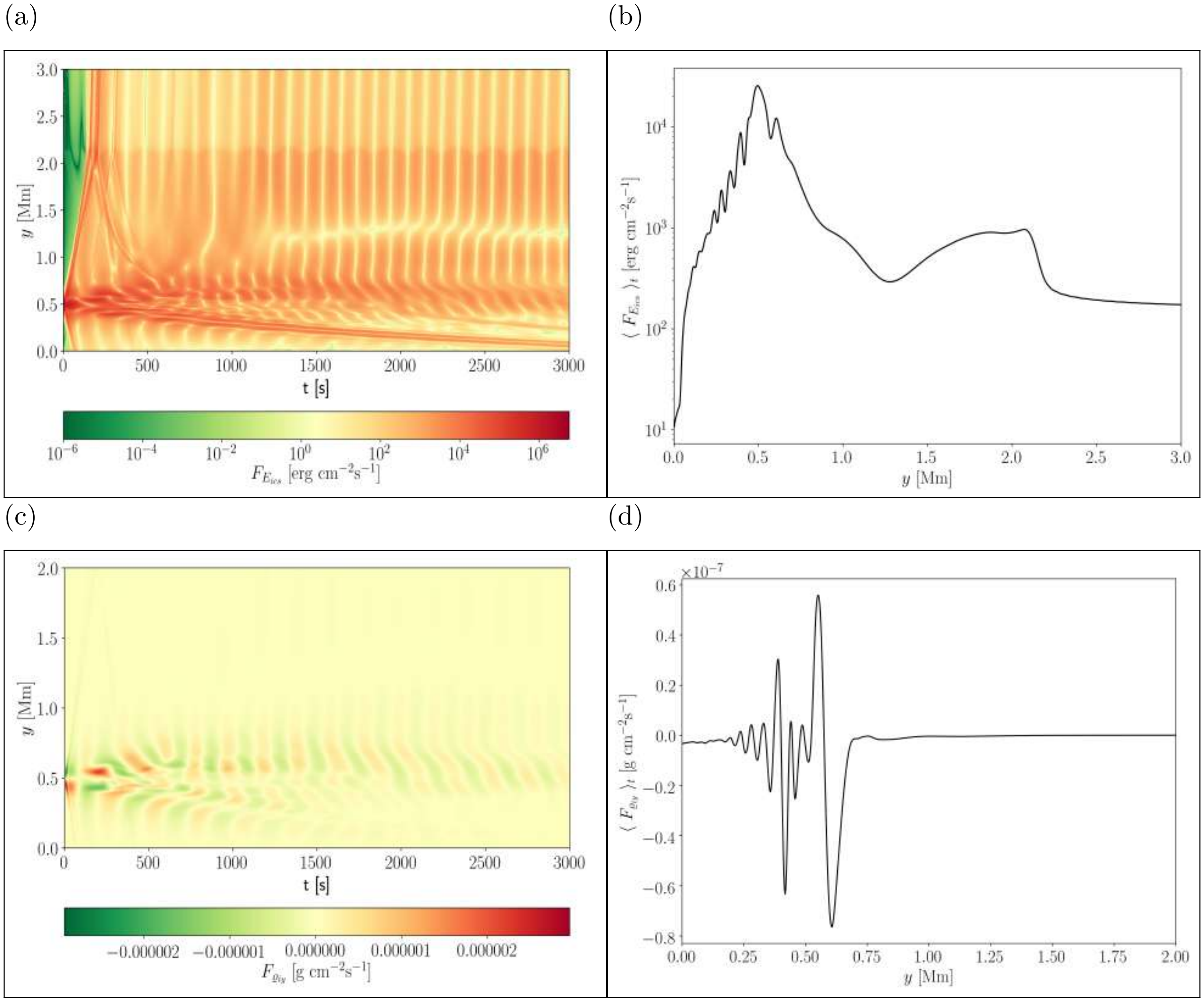

Figure 6.6: Time-distance plot for kinetic energy flux, $F_E(x=0,y,t)$ (a), and its corresponding vertical profile averaged over time (b). Time-distance plot for the vertical flux of total mass density (c), and its corresponding vertical profile averaged over time (d). These plots correspond to Fig. 6.4 and represent the variation of the energy flux (a, b) and mass flux (c, d) due to MAWs.

modifications in wave propagation, resulting in a sharp transition and a downward flow of some energy.

The time-distance plot also highlights the height-dependent dissipation, with a sharp drop in flux observed in $1.0 < y < 1.5$ Mm, coinciding with regions of enhanced ion-neutral collisions. Within this region, the flux diminishes by four orders of magnitude from 10^6 to $10^2\,\mathrm{erg\,cm^{-2}\,s^{-1}}$, indicating substantial conversion of wave energy into thermal energy via ion-neutral friction. In the upper regions, particularly for $y > 2.0$, a sustained residual flux exceeding $10^2\,\mathrm{erg\,cm^{-2}s^{-1}}$ persists up to 3000 s. As the waves continue to propagate through the system, the kinetic energy flux decreases further due to ion-neutral collisions and the wave dispersal effect. In summary, the sustained residual flux in the upper chromosphere suggests that a portion of the wave energy continues to be transported upward despite significant damping in the lower region.

Figure 6.6 (b) shows the corresponding time-averaged vertical profile of the kinetic energy flux associated with the slow MAWs, defined as

$$\langle F_E(x=0,y,t)\rangle = \frac{1}{t_2-t_1}\int_{t_1}^{t_2} F_E(x=0,y,t)\,dt \tag{6.19}$$

where $t_1 = 0$ and $t_2 = 3000\,\mathrm{s}$, and other symbols have their usual meaning. As expected, the average profile displays a sharp initial peak in kinetic energy flux at the launch site (i.e., $y =$ 0.5 Mm). This peak corresponds to the immediate reaction to the launched initial Gaussian pulse, and the observed elevated flux reflects the concentrated energy flux carried by MAWs at the early stages of propagation. However, a notable drop in flux occurs around $y \approx 1.2\,\mathrm{Mm}$, where it falls from approximately 10^6 to $10^{2.5}\,\mathrm{erg\,cm^{-2}s^{-1}}$. This sharp fall in $0.5 \le y \le 1.3$ Mm is mainly attributed to ion-neutral collisions, which are particularly effective in the mid chromosphere. In other words, for $y < 1.2$ Mm, the weak collisional coupling causes mild dispersion of the waves, whereas for $y > 1.2$ Mm, the relatively higher neutral density causes strong wave dissipation. This trend suggests that two-fluid thermalization here becomes the primary mechanism for energy transfer. Interestingly, despite the dissipation in the mid-chromosphere, the kinetic energy flux shows another local peak near the transition region, primarily attributed to the strong sound speed gradient (Eq. 6.18). As mass density decreases with height, the corresponding increase in sound speed enables efficient wave propagation, resulting in a local rise in the energy flux. Beyond the transition region, the energy flux gradually declines and ultimately stabilizes at a steady value. This local decrease stems from a combination of factors: geometric spreading in the expanding magnetic flux tubes, which dilutes the wave energy flux; wave reflection, which is most pronounced at the steep gradients near the transition region; and competing energy sinks, such as radiative losses, thermal conduction, and gravitational work. Comparing the peak values of kinetic energy flux for MAWs to the radiative losses detailed in Tab. 1 of Withbroe et al. (1977), it can be inferred that the MAW-driven energy flux transport is approximately two orders of magnitude insufficient to balance the chromospheric radiative losses. These results indicate that slow MAWs alone cannot heat the solar corona, as some of their energy is either reflected downward or converted into non-kinetic forms of energy.

MHD waves can give rise to mass flows in the plasma by inducing oscillations in plasma density and the magnetic field. Such mass flow is generated by the interaction of the wave with the plasma's inertia and the magnetic field tension, which serves as a restoring force. Therefore, as the MHD waves propagate in the medium, they perturb the equilibrated system and induce plasma fluxes. The time-distance profile of ion mass flux is shown in Fig. 6.6 (c), defined as

$$F_m(x = 0, y, t) = \varrho_i V_{iy} \tag{6.20}$$

In the plot, positive mass flux values (shown in red) indicate upflows where plasma moves away from the photosphere toward higher layers, while negative mass flux values (shown in green) signify downflow plasma motion. The observed initial bands near $y \approx 0.5$ Mm are generated due to strong initial upflows and downflows caused by the source perturbations. However, these bands gradually fade due to significant ion-neutral collisional damping in the mid-chromosphere, where wave kinetic energy is efficiently dissipated and converted into thermal energy. In addition, these bands are primarily confined below $y \approx 1$ Mm, indicating that the vertical range over which MAWs significantly influence mass flux is limited, and their effects are primarily localized in the lower chromospheric layers. The limited vertical extent of these oscillations also demonstrates that single-fluid MHD models may overestimate wave propagation and neglect crucial damping effects inherent in partially ionized plasmas. These results are in good agreement with Zaqarashvili et al. (2011), who demonstrate how single-fluid MHD models may overestimate wave propagation and miss crucial damping effects observed in a two-fluid framework.

Figure 6.6 (d) shows the time-averaged profile of mass flow $\langle F_m(x = 0, y, t)\rangle$, which is defined similarly to Eq. 6.19. In the lower region ($0 \leq y \leq 0.25$ Mm), the average flux is effectively zero, indicating limited net vertical mass motion. However, in the upper photosphere and lower chromosphere, the oscillatory character of the mass flux indicates a response to MAWs, with values remaining nearly constant throughout this region. The highest magnitude reaches $7 \times 10^{-8}\,\mathrm{g\,cm^{-2}\,s^{-1}}$ near $y \approx 0.75$ Mm. This oscillatory mass flux reflects a weak but persistent mass transport driven by wave motion. Notably, this value is approximately an order of magnitude smaller than the horizontally averaged total vertical mass flux, $\langle F_m(y, t)\rangle$, reported by Wójcik et al. (2019) (see their Fig. 5), where the authors reported results of numerical simulations of plasma outflows in the context of the origin of the solar wind. We conclude that the ion mass flux observed here is insufficient to fully compensate for solar mass losses in the low corona (Withbroe et al., 1977).

Coupled Alfvén and MAWs - the case of $\mathbf{B}_z = 2$ Gs

The coupling of MHD waves is a very complex phenomenon that facilitates energy transfer between different wave modes and influences the dynamics of the solar atmosphere (Sec. 4.3 & 4.4). In the current configuration, the magnetic field exhibits a small transverse component with $B_z = 2$ G, enabling the excitation of shear Alfvén modes. Under this configuration, the horizontal pulse now excites both Alfvén and MAWs in the system, which are linearly coupled (Murawski, 2002). Snapshots shown in Fig. 6.7 display $V_{iz}(x, y)$ overlaid by $\mathbf{V}_i$ (arrows) at $t = 100$ s (a) and $t = 135$ s (b). At $t \approx 100$, a rising red arc in V_{iz} is observed, followed by a

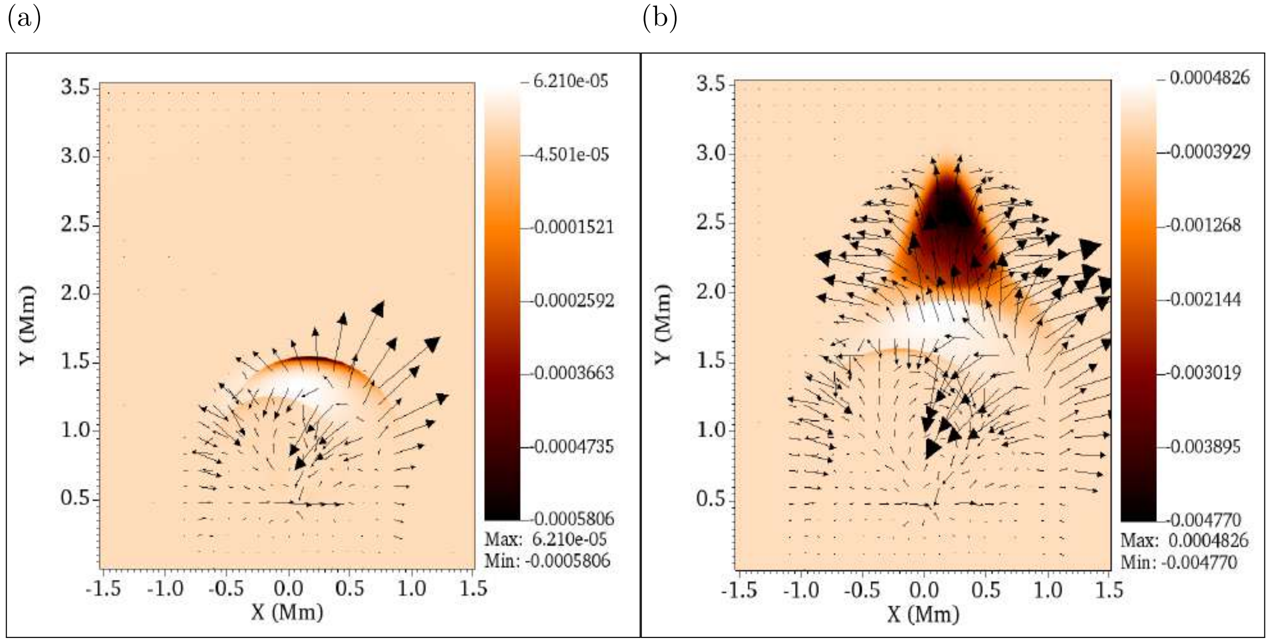

Figure 6.7: Snapshots showing the transversal component of the ion velocity V_{iz} (color map), measured in $\mathrm{km\,s^{-1}}$, overlaid by V_i (arrows) at $t = 100$ s (a) and $t = 135$ s (b) for a magnetic field $B = [0, 10, 2]$ Gs. This setup results in the excitation of MAWs that are coupled with Alfvén waves. The black arrows denote the direction of plasma motion.

steepening of the red arc at $t \approx 135$, indicating the development of a steep velocity gradient. The presence of these spatial characteristics in the profile indicates that the perturbation in V_{iz} is non-zero. These perturbations are coupled to V_{ix} and V_{iy}, indicating the coexistence and interaction of Alfvén-MAWs, which demonstrates the presence of mode coupling in the system. Following the analogy with Case 1, we present the time-distance plots to analyze the wave modes excited under the current configuration. Figure 6.8 shows the time-distance plots for the ion velocity components: V_{ix} (a), V_{iy} (b), and V_{iz} (c), all collected along y at $x = 0$. The oscillatory patterns observed in these plots indicate the propagation of linearly coupled Alfvén-MAWs. The profiles for V_{ix} (a) and V_{iy} (b) resemble those shown in Fig. 6.5, which were already discussed in detail in the previous case. However, the time-distance plot for V_{iz} (c) distinctly displays oscillations with a maximum magnitude of approximately $|V_{iz}| \approx 3\ \mathrm{km\,s^{-1}}$ near the transition region. These vertical oscillations were absent when the B_z component of the magnetic field was set to zero. In this 2.5-D configuration, the oscillatory pattern in V_{iz} is a clear signature of the Alfvénic waves. This interpretation is consistent with both theoretical predictions and recent 2.5-D two-fluid models of the chromosphere, which show that a non-zero transverse magnetic field enables coupling to Alfvén modes and facilitates their propagation (see, e.g., Khomenko et al. (2011)). Similar to the previous case, the oscillatory signature corresponding to the fast MAWs (V_{ix}) decreases over time. Consequently, in the present case, the coupled Alfvén and slow MAWs are mainly responsible for energy and mass

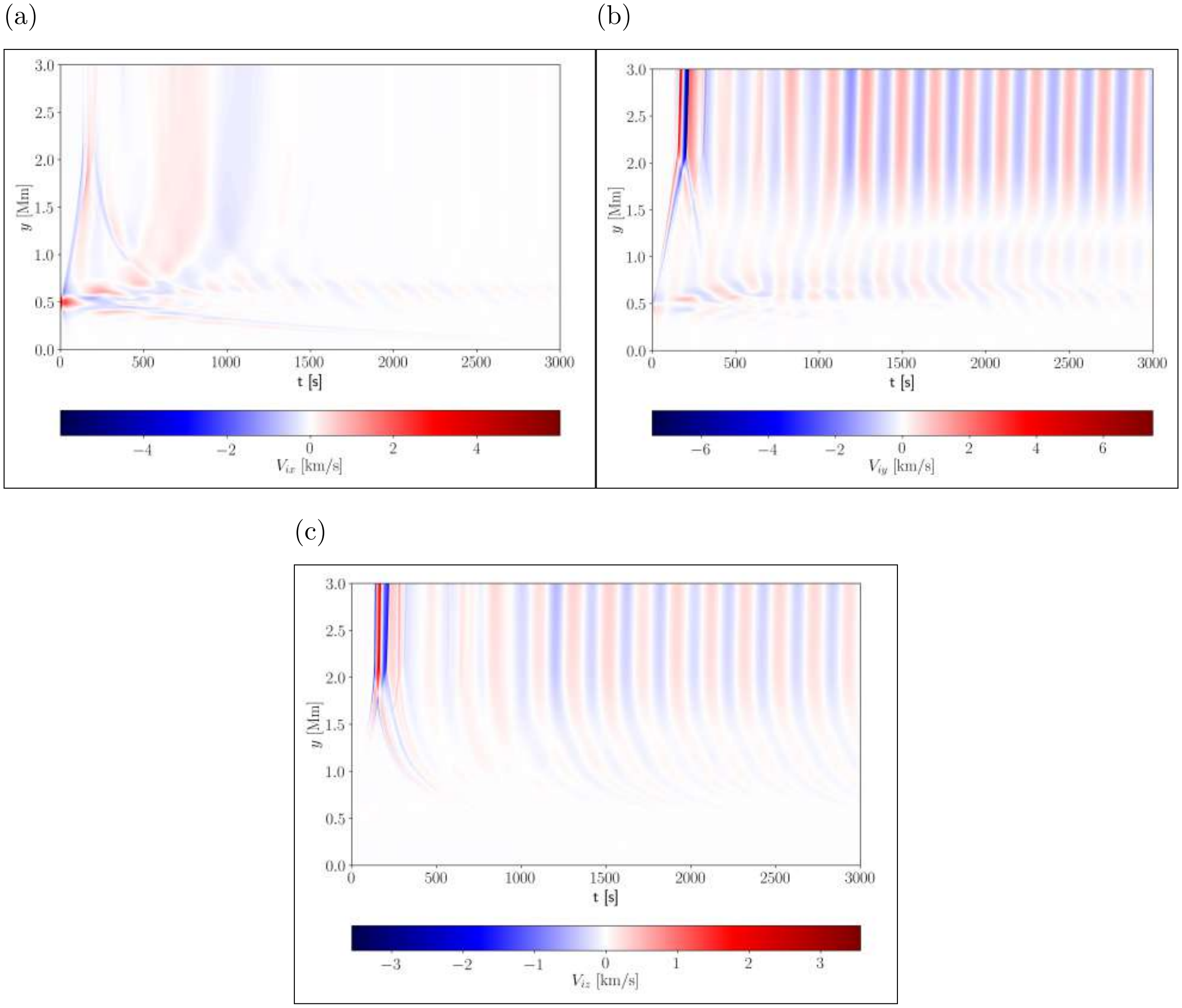

Figure 6.8: Time-distance plot for V_{ix} (a), V_{iy} (b), and V_{iz} (c) belonging to coupled Alfvén–MAWs for $B = [0, 10, 2]$ Gs. These plots correspond to the slices taken at $x = 0$ along y. The visible bands indicate the propagation of the waves.

flux transport across the solar atmosphere.

Figure 6.9 shows the time-distance plots for the vertical kinetic energy flux $F_E\,(x = 0, y, t)$ (a) and its corresponding time-averaged profile (b), both attributed to slow MAWs. The qualitative resemblance to the kinetic energy flux plot shown in Fig. 6.6 (a, b) suggests that the incorporation of a small transverse magnetic field component has only a minimal impact on the overall energy transport behavior. While this configuration allows the excitation of Alfvén waves, the related change appears insufficient to affect the vertical kinetic energy flow of the MAWs. The x-directed Gaussian pulse generates the compressible MAWs (both fast and slow) in both cases, which are the primary carriers of acoustic energy across the solar atmosphere. Even in Case 2, when a small Alfvénic component emerges in V_{iz}, the Alfvén wave conveys essentially no acoustic kinetic flux. This result is consistent with the incompressible nature of Alfvén waves, which do not transport energy in the form of compressive kinetic flux.

Similarly, Fig. 6.9 displays the time-distance plots for vertical mass flux (e) and its corresponding time-averaged profile (f), which also show no significant differences compared to the mass flux profile in Fig. 6.6 (c–d). This result again reflects the incompressible nature of Alfvén waves ($\nabla \cdot \mathbf{V} = 0$) and their inability to drive mass flux in the present setup. In summary, both F_E and F_m plots presented here remain dominated by the contribution of MAWs. Including a small $\mathbf{B}_z$ component does not qualitatively alter the dynamics of compressible waves. Thus, the propagation and transport characteristics of the MAWs remain unaffected.

A key point of interest lies in the kinetic energy flux associated with the Alfvén waves, given as

$$F_E(x = 0, y, t) \approx \frac{1}{2}\varrho_i \mathbf{V}_i^2 C_A \tag{6.21}$$

Figure 6.9 (c) displays the corresponding time-distance plots in which the propagation paths resemble those of MAWs, owing to both wave families being guided by the stratified, field-aligned structure. The peak F_E here is $10^4\,\mathrm{erg\,cm^{-2}s^{-1}}$, which is nearly two orders of magnitude lower than the kinetic flux associated with MAWs. The corresponding time-averaged profile shown in Fig. 6.9 (d) illustrates this trend even more clearly. This observed disparity in energy flux between Alfvén and MAWs arises from their fundamental properties and energy transport mechanisms. Alfvén waves, which are transverse and incompressible, do not induce significant plasma compression and therefore transport relatively less energy in the form of kinetic flux compared to MAWs. As expected, a dip in the energy flux is observed near $y \approx 1.0 - 1.5$ Mm, caused by ion-neutral friction, which results in the partial dissipation of waves. Beyond $y > 1.3\,$Mm, a local increase in the energy flux is observed, predominantly driven by atmospheric stratification and the steep gradient in Alfvén speed. Notably, this local peak is more pronounced than that observed in the MAW case, as the Alfvén speed increases more rapidly with height than the sound speed in the same region (see Fig. 6.1 c & d).

6.2.9 Comparison

The excited waves in the two-fluid plasma traverse through the photosphere and chromosphere, continuously converting a portion of the wave energy into heat through dissipation caused by ion-neutral collisions. Figure 6.10 shows the time–distance plot of the total thermal energy rate Q due to the first term on the RHS of Eqs. 6.10–6.11. Panel (a) shows the case of $B_z = 0$, while panel (b) shows the case of $B_z = 2$ Gs, offering direct insights into the spatial and temporal evolution of thermal energy deposition due to ion–neutral friction. The first term of Q (Eq. 6.10) is primarily governed by three main parameters: ion–neutral drift,

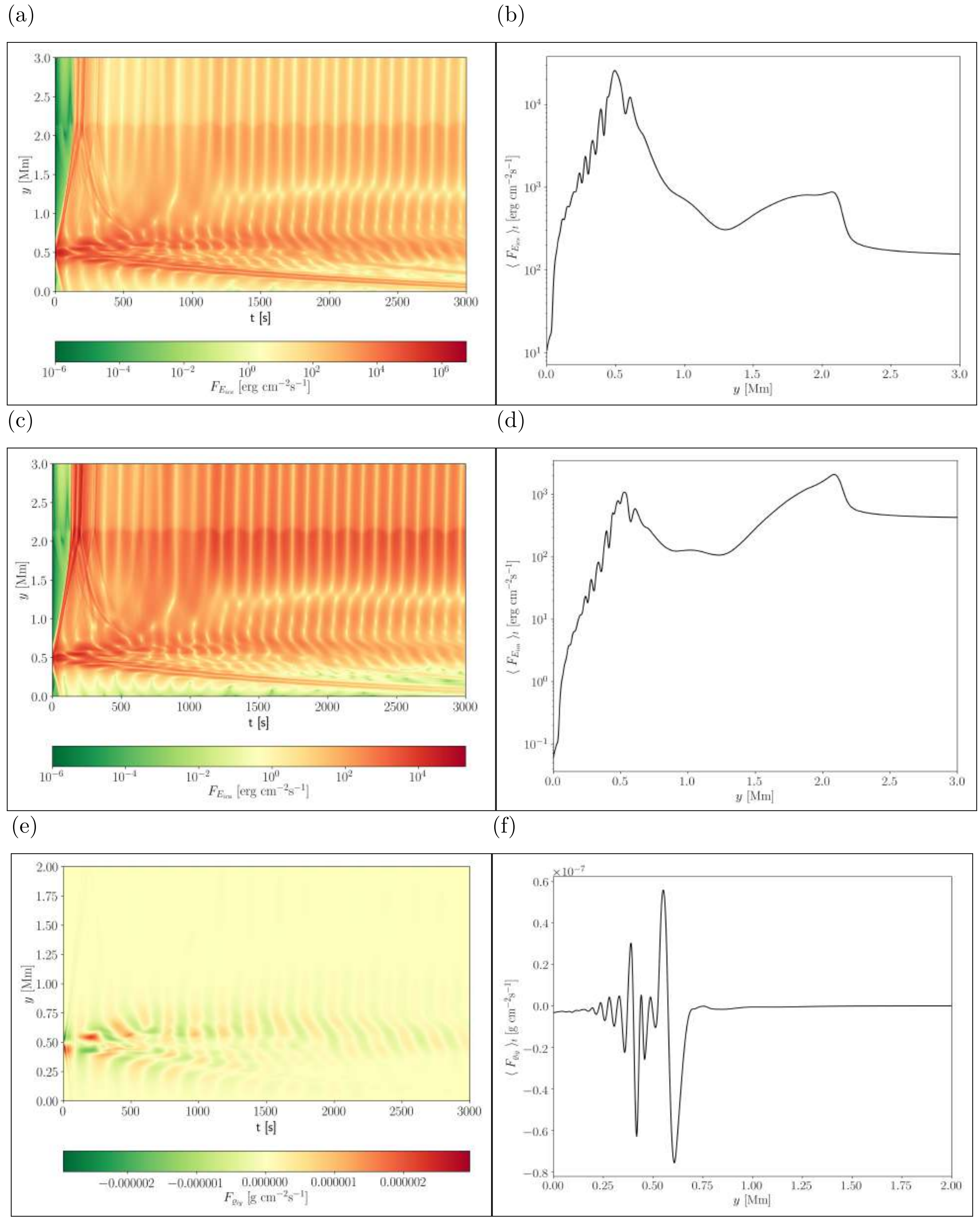

Figure 6.9: Time-distance plots for kinetic energy fluxes (a, c) and their corresponding time-averaged vertical profiles (b, d) for coupled Alfvén–MAWs. The top panels correspond to MAWs, while the middle panels correspond to Alfvén waves. Time-distance plot for the vertical flux of total mass density (e) and its time-averaged vertical profile (f) for coupled Alfvén–MAWs.

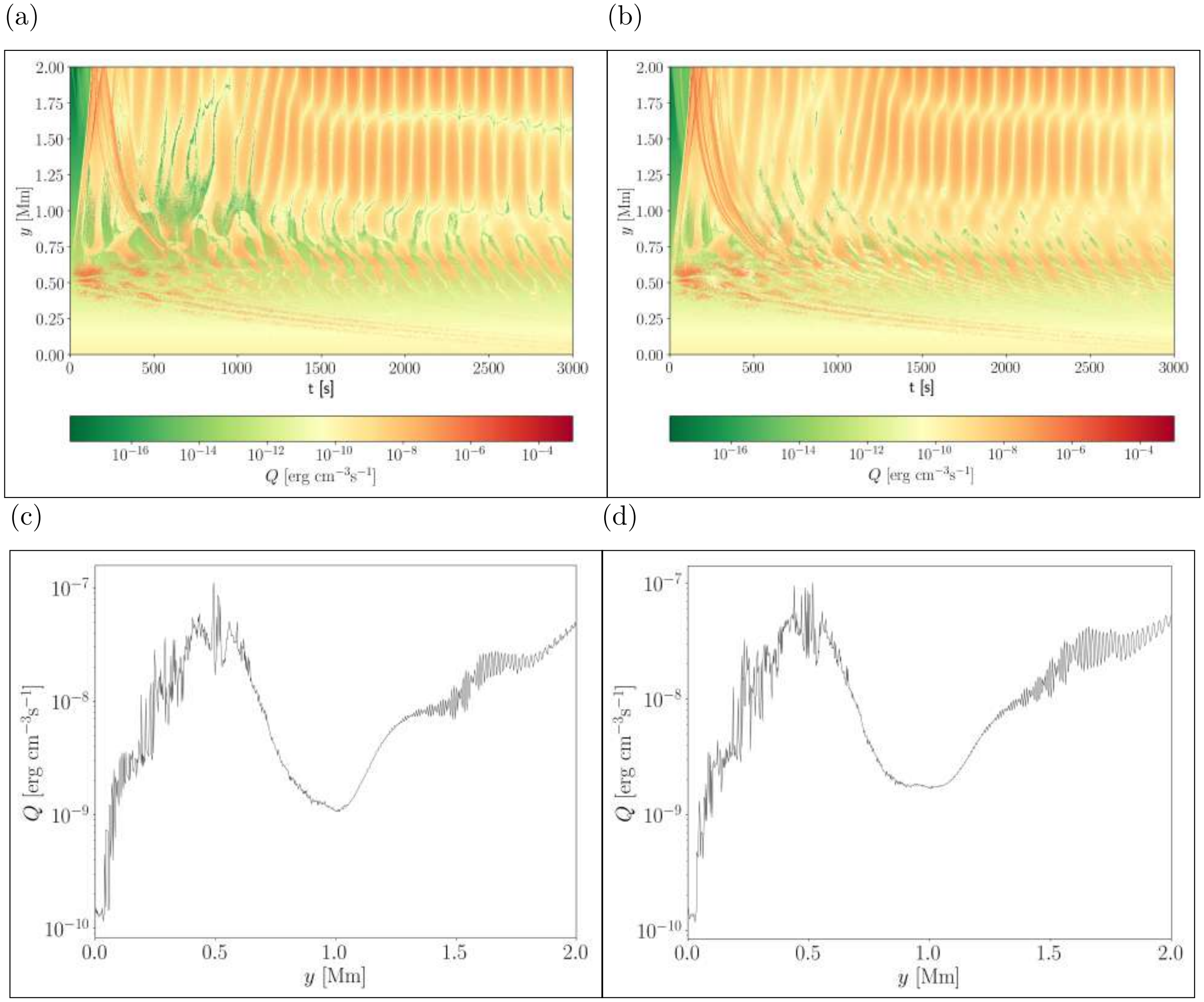

Figure 6.10: Time-distance plots for the thermal energy rate Q (a, b) and the corresponding vertical time-averaged profiles (c, d) in Case 1 (a, c) and Case 2 (b, d). The profiles together represent the thermal energy rate due to the first term on the RHS in Eq. 6.10.

$|\mathbf{V}_i - \mathbf{V}_n|$ (the primary driver of heating), collision frequency ν_{in}, and the product of ion and neutral densities $\varrho_i\, \varrho_n$. In panel (a), where only pure MAWs are excited, the ion–neutral drift remains relatively weak as ions and neutrals move together in compressive wave modes, resulting in minimal decoupling and low frictional heating. This is reflected in the presence of faint, greenish patches confined to regions below $y \leq 1.5$ Mm, suggesting limited local thermal energy deposition. In contrast, in panel (b), with $B_z = 2$ Gs, coupled Alfvén–MAWs are excited, where ions follow and neutrals lag behind the magnetic perturbations. This decoupling leads to enhanced frictional heating. Compared to Case 1, the heating distribution here is more widespread in the chromosphere. From these results, we can infer that coupled Alfvén–MAWs are more efficient and effective in heating the plasma than MAWs alone.

Figure 6.10 also presents the time-averaged profile for Q as a function of y for the cases

$B_z = 0$ (c) and $B_z = 2$ Gs (d). Notably, both plots exhibit a similar overall pattern. This is because the short-lived bursts of heating observed in Case 2 (Fig. 6.10 b) are averaged over time, resulting in a smoothing out of the differences so that they closely resemble those of Case 1 (Fig. 6.10 a). Consequently, the transient increase in Case 2 and the prolonged moderate heating in Case 1 converge toward similar mean values. In both cases, as expected, thermal energy deposition peaks at $y \approx 1.5$ Mm, corresponding to the mid-chromospheric layer. Although the time–distance plots reveal that the instantaneous heating patterns differ due to the presence or absence of Alfvén waves, the time-averaged profile suggests that chromospheric heating is inevitable when waves propagate through neutral-rich layers, regardless of the field orientation. In other words, the geometry of the magnetic field here influences the temporal characteristics of energy release but does not significantly alter the location of peak heating. These results confirm that collisional heating peaks in the middle of the chromosphere, regardless of the wave excitation mechanism or magnetic field configuration.

6.3 Granulation-generated waves in two-fluid plasma

6.3.1 Objectives

The primary objective of this study is to investigate waves generated by solar granulation, with a focus on how ion–neutral collisions damp these waves and their potential role in heating the upper solar chromosphere and associated plasma outflows (Murawski et al., 2022). This research contributes to the broader effort to understand chromospheric heating mechanisms and plasma outflows, with an emphasis on waves driven by the process of solar granulation.

6.3.2 Governing equation of the two-fluid numerical model

The numerical model adopted in this study builds upon the frameworks described in Sec. 6.2.2, with the inclusion of additional physical effects in the momentum and energy equations. The momentum equations are extended to include the viscous (stress-tensor) force, represented by the divergence of the stress tensor $\nabla \cdot \mathbf{\Pi}_s$, where s denotes the plasma species. As a result, the momentum equations (Eqs. 6.3 & 6.4) are modified to

$$\frac{\partial(\varrho_i \mathbf{V}_i)}{\partial t} + \nabla \cdot (\varrho_i \mathbf{V}_i \mathbf{V}_i + p_{ie}\mathbf{I}) = \varrho_i \mathbf{g} + \frac{1}{\mu}(\nabla \times \mathbf{B}) \times \mathbf{B} + \nabla \cdot \mathbf{\Pi}_i + \mathbf{S}_i \tag{6.22}$$

$$\frac{\partial(\varrho_n \mathbf{V}_n)}{\partial t} + \nabla \cdot (\varrho_n \mathbf{V}_n \mathbf{V}_n + p_n\mathbf{I}) = \varrho_n \mathbf{g} + \nabla \cdot \mathbf{\Pi}_n + \mathbf{S}_n \tag{6.23}$$

Here, $\mathbf{\Pi}_{i,n}$ denotes the viscosity tensor (Leake et al., 2012). The energy equation is also extended to consider relevant physical processes occurring in the solar atmosphere. This includes the resistive (Ohmic) energy-flux divergence, given by $\nabla \cdot \left[\frac{\eta}{\mu}(\nabla \times \mathbf{B}) \times \mathbf{B}\right]$; the divergence of viscous heating flux $\nabla \cdot (\mathbf{V}_i \Pi_i)$; the thermal conduction term q_s for species s, modeled according to Spitzer (1962); and radiative losses L_r, approximated using thick radiation for the lower layers of the solar atmosphere (Abbett et al., 2012), while thin radiation is applied to the upper layers (Moore et al., 1972). The modified energy equation incorporating these terms is expressed as

$$\frac{\partial E_i}{\partial t} + \nabla \cdot \left[\left(E_i + p_{ie} + \frac{\mathbf{B}^2}{2\mu}\right)\mathbf{V}_i - \frac{\mathbf{B}}{\mu}(\mathbf{V}_i \cdot \mathbf{B})\right] + \nabla \cdot \left[\frac{\eta}{\mu}(\nabla \times \mathbf{B}) \times \mathbf{B}\right] = (\varrho_i \mathbf{g} + \mathbf{S}_i) \cdot \mathbf{V}_i + Q_i + \nabla \cdot (\mathbf{V}_i \cdot \Pi_i) + q_i - L_r \tag{6.24}$$

$$\frac{\partial E_n}{\partial t} + \nabla \cdot [(E_n + p_n)\mathbf{V}_n)] = (\varrho_n \mathbf{g} + \mathbf{S}_n) \cdot \mathbf{V}_n + Q_n + \nabla \cdot (\mathbf{V}_n \cdot \Pi_n) + q_n - L_n \tag{6.25}$$

Here, η denotes the coefficient of magnetic resistivity. All other equations in the current model are identical to those discussed in Sec. 6.2.2.

6.3.3 Numerical setup and adopted magnetic field configuration

To examine the propagation of granulation-driven waves, their dissipation, and associated heating in the gravitationally stratified and partially ionized solar atmosphere (Ballester et al., 2018), we adopt the same initial settings of the magnetohydrostatic equilibrium as detailed in Sec. 6.2.3, as well as the same numerical scheme employed in the code JOANNA (Sec. 6.2.6). In the present model, however, we implement a modified computational box to incorporate a convectively unstable region located just below the photosphere in the simulation. The 2-D computational box spans -10.24 Mm $\leq x \leq 10.24$ Mm and -3 Mm $\leq y \leq 20$ Mm. Along the horizontal direction, the grid is divided evenly into 1024 numerical cells, with each cell having a size of $\Delta x = 20$ km. Vertically, the region between -3 Mm $\leq y \leq 7.24$ Mm is uniformly divided into 512 cells, resulting in each cell having a size of $\Delta y = 20$ km, while the upper portion of the domain (7.25 Mm $\leq y \leq$ 20 Mm) is covered with 32 vertically stretched cells to capture the large coronal dynamics.

This computational box ensures that the region of interest has a spatial resolution of 20 km $\times$ 20 km. At $t = 0$ s, all plasma quantities are set to their equilibrium values at the top and bottom boundaries, while periodic boundary conditions are applied at the lateral sides. Physically, this setup differs from the impulsively generated waves case, where a small, high-resolution box is intended to follow the initial impulsive pulse and its subsequent wavefront. Here, a larger computational box accommodates the convection zone below the photosphere ($y < 0$) and a broader horizontal span to allow multiple granules to form and self-organize. Additionally, in the impulsive case, the perturbation typically originates at the photosphere ($y = 0$ Mm) and extends into the solar corona (up to 40 Mm) to follow upward-propagating waves. The inclusion of a convection zone in the present model necessitates that the vertical domain begin at $y = -3$ Mm. This allows convection to self-organize into granules, which then naturally excite waves into the photosphere and chromosphere. The total duration of the numerical simulation is 10^4 s.

The initial magnetohydrostatic equilibrium is overlaid by the following potential magnetic configuration forming closed loops, which at $t = 0$ resembles an arcade (Low, 1985). This curved structure of magnetic topology connects two regions of opposite polarity in the quiet region of the solar surface (Fig. 6.11 a) defined as

$$B_x = B_a \cos\left(\frac{x}{\Lambda_B}\right) \exp\left(-\frac{y}{\Lambda_B}\right) \tag{6.26}$$

$$B_y = -B_a \sin\left(\frac{x}{\Lambda_B}\right) \exp\left(-\frac{y}{\Lambda_B}\right) \tag{6.27}$$

$$B_z = B_t \tag{6.28}$$

Here, $B_a = 4$ Gs denotes the spatially averaged magnetic field strength of the arcade structure at the solar surface ($y = 0$). This value is characteristic of the diffuse fields commonly observed in the quiet Sun's chromosphere or low corona, where small-scale flux emerges from granules and merges. Although photospheric fields in the intergranular lanes can reach $10^3 \sim 10^4$ G in local regions, such strong fields are commonly concentrated in flux tubes on sub-arcsecond spatial scales. As these fields fan out into the upper atmosphere, the average field strength over a typical granule (≈ 1 Mm) drops to just a few gauss. Thus, the field value adopted in the present model appropriately reflects the average magnetic flux per unit area (Mx/cm^2). The current model concentrates on the quiet region of the solar atmosphere and does not capture the highly localized and intense magnetic fields at granular scales. Therefore, the adopted values here are consistent with commonly observed phenomena in the quiet Sun.

The transversal component of the magnetic field is specified as $B_t = 2$ G following (Yang et al., 2020), and the magnetic scale height is defined as $\Lambda_B = 2L/\pi$, where $L = 5.12$ Mm is the half-width of the magnetic arcade. The arcade is initially rooted in the dense convective zone with its footpoints set at $x = -5.12$ Mm and $x = 5.12$ Mm, spreading into the photosphere, chromosphere, and lower corona. Notably, the adopted magnetic arcade is analytically simple, making it a suitable starting point for studies on wave propagation and energy transfer in a magnetic arcade. All other aspects of the numerical setup remain unchanged from those detailed in Sec. 6.2.6.

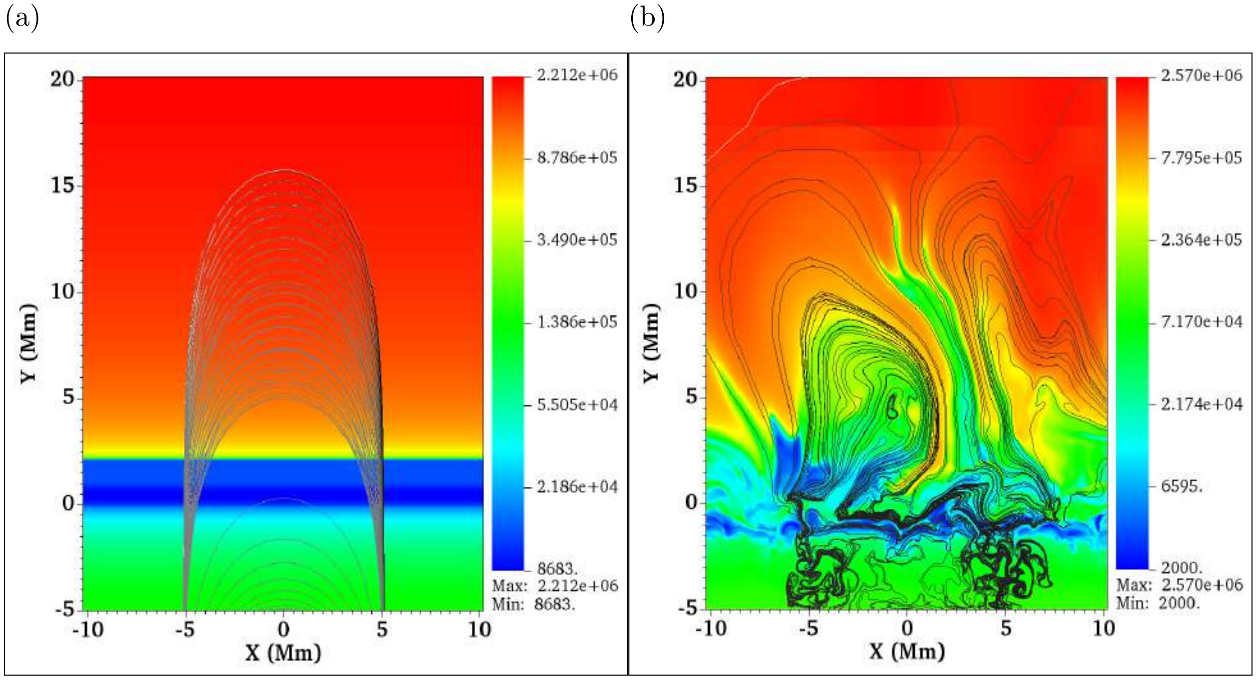

Figure 6.11: The spatial profiles of $\log T_i$ at two distinct time points: (a) the initial state at $t = 0$ s and (b) the evolved state at $t = 8870$ s. Panel (a) shows the unperturbed magnetic arcade, while panel (b) shows the perturbed magnetic arcade.

6.3.4 Numerical results

Heating of the solar chromosphere

The process of solar granulation dynamically alters the initially set magnetohydrostatic equilibrium. Figure 6.11 shows spatial profiles (color maps) of ion temperature $\log T_i$ (in K) at $t = 0$ s (a) and $t = 8870$ s (b). The latter time was chosen to capture the fully developed state of both granulation and magnetic loops, providing insight into both hot and cool plasma and their corresponding temperature distributions across the adopted spatial domain. At $t = 0$ (panel a), the temperature spatial profile overlaid with the unperturbed magnetic arcade (Eqs. 6.28 - 6.30), rooted at $x = \pm 5.12$ Mm, exhibits a smooth, symmetric structure. The temperature ranges from approximately 8,683 K in the cooler chromospheric regions to an expected peak value of 2.21 MK at transition-region/coronal heights. As the simulation evolves, granulation injects mechanical energy into the system via turbulent photospheric motion, exciting a broad spectrum of MHD waves, including MAWs, neutral acoustic-gravity waves, p-modes, Alfvén waves, etc., all driven by convective instabilities (Leighton, 1963; Roth et al., 2010; Murawski et al., 2013; Kwak et al., 2020). Over time, these excited waves propagate, disrupt the initial equilibrium, and transform the initial symmetrical temperature structure into a more complex and asymmetric one. This behavior suggests localized heating and reveals wave-driven dynamic perturbations. Figure 6.11 (panel b) shows the evolved state, with the peak temperature increasing to 2.57 MK, indicating a 16.2 % rise from the initial peak temperature (2.21 MK). The minimum temperature drops to 2000 K, indicating enhanced thermal contrast in the spatial domain.

Granular flows at the base of the magnetized solar atmosphere buffet the plasma, inducing a substantial reconfiguration of the initial magnetic arcade. This results in the formation of small flux tubes and the reshuffling of magnetic field lines (represented by the black lines). The distorted magnetic field arcade is visibly filled with hot and low-density plasma. This distortion in the arcade plays a crucial role in channeling wave energy along the field lines, thereby concentrating heating in localized regions, particularly near $x \approx 5$ Mm (closer to the loop apexes). In these regions, thermal pressure gradients increase along an extended vertical magnetic funnel, driving plasma outflows upward. These plasma outflows are evident from the one-to-one correspondence with the ion vertical component V_{iy} (Fig. 6.15). Some downflows are also observed, driven by the gravitational force (indicated by blue patches). We will discuss the plasma outflows and downflows in detail in a later section. Nevertheless, the two-fluid waves accompany these upflows and downflows: dense plasma is typically associated with upward-propagating compression, whereas rarefied plasma accompanies downward flows. These excited waves rise through the photosphere and chromosphere, ultimately penetrating the solar corona. In addition to these large-scale dynamics, several spatial features, such as jets, can also be observed. The tallest of these jets reaches approximately $y \approx 15$ Mm. To the right, a narrower jet appears, while on the left side of the domain, a shorter jet is observed to be slightly tilted to the left. A recent paper by Skirvin et al. (2023) offers a comprehensive study of jets and their generation in the lower solar atmosphere. Earlier studies by James et al. (2002), James et al. (2003), and Erdélyi et al. (2004) addressed small-scale solar jets and their formation mechanisms. Notably, these distinctive flow and jet properties primarily stem from the convectively unstable zone below the photosphere ($y \leq 0$, Fig. 6.11 b, Fig. 6.15). This region plays a vital role in driving the dynamic behavior throughout the solar atmosphere.

The primary mode of interaction between the plasma species in this model is ion-neutral collisions. As previously discussed, these collisions predominantly affect the motion of ions constrained by the magnetic field and contribute to the heating of the chromosphere and corona. Figure 6.12 displays the snapshot of the spatial profile for the ion-neutral drift $V_i - V_n$ (in units of km s^{-1}, panel a) alongside the corresponding spatial distribution of the heating rate Q_i (panel b) in $\mathrm{erg\,cm^{-2}\,s^{-1}}$, calculated by the first term on the RHS of Eq. 6.10 at $t = 8870\,\mathrm{s}$. The spatial profile of $V_i - V_n$ reveals regions of strong decoupling between charged and neutral particles, where their motion diverges due to differing governing forces: magnetic tension for the ions and pressure gradients for the neutrals. These differential motions manifest as narrow lanes of high drift near $x \approx 0, y \approx 5 - 10$ Mm, aligning with magnetic null points

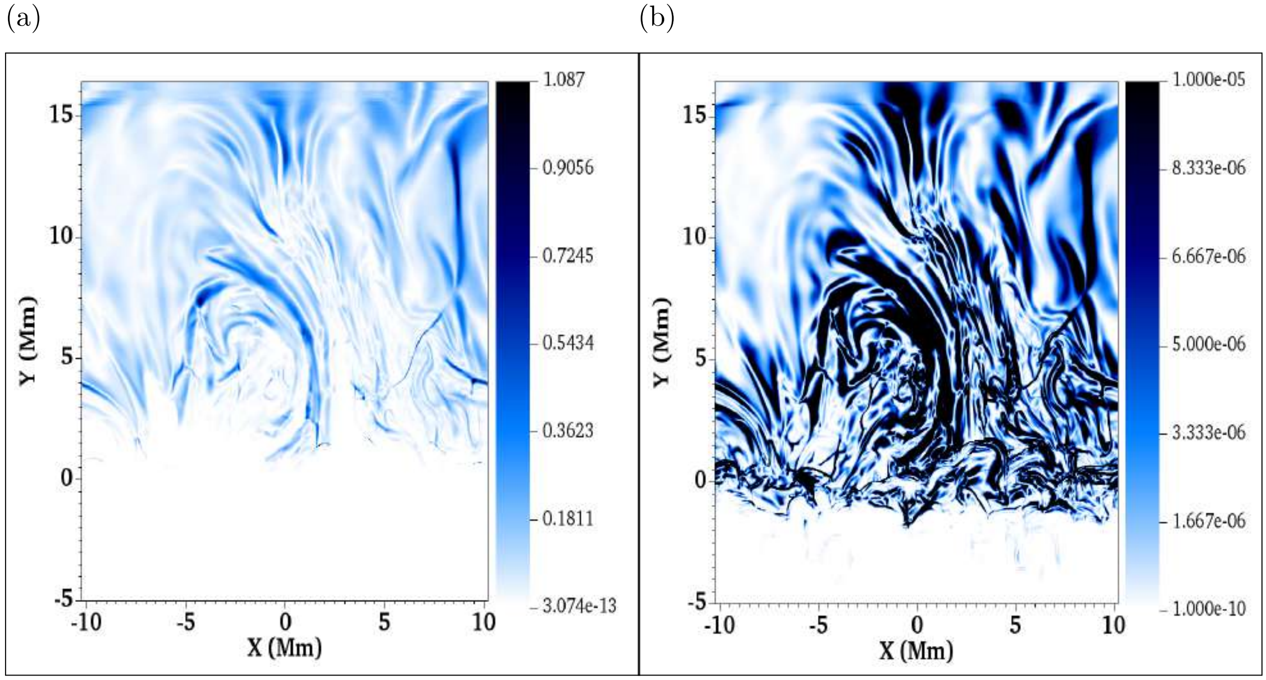

Figure 6.12: (a) The spatial profile of $V_i - V_n$ measured in units of $\mathrm{km\,s^{-1}}$ at $t = 8870\,\mathrm{s}$. This profile provides an insightful visualization of the velocity drift across the simulation domain. (b) Snapshot of the spatial profile of the energy flux Q_i, measured in $\mathrm{erg\,cm^{-2}\,s^{-1}}$, at $t = 8870\,\mathrm{s}$. Both profiles exhibit a one-to-one correspondence to some extent, suggesting that the motion of plasma and the energy transport in our model are closely tied to the relative motion between the ions and the neutrals.

or arcade apexes where field-line curvature maximizes velocity shear. These localized shear zones are driven by waves excited by granulation.

The spatial profile of Q_i quantifies frictional dissipation due to ion-neutral collisions. This heating is localized and peaks in the same region where $|V_i - V_n|$ is highest, confirming the relationship $Q_i \propto (V_i - V_n)^2$. In other words, these heating hot spots are the primary contributors to the observed rise in chromospheric temperature. Furthermore, the observed asymmetric distribution of Q_i generates pressure gradients that accelerate ions along field lines, resulting in the observed plasma outflows (Fig. 6.15). Martínez-Sykora et al. (2020) conducted a detailed study on the role of wave-induced energy dispersion and its conversion into thermal energy in the partially ionized solar atmosphere.

In our model, the system undergoes an initial transient phase lasting approximately 3000 s, after which it evolves into a quasi-stable state that persists until the final simulation time, $max(t) = 10^4$ s. During this quasi-stable phase, the transition region, initially located at $y \approx 2.1$, undergoes periodic vertical displacement, leading to oscillatory movements around its original position. These oscillations arise from the imbalance between induced wave heating and rapid radiative cooling. The upward motion of the transition region is caused by pressure

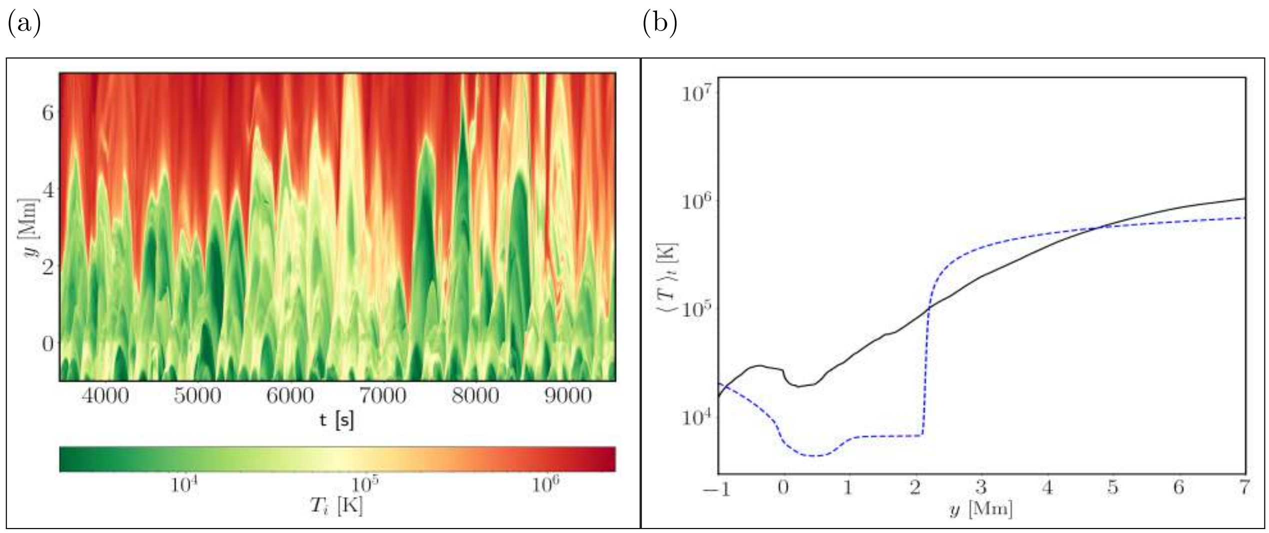

Figure 6.13: (a)Time–distance plots for the temperature of the ions T_i, measured in kelvins. This plot is evaluated from the slit collected along the y-direction at $x = 0$ Mm, corresponding to Fig. 6.11. (b) The corresponding time-averaged profile for T_i (solid black) and equilibrium temperature T (dashed blue), adopted from the model of Avrett et al. (2008a), initially set equal for ions and neutrals (Fig. 6.1 a).

accumulation during localized heating events, while the downward movement occurs with subsequent cooling. The time-distance plot for T_i (Fig. 6.13 a), collected along the y-axis at $x = 0$, displays these oscillations. The chosen time interval in this plot highlights only the quasi-stable state, characterized by fully developed convection and continuous wave activity, which follows the initial transient period (not shown here). Figure 6.13 (panel b) presents the corresponding time-averaged vertical profile of T_i (black solid) from our simulation, compared against the initial equilibrium temperature T_i following Avrett et al. (2008a). The simulation profile reveals a clear departure from the initial equilibrium model temperature, highlighting ion-neutral decoupling as the key mechanism of chromospheric and coronal heating, thus validating the two-fluid framework.

Figure 6.14 (a) shows the time-distance plot of the relative ion temperature perturbation, presenting a more precise visualization of the deviation of the ion temperature from the background temperature profile $T(y)$ (Fig. 6.1 a) across different layers of the solar atmosphere. The relative ion temperature perturbation is defined as

$$\frac{\delta T_i(y,t)}{T(y)} = \frac{T_i(y,t) - T(y)}{T(y)} \tag{6.29}$$

The key feature of this profile is inclined streaks, which represent upward-propagating waves. As these waves rise, they steepen into shocks. Notably, the perturbations become more prominent for $t > 5000$ s, indicating resonant wave trapping in the magnetic arcade. Figure

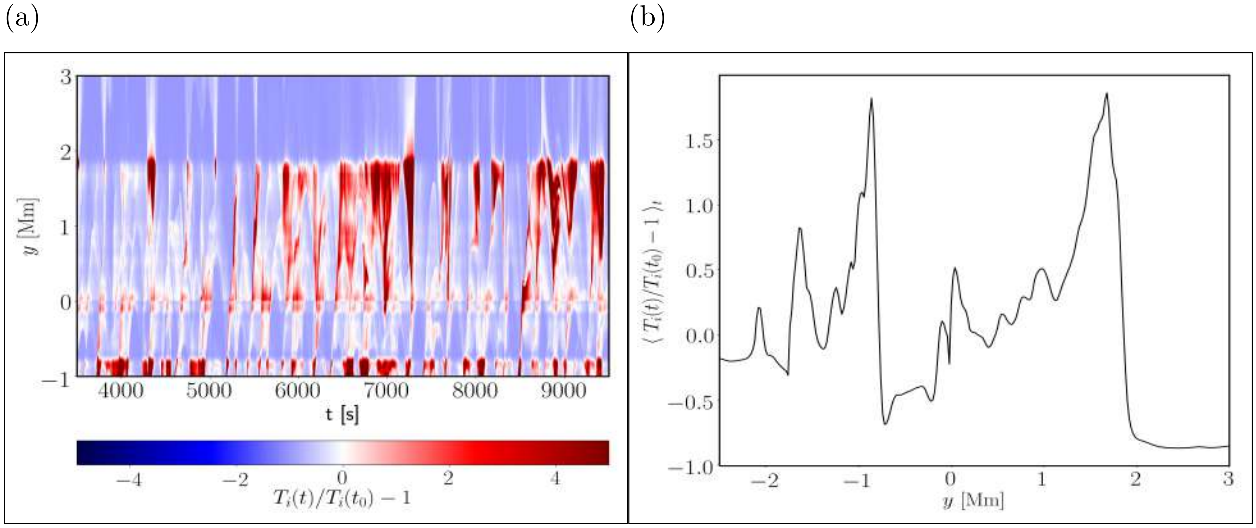

Figure 6.14: (a)Time–distance plots for the relative ion temperature perturbation $<\delta T_i(x = 0, y, t)/T(y)>_t$, calculated as the deviation of $T_i(x = 0, y, t)$ from the model temperature $T(y)$ adopted from Avrett et al. (2008b) (Fig. 6.1 a). (b) The corresponding time-averaged profile displaying its overall variation with height.

6.14 (b) displays the corresponding time-averaged vertical profile of $\delta T_\mathrm{i}(y, t)/T(y)$, given by

$$\left\langle \frac{\delta T_i(y,t)}{T(y)} \right\rangle_t = \frac{1}{t_2 - t_1} \int_{t_1}^{t_2} \frac{\delta T_i(y,t)}{T(y)}\, dt \tag{6.30}$$

with $t_1 = 3500$ s and $t_2 = 9500$ s. This profile quantifies net heating or cooling relative to the equilibrium model temperature $T(y)$ (Avrett et al., 2008a). The plot reveals localized peaks, particularly intense vertical bands near $y \approx 1.5$ Mm, indicating standing waves formed due to wave reflection at the steep density gradient of the transition region. This peak is followed by a sharp drop, suggesting rapid cooling or the spatial spreading of the localized thermal energy. Together with the results obtained in Figs. 6.13 & 6.14, we infer that the presence of significant localized variation in ion temperature provides evidence of a wave-driven heating process in the upper photosphere and chromosphere.

Plasma outflows

The ongoing process of solar granulation propels cooler plasma from beneath the photosphere upward into the transition region and lower solar corona, potentially contributing to plasma outflow. Figure 6.15 shows the snapshot of the spatial distribution of the vertical component of ion velocity, V_{iy}, measured in units of km s^{-1} at $t = 8870$ s, capturing the dynamical response to granulation across various layers of the solar atmosphere. This distribution highlights the presence of bidirectional jets generated by wave dissipation in the magnetic arcade. Plasma upflow velocities reaching approximately 40 km s^{-1} originate from thermal expansion in heated

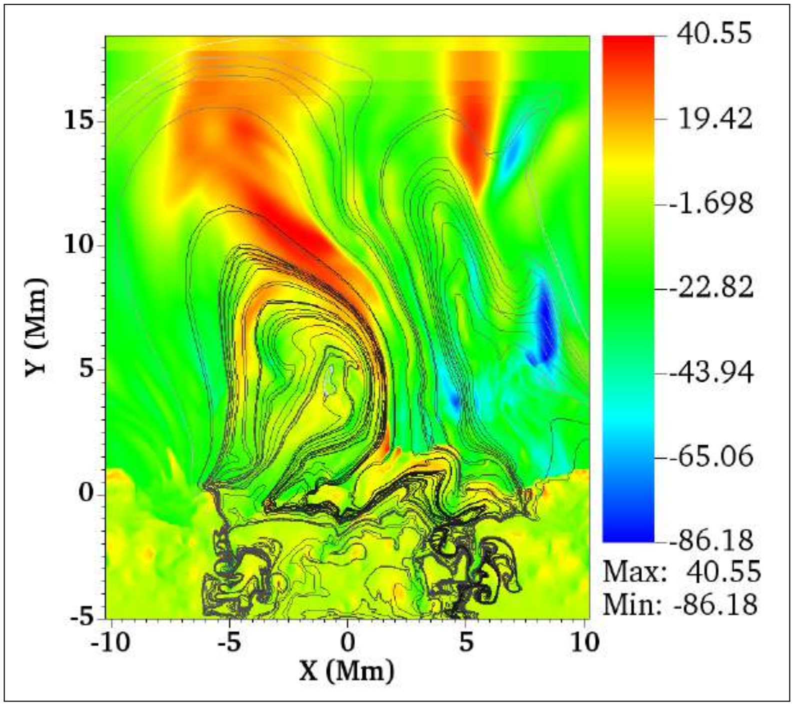

Figure 6.15: Snapshot of the spatial profile of the vertical component of ion velocity V_{iy}, measured in $\mathrm{km\,s^{-1}}$, at $t = 8870$ s. This profile provides an insightful visualization of ion motion, highlighting regions of ascent (red patches) and descent (blue patches) in the solar atmosphere.

regions that coincide with localized temperature rises (hot spots in T_i). On the other hand, downflow velocities reaching up to $-86\,\mathrm{km\,s^{-1}}$, visible as narrow blue patches, arise from gravitational forces and radiative cooling regions. Moreover, due to the low resistivity in the lower corona, a considerable amount of plasma remains confined along the distorted and elongated magnetic field lines. This plasma localization leads to upflow/downflow lanes, particularly near $x \approx 0$ and $y \approx 5 - 10\,\mathrm{Mm}$, where the interplay between wave-induced forces and magnetic geometry is most pronounced. These upflows may escape and ultimately lead to plasma outflows into higher layers of the solar atmosphere. While such plasma outflows are often associated with open magnetic field lines (Murawski et al., 2022), their presence in this model may initially appear contradictory. The results here suggest that plasma outflow may still occur even with a closed magnetic field, especially when the magnetic field is highly curved and dynamically evolving. The upward-curving magnetic field lines guide and accelerate ions, enabling outflows even in topologically closed regions. Additionally, in the lower coronal region, the condition $\beta \ll 1$ suggests that the magnetic field effectively governs plasma motion.

As the waves are excited and propagate into the upper layers of the solar atmosphere, they induce oscillatory motions in the plasma, resulting in periodic variations in ion velocity. Figure 6.16 (panel a) shows the time-distance plot for V_{iy} collected along the y-axis at $x = 0$,

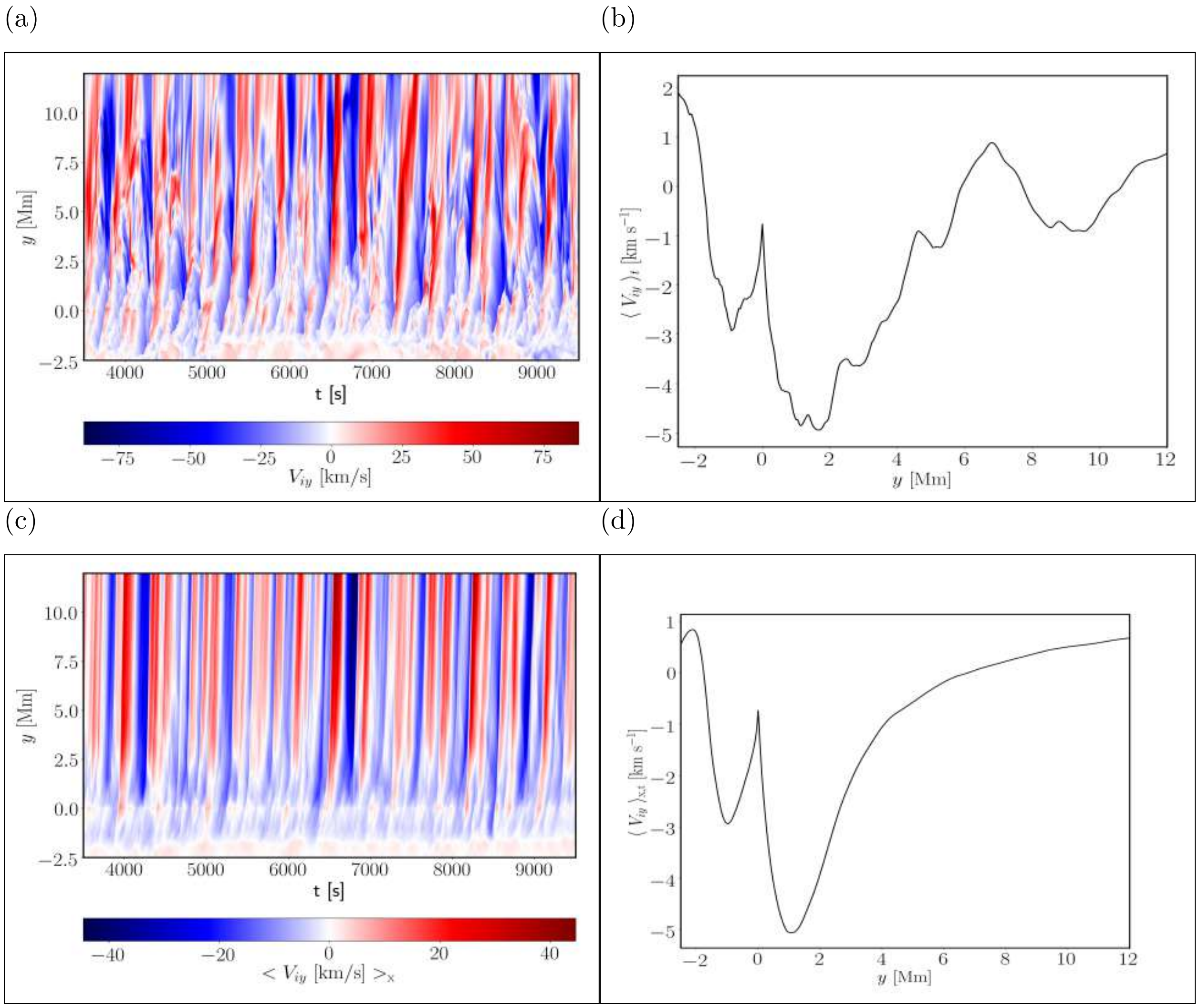

Figure 6.16: The time-distance plot for the vertical component of the ion velocity V_{iy}, measured in units of $\mathrm{km\,s^{-1}}$ (a, c), and its corresponding time-averaged profile (b, d). The upper panels are collected along y at $x = 0$, whereas the lower panels provide their spatial average. These profiles together show the temporal–spatial evolution of V_{iy}.

revealing quasi-periodic red and blue bands. Overall, these patterns reflect a continuous train of upward-propagating waves, manifesting as periodic oscillations in the solar atmosphere. Figure 6.16 (panel c) illustrates the horizontally averaged plot $\langle V_{iy} \rangle_x$, given by

$$\langle V_{iy} \rangle_x = \frac{1}{x_2 - x_1} \int_{x_1}^{x_2} V_{iy} \, dx \tag{6.31}$$

with $x_2 = -x_1 = 10.24$ Mm. The profile shows a quasi-periodic pattern of alternating red and blue bands, similar to the one observed in panel (a), confirming that the granulation-excited waves are not just confined to an isolated flux tube but coherently affect the entire magnetic arcade. These waves induce motions that capture the self-regulating mass-energy cycle in the magnetic arcade, where upward-propagating waves steepen into shocks, heating ions via ion-neutral collisions. The key observations include the inclined streaks and diagonal patterns that trace an upward-propagating wavefront. Additionally, the observed dark streaks near $y = 5\,\mathrm{Mm}$, $t = 7000\,\mathrm{s}$ indicate nonlinear wave steepening and the formation of shocks. Notably, the horizontal averaging here smooths out the lateral variations in V_{iy}, leading to sharper bands compared to those observed in panel (a).

Plasma outflows may serve as a potential source of the solar wind (Wójcik et al., 2019). Figure 6.16 displays the time-averaged profile for V_{iy}, denoted as $\langle V_{iy}\rangle_t$ (panel b). The horizontal time-averaged profile, denoted as $\langle V_{iy}\rangle_{x,t}$ (panel d), is defined in the same way as in Eq. 6.19. Both panels exhibit similar overall trends; however, panel (d) shows a smoother, more gradual profile with height due to additional horizontal averaging. Physically, two mechanisms contribute to the observed plasma outflow in our simulation: (i) wave-driven pressure/momentum transfer, where upward-propagating waves carry momentum that can impart a net upward push to the plasma; and (ii) thermal expansion—as wave dissipation heats the upper chromosphere, the local pressure increases, leading to bulk plasma outflow. In both profiles, downflows outweigh upflows for $y < 0$, owing to radiative cooling, which dominates post-heating phases and contributes to refilling the chromospheric mass. In contrast, for $y > 2.1$ Mm, there is a noticeable shift from downflow to upflow, indicating the emergence of plasma outflows in the upper solar atmosphere. Moreover, the presence of a magnetic arcade, as opposed to simple straight magnetic field lines (Murawski et al., 2022), can partially accommodate plasma, thereby limiting plasma outflows to some degree. However, as argued earlier, plasma can still escape at higher heights through field-guided outflows even with such a closed magnetic field setup.

In summary, both profiles demonstrate that while the chromospheric plasma undergoes oscillatory motion, it also exhibits a slight net upward drift at coronal heights. This finding offers crucial insight into wave-driven mass transport in the solar atmosphere. Such plasma outflows are important, as they can feed into the solar wind and ultimately alter its characteristics in the upper regions of the solar atmosphere. Recently, Tian et al. (2021) provided a detailed overview of plasma outflows in the solar atmosphere.

Two-fluid effects: ion-neutral drift and wave period in the solar atmosphere

Ion-neutral drift refers to the velocity difference between charged particles (ions) and neutral particles, and it becomes particularly significant in partially ionized plasma, where neutral particles cannot be ignored. Such drifts play a crucial role in the transfer of momentum and energy in the solar atmosphere. Figure 6.17 (panel a) displays the time–distance plot for ion-neutral drift of the vertical velocity component given as $V_{iy} - V_{ny} = \delta V$. The plot highlights the key regions of interest, particularly above the photosphere, where quasi-periodic signatures

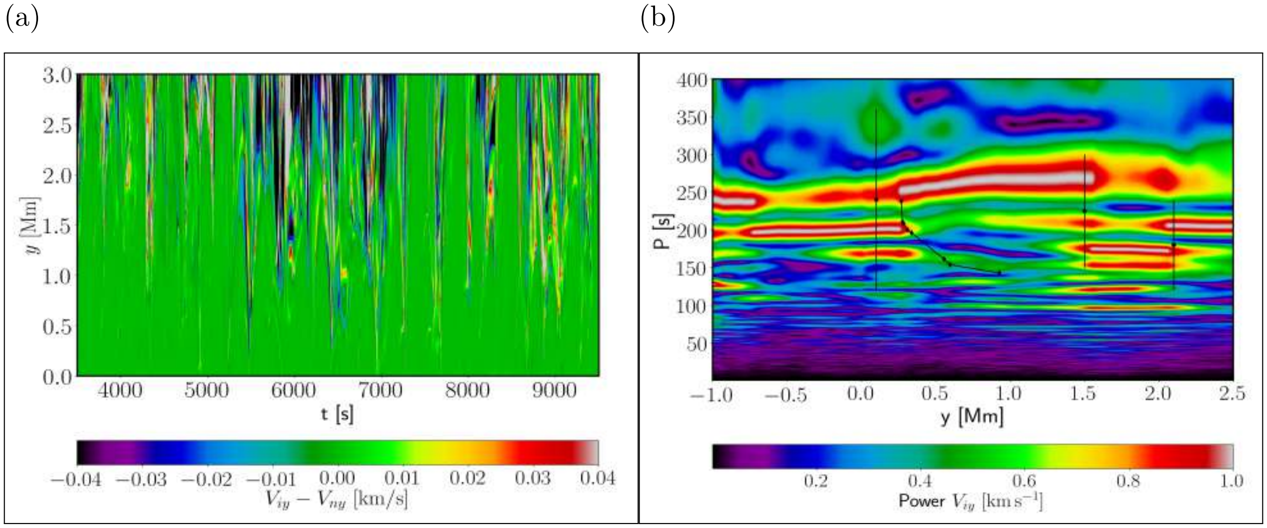

Figure 6.17: (a) Time-distance plot for $V_{iy} - V_{ny}$, measured in $\mathrm{km\,s^{-1}}$, collected at $x = 0$ along the y-axis. The plot highlights the regions of increased velocity drift. (b) Variation of wave periods (P) with height (y). The minimum and maximum Fourier power amplitudes are normalized to 0 and 1, respectively.

(seen as oblique stripes) propagate from the lower to upper chromosphere. It is apparent from the profile in the lower photosphere that the drift is nearly zero, indicating strong collisional coupling; however, at greater heights, the drift amplitude grows substantially. This growth indicates partial decoupling between constituent species, driven by the decrease in both the mass density and collision frequency in the chromosphere.

As a result of partial ionization, ions and neutrals respond differently to wave propagation, where each upward-propagating wave packet produces an increasing ion–neutral velocity drift with height. The peak magnitude 0.04 km s^{-1} (red/yellow regions) is observed in the upper chromosphere, transition region, and lower corona. These regions coincide with those where waves steepen and a differential response occurs between the fluid components, where either ions or neutrals begin to lag behind the other. Notably, these observed ion-neutral drifts are directly tied to collisional heating at a rate proportional to $\alpha_{in}|\delta V|^2$ (Eq. 6.10 & 6.11). Accordingly, the regions exhibiting relatively large ion-neutral drift correspond to regions of enhanced wave energy dissipation via ion-neutral collisions. In particular, the peak drifts appear in the range $y \sim 1-3$ Mm, consistent with earlier studies reporting maximal collisional heating in the middle chromosphere (Pelekhata et al., 2021). Furthermore, in our model, the magnitude of the ion-neutral drift is significantly lower than that reported by Murawski et al. (2022) (see Fig. 3). This discrepancy is attributed to differences in the magnetic field geometry and physical assumptions. In Murawski et al. (2022), the presence of simpler vertical-field geometry and a dynamic ionization and recombination process allows ideal conditions for ions to decouple from neutrals. In contrast, our model employs a curved-arcade field without ionization/recombination terms, resulting in stronger coupling between ions and neutrals; consequently, the peak ion–neutral velocity drift is smaller. Additionally, the absence of sharp discontinuities and the presence of smooth drift envelopes indicate that no shock formation occurs here. This behavior is consistent with recent two-fluid models presented by Wójcik et al. (2020), where the authors reported that granulation-driven waves can heat the chromosphere without shock formation, as wave energy is gradually dissipated through ion-neutral friction. Similarly, Niedziela et al. (2021) showed in impulsive MAWs simulations that the ion–neutral drift grows with height and acts as the leading heating mechanism.

In summary, the profile in Fig. 6.17 shows a gradual, height-dependent increase rather than a shock front. This trend highlights heating scenarios generated by continuous wave spectra in places with large δV, resulting in increased collisional heating. This finding broadens the standard understanding of shock-dominated heating to include more subtle but persistent wave-driven mechanisms in the partially ionized solar atmosphere.

The stratified nature of the solar atmosphere affects wave propagation and associated wave heating (Lamb, 1917; Biermann, 1946; Schwarzschild, 1948). It is essential to acknowledge that the spectrum of such excited waves is broad and complex, making it challenging to isolate and visualize each mode individually. Figure 6.17 (b) shows the contour plot of wave periods (P) vs. height (y) obtained from the Fourier transformation of the ion-vertical velocity signal V_{iy} (Fig. 6.15). This Fourier spectrum identifies the dominant wave periods that carry power across the solar atmosphere.

In the lower atmosphere (photosphere), a wide range of periods, typically $300 - 600$ s, are excited by convective motion. However, as the waves propagate upward, the spectrum narrows. In the chromosphere, a more confined band of wave periods becomes dominant. In particular, a strong power band is observed near the acoustic cutoff of $200 - 250$ s at lower chromospheric heights. For $y > 2$ Mm, the dominant power shifts toward shorter periods around $150 - 180$ s. This trend reflects the well-known acoustic cutoff effect, where only waves with a period below the cutoff value ($P < P_{\mathrm{cut-off}}$) can propagate, while longer-period waves become evanescent. Furthermore, the adopted magnetic field geometry also influences this filtering. In a region where the field is nearly horizontal (above the arcade core), the acoustic cutoff period is relatively large (~ 230 s), allowing longer wave periods ($180 - 240$ s) to propagate up to ~ 2 Mm. As the magnetic field line bends upward, the cutoff wave period decreases, and waves with shorter periods $\sim 120 - 180$ s begin to dominate in the upper regions. In other words, the trend suggests that the dominant period tends to decrease with height. This finding is in good agreement with earlier two-fluid numerical simulation results by Kuźma et al. (2021), where the authors reported that granulation-driven MAWs shift their main 5-minute period to shorter periods ~ 220 s in the chromosphere, with only shorter periods able to penetrate the transition region. Similarly, Kuźma et al. (2024)

confirmed comparable findings of wave period filtering in their recent numerical simulations of granulation-excited waves.

The variation of wave periods with height also provides insight into their influence on the plasma. Notably, shorter-period (higher-frequency) waves generally dissipate energy more rapidly through collisions and can reach higher altitudes, whereas long-period waves tend to be filtered out. For example, the $180-240$ s wave period dominates at lower chromospheric heights. As they propagate upward, their amplitude is diminished by friction and cutoff, transferring energy to shorter-period modes higher up. In other words, the period–height plots highlight which waves survive and where they can heat the plasma. The observed shift to $\sim 120-180$ s periods in the upper chromosphere implies that high-frequency components of the convective spectrum are responsible for heating the upper layers. The obtained distribution of wave periods also moderately aligns with observational data from Wiśniewska et al. (2016) and Kayshap et al. (2018), denoted respectively by diamonds and dots. The vertical error bars for the dots show the range of periods identified by these observations at three different heights. This alignment of P with observational data suggests that the two-fluid equations in the present model can explain the numerically obtained wave periods resulting from solar granulation.

To conclude, the two panels in Fig. 6.17 collectively show that convective instabilities excite a wide range of waves; however, only those with sufficiently short periods may survive into the upper chromosphere.

6.4 Summary

This chapter presents the numerical results on local chromospheric heating and associated plasma outflows. We employed a two-fluid MHD model consisting of a separate set of equations for charged species (ions + electrons) and neutral hydrogen, for a stratified solar atmosphere. These equations are solved using the JOANNA numerical code (Sec. 5.9). Our investigation focuses on wave-driven heating in the partly ionized chromosphere, yielding a consistent conclusion: ion–neutral collisions serve as the primary dissipation mechanism that converts a portion of the wave energy into thermal energy and drives associated plasma outflows. The performed 2.5-D numerical simulation tracks the excited wave propagation, revealing that as the waves propagate into the middle and upper chromosphere, collisional interactions between ions and neutrals lead to wave energy dissipation and localized heating.

In the first part of the study (Sec. 6.2), we explicitly identify fast/slow MAWs and Alfvénic waves in the solar atmosphere. A localized Gaussian pulse is launched (at $t = 0$ s) in the horizontal components of ion and neutral velocities at the top of the photosphere, causing the impulsive excitation of waves in a two-fluid plasma. We examine two scenarios of transverse magnetic fields: $B_z = 0$ Gs, supporting only MAWs, and $B_z = 2$ Gs, allowing the excitation of linearly coupled Alfvén-MAWs. The obtained results indicate that the coupled Alfvén-MAWs are more effective at chromospheric heating than MAWs alone. However, in both scenarios, ion–neutral collisions are modeled as the only wave energy dissipation mechanism, which does not yield adequate heating to match chromospheric radiative losses, as estimated by Withbroe et al. (1977). Similarly, the generated plasma outflows, which correspond to mass flux, are comparable in both cases and remain inadequate to offset the mass loss caused by the solar wind.

In the second part of the study (Sec. 6.3), we adopt a more realistic numerical model that incorporates convective dynamics and a 2-D magnetic arcade structure. We again employ the JOANNA code to solve the two-fluid equations for ions + electrons and neutrals coupled by collisions. Unlike in the first part, where waves are excited by the Gaussian pulse, wave excitation here arises from self-consistent solar granulation imposed beneath the photosphere. The convective instabilities naturally excite a spectrum of MHD waves that propagate upward into the chromosphere, where ion–neutral collisions dissipate a portion of the wave energy into thermal energy, leading to localized heating and plasma outflows.

Together, these studies consistently reveal that whether waves are generated by impulsive events or sustained granulation, they can contribute to chromospheric heating via ion–neutral collisions. The results, however, highlight that the obtained heating and mass flux are insufficient to fully counteract observed radiative losses or supply the entire solar wind. Notably, the wave phenomena and heating of the solar atmosphere are much more complex than described in the present study; therefore, more accurate simulations incorporating non-ideal and non-adiabatic effects are essential to improve the accuracy of such studies. Nevertheless, the insights gained from these local two-fluid models lay the foundation for developing a comprehensive global coronal model relevant to space-weather prediction. While the study in this chapter focuses on a local region of the solar atmosphere (the chromosphere and lower corona) and transient wave dynamics, a global model must also account for the steady-state structure of the full corona and the solar wind.

In this context, the results from such a study can provide both conceptual and quantitative support for the essential characteristics required for the development of the COCONUT-MF global coronal model. COCONUT-MF builds upon such localized physics by incorporating multi-fluid plasma dynamics, empirical heating prescriptions, and realistic energy transport mechanisms to simulate the corona under various solar conditions. This seamless transition from local two-fluid physics to a global simulation framework improves the physical realism of space-weather modeling, as discussed in the following and final chapter of this thesis.

Chapter 7

Numerical results: The Global Aspects

7.1 Introduction

Chapter 6 presented localized two-fluid simulations of the partially ionized solar atmosphere, highlighting that ion–neutral collisions can play a crucial role in the exchange of momentum and energy. These simulations confirmed that MHD waves can deposit heat at chromospheric heights and beyond (Soler et al., 2015). Such frictional heating due to ion–neutral drift, along with other heating mechanisms such as magnetic reconnection (DC heating), shock and compressive heating, etc., has emerged as a key mechanism for transporting energy into the chromosphere (Orta et al., 2003). Building on these insights, the current chapter extends the investigation to global aspects of the solar atmosphere by integrating comparable physics into its steady-state equations for momentum and energy. This approach ensures that the solution for large-spatial-scale coronal heating correctly captures the underlying microscale energy exchanges.

As discussed in Sec. 6.1, we recognize that local two-fluid studies typically focus on simulating short-timescale events on the order of seconds to minutes in a limited spatial domain of the solar atmosphere. These simulations capture transient phenomena—for example, an impulsive launch of MHD waves, or a series of shocks passing through a flux tube, followed by their damping and heating of the plasma. The local simulation presented in Chapter 6 suggests how waves propagate, dissipate, and how plasma is accelerated locally in real time. Collectively, these findings indeed support a broader picture in which numerous small-scale, intermittent bursts of energy and mass flux events sustain coronal heating and the solar wind (Sterling et al., 2024; Pontin et al., 2023; Chitta et al., 2023; Chitta et al., 2022).

In contrast, the global COOLFluiD Coronal Unstructured MultiFluid (COCONUT-MF hereafter), adopted in this chapter, is a steady-state solver. As such, it cannot directly capture time-dependent transient phenomena. Moreover, the spatial resolution of global models, with grid cells spanning tens of thousands of kilometers, is far too coarse to resolve fine-scale dynamics such as MHD waves and shocks (Brchnelova et al., 2023). This discrepancy poses a key challenge in solar physics: bridging local simulations to global modeling, particularly when transitioning from small-scale, explicitly time-dependent dynamics to large-scale, assumed steady-state dynamics. To bridge this gap and to achieve a steady state in a global solution, the cumulative impacts of transitory events, as indicated by local simulations, must be taken into account. The notion is that, on average, intermittent injections of energy from numerous small-scale events can collectively contribute to a quasi-continuous background heating and sustained plasma outflow. Accordingly, the global multi-fluid equations (Sec. 7.3) are augmented with source and sink terms that represent the time-averaged influence of a vast number of localized and short-lived events.

In practice, the physics of small-scale dynamics is encoded into the global model using practical terms. For example, collision terms capture momentum and heat transfer from neutral–ion drift (as observed in the local simulation), while heating functions encode energy from wave dissipation and other heating events. This approach enables us to simulate the entire solar corona and solar wind, extending from the upper chromosphere to several solar radii, without explicitly resolving every turbulent eddy or wave train, while remaining faithful to the physical processes recognized at the small scale. Finally, it is essential to establish a connection between the specific mechanisms captured in the small-scale models and the standard empirical terms used in global coronal modeling—notably coronal heating, thermal conduction, and radiative cooling (Sec. 7.3). In most global frameworks, coronal heating is introduced as an adjustable source term, whose form is often motivated by insights from studies of candidate heating mechanisms. Indeed, empirical heating profiles are often crafted to scale with density or magnetic field strength, reflecting assumptions consistent with wave dissipation (Groth et al., 2000; Manchester IV et al., 2004; Hosteaux et al., 2018; Talpeanu et al., 2020; Talpeanu et al., 2022). In the present global COCONUT-MF model, this heating is not arbitrarily imposed. Instead, it is parameterized based on the physical insights gained from localized simulations, thereby providing a more physically grounded approach. The detailed formulation of these terms is elaborated in Sec. 7.3.

Driven by the arguments mentioned above, we aim for an advanced representation of coronal dynamics, emphasizing the significance of the multi-fluid model. The current model extends the polytropic MF-MHD framework introduced by Brchnelova et al. (2023) by incorporating additional source and sink elements into the energy equations, with potential applications for space weather forecasting. To achieve this, we adopt a novel, data-driven 3D global coronal model known as COCONUT (COolfluid COronal uNstrUcTured) (Perri et al., 2022; Perri et al., 2023), developed within the Computational Object-Oriented Libraries for Fluid Dynamics (COOLFluiD) numerical code (Lani et al., 2005). COCONUT is designed to replace conventional semi-empirical models, such as the Wang–Sheeley–Arge (WSA) model (Wang et al., 1990), which are commonly used for operational space weather forecasting. COCONUT has demonstrated its robustness and accuracy through a series of benchmark tests, handling standard dipole and quadrupole configurations as well as realistic magnetograms corresponding to both solar minimum and solar maximum (Kuźma et al., 2023).

7.2 Governing equations of the two-fluid global model

The model treats ions + electrons as a single charged fluid and neutrals as a separate fluid, consistent with the two-fluid formulation presented in Sec. 6.2.2. While Chapter 6 presents the detailed general form of the equations in the regime of MF-MHD, the present subsection provides the exact adopted form of the equations implemented in the COCONUT-MF model.

(a) Continuity equations

$$\frac{\partial n_i}{\partial t} + \nabla \cdot (n_i \mathbf{V}_i) = \Gamma_i^{ion} + \Gamma_i^{rec} \tag{7.1}$$

$$\frac{\partial n_n}{\partial t} + \nabla \cdot (n_n \mathbf{V}_n) = \Gamma_n^{rec} + \Gamma_n^{ion} \tag{7.2}$$

These equations include source and sink terms associated with ionization and recombination processes. Here, the Γ terms denote the rates of ionization and recombination, defined as

$$\Gamma_n^{ion} \equiv -n_n v^{ion}, \qquad \Gamma_i^{rec} \equiv -n_i v^{rec} \tag{7.3}$$

By number conservation, ionization of neutrals produces ions, i.e., $\Gamma_i^{ion} = -\Gamma_n^{ion}$, and recombination of ions produces neutrals, i.e., $\Gamma_n^{rec} = -\Gamma_i^{rec}$. The rate coefficients $v^{ion,rec}$ are given by

$$v^{ion} = n_e \left\{ \frac{2.91 \times 10^{-14}}{0.232 + \phi_{ion}/T_e^*} \right\} \left(\frac{\phi_{ion}}{T_e^*} \right)^{0.39} e^{-\phi_{ion}/T_e^*} \,\mathrm{m^3\,s^{-1}}, \;\; v^{\mathrm{rec}} = 2.6 \times 10^{-19} \frac{n_\mathrm{e}}{\sqrt{T_e^*}} \,\mathrm{m^3\,s^{-1}} \tag{7.4}$$

Here, T_e^* is the electron temperature in units of eV. The ionization potential ϕ_{ion} of hydrogen is 13.6 eV. The exponential factor in v^{ion} and the $T_e^{*\,-1/2}$ dependence in v^{rec} stem from standard plasma rate formulations, explained in Meier et al. (2012b).

(b) Momentum equations

$$\frac{\partial}{\partial t}(m_i n_i \mathbf{V}_i) + \nabla \cdot (m_i n_i \mathbf{V}_i \mathbf{V}_i + \mathbb{P}_i) = q_i n_i (\mathbf{E} + \mathbf{V_i} \times \mathbf{B}) + \mathbf{R}_i^{in} + \mathbf{S}_i^{ion} + \mathbf{S}_i^{ex} + m_i n_i \mathbf{g} \tag{7.5}$$

$$\frac{\partial}{\partial t}(m_n n_n \mathbf{V}_n) + \nabla \cdot (m_n n_n \mathbf{V}_n \mathbf{V}_n + \mathbb{P}_n) = \mathbf{S}_n^{ion} + \mathbf{S}_n^{ex} + m_n n_n \mathbf{g} - \mathbf{R}_n^{in} \tag{7.6}$$

Here, $\mathbf{R}_i^{in}$, $\mathbf{R}_n^{ni}$ denote the collision momentum transfer terms, defined as

$$\mathbf{R}_i^{in} = -\mathbf{R}_n^{ni} = m_{in} n_i v_{in} (\mathbf{V}_n - \mathbf{V}_i) \tag{7.7}$$

with the ion–neutral ν_{in} and neutral–ion ν_{ni} collision frequencies given by

$$\nu_{in} = n_n \Sigma_{in} \sqrt{\frac{8 k_B T_{in}}{\pi m_{in}}}\,, \quad \nu_{ni} = n_n \Sigma_{ni} \sqrt{\frac{8 k_B T_{in}}{\pi m_{ni}}} \tag{7.8}$$

Here, Σ_{ni} and Σ_{in} represent the collisional cross sections, taken here as equal to 1.41×10^{-19} m^2, while $T_{in,ni}$ and $m_{in,ni}$ are respectively the average temperature and mass, defined as

$$T_{in} = T_{ni} = \frac{T_i + T_n}{2}\,, \qquad m_{in} = m_{ni} = \frac{m_i m_n}{m_i + m_n} \tag{7.9}$$

Here, the term $\mathbf{S}_i^{ion} = -\,\mathbf{S}_n^{ion}$ accounts for momentum gained or lost due to mass transfer during ionization/recombination, defined as

$$\mathbf{S}_i^{ion} = -\mathbf{S}_n^{ion} = \Gamma_i^{ion} m_n \mathbf{V}_n - \Gamma_n^{rec} m_i \mathbf{V}_i \tag{7.10}$$

The symbol Γ^{ex} denotes the charge-exchange collision rate. The term $\mathbf{S}_i^{ex} = -\,\mathbf{S}_n^{ex}$ represents momentum transfer due to charge-exchange collisions, modeled as

$$\mathbf{S}_i^{ex} = -\mathbf{S}_n^{ex} = \Gamma^{ex} m_i (\mathbf{V}_n - \mathbf{V}_i) + \mathbf{R}_{in}^{ex} - \mathbf{R}_{ni}^{ex} \tag{7.11}$$

The terms $\mathbf{R}_{in}^{ex}$ and $\mathbf{R}_{ni}^{ex}$ represent the momentum transfer caused by charge exchange, expressed as

$$\mathbf{R}_{in}^{ex} = -\frac{m_i \sigma_{ex} n_i n_n V_{ex} \mathbf{V}_{in} v_{T_i}^2}{\sqrt{\left(\frac{16}{\pi}\nu_{T_i}^2 + 4 v_{in}^2\right) + \frac{9\pi}{4} v_{T_n}^2}}\,, \qquad \mathbf{R}_{ni}^{ex} = -\frac{m_i \sigma_{ex} n_i n_n V_{ex} \mathbf{V}_{in} v_{T_i}^2}{\sqrt{\left(\frac{16}{\pi} v_{T_n}^2 + 4 v_{in}^2\right) + \frac{9\pi}{4} v_{T_i}^2}} \tag{7.12}$$

Here,

$$v_{in}^2 \equiv |\mathbf{V}_i - \mathbf{V}_n|^2, \qquad V_{ex} \equiv \sqrt{v_{in}^2 + \frac{4}{\pi}\left(v_{T_i}^2 + v_{T_n}^2\right)} \tag{7.13}$$

The symbols v_{T_i} and v_{T_n} respectively denote the thermal velocities of the ions and neutrals, expressed as

$$v_{T_i} = \sqrt{\frac{2 k_B T_i}{m_\alpha}}, \qquad v_{T_n} = \sqrt{\frac{2 k_B T_n}{m_\alpha}} \tag{7.14}$$

Here, σ_{ex} stands for the cross-section for charge exchange, taken as $1.09 \times 10^{-18} - 7.15 \times \ln V_{ex}$ m^2. The charge-exchange reaction rate term Γ^{ex} (Eq. 7.11) is defined as (Meier et al., 2012b)

$$\Gamma^{ex} = n_i n_n \sigma_{ex} V_{ex}^2 \text{ m}^2 \tag{7.15}$$

(c) Energy equations

$$\frac{\partial \varepsilon_i}{\partial t} + \nabla \cdot (\varepsilon_i \mathbf{V}_i + \mathbf{V}_i \cdot \mathbb{P}_i + \mathbf{h}_i) = \mathbf{V}_i \cdot (q_i n_i \mathbf{E} + \mathbf{R}_i^{in} + m_i n_i \mathbf{g}) + Q_i^{in} + S_i^{ion} + S_i^{ex} + S \tag{7.16}$$

$$\frac{\partial \varepsilon_n}{\partial t} + \nabla \cdot (\varepsilon_n \mathbf{V}_n + \mathbf{V}_n \cdot \mathbb{P}_n + \mathbf{h}_n) = -\mathbf{V}_n \cdot (\mathbf{R}_i^{in} + m_n n_n \mathbf{g}) + Q_n^{ni} + S_n^{ion} + S_n^{ex} \tag{7.17}$$

Here, ε_i and ε_n respectively represent the total energy of the ion and neutral fluids. The term $Q_i^{in}(= -Q_n^{ni})$ denotes the net energy transfer to the ion fluid from collisions (the negative of that to neutrals). We use the form consistent with the formulations by Meier et al. (2012b)

$$Q_i^{in}(= -Q_n^{ni}) = \mathbf{R}_i^{in} \cdot (\mathbf{V}_n - \mathbf{V}_i) + m_{in} n_i \nu_{in} (T_n - T_i) \tag{7.18}$$

The terms S_i^{ion} and S_n^{ion} account for ionization/recombination energy transfer, given by

$$S_i^{ion} = \frac{m_i}{m_n} \left[\frac{1}{2} \Gamma_i^{ion} m_n V_n^2 + Q_n^{ion} \right] - \frac{1}{2} \Gamma^{rec} m_i V_i^2 - Q_i^{rec} \tag{7.19}$$

$$S_n^{ion} = \left[\frac{1}{2} \Gamma_n^{rec} m_i V_i^2 + Q_i^{rec} \right] - \frac{1}{2} \Gamma_i^{ion} m_n V_n^2 - Q_n^{ion} \tag{7.20}$$

Here, the terms Q_n^{ion} and Q_i^{rec} are defined as

$$Q_n^{ion} \equiv \frac{3}{2} \Gamma_i^{ion} k_B T_n \ , \qquad Q_i^{rec} \equiv \frac{3}{2} \Gamma_n^{rec} k_B T_i \tag{7.21}$$

Similarly, S_i^{ex} and S_n^{ex} represent the energy transfer terms due to charge exchange, given by

$$S_i^{ex} = \frac{1}{2} \Gamma^{ex} m_i (V_n^2 - V_i^2) + \mathbf{V}_n \cdot \mathbf{R}_{in}^{ex} - \mathbf{V}_i \cdot \mathbf{R}_{ni}^{ex} + Q_{in}^{ex} - Q_{ni}^{ex} \tag{7.22}$$

$$S_n^{ex} = \frac{1}{2} \Gamma^{ex} m_i (V_i^2 - V_n^2) + \mathbf{V}_i \cdot \mathbf{R}_{ni}^{ex} - \mathbf{V}_n \cdot \mathbf{R}_{in}^{ex} + Q_{ni}^{ex} - Q_{in}^{ex} \tag{7.23}$$

Here, terms Q_{in}^{ex} and Q_{ni}^{ex} denotes energy transfer involved in charge exchange (Soler et al., 2022) defined as

$$Q_{in}^{ex} \approx \frac{3}{4} \sigma_{ex} V_{ex} m_i n_i n_n v_{T_n}^2 \sqrt{\frac{4}{\pi} v_{T_i}^2 + \frac{64}{9\pi} v_{T_n}^2 + v_{in}^2} \tag{7.24}$$

$$Q_{ni}^{ex} \approx \frac{3}{4}\,\sigma_{ex}\,V_{ex}\,m_i\,n_i\,n_n\,v_{T_i}^2\,\sqrt{\frac{4}{\pi}\,v_{T_n}^2 + \frac{64}{9\pi}\,v_{T_i}^2 + v_{in}^2} \tag{7.25}$$

Finally, the term S in the ion energy equation serves as a placeholder for additional energy gains/losses resulting from non-ideal processes, such as thermal conduction, radiative cooling, and any explicit heating mechanisms. The details of these terms are provided in Sec. 7.3.

Maxwell's equations with divergence cleaning

The above set of MF-MHD equations is closed by Maxwell's equations for the electromagnetic fields $(\mathbf{E}, \mathbf{B})$, supplemented by a divergence-cleaning approach to enforce $\nabla \cdot \mathbf{B} = 0$ and $\nabla \cdot \mathbf{E} = \sigma_t/\varepsilon_0$ at all times. We use the hyperbolic divergence-cleaning method of Dedner et al. (2002), in which two scalar potentials, ψ and ϕ, are introduced. The Maxwell equations in this formulation are outlined as follows:

$$\frac{\partial \phi}{\partial t} + \nabla \cdot \mathbf{E} = \frac{\sigma_{\mathrm{t}}}{\epsilon_0}\,, \quad \frac{\partial \psi}{\partial t} + c^2\,\nabla \cdot \mathbf{B} = 0 \tag{7.26}$$

$$\frac{\partial \mathbf{E}}{\partial t} - c^2 \nabla \times \mathbf{B} + (\chi c)^2 \nabla \phi = -\frac{\mathbf{J}}{\mu_0}\,, \quad \text{and} \quad \frac{\partial \mathbf{B}}{\partial t} + \nabla \times \mathbf{E} + \gamma^2\,\nabla \psi = 0 \tag{7.27}$$

The symbols used in the above set of equations are defined as follows: the subscripts i and n refer, respectively, to the ion and neutral counterparts. The symbols $\rho_{i,n} = n_{i,n} m_{i,n}$ are the mass densities of the ions and neutrals, where $n_{i,n}$ represent the number densities and $m_{i,n}$ denote the masses of the ion and neutral. The vectors $\mathbf{V}_{i,n}$ denote the velocities of the ions and neutrals, while $T_{i,n,e}$ denotes the temperatures of the ions, neutrals, and electrons, measured in electron volts (eV). The tensor $\mathbb{P}_{i,n}$ represents the pressures of the ions and neutrals. The symbols $\mathbf{E}$ and $\mathbf{B}$ denote the electric and magnetic fields, respectively. Additionally, σ_t and $\mathbf{J}$ denote the total charge and electric current densities, respectively. The Lagrange multipliers are denoted by ψ and ϕ, while Σ represents the collision cross section. A reduced adiabatic index (γ) of 1.05 is adopted (Perri et al., 2022). The speed of light is defined as $c = 1/\sqrt{\epsilon_0 \mu_0}$, where ϵ_0 and μ_0 are, respectively, the magnetic permeability and electric permittivity of free space. The acceleration due to gravity, $|\mathbf{g}|$, at the solar surface is taken here as $274\,\mathrm{m\,s^{-2}}$ and is directed radially inward. The other symbols carry their conventional meanings.

7.3 Empirical coronal source and sink terms

To reproduce a realistic steady-state solar corona, our model incorporates energy source and sink terms, which are collectively represented by S in the ion energy equation. These terms account for physical processes not captured by ideal collisional MHD alone, namely anisotropic thermal conduction, optically thin radiative cooling, and coronal heating. The adopted formulation for these processes follows the prescription by Mikić et al. (1999), that is

$$S = U_{TC} + U_{rad} + U_H \tag{7.28}$$

Here, U_{TC} denotes the thermal conduction term, U_{rad} represents the radiative loss term corresponding to cooling due to radiation, and U_H is an empirical heating term that parameterizes the energy input from coronal heating mechanisms. We describe each term briefly below.

Anisotropic thermal conduction (U_{TC})

In the solar corona, thermal conduction is anisotropic due to the strong magnetic field; heat is transported predominantly along magnetic field lines, while conduction perpendicular to the field is suppressed. To account for this behavior in our multi-fluid model, we have incorporated the formulation from Braginskii (1965). Mathematically, the conductive heat flux is then

$$U_{TC} = -\mathbf{k}\,\nabla\,T \tag{7.29}$$

Here, $\mathbf{k}$ is the conductivity tensor encapsulating both parallel and perpendicular conductivity components, and T is the temperature of the plasma species. This term, U_{TC}, is incorporated into the ion energy equation and does not directly appear in the neutral energy equation, as thermal conduction by neutrals is negligible compared to ion conduction.

Optically thin radiative losses (U_{rad})

Coronal plasma continuously loses energy through radiation. To account for this, we include a radiative cooling term in the energy equation adopted from Rosner et al. (1978), given by

$$U_{rad} = -n_e n_p\,\Lambda(T) \tag{7.30}$$

Here, n_e and n_p are, respectively, the electron and proton densities, and $\Lambda(T)$ is the radiative loss function representing energy loss from an optically thin plasma expressed in a convenient analytic form (Gronenschild et al., 1978). The term U_{rad} is only applied to the energy equation for ions, under the assumption that electrons and ions rapidly equilibrate their temperatures.

The mass density of neutrals is very low in the solar corona due to the exceptionally high temperature; therefore, their contribution to radiative losses is omitted.

Empirical coronal heating (U_H)

Finally, as discussed earlier in Sec. 6.1 & 7.1, the detailed mechanism that heats the solar corona remains an open question. The leading theories include dissipation of MHD waves (Chapter 6), small-scale magnetic reconnection (nano-flares), and turbulent heating, all ultimately powered by the Sun's magnetic field (Browning, 1991; Klimchuk, 2006; Parnell et al., 2012; De Moortel et al., 2015; Schmelz et al., 2015; Bose et al., 2024). Given the complexity and computational cost of explicitly modeling these complicated processes in a global model, we adopt a simplified, parametric heating function U_H to represent the heating rate (Mikić et al., 1999; Pevtsov et al., 2003; Lionello et al., 2008). This approach establishes a relationship between the heating and the magnetic field, which locally varies with the field intensity $B(r)$, thereby aligning with the concept that regions with stronger magnetic fields will be affected by the heating more strongly, whether through waves or reconnection. The heating function, according to (Downs et al., 2010), is given as follows:

$$U_H = B(r)\, U_0 \exp\left(-\frac{r - R_S}{\lambda}\right) \tag{7.31}$$

Here, r is the radial distance from the Sun's center, R_S is the solar radius, and $B(r)$ is the local magnetic field strength. The constants U_0 and λ (heating scale height) are tuned to $4 \times 10^{-5}\,\mathrm{erg\,cm^{-3}\,s^{-1}G^{-1}}$. The expression encodes two general observational constraints: (1) coronal heating scales with magnetic field strength, and (2) heating is concentrated in the lower corona and falls off with height. The chosen exponential profile is a simple yet effective method for localizing heating near the Sun. Moreover, the adopted U_H is also a simple form, unlike Mikić et al. (1999), where they consider latitude $\lambda(\theta)$ dependence. The approach also differs from some earlier papers (e.g., Mikić et al. (1999)) in that we do not include resistive and viscous heating explicitly, which are presumed to be negligible due to other dominating terms present in the source-sink term S.

In a nutshell, $S = U_{TC} + U_{rad} + U_H$ provides a simple but effective way to maintain the quasi-steady corona in our two-fluid model, where heating injects energy, thermal conduction distributes it, and radiation removes it—the trio thus maintaining the energy balance in the global two-fluid model.

7.4 Numerical set-up and boundary conditions

The preliminary information on the adopted COOLFluid code is given in Sec. 5.9. The adopted COOLFluid code employs a second-order accurate Finite Volume Method (FVM) for solving the 3-D MF-MHD equations (Sec. 7.2) using a sixth-level subdivided geodesic polyhedron unstructured mesh. The numerical domain radially stretches from $r = 1.01\,R_\odot$ (lower corona) to $r = 25.0\,R_\odot$ (0.1 AU), thereby representing the inner and outer boundaries with a total of 373,760 cells (Brchnelova et al., 2022). This numerical resolution is sufficient to resolve the essential characteristics of the MF-MHD without considering the rotation of the Sun. Moreover, the position of the outer boundary condition is supported by the Parker solar wind model, which estimates that beyond approximately 0.1 AU, the solar wind is supersonic and super-Alfvénic. This positioning allows for a one-way coupling with heliospheric models, as quantities cannot be returned to the lower coronal domain. The adopted code employs the Harten–Lax–van Leer (HLL) technique to reconstruct fluxes at cell interfaces (Yalim et al., 2011), and the Venkatakrishnan limiter is used to limit the reconstructed fluxes (Venkatakrishnan, 1993) (Sec. 5.7). At the inner boundary, the following parameters are set for the ions: the ion mass density is set to $\rho_{i_s} = 1.67 \times 10^{-13}\,\mathrm{kg\,m^{-3}}$, and the neutral mass density is set to $\rho_{n_s} = 1.67 \times 10^{-19}\,\mathrm{kg\,m^{-3}}$. The initial solar surface temperature is assumed to be equal for both species, i.e., $T_i = T_n = 1.8 \times 10^6\,\mathrm{K}$. The outflow velocity for both ions and neutrals parallel to the magnetic field is set at $1935.7\,\mathrm{m\,s^{-1}}$. This value exceeds the typical observed values at the lower boundary; however, it serves as the necessary boundary condition to initiate plasma outflow in the global simulation framework.

7.5 Influence of source-sink terms on plasma dynamics

This model applies to MF-MHD numerical simulations on real data-driven cases corresponding to the solar minimum (August 1, 2008) and solar maximum (March 9, 2016). In each case, we compare two numerical simulation setups: one that incorporates the source and sink terms in the ion energy equation, which includes radiative cooling, thermal conduction, and empirical heating (Sec. 7.3), and a baseline model that excludes these terms. The two chosen magnetograms highlight solar cycle extremes, serving as representative cases for broader solar minimum and maximum conditions. Naturally, future work may include a broader dataset of other dates; however, the literature survey and the tests performed in the past (Kuźma et al., 2023) provide a robust basis for the present comparison. Figure 7.1 shows the photospheric radial magnetic field B_r input at the inner boundary (at the solar surface) for the two adopted cases serving as the magnetic boundary conditions for the coronal simulations; the left hemisphere (panel a) corresponds to the August 1, 2008 magnetogram (solar minimum) and the

(a) **Solar Minimum** (b) **Solar Maximum**

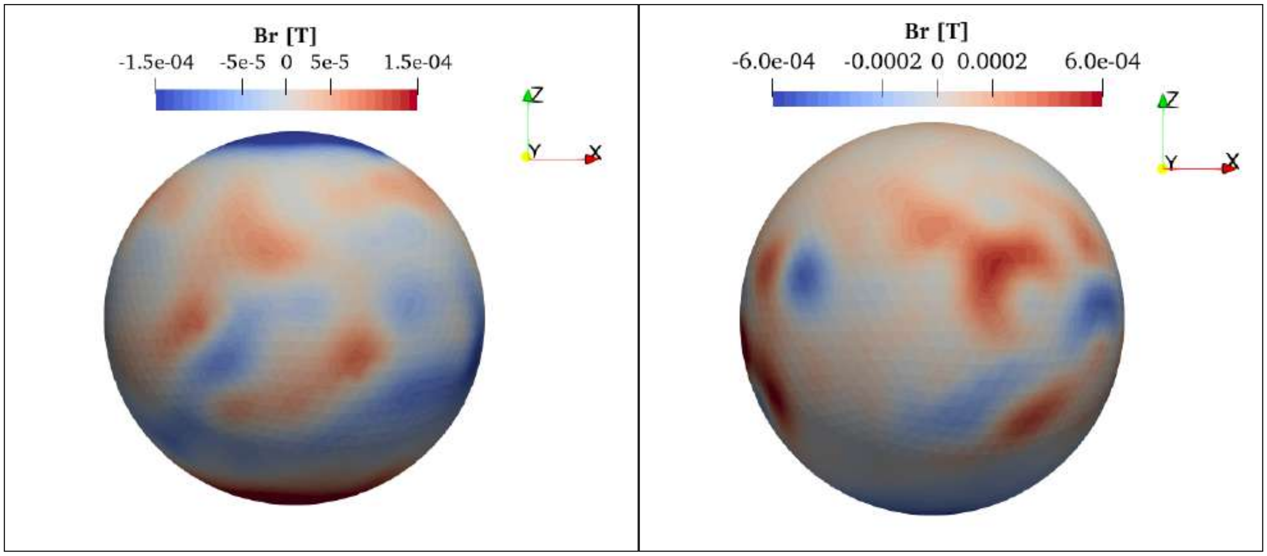

Figure 7.1: The snapshot of the radial magnetic field B_r input at the inner boundary. The left sphere represents the magnetic map for August 1, 2008, corresponding to the solar minimum, while the right sphere represents the magnetic map for March 9, 2016, corresponding to the solar maximum.

right hemisphere (panel b) to the March 9, 2016 magnetogram (solar maximum) (Brchnelova et al., 2023).

It is crucial to note that this study focuses solely on the impact of external source and sink terms in the two-fluid model. Prior work by Brchnelova et al. (2023) examined internal thermodynamic contributions such as ionization, recombination, and charge-exchange heating, etc. Therefore, these heating terms are excluded to avoid their influence on the external source and sink terms. In the following subsection, we present numerical results and compare Case 1 (source-sink on) and Case 2 (source-sink off). All the performed simulations were evolved until a quasi-steady state was reached.

7.5.1 Numerical results for the case of the solar minimum

The *solar minimum* is a period in the solar cycle of the Sun marked by relatively lower solar activity. The source and sink terms can substantially impact the velocity, temperature, and density structure of the plasma species. To visualize these effects, we present comparative contour plots of Case 1 and Case 2 to comprehend how the incorporated source-sink terms affect the characteristics of the plasma and their role in shaping the plasma in the solar atmosphere.

Solar Minimum

With Source-Sink Term (Case 1) **Without Source-Sink Term (Case 2)**

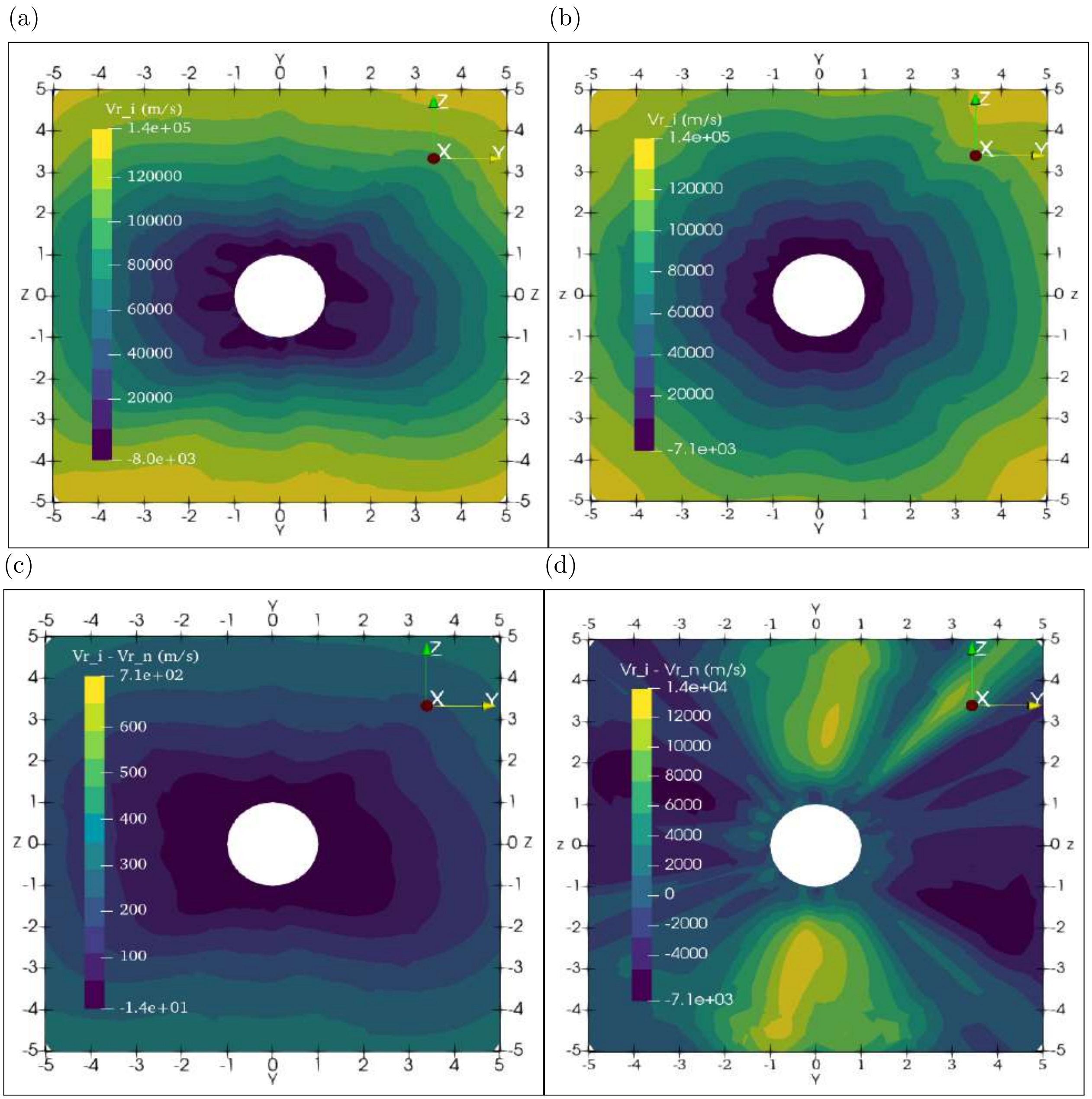

Figure 7.2: The contour plots for V_{i_r} (a, b) and $V_{i_r} - V_{n_r}$ (c, d) with (a, c) and without (b, d) source–sink terms. All velocities are expressed in $\mathrm{m\,s^{-1}}$. These visualizations highlight the influence of the source–sink term on the plasma characteristics. All plots presented here are related to the case of the solar minimum.

Radial velocity

Figure 7.2 compares the ion radial outflow velocity V_{i_r} for Case 1 (panel a) and Case 2 (panel b). In Case 1, the ion velocity exhibits a broad positive outflow envelope with localized small-scale lobes in the azimuthal direction around the central region. The flow peaks at roughly 1.4×10^5 $\mathrm{m\,s^{-1}}$ ($\approx 140\,\mathrm{km\,s^{-1}}$) in the upper corona (around 4–5 $R_\odot$), which is of the order of typical slow solar wind speeds at these heights. Moreover, these contours are nearly concentric and smooth. Physically, in Case 1, the local temperature and pressure are modified due to the presence of the additional source-sink terms. Moreover, the heating term proportional to $B(r)\,\exp\left(-(r - R_\mathrm{S})/\lambda\right)$ injects energy preferentially near strong-field footpoints. As a result, closed-field loop regions heat up and trap high-pressure plasma, forming a distinctive petal-like dark pattern around the limb. Along open flux tubes, the injected heat escapes radially, lifting the bulk ion flow outward and inflating the surrounding plasma. Near the surface, gravity initially dominates, so the flow is still slow, but farther out the pressure gradient overcomes gravity, accelerating the plasma up to $\approx 140\,\mathrm{km\,s^{-1}}$ to produce the plasma outflow. In Case 2, however, EM and gravitational forces nearly balance each other in the absence of external source-sink terms; as a result, the plasma remains in a low-energy, nearly isothermal state. Consequently, the velocity distribution here is relatively more uniform, with essentially a weakly diverging outflow pattern. Lastly, this obtained contrast in radial velocity flow leads us to the important conclusion that the inclusion or exclusion of such a source-sink term in the ion energy can establish a balance between plasma inflows and outflows. Dominant gravitational forces can cause plasma inflow, whereas heat, pressure, and magnetic forces promote plasma outflow.

Ion-neutral drift velocity

Figure 7.2 presents the ion-neutral radial drift of ions $V_{i_r} - V_{n_r}$ for Case 1 (panel c) and Case 2 (panel d). In Case 1, $V_{i_r} - V_{n_r}$ is relatively small, reaching a peak of $\approx 7 \times 10^2$ $\mathrm{m\,s^{-1}}$, whereas in Case 2, the peak $V_{i_r} - V_{n_r}$ is $\approx 1.4 \times 10^4$ $\mathrm{m\,s^{-1}}$. Physically, the heating terms in Case 1 keep the ions relatively hot and fast, and frequent ion-neutral collisions (including charge exchange) keep the ions and neutrals tightly coupled. As a result, the observed relative velocity between the fluids is almost suppressed, giving a smooth, low-drift pattern. In Case 2, due to the absence of source-sink terms, ions accelerate only under the residual pressure gradient and electromagnetic forces. Meanwhile, neutrals remain a relatively inertial species, affected only by gravity and friction. This difference causes significant decoupling between the two species, where the drift reaches almost 20 times higher in localized radial spikes emanating from the inner region. Finally, the apparent contrast here suggests that the incorporated source-sink terms can significantly hinder ion-neutral drift by bringing the ion and neutral temperatures closer together through ion-neutral collisions; however, in Case 2, they allow for significant decoupling.

Solar Minimum

With Source-Sink Term (Case 1) **Without Source-Sink Term (Case 2)**

(a) (b) (c) (d)

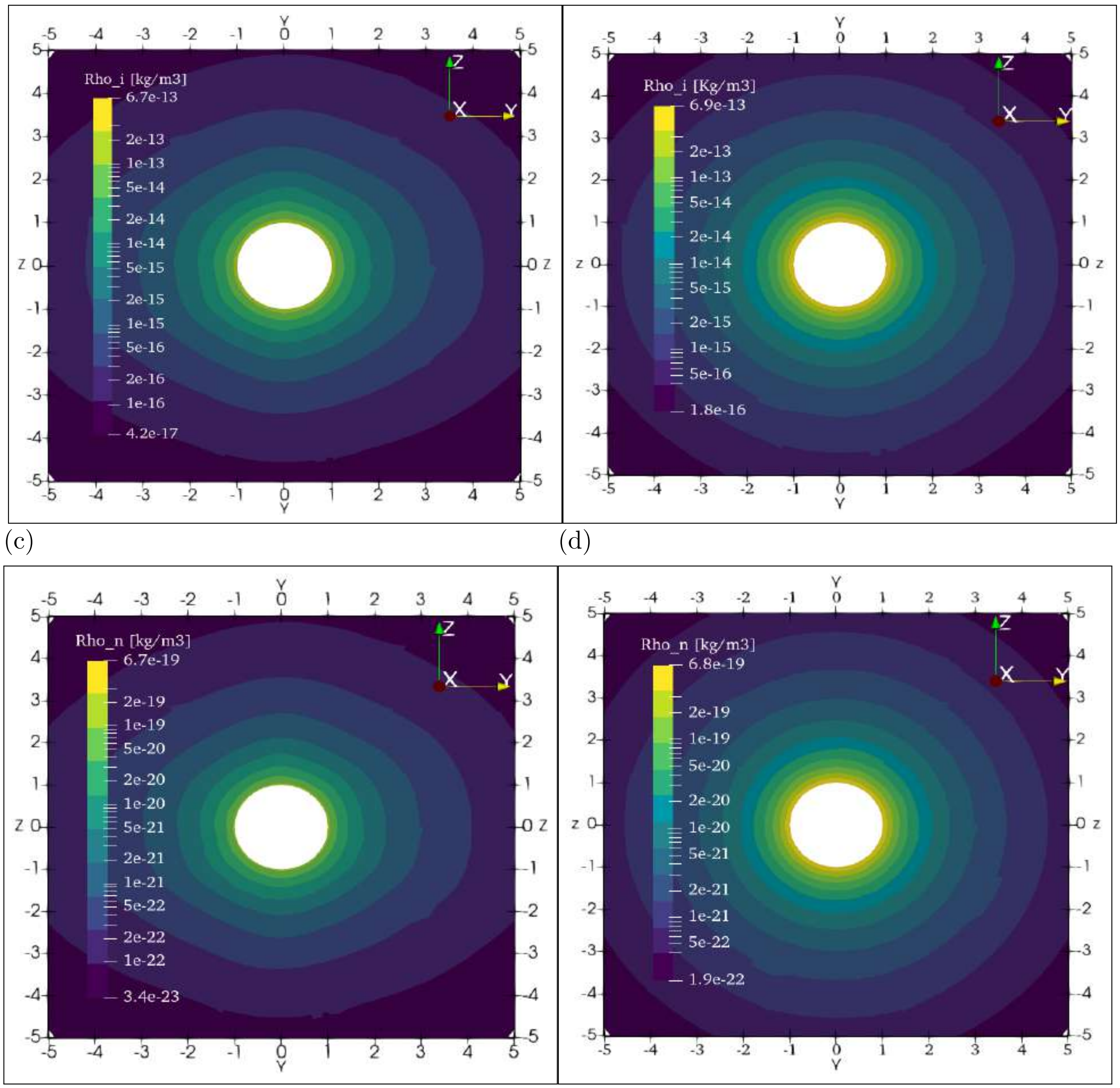

Figure 7.3: The contour plots of $\log \varrho_i$ (a, b) and $\log \varrho_n$ (c, d) with (a, c) and without (b, d) source–sink terms. All densities are measured in $\mathrm{kg\,m^{-3}}$. All plots here correspond to the case of the solar minimum.

Mass density

Source-sink terms can substantially modify the ion and neutral density structures of the plasma. The panels in Fig. 7.3 display the contour plots of $\log \varrho_i$ (a, b) and $\log \varrho_n$ (c, d) in Case

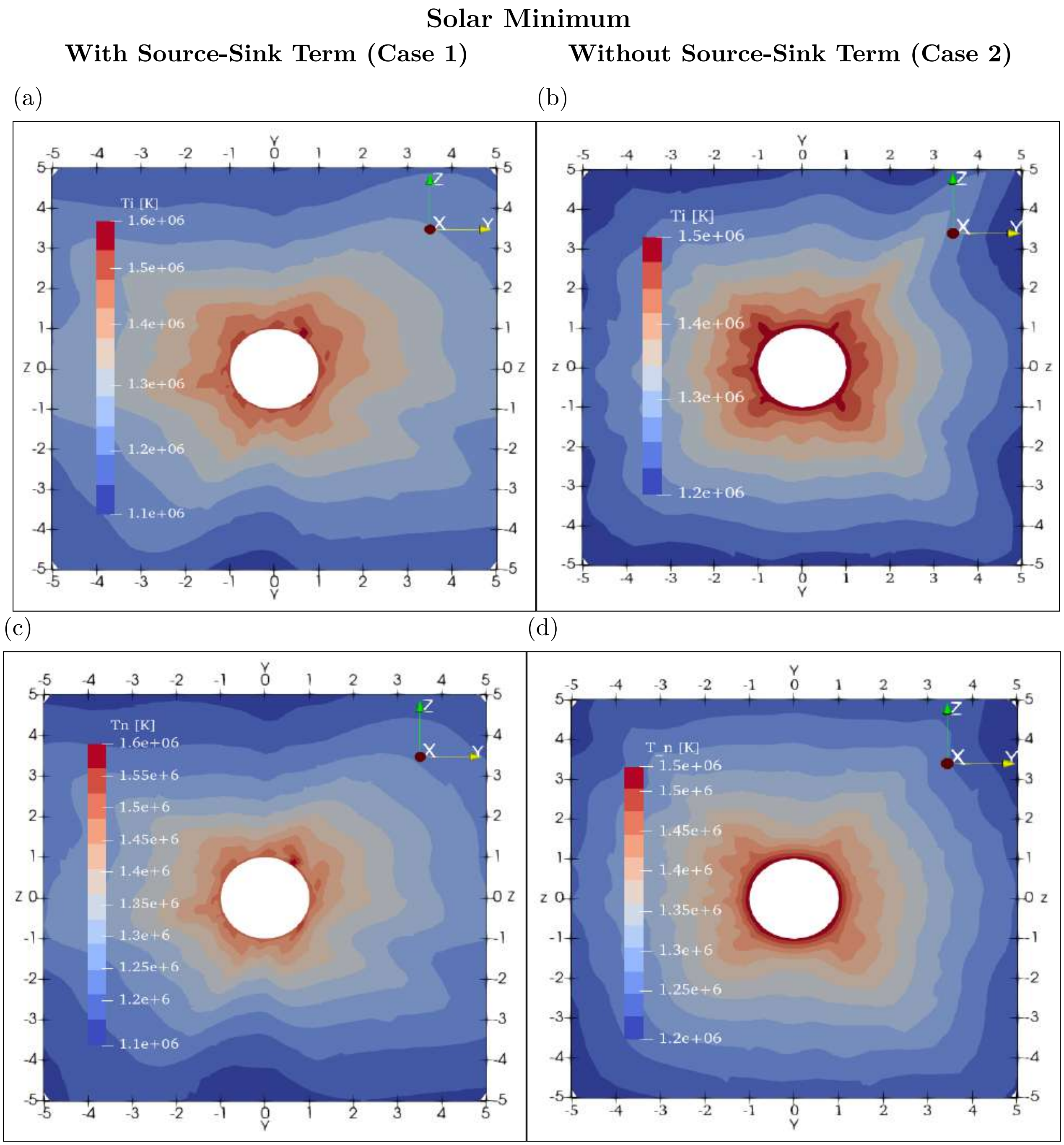

Figure 7.4: The contour plots of $\log T_i$ (a, b) and $\log T_n$ (c, d), with (a, c) and without (b, d) source–sink terms. The temperatures are expressed in K. All the plots here correspond to the case of the solar minimum.

1 (a, c) and Case 2 (b, d). In Case 1, the ion mass density exhibits modest radial stratification, with an expanded inner corona and shallower density gradients. Here, the source heating raises the plasma pressure, supporting the ion fluid against gravity and therefore maintaining

a relatively denser inner corona. On the other hand, in Case 2, the density decreases more steeply with radius, resulting in a strong radial gradient. This behavior results from cooling due to the adiabatic expansion of the plasma. The neutral density plot also exhibits similar qualitative behavior, where, in Case 1, the neutrals are carried upward by collisions, resulting in a relatively flat profile. In contrast, in Case 2, the mass density closely follows the steep drop, similar to the ion density. Together, Fig. 7.3 demonstrates that heating-cooling processes can reshape the mass flow structure, where Case 1 maintains weak radial stratification, and Case 2 gives a relatively strong radial gradient.

Temperature

Incorporating the local source and sink terms will undoubtedly alter the temperature distribution of the plasma. Figure 7.4 shows the log T_i (a, b) and log T_n (c, d) for Case 1 (a, c) and Case 2 (b, d). Both cases show a contrast in terms of thermal and spatial structure. In Case 1, both the ions (panel a) and neutrals (panel c) can be seen attaining peak temperatures of 1.6×10^6 K in the low corona. Both panels display a similar, partially broad, reddish shell ($\sim 1.4 - 1.6$ MK) that fills the lower corona, primarily located in the low corona and fading only gradually with radius. These broad, hot regions originate from magnetic-dependent empirical heating, deposited mainly below $\sim 2\,R_\odot$. Thermal conduction and radiative losses further redistribute this heat, allowing high temperatures to extend into the upper corona. We note that the neutrals, which are not directly heated, are nevertheless collisionally coupled to the ions; thus, the neutral temperature is raised almost to the ion temperature. Therefore, the ion and neutral temperature maps in Case 1 are similar and remain high over a large volume. In Case 2, however, the plasma cools due to adiabatic expansion. Consequently, it preserves a narrow, very hot rim directly over the surface (above $\sim 2\,R_\odot$) — red/orange regions — which then rapidly drop to $\sim 0.1 - 0.2$ MK (blue) by $r \sim 3 - 4\,R_\odot$ (b & d). In particular, without source heating, the temperature profile is relatively cooler and symmetric radially.

7.5.2 Numerical results for the case of the solar maximum

This subsection presents the numerical results for the case of *solar maximum*, a period in the solar cycle with significantly more vigorous magnetic activity.

Ion radial velocity

The upper panels of Fig. 7.5 display the contour plots of V_{i_r} for Cases 1 (a) and 2 (b). The contour plot in panel (a) displays fan-shaped outflow channels reaching magnitudes of $\approx 2\times10^4\,\mathrm{m\,s^{-1}}$ (yellow regions), alongside narrow wedges of inflow lobes (dark/purple regions)

Solar Maximum

With Source-Sink Term (Case 1) **Without Source-sink Term (Case 2)**

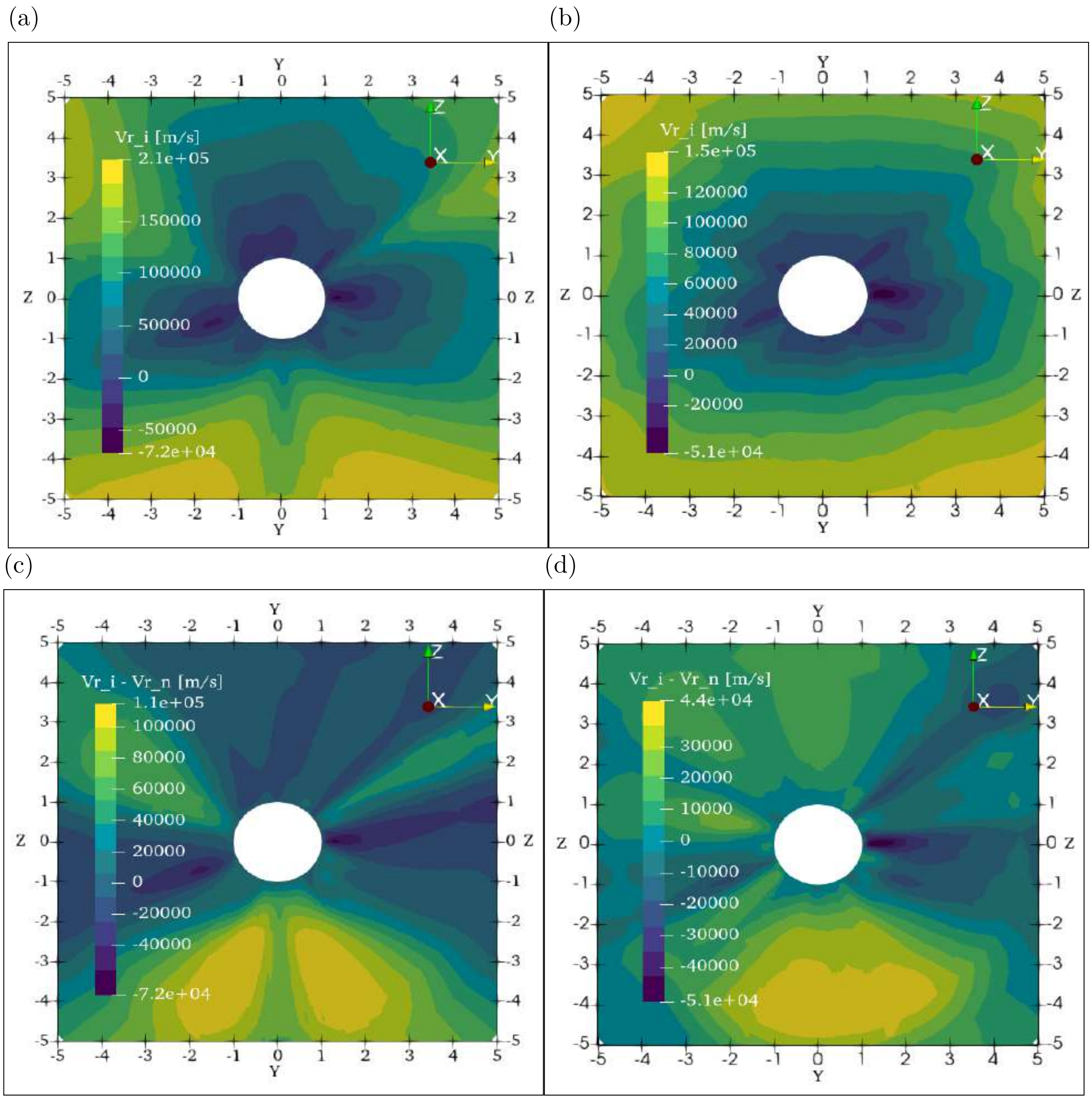

Figure 7.5: The contour plots for V_{i_r} (a, b) and $V_{i_r} - V_{n_r}$ (c, d) with (a, c) and without (b, d) source–sink terms. All velocities are measured in $\mathrm{m\,s^{-1}}$. All plots presented here are related to the case of the solar maximum.

dipping down to $\approx -7 \times 10^4\,\mathrm{m\,s^{-1}}$. These vigorous jets are driven by the significant localized heating that occurs above active regions of the solar atmosphere, where magnetic field strengths ($|\mathbf{B}|$) are particularly strong. This leads to dominant and patchy empirical heating

Solar Maximum

With Source-Sink Term (Case 1) **Without Source-Sink Term (Case 2)**

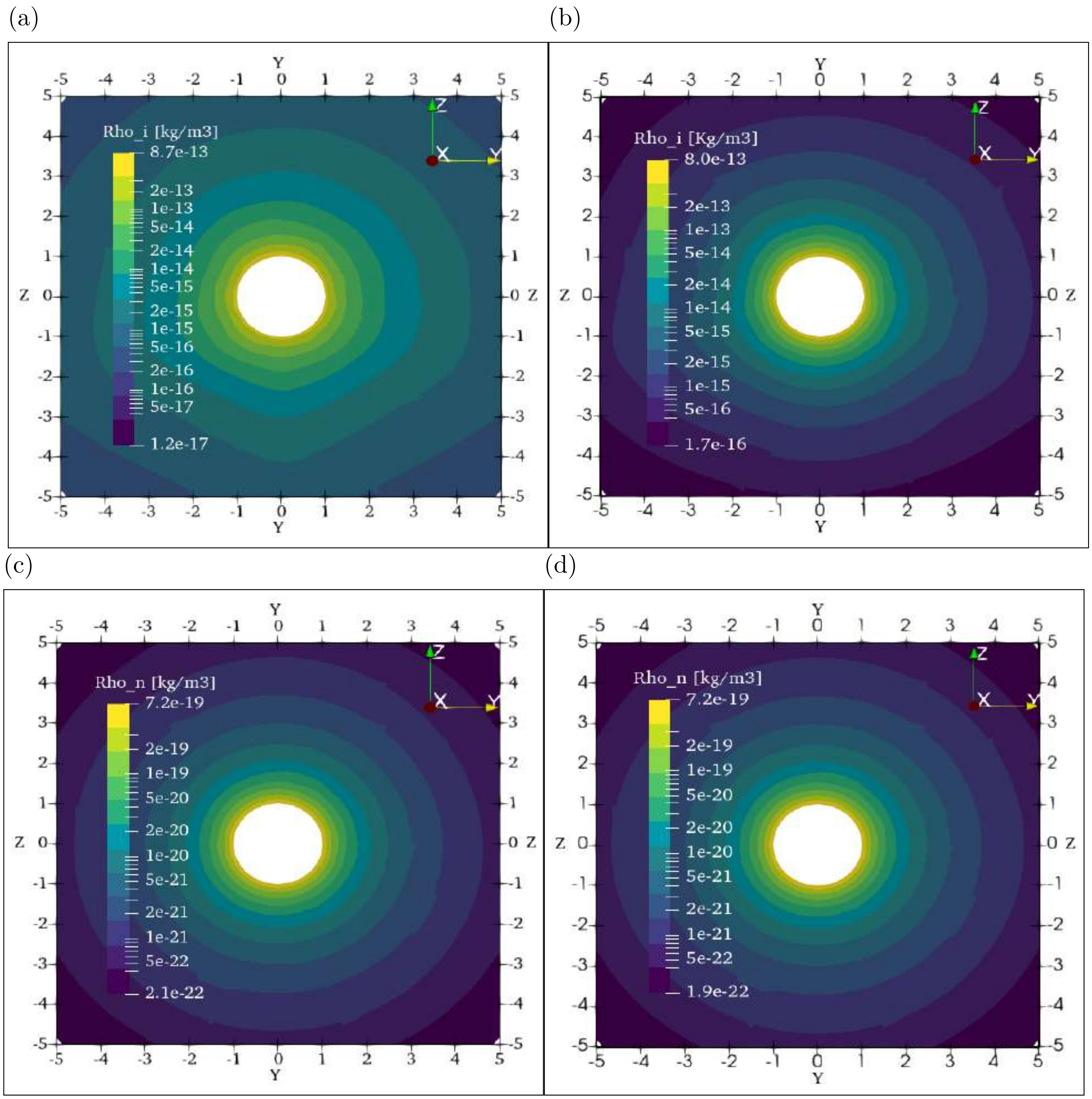

Figure 7.6: The contour plots of $\log \varrho_i$ (a, b) and $\log \varrho_n$ (c, d) with (a, c) and without (b, d) source–sink terms. All densities are measured in $\mathrm{kg\,m^{-3}}$. All plots here correspond to the case of the solar maximum.

in these regions. The steep pressure gradients present in the heated funnels accelerate fast plasma outflows to $\sim 2 \times 10^5\ \mathrm{m\,s^{-1}}$. In contrast, the contour plot in panel (b) indicates a more gentle, ring-like flow wherein the absence of additional heating and cooling leads to weaker

Solar Maximum

With Source-sink Term (Case 1) **Without Source-sink Term (Case 2)**

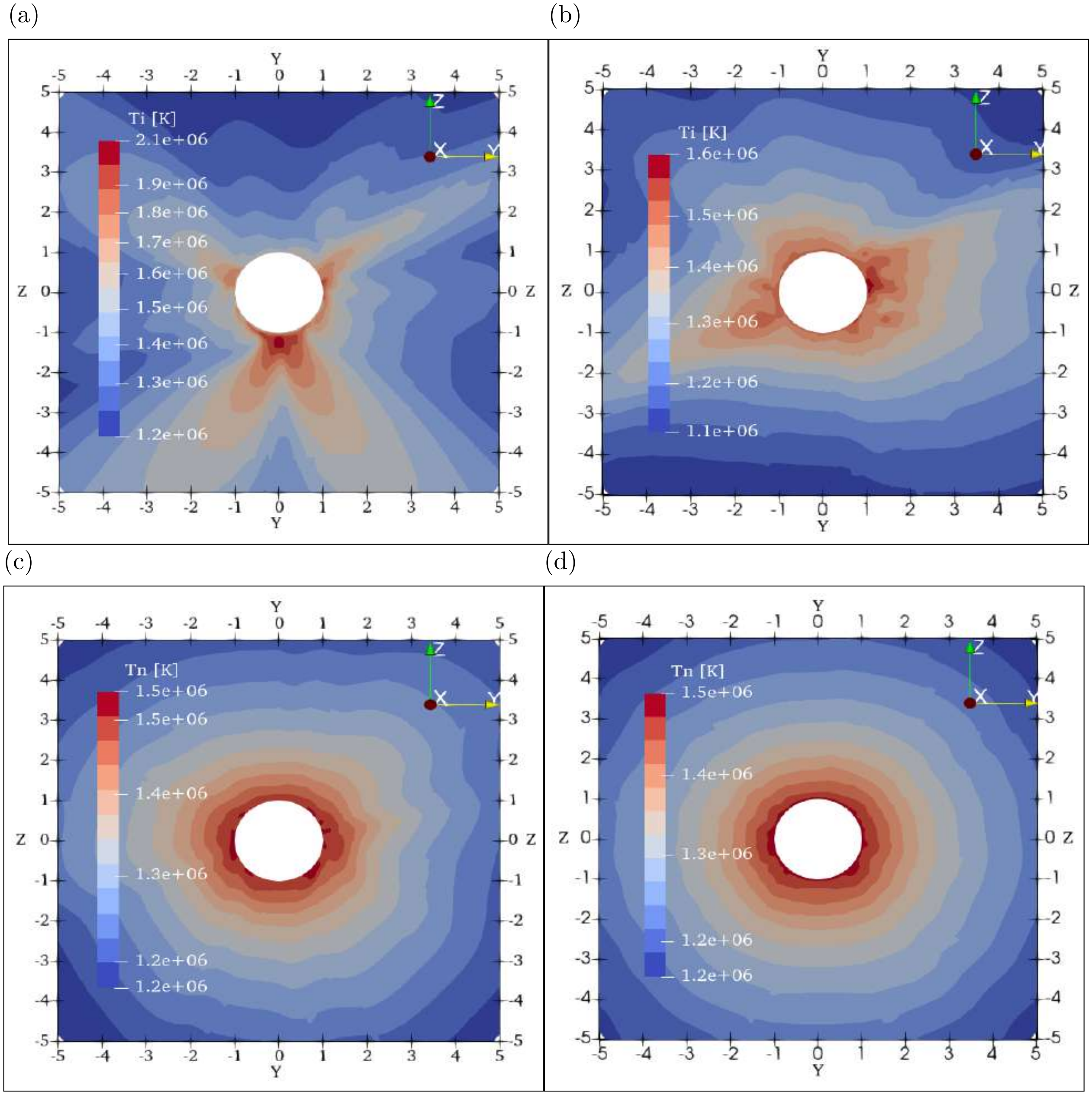

Figure 7.7: The contour plots of $\log T_i$ (a, b) and $\log T_n$ (c, d), with (a, c) and without (b, d) source–sink terms. The temperatures are expressed in K. All the plots here correspond to the case of the solar maximum.

driving pressure gradients, allowing the plasma to expand more slowly and uniformly.

Ion radial velocity drift

The lower panels of Fig. 7.5 present the contour plots of the radial velocity drift of ions $V_{i_r} - V_{n_r}$ for Case 1 (c) and Case 2 (d). Panel (c) shows significant drift, reaching up to $10^5\,\mathrm{m\,s^{-1}}$ (yellow regions), which clearly aligns with the plasma outflow channels. This behavior again arises due to the strong magnetic field strength $|\mathbf{B}|$, characteristic of active regions, which drives intense heating and produces substantial velocity differences between ions and neutrals, thereby overpowering the collisional coupling. Interestingly, panel (d) also reveals similarly distinct drift patterns. This consistent behavior suggests that during solar maximum, the overall magnetic activity and associated heating are so intense that thermal coupling cannot keep pace with the large, pressure-driven jets. Consequently, the ion and neutral flows decouple comparably in both cases. Physically, regions with significant drift may align with regions where enhanced wave damping or frictional heating is likely to happen. Overall, the distinct patterns observed in both cases highlight the influence of the heating-cooling mechanism in reshaping coupling-decoupling in the upper solar atmosphere. Notably, strong heating during intense solar activity does not significantly reduce decoupling; rather, ions experience much greater acceleration than neutrals in both scenarios.

Mass density

Figure 7.6 presents the $\log \varrho_i$ (a, b) and $\log \varrho_n$ (c, d) for Cases 1 (a, c) and 2 (b, d). Notably, all figures display a general spherical symmetry of large-scale density, but a few variations are apparent. In Case 1 (panel a), the radial density gradient is relatively shallow: the inner corona is considerably inflated. It retains a higher density at greater radii due to the additional pressure support from heating. In Case 2 (panel b), the density decreases more rapidly with radius: the inner part is relatively dense (yellow), but the outer corona is relatively sparse (blue). Panels (c) and (d) show no apparent difference, revealing that the source-sink terms have a minimal direct effect on neutral density. Overall, the panels in Fig. 7.6 suggest that the source-sink terms alter the mass distribution of ions, with minimal change in the distribution of neutrals in both cases.

Temperature distribution

Finally, Fig. 7.7 shows the $\log T_i$ (a, b) and $\log T_n$ (c, d) for Case 1 (a, c) and Case 2 (b, d). In Case 1 (panel a), a highly unstructured, narrow, funnel-like channel of very hot plasma ($\sim 2.0 \times 10^6$ K) forms along magnetic field lines. Panel (b) in Case 2 reveals a distinct structure with only a moderately hot layer that forms near the surface. Panels (c) and (d) in both cases yield concentric temperature contours, due to the absence of influence from the source-sink terms on neutrals and the dominance of collisional coupling. Together, all panels suggest that Case 1 leads to a corona with extremely hot patches and steep gradients. In contrast, Case 2 yields a smoother and relatively cooler plasma with comparatively less steep gradients.

Comparison and performance of the model

The coronal magnetic field structure is influenced by the implementation of source-sink terms (Johnson et al., 2024). Figure 7.8 shows four snapshots of the radial photospheric field $\mathbf{B}_r$, where red represents outward while blue denotes inward field lines, illustrating the influence of the source-sink terms. Panels (a) and (b) correspond to the solar minimum case for Case 1 and Case 2, respectively. In both cases, the field lines tend to be predominantly unipolar, featuring extensive polar coronal holes. However, panel (a) shows only minor localized alterations; for instance, heating expands a low-latitude flux tube, slightly distorting the northern polar hole and leading to a minor concentration of flux at mid-latitudes. We note that these minor alterations do not increase **B** strength in either case; instead, they redistribute the existing field by enhancing magnetic cavities.

Similarly, panels (c) and (d) correspond to the solar maximum conditions for Case 1 and Case 2, respectively. In both panels, the field is highly complex, with active regions (intermixed red and blue) and disordered open field lines. Here, the overarching magnetic field structure dictated by the strong magnetic map makes the impact of the source-sink terms much less apparent. Overall, Fig. 7.8 reveals that the source-sink terms can locally shape the coronal field configuration, most apparent during solar minimum, while the underlying photospheric magnetic field primarily governs the global field topology.

The introduction of the new source-sink term can influence the model performance depending on the solver's efficiency, problem complexity, and the stiffness of the terms themselves. In this study, performance is evaluated in terms of the residuals of key variables and wall-clock time. The residuals for density and temperature are measured after one hour of wall-clock runtime on our computational cluster. The residual of the physical quantity f is defined as

$$\mathrm{res}(f) = \log \sqrt{\Sigma_i \left(f_i^t - f_i^{t+1} \right)^2} \tag{7.32}$$

Here, i and t respectively denote the spatial and temporal indices. In the current model, the multi-fluid equations are solved in dimensional form; therefore, the results can be converted to non-dimensional form by referencing a characteristic temperature $T_{ref} = 2.3 \times 10^{11}$ K. Using Eq. 7.32, we obtain

$$\mathrm{res(f^*)} = \mathrm{res(f)} - \log(2.3 \times 10^{11}) \tag{7.33}$$

$$\mathrm{res(f^*)} \approx \mathrm{res(f)} - 11.36 \tag{7.34}$$

Solar Maximum

With Source-sink Term (Case 1) **Without Source-sink Term (Case 2)**

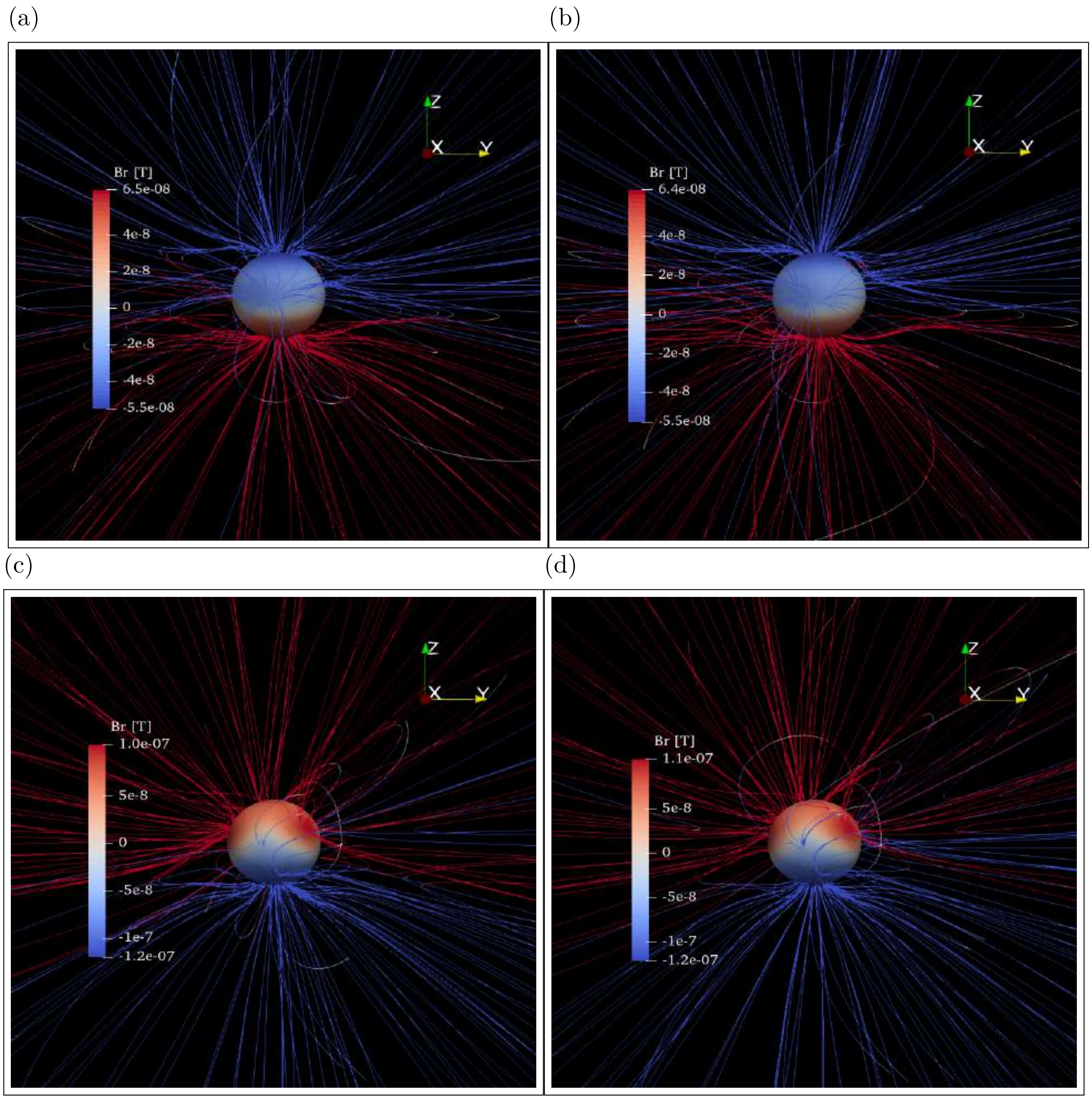

Figure 7.8: The snapshots of the full two-fluid MHD COCONUT solution comparing scenarios with (a, c) and without (b, d) the source–sink term for solar minimum (a, b) and solar maximum (c, d). The solar surface shows the simulated radial magnetic field $\mathbf{B}_r$.

If the residual of a parameter in the non-dimensional simulation is -7, this implies that the cumulative difference in the flow-field variable between two successive iterations is 10^{-7}. Such a residual generally indicates that the solution has converged satisfactorily. Following this,

(a) Solar Minimum				(b) Solar Maximum			
Case 1		**Case 2**		**Case 1**		**Case 2**	
Variable	**Residual**	**Variable**	**Residual**	**Variable**	**Residual**	**Variable**	**Residual**
T_i	-7.36	T_i	-7.01	T_i	-7.96	T_i	-7.46
ϱ_i	-20.0	ϱ_i	-19.35	ϱ_i	-20.0	ϱ_i	-19.28

Table 7.1: Comparison of residuals for solar minimum and maximum for Case 1 and Case 2

Table 7.1 summarizes the numerical convergence of the simulations. All numerical simulations were performed on a single node with 2 Xeon E5-2670 v3 CPUs@2.3GHz (Haswell), 96 cores/24 threads each, on the LUNAR cluster at UMCS Lublin, Poland.

In both tables, the first row lists the residual for T_i, and the second row lists the residual for ϱ_i. Across all cases, the residual for T_i ranges from $-7 \sim -8$, while the residual for ϱ_i lies in $-19 \sim -20$. These values are well below the typical convergence thresholds. Additionally, these minimal residuals (on the order of 10^{-7} for temperature and 10^{-20} for density in dimensionless terms) indicate that both models reach well-converged steady states within a few tens of thousands of iterations. Fig. 7.9 compares the T_i residual against the number of iterations for the solar minimum (a) and the solar maximum case (b). The purple curve corresponds to Case 1, while the green curve corresponds to Case 2. For the solar minimum (a), the residual after $20,000$ iterations is about 4.6 (≈ -6.76 in non-dimensional units) for Case 1 and 3.6 (≈ -7.36 in non-dimensional units) for Case 2. For the solar maximum, the corresponding residuals are approximately 4 (≈ -7.36) for Case 1 and about 3.4 (≈ -7.96) for Case 2. These small values confirm that the steady-state solutions are well converged. The integrated quantities in Tab. 7.1 and the visible trend in Fig. 7.9 together indicate that neither case experiences significant oscillations or convergence failure. Furthermore, all curves converge to steady values characteristic of a converged MHD solution. Moreover, the computational cost is also comparable between the two cases: on our cluster, a steady solution is obtained in roughly one hour of wall-clock time. This leads us to conclude that incorporating a new source-sink term does not significantly increase the required runtime, implying that the additional physics can be included in operational or production runs (e.g., for space weather forecasting) with only a modest performance cost.

7.6 Summary

In this study, we have extended the realism of a global two-fluid COCONUT coronal model by including physics-based source and sink terms in the ion energy equation. These include thermal conduction, optically thin radiative losses, and empirical heating functions proportional to the magnetic field strength. These terms have physical correspondences with the dominant

(a) **Solar Minimum** (b) **Solar Maximum**

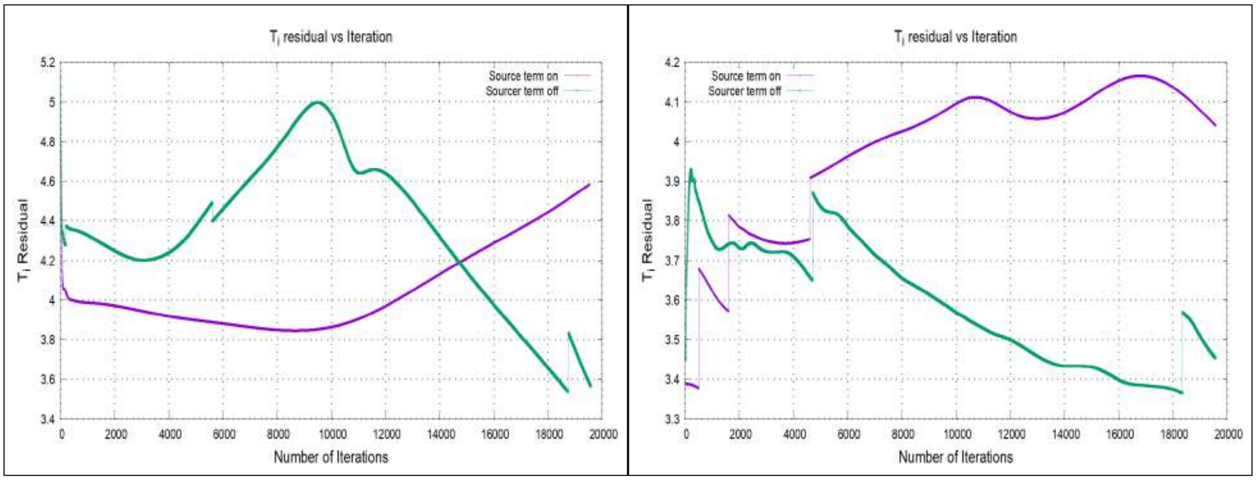

Figure 7.9: The variation of the residual of T_i with iteration count in the numerical simulation for solar minimum (a) and solar maximum (b). The red curve represents Case 1, while the green curve represents Case 2.

thermodynamic processes thought to heat and cool the solar corona in the chromosphere, transition region, and corona system.

We applied the extended model to two data-driven cases (solar minimum and solar maximum) and examined how the inclusion of these terms affects the steady-state coronal solution. With the heating and cooling activated (Case 1), the model self-consistently produces a hot ($\sim 10^6$–10^7 K), high-pressure corona with structured outflows. The obtained results suggest that the thermal pressure and heating effects provided by the source-sink terms are required to balance gravity and drive the plasma outward, which remain absent in Case 2. Moreover, we find that incorporating the source terms does not pose any severe numerical difficulties. Both Case 1 and Case 2 reach comparable residual levels, confirming the model's stability. The convergence behavior and computational cost remain acceptable, indicating that the extended model can be utilized in operational space-weather pipelines.

Of course, our model remains a simplified representation of the solar corona, treating the corona as a thermodynamic fluid and employing empirical heating prescriptions. It does not capture the detailed microphysics of coronal heating (e.g., wave-particle interactions, turbulence, reconnection-driven nano-flares) nor the global-scale solar wind acceleration mechanism. Additionally, it does not account for kinetic scales or wave propagation effects. Hence, while the empirical heating term produces a reasonable large-scale temperature distribution, it is not derived from first principles. In addition, we modeled a global steady state and thus have not addressed time-dependent phenomena such as flares or coronal mass ejections.

Nevertheless, in conclusion, our enhanced two-fluid model demonstrates that including radiative losses, thermal conduction, and magnetic-field-dependent heating is critical for reproducing the corona's thermodynamics. These source terms yield a hot, structured corona and drive realistic solar wind outflows in both quiet and active conditions. Neglecting them leads to a nearly hydrostatic corona. Therefore, any predictive global coronal model (especially for space-weather forecasting) should include such thermodynamic source and sink terms to achieve physically meaningful results.

Chapter 8

Summary and outlook

This thesis presents multi-scale numerical simulations to enhance our understanding of the plasma heating of the upper solar atmosphere and the generation of plasma outflows. The study combines local and global numerical simulations to associate the influence of local-scale dissipation processes on the large scale. On the local scale, we first examined how impulsive perturbations excite and couple MHD waves in a partially ionized two-fluid plasma, and how ion-neutral collisions dissipate wave energy into heat, thereby driving the plasma outflows. This is followed by performing the numerical simulation in a more realistic setting, which includes solar granulation as a physical driver of the dynamics of an overlying magnetic arc. This configuration excites a broad spectrum of waves, unlike impulsive perturbations, which limit us to a few MHD modes. The obtained result highlights that the granular excited waves undergo partial dissipation through ion-neutral collisions, causing localized heating and plasma outflows in the solar chromosphere. These consistent results demonstrate that the physical mechanism established in the first model is also applicable to realistic local solar atmospheric conditions. After establishing local physics and gathering local insights, supporting the broader perspective that the cumulative effect of numerous small-scale, intermittent energy release events may sustain the solar corona, these local aspects are applied at the global scale by incorporating parameterized source–sink terms into the steady-state multi-fluid COCONUT model. This extension allows us to assess the cumulative influence of numerous localized dissipation events on global coronal heating and plasma outflows.

In summary, this study strengthens the case for MHD wave dissipation as a potential candidate for coronal heating and driving plasma outflows, thereby bridging the gap between local-scale dissipation processes and their influence on the large-scale global model for the solar corona and wind, with potential applications to space weather prediction.

Next steps and outlook

The work presented in this thesis represents a significant step toward advancing the modeling of the solar atmosphere and its potential applications. Additional work is, however, required to extend and refine the modeling approaches presented here, for example, by incorporating more realistic physics. Here are some suggested future outlooks based on the heating of the solar atmosphere and the origin of the solar wind.

1. The presented COCONUT-MF model is a steady-state model, thus unable to capture the propagation and damping of MHD waves and other transient phenomena. A crucial follow-up would be to incorporate time dependency into the wave transport module. This would allow the global model to more accurately capture the wave spectra in the solar corona and solar wind.

2. The two-fluid model treats the ions and electrons as a single charged fluid, while neutrals are treated as another. The two-fluid model can be extended to a three-fluid model by treating ions, electrons, and neutrals all as separate entities. The three-fluid approach would enable the capture of electron heating and Hall effects, thereby extending the model within the framework of fluid dynamics to account for kinetic effects.

3. A logical step would also include validation of the model predictions against multi-instrument observations from IRIS, SDO/AIA, PSP, etc. In particular, it would be instructive to compare the predicted heating profiles and upflow speeds with the observed transition-region and coronal signatures. This would strengthen the credibility of the model for application in space weather forecasting.

4. The global model presented in this thesis could be extended outward and coupled with heliospheric models, such as EUHFORIA. This extension would complete the entire Sun–Earth orbit (and beyond) chain, from small-scale phenomena to the heliosphere, thereby making the model directly relevant to space weather forecasting.

5. The current local model employs the Gaussian pulse driver along with a simple magnetic field configuration, which is indeed a proxy and a rough assumption. A step toward more realistic numerical simulations would involve using photospheric velocity along with magnetic field maps from observations (e.g., SDO/HMI and DKIST) as a boundary driver. This approach is expected to enhance the model's accuracy and make it more comparable to actual events.

The ideas outlined above present just a small fraction of the extensive possibilities related to improving coronal and heliospheric modeling, thus leaving a large portion of the scientific domain to be explored. With this, the thesis aims to enhance our understanding of solar atmosphere heating and the subsequent generation of plasma outflows, while bridging the gap between wave dissipation on the local scale and its influence on coronal dynamics on the global scale.

Science is a perpetual search for truth

$\cdots\cdots$ *Subrahmanyan Chandrasekhar*

References

[1] W. P. Abbett and G. H. Fisher. "Radiative cooling in MHD models of the quiet Sun convection zone and corona". In: *Solar Physics* 277 (2012), pp. 3–20.

[2] H. Alfvén. "Existence of electromagnetic-hydrodynamic waves". In: *Nature* 150.3805 (1942), pp. 405–406.

[3] V. Andretta and H. P. Jones. "On the role of the solar corona and transition region in the excitation of the spectrum of neutral helium". In: *The Astrophysical Journal* 489.1 (1997), p. 375.

[4] I. Arregui. "Wave heating of the solar atmosphere". In: *Philosophical Transactions of the Royal Society A: Mathematical, Physical and Engineering Sciences* 373.2042 (2015), p. 20140261.

[5] E. H. Avrett and R. Loeser. "Models of the Solar Chromosphere and Transition Region from SUMER and HRTS Observations: Formation of the Extreme-Ultraviolet Spectrum of Hydrogen, Carbon, and Oxygen". In: 175.1 (Mar. 2008), pp. 229–276.

[6] E. H. Avrett and R. Loeser. "Models of the Solar Chromosphere and Transition Region from SUMER and HRTS Observations: Formation of the Extreme-Ultraviolet Spectrum of Hydrogen, Carbon, and Oxygen". en. In: *The Astrophysical Journal Supplement Series* 175.1 (Mar. 2008), pp. 229–276.

[7] S. Bale, J. Drake, M. McManus, M. Desai, S. Badman, D. Larson, M. Swisdak, T. Horbury, N. Raouafi, T. Phan, et al. "Interchange reconnection as the source of the fast solar wind within coronal holes". In: *Nature* 618.7964 (2023), pp. 252–256.

[8] J. Ballester, R. Soler, J. Terradas, and M. Carbonell. "Nonlinear coupling of Alfvén and slow magnetoacoustic waves in partially ionized solar plasmas". In: *Astronomy & Astrophysics* 641 (2020), A48.

[9] J. L. Ballester. "Nonlinear coupling of alfvén and slow magnetoacoustic waves in partially ionized solar plasmas: The effect of thermal misbalance". In: *Physics* 5.2 (2023), pp. 331–351.

[10] J. L. Ballester, I. Alexeev, M. Collados, T. Downes, R. F. Pfaff, H. Gilbert, M. Khodachenko, E. Khomenko, I. F. Shaikhislamov, R. Soler, et al. "Partially ionized plasmas in astrophysics". In: *Space Science Reviews* 214 (2018), pp. 1–149.

[11] T. Baratashvili, M. Brchnelova, L. Linan, A. Lani, and S. Poedts. “The operationally ready full 3D magnetohydrodynamic model from the Sun to Earth: COCONUT+ Icarus”. In: *Astronomy & Astrophysics* 690 (2024), A184.

[12] A. F. Battaglia, J. R. C. Cuissa, F. Calvo, A. A. Bossart, and O. Steiner. “The Alfvénic nature of chromospheric swirls”. In: *Astronomy & Astrophysics* 649 (2021), A121.

[13] L. Bierman. “Inhomogeneous stellar atmosphere models”. In: *Naturwissenschaften* 33 (1946), p. 118.

[14] L. Biermann. “Zur Deutung der chromosphärischen Turbulenz und des Exzesses der UV-Strahlung der Sonne”. In: *Naturwissenschaften* 33.4 (1946), pp. 118–119.

[15] L. Biermann. “Kometenschweife und solare Korpuskularstrahlung”. In: *Zeitschrift für Astrophysik, Vol. 29, p. 274* 29 (1951), p. 274.

[16] T. J. Bogdan et al. “Waves in the Magnetized Solar Atmosphere. II. Waves from Localized Sources in Magnetic Flux Concentrations”. In: 599.1 (Dec. 2003), pp. 626–660.

[17] S. Bose, B. De Pontieu, V. Hansteen, A. Sainz Dalda, S. Savage, and A. Winebarger. “Chromospheric and coronal heating in an active region plage by dissipation of currents from braiding”. In: *Nature Astronomy* 8.6 (2024), pp. 697–705.

[18] T. J. M. Boyd and J. J. Sanderson. “Particle orbit theory”. In: *The Physics of Plasmas*. Cambridge University Press, 2003, pp. 12–47.

[19] S. I. Braginskii. “Transport Processes in a Plasma”. In: *Reviews of Plasma Physics* 1 (Jan. 1965), p. 205.

[20] B. P. Braileanu, V. Lukin, E. Khomenko, and Á. De Vicente. “Two-fluid simulations of waves in the solar chromosphere-I. Numerical code verification”. In: *Astronomy & Astrophysics* 627 (2019), A25.

[21] M. Brchnelova, B. Kuźma, F. Zhang, A. Lani, and S. Poedts. “COCONUT-MF: Two-fluid ion-neutral global coronal modelling”. In: *Astronomy & Astrophysics* 678 (2023), A117.

[22] M. Brchnelova, S. Poedts, and A. Lani. “Towards faster and more physical MHD and multi-fluid data-driven global coronal models”. In: (2024).

[23] M. Brchnelova, F. Zhang, P. Leitner, B. Perri, A. Lani, and S. Poedts. “Effects of mesh topology on MHD solution features in coronal simulations”. In: *Journal of Plasma Physics* 88.2 (2022), p. 905880205.

[24] M. Brio and C. C. Wu. "An upwind differencing scheme for the equations of ideal magnetohydrodynamics". In: *Journal of computational physics* 75.2 (1988), pp. 400–422.

[25] P. Browning. "Mechanisms of solar coronal heating". In: *Plasma Physics and Controlled Fusion* 33.6 (1991), p. 539.

[26] M. Carbonell, P. Forteza, R. Oliver, and J. Ballester. "The spatial damping of magnetohydrodynamic waves in a flowing partially ionised prominence plasma". In: *Astronomy & Astrophysics* 515 (2010), A80.

[27] S. Chapman and T. G. Cowling. *The mathematical theory of non-uniform gases. an account of the kinetic theory of viscosity, thermal conduction and diffusion in gases.* 1970.

[28] S. C. Chapra, R. P. Canale, et al. *Numerical methods for engineers.* Vol. 1221. Mcgraw-hill New York, 2011.

[29] V. Chaturmutha, B. Fleck, and S. M. Jefferies. "Wave Reflection in the Solar Atmosphere". In: *The Astrophysical Journal* 966.2 (2024), p. 200.

[30] K. Chaudhary, A. M. Imam, S. Z. H. Rizvi, and J. Ali. "Plasma kinetic theory". In: *Kinetic Theory; InTech: Rijeka, Croatia* (2018), pp. 107–127.

[31] F. F. Chen et al. *Introduction to plasma physics and controlled fusion.* Vol. 1. Springer, 1984.

[32] X. Cheng, E. R. Priest, H. Li, J. Chen, G. Aulanier, L. P. Chitta, Y. Wang, H. Peter, X. Zhu, C. Xing, et al. "Ultra-high-resolution observations of persistent null-point reconnection in the solar corona". In: *Nature Communications* 14.1 (2023), p. 2107.

[33] L. P. Chitta, A. N. Zhukov, D. Berghmans, H. Peter, S. Parenti, S. Mandal, R. Aznar Cuadrado, U. Schühle, L. Teriaca, F. Auchère, et al. "Picoflare jets power the solar wind emerging from a coronal hole on the Sun". In: *Science* 381.6660 (2023), pp. 867–872.

[34] L. P. Chitta, H. Peter, S. Parenti, D. Berghmans, F. Auchère, S. K. Solanki, R. A. Cuadrado, U. Schühle, L. Teriaca, S. Mandal, et al. "Solar coronal heating from small-scale magnetic braids". In: *Astronomy & Astrophysics* 667 (2022), A166.

[35] A. R. Choudhuri. *Astrophysics for physicists.* Cambridge University Press, 2010.

[36] L. D. Cloutman. "Numerical simulation of the solar granulation". In: *International Astronomical Union Colloquium.* Vol. 58. Cambridge University Press. 1980, pp. 293–299.

[37] P. Colella and P. R. Woodward. “The piecewise parabolic method (PPM) for gas-dynamical simulations”. In: *Journal of computational physics* 54.1 (1984), pp. 174–201.

[38] R. Courant, K. Friedrichs, and H. Lewy. “Über die partiellen Differenzengleichungen der mathematischen Physik”. In: *Mathematische Annalen* 100 (Jan. 1928), pp. 32–74.

[39] N. F. Cramer. *The physics of Alfvén waves*. John Wiley & Sons, 2011.

[40] S. R. Cranmer, S. E. Gibson, and P. Riley. “Origins of the ambient solar wind: implications for space weather”. In: *Space Science Reviews* 212 (2017), pp. 1345–1384.

[41] S. R. Cranmer and A. R. Winebarger. “The properties of the solar corona and its connection to the solar wind”. In: *Annual Review of Astronomy and Astrophysics* 57.1 (2019), pp. 157–187.

[42] W. Dai and P. R. Woodward. “On the divergence-free condition and conservation laws in numerical simulations for supersonic magnetohydrodynamical flows”. In: *The Astrophysical Journal* 494.1 (1998), p. 317.

[43] L. Data. “VisIt: An End-User Tool for Visualizing and Analyzing Very”. In: *High Performance Visualization*. Chapman and Hall/CRC, 2012, pp. 395–410.

[44] I. De Moortel and P. Browning. “Recent advances in coronal heating”. In: *Philosophical Transactions of the Royal Society A: Mathematical, Physical and Engineering Sciences* 373.2042 (2015), p. 20140269.

[45] I. De Moortel, A. W. Hood, C. Gerrard, and S. Brooks. “The damping of slow MHD waves in solar coronal magnetic fields-III. The effect of mode coupling”. In: *Astronomy & Astrophysics* 425.2 (2004), pp. 741–752.

[46] A. Dedner, F. Kemm, D. Kröner, C. .-. Munz, T. Schnitzer, and M. Wesenberg. “Hyperbolic Divergence Cleaning for the MHD Equations”. In: *Journal of Computational Physics* 175.2 (Jan. 2002), pp. 645–673.

[47] R. O. Dendy. *Plasma physics: an introductory course*. Cambridge University Press, 1995.

[48] E. Deriaz and P. Haldenwang. “Non-linear CFL conditions issued from the von Neumann stability analysis for the transport equation”. In: *Journal of Scientific Computing* 85.1 (2020), p. 5.

[49] C. Downs, I. I. Roussev, B. van der Holst, N. Lugaz, I. V. Sokolov, and T. I. Gombosi. “Toward a realistic thermodynamic magnetohydrodynamic model of the global solar corona”. In: *The Astrophysical Journal* 712.2 (2010), p. 1219.

[50] R. K. Dubey. "On the stability of Forward in Time and Centred in Space (FTCS) scheme for scalar hyperbolic equation". In: *arXiv preprint arXiv:1503.02629* (2015).

[51] D. R. Durran. *Numerical Methods for Fluid Dynamics*. 2010.

[52] A. S. Eddington. "The envelopes of comet morehouse (1908 c)". In: *Monthly Notices of the Royal Astronomical Society* 70.5 (1910), pp. 442–458.

[53] J. F. Epperson. *An introduction to numerical methods and analysis*. John Wiley & Sons, 2013.

[54] R. Erdelyi and V. Fedun. "Are there Alfvén waves in the solar atmosphere?" In: *Science* 318.5856 (2007), pp. 1572–1574.

[55] R. Erdélyi and S. James. "Can ion-neutral damping help to form spicules?. II. Random driver". In: *Astronomy and Astrophysics* 427 (2004), pp. 1055–1064.

[56] E. H. B. M. Gronenschild and R. Mewe. "Calculated X-radiation from optically thin plasmas. III. Abundance effects on continuum emission." In: 32 (May 1978), pp. 283–305.

[57] C. P. Groth, D. L. De Zeeuw, T. I. Gombosi, and K. G. Powell. "Global three-dimensional MHD simulation of a space weather event: CME formation, interplanetary propagation, and interaction with the magnetosphere". In: *Journal of Geophysical Research: Space Physics* 105.A11 (2000), pp. 25053–25078.

[58] M. Hahn. "Evidence for wave heating in the solar corona". In: *Annals of the New York Academy of Sciences* 1293.1 (2013), pp. 45–53.

[59] G. Hansen, A. Zardecki, D. Greening, and R. Bos. "A finite element method for unstructured grid smoothing". In: *Journal of Computational Physics* 194.2 (2004), pp. 611–631.

[60] D. H. Hathaway. "The solar cycle". In: *Living reviews in solar physics* 12.1 (2015), p. 4.

[61] S. Hosteaux, E. Chané, B. Decraemer, D.-C. Talpeanu, and S. Poedts. "Ultrahigh-resolution model of a breakout CME embedded in the solar wind". In: *Astronomy & Astrophysics* 620 (2018), A57.

[62] T. A. Howson, I. De Moortel, P. Antolin, T. Van Doorsselaere, and A. N. Wright. "Resonant absorption in expanding coronal magnetic flux tubes with uniform density". In: *Astronomy & Astrophysics* 631 (2019), A105.

[63] U. S. Inan and M. Gołkowski. *Principles of plasma physics for engineers and scientists*. Cambridge University Press, 2010.

[64] S. James and R. Erdélyi. “Spicule formation by ion-neutral damping”. In: *Solar Variability: From Core to Outer Frontiers*. Vol. 506. 2002, pp. 649–652.

[65] S. James, R. Erdélyi, and B. De Pontieu. “Can ion-neutral damping help to form spicules?” In: *Astronomy & Astrophysics* 406.2 (2003), pp. 715–724.

[66] D. B. Jess, M. Mathioudakis, R. Erdélyi, P. J. Crockett, F. P. Keenan, and D. J. Christian. “Alfvén waves in the lower solar atmosphere”. In: *Science* 323.5921 (2009), pp. 1582–1585.

[67] G. S. Jiang and C. W. Shu. “Efficient implementation of weighted ENO schemes”. In: *Journal of computational physics* 126.1 (1996), pp. 202–228.

[68] D. Johnson, A. W. Hood, P. Cargill, J. Reid, and C. D. Johnston. “The thermodynamic response of heating at coronal null points”. In: *Monthly Notices of the Royal Astronomical Society* 532.4 (2024), pp. 4261–4271.

[69] P. G. Judge. “Inevitable consequences of ion–neutral damping of intermediate MHD waves in Sun-like stars”. In: *Monthly Notices of the Royal Astronomical Society* 498.2 (2020), pp. 2018–2029.

[70] P. Kayshap, K. Murawski, A. Srivastava, Z. Musielak, and B. Dwivedi. “Vertical propagation of acoustic waves in the solar internetworkas observed by IRIS”. In: *Monthly Notices of the Royal Astronomical Society* 479.4 (2018), pp. 5512–5521.

[71] D. I. Ketcheson, R. J. LeVeque, and M. J. Del Razo. *Riemann problems and Jupyter solutions*. Vol. 16. SIAM, 2020.

[72] E. Khomenko, M. Collados, A. Díaz, and N. Vitas. “Fluid description of multi-component solar partially ionized plasma”. In: *Physics of Plasmas* 21.9, 092901 (Sept. 2014), p. 092901.

[73] E. Khomenko and P. S. Cally. “Numerical simulations of conversion to Alfvén waves in solar active regions”. In: *Journal of Physics: Conference Series*. Vol. 271. 1. IOP Publishing. 2011, p. 012042.

[74] E. Khomenko, M. Collados, A. Diaz, and N. Vitas. “Fluid description of multi-component solar partially ionized plasma”. In: *Physics of Plasmas* 21.9 (2014).

[75] E. Khomenko, V. Lukin, and B. Popescu Braileanu. “Effects of neutrals on magnetic Rayleigh Taylor instability in solar prominences”. In: *43rd COSPAR Scientific Assembly. Held 28 January - 4 February*. Vol. 43. Jan. 2021, 976, p. 976.

[76] J. Kiusalaas. *Numerical methods in engineering with Python*. Cambridge university press, 2010.

[77] J. A. Klimchuk. “On solving the coronal heating problem”. In: *Solar Physics* 234 (2006), pp. 41–77.

[78] H. Koskinen. *Physics of space storms: From the solar surface to the Earth*. Springer Science & Business Media, 2011.

[79] P. O. Krehl. “The classical Rankine-Hugoniot jump conditions, an important cornerstone of modern shock wave physics: ideal assumptions vs. reality”. In: *The European Physical Journal H* 40.2 (2015), pp. 159–204.

[80] M. Krogulec, Z. Musielak, S. Suess, S. Nerney, and R. Moore. “Reflection of Alfvén waves in the solar wind”. In: *Journal of Geophysical Research: Space Physics* 99.A12 (1994), pp. 23489–23501.

[81] T. P. J. Krüger, R. Burger, M. Hitge, et al. “The effect of a Fisk-Parker hybrid magnetic field on cosmic rays in the heliosphere”. In: (2005).

[82] M. Kumar, K. Murawski, L. Kadowaki, B. Kuźma, and E. Kilpua. “Impulsively generated waves in two-fluid plasma in the solar chromosphere: Heating and generation of plasma outflows”. In: *Astronomy and Astrophysics* 681 (2024), A60.

[83] M. Kumar, K. Murawski, B. Kuźma, E. Kilpua, S. Poedts, and R. Erdélyi. “Numerical Experiment on the Influence of Granulation-induced Waves on Solar Chromosphere Heating and Plasma Outflows in a Magnetic Arcade”. In: *The Astrophysical Journal* 975.1 (2024), p. 3.

[84] B. Kuźma, L. H. Kadowaki, K. Murawski, Z. E. Musielak, S. Poedts, D. Yuan, and X. Feng. “Magnetoacoustic cutoff effect in numerical simulations of the partially ionized solar atmosphere”. In: *Philosophical Transactions of the Royal Society A* 382.2272 (2024), p. 20230218.

[85] B. Kuźma, M. Brchnelova, B. Perri, T. Baratashvili, F. Zhang, A. Lani, and S. Poedts. “COCONUT, a Novel Fast-converging MHD Model for Solar Corona Simulations. III. Impact of the Preprocessing of the Magnetic Map on the Modeling of the Solar Cycle Activity and Comparison with Observations”. In: *The Astrophysical Journal* 942.1 (2023), p. 31.

[86] B. Kuźma, K. Murawski, Z. E. Musielak, S. Poedts, and D. Wójcik. “Spatial variation in the periods of ion and neutral waves in a solar magnetic arcade”. In: *Astronomy & Astrophysics* 652 (2021), A88.

[87] B. Kuźma, D. Wójcik, and K. Murawski. “Heating of a quiet region of the solar chromosphere by ion and neutral acoustic waves”. In: *The Astrophysical Journal* 878.2 (2019), p. 81.

[88] H. Kwak, J. Chae, M. S. Madjarska, K. Cho, and D. Song. "Impulsive wave excitation by rapidly changing granules". In: *Astronomy & Astrophysics* 642 (2020), A154.

[89] H. Lamb. "On waves in an elastic plate". In: *Proceedings of the Royal Society of London. Series A, Containing papers of a mathematical and physical character* 93.648 (1917), pp. 114–128.

[90] A. Lani, T. Quintino, D. Kimpe, H. Deconinck, S. Vandewalle, and S. Poedts. "The COOLFluiD framework: design solutions for high performance object oriented scientific computing software". In: *Computational Science–ICCS 2005: 5th International Conference, Atlanta, GA, USA, May 22-25, 2005. Proceedings, Part I 5*. Springer. 2005, pp. 279–286.

[91] A. Lani, N. Villedie, K. Bensassi, L. Koloszar, M. Vymazal, S. M. Yalim, and M. Panesi. "COOLFluiD: an open computational platform for multi-physics simulation and research". In: *21st AIAA computational fluid dynamics conference*. 2013, p. 2589.

[92] J. E. Leake, V. S. Lukin, M. G. Linton, and E. T. Meier. "Multi-fluid simulations of chromospheric magnetic reconnection in a weakly ionized reacting plasma". In: *The Astrophysical Journal* 760.2 (2012), p. 109.

[93] R. B. Leighton. "The solar granulation". In: *Annual Review of Astronomy and Astrophysics, vol. 1, p. 19* 1 (1963), p. 19.

[94] R. J. LeVeque and R. J. Leveque. *Numerical methods for conservation laws*. Vol. 132. Springer, 1992.

[95] L. Linan, T. Baratashvili, A. Lani, B. Schmieder, M. Brchnelova, J. Guo, and S. Poedts. "Coronal mass ejection propagation in the dynamically coupled space weather tool: COCONUT+ EUHFORIA". In: *Astronomy & Astrophysics* 693 (2025), A229.

[96] J. G. Linhart and D. Rose. *Plasma physics*. 1961.

[97] R. Lionello, J. A. Linker, and Z. Mikić. "Multispectral emission of the Sun during the first whole Sun month: Magnetohydrodynamic simulations". In: *The Astrophysical Journal* 690.1 (2008), p. 902.

[98] X. D. Liu, S. Osher, and T. Chan. "Weighted essentially non-oscillatory schemes". In: *Journal of computational physics* 115.1 (1994), pp. 200–212.

[99] B. Low. "Three-dimensional structures of magnetostatic atmospheres. I-Theory". In: *Astrophysical Journal, Part 1 (ISSN 0004-637X), vol. 293, June 1, 1985, p. 31-43.* 293 (1985), pp. 31–43.

[100] W. B. Manchester IV, T. I. Gombosi, I. Roussev, A. Ridley, D. L. De Zeeuw, I. Sokolov, K. G. Powell, and G. Tóth. "Modeling a space weather event from the Sun to the Earth: CME generation and interplanetary propagation". In: *Journal of Geophysical Research: Space Physics* 109.A2 (2004).

[101] Y. G. Maneva, A. A. Laguna, A. Lani, and S. Poedts. "Multi-fluid modeling of magnetosonic wave propagation in the solar chromosphere: effects of impact ionization and radiative recombination". In: *The Astrophysical Journal* 836.2 (2017), p. 197.

[102] M. Martínez-Fuentes and d. Herrera-Velázquez. "On the accuracy of the Debye shielding model". In: *Revista mexicana de física E* 63.1 (2017), pp. 63–67.

[103] D. Martínez-Gómez, R. Oliver, E. Khomenko, and M. Collados. "Large ion-neutral drift velocities and plasma heating in partially ionized coronal rain blobs". In: *The Astrophysical Journal Letters* 940.2 (2022), p. L47.

[104] J. Martínez-Sykora, B. De Pontieu, V. Hansteen, and M. Carlsson. "The role of partial ionization effects in the chromosphere". In: *Philosophical Transactions of the Royal Society A: Mathematical, Physical and Engineering Sciences* 373.2042 (2015), p. 20140268.

[105] J. Martínez-Sykora, M. Szydlarski, V. H. Hansteen, and B. De Pontieu. "On the velocity drift between ions in the solar atmosphere". In: *The Astrophysical Journal* 900.2 (2020), p. 101.

[106] C. P. McNally, W. Lyra, and J. C. Passy. "A well-posed Kelvin–Helmholtz instability test and comparison". In: *The Astrophysical Journal Supplement Series* 201.2 (2012), p. 18.

[107] E. T. Meier and U. Shumlak. "Publisher's Note: "A general nonlinear fluid model for reacting plasma-neutral mixtures [Phys. Plasmas 19, 072508 (2012)]". In: *Physics of Plasmas* 19.8, 089902 (Aug. 2012), p. 089902.

[108] E. Meier and U. Shumlak. "A general nonlinear fluid model for reacting plasma-neutral mixtures". In: *Physics of Plasmas* 19.7 (2012).

[109] L. Melis, R. Soler, and J. L. Ballester. "Alfvén wave heating in partially ionized thin threads of solar prominences". In: *Astronomy & Astrophysics* 650 (2021), A45.

[110] C. Meringolo, F. Pucci, G. Nisticò, O. Pezzi, S. Servidio, and F. Malara. "Joint action of phase mixing and nonlinear effects in MHD waves propagating in coronal loops". In: *Astronomy & Astrophysics* 688 (2024), A12.

[111] N. Meyer-Vernet. *Basics of the solar wind*. Cambridge University Press, 2007.

[112] A. Mignone, M. Ugliano, and G. Bodo. "A five-wave Harten-Lax-van Leer Riemann solver for relativistic magnetohydrodynamics". In: 393.4 (Mar. 2009), pp. 1141–1156.

[113] Z. Mikić, J. A. Linker, D. D. Schnack, R. Lionello, and A. Tarditi. “Magnetohydrodynamic modeling of the global solar corona”. In: *Physics of Plasmas* 6.5 (1999), pp. 2217–2224.

[114] T. Minoshima and T. Miyoshi. “A low-dissipation HLLD approximate Riemann solver for a very wide range of Mach numbers”. In: *Journal of Computational Physics* 446 (2021), p. 110639.

[115] A. P. Misra, R. Dey, and V. Krishan. “Coupling of Alfvén and magnetosonic waves in rotating Hall magnetoplasmas”. In: *Physics of Plasmas* 32.6 (2025).

[116] T. Miyoshi and K. Kusano. “A Robust MHD Scheme in Space Weather Modeling: A Carbuncle-Free HLL-type Solver”. In: *AGU Fall Meeting Abstracts*. Vol. 2007. Dec. 2007, SM41A-0311, SM41A–0311.

[117] T. Miyoshi and K. Kusano. “A multi-state HLL approximate Riemann solver for ideal magnetohydrodynamics”. In: *Journal of Computational Physics* 208.1 (2005), pp. 315–344.

[118] B. Mondal et al. “Determining the Nanoflare Heating Frequency of an X-Ray Bright Point Observed by MaGIXS”. In: 967.1, 23 (May 2024), p. 23.

[119] R. Moore and P. Fung. “Structure of the chromosphere-corona transition region”. In: *Solar Physics* 23 (1972), pp. 78–102.

[120] R. Morton, S. Tomczyk, and R. Pinto. “Investigating Alfvénic wave propagation in coronal open-field regions”. In: *Nature Communications* 6.1 (2015), p. 7813.

[121] R. Morton, M. Weberg, and J. McLaughlin. “A basal contribution from p-modes to the Alfvénic wave flux in the Sun’s corona”. In: *Nature Astronomy* 3.3 (2019), pp. 223–229.

[122] K. Murawski. “Alfven-magnetosonic waves interaction”. In: *Acta Physica Polonica A* 81.3 (1992), pp. 335–351.

[123] K. Murawski, Z. E. Musielak, S. Poedts, A. K. Srivastava, and L. Kadowaki. “Two-fluid numerical model of chromospheric heating and plasma outflows in a quiet-Sun”. In: 367.11, 111 (Nov. 2022), p. 111.

[124] K. Murawski, A. Srivastava, J. McLaughlin, and R. Oliver. “Numerical Simulations of Magnetoacoustic–Gravity Waves in the Solar Atmosphere”. In: *Solar Physics* 283 (2013), pp. 383–399.

[125] K. Murawski. “Analytical and numerical methods for wave propagation in fluid media”. In: 7 (2002).

[126] K. Murawski, Z. Musielak, and D. Wójcik. “3D numerical simulations of solar quiet chromosphere wave heating”. In: *The Astrophysical Journal Letters* 896.1 (2020), p. L1.

[127] K. Murawski, A. Solovev, Z. Musielak, A. Srivastava, and J. Kraśkiewicz. "Torsional Alfvén waves in solar magnetic flux tubes of axial symmetry". In: *Astronomy & Astrophysics* 577 (2015), A126.

[128] Z. Musielak and P. Ulmschneider. "Excitation of transverse magnetic tube waves in stellar convection zones-I. Analytical approach". In: *Astronomy & Astrophysics* 370.2 (2001), pp. 541–554.

[129] V. M. Nakariakov and D. Y. Kolotkov. "Magnetohydrodynamic waves in the solar corona". In: *Annual Review of Astronomy and Astrophysics* 58.1 (2020), pp. 441–481.

[130] V. Nakariakov, B. Roberts, and K. Murawski. "Nonlinear coupling of MHD waves in inhomogeneous steady flows". In: *Astronomy and Astrophysics, v. 332, p. 795-804 (1998)* 332 (1998), pp. 795–804.

[131] U. Narain and P. Ulmschneider. "Chromospheric and coronal heating mechanisms". In: *Space Science Reviews* 54.3 (1990), pp. 377–445.

[132] U. Narain and P. Ulmschneider. "Chromospheric and coronal heating mechanisms II". In: *Space Science Reviews* 75.3 (1996), pp. 453–509.

[133] R. Niedziela, K. Murawski, and S. Poedts. "Chromospheric heating and generation of plasma outflows by impulsively generated two-fluid magnetoacoustic waves". In: *Astronomy & Astrophysics* 652 (2021), A124.

[134] R. Niedziela, K. Murawski, L. Kadowaki, T. Zaqarashvili, and S. Poedts. "Impulsively generated two-fluid magnetoacoustic-gravity waves: Solar chromosphere heating and plasma outflows". In: *Astronomy & Astrophysics* 668 (2022), A32.

[135] R. Niedziela, K. Murawski, and A. Srivastava. "Numerical experiments on granulation-generated two-fluid waves and flows in a solar magnetic carpet". In: *Monthly Notices of the Royal Astronomical Society* 534.3 (2024), pp. 2998–3004.

[136] L. Ofman, V. Nakariakov, and C. DeForest. "Slow magnetosonic waves in coronal plumes". In: *The Astrophysical Journal* 514.1 (1999), p. 441.

[137] L. Ofman. "MHD waves and heating in coronal holes". In: *Space Science Reviews* 120 (2005), pp. 67–94.

[138] S. Ohtani, A. Miura, and T. Tamao. "Coupling between Alfvén and slow magnetosonic waves in an inhomogeneous finite-β plasma—I. Coupled equations and physical mechanism". In: *Planetary and space science* 37.5 (1989), pp. 567–577.

[139] R. Oliver, R. Soler, J. Terradas, and T. V. Zaqarashvili. "Dynamics of Coronal Rain and Descending Plasma Blobs in Solar Prominences. II. Partially Ionized Case". In: 818.2, 128 (Feb. 2016), p. 128.

[140] S. A. Orszag and C. M. Tang. "Small-scale structure of two-dimensional magnetohydrodynamic turbulence". In: *Journal of Fluid Mechanics* 90.1 (1979), pp. 129–143.

[141] J. Orta, M. Huerta, and G. Boynton. "Magnetohydrodynamic shock heating of the solar corona". In: *The Astrophysical Journal* 596.1 (2003), p. 646.

[142] M. K. Pandey, L. Prasad, and S. Gariya. "Coronal heating by coupling of the magnetosonic and phase-mixed Alfvén waves". In: *94.30. cq* (2010).

[143] S. Parenti. "Solar prominences: observations". In: *Living Reviews in Solar Physics* 11 (2014), pp. 1–88.

[144] E. Parker. "Dynamical theory of the solar wind". In: *Space Science Reviews* 4.5 (1965), pp. 666–708.

[145] E. N. Parker. "Dynamics of the interplanetary gas and magnetic fields." In: *Astrophysical Journal, vol. 128, p. 664* 128 (1958), p. 664.

[146] C. E. Parnell and I. De Moortel. "A contemporary view of coronal heating". In: *Philosophical Transactions of the Royal Society A: Mathematical, Physical and Engineering Sciences* 370.1970 (2012), pp. 3217–3240.

[147] S. Pathare, S. Huli, M. Nachane, S. Ladage, and H. Pradhan. "Understanding thermal equilibrium through activities". In: *Physics Education* 50.2 (2015), p. 146.

[148] C. H. Payne. "Stellar Atmospheres; a Contribution to the Observational Study of High Temperature in the Reversing Layers of Stars." In: (1925).

[149] M. Pelekhata, K. Murawski, and S. Poedts. "Solar chromosphere heating and generation of plasma outflows by impulsively generated two-fluid Alfvén waves". In: *Astronomy & Astrophysics* 652 (2021), A114.

[150] B. Perri, B. Kuźma, M. Brchnelova, T. Baratashvili, F. Zhang, P. Leitner, A. Lani, and S. Poedts. "COCONUT, a Novel Fast-converging MHD Model for Solar Corona Simulations. II. Assessing the Impact of the Input Magnetic Map on Space-weather Forecasting at Minimum of Activity". In: *The Astrophysical Journal* 943.2 (2023), p. 124.

[151] B. Perri, P. Leitner, M. Brchnelova, T. Baratashvili, B. Kuźma, F. Zhang, A. Lani, and S. Poedts. "COCONUT, a novel fast-converging MHD model for solar corona simulations: I. Benchmarking and optimization of polytropic solutions". In: *The Astrophysical Journal* 936.1 (2022), p. 19.

[152] N. Petrukhin. "Refraction of acoustogravity waves in the solar atmosphere". In: *Sov. Astron.(Engl. Transl.);(United States)* 25.6 (1981).

[153] A. A. Pevtsov, G. H. Fisher, L. W. Acton, D. W. Longcope, C. M. Johns-Krull, C. C. Kankelborg, and T. R. Metcalf. “The relationship between X-ray radiance and magnetic flux”. In: *The Astrophysical Journal* 598.2 (2003), p. 1387.

[154] D. Pontin, E. Priest, L. Chitta, and V. Titov. “Coronal heating and solar wind generation by flux cancellation reconnection”. In: *The Astrophysical Journal* 960.1 (2023), p. 51.

[155] E. Priest. *Magnetohydrodynamics of the Sun*. Cambridge University Press, 2014.

[156] I. Rapp-Kindner, K. Ősz, and G. Lente. “The ideal gas law: derivations and intellectual background”. In: *ChemTexts* 11.1 (2024), p. 1.

[157] B. Roberts. *MHD waves in the solar atmosphere*. Cambridge University Press, 2019.

[158] R. Rosner, W. H. Tucker, and G. Vaiana. “Dynamics of the quiescent solar corona”. In: *Astrophysical Journal, Part 1, vol. 220, Mar. 1, 1978, p. 643-645, 647, 649-653, 655-665. Research supported by the Smithsonian Institution;* 220 (1978), pp. 643–645.

[159] M. Roth, M. Franz, N. B. González, V. M. Pillet, J. Bonet, A. Gandorfer, P. Barthol, S. Solanki, T. Berkefeld, W. Schmidt, et al. “Surface waves in solar granulation observed with SUNRISE”. In: *The Astrophysical Journal Letters* 723.2 (2010), p. L175.

[160] D. A. Russell. “Acoustics and vibration animations”. In: *Graduate Program in Acoustics, The Pennsylvania State University* (2014).

[161] I. Sadrehaghighi. *Unstructured Meshing for CFD*. Oct. 2022.

[162] S. Sahoo. *Understanding Simpson’s 1/3 Rule: A Comprehensive Guide for Researchers and Engineers*. July 2025.

[163] T. Sakurai. “Heating mechanisms of the solar corona”. In: *Proceedings of the Japan Academy, Series B* 93.2 (2017), pp. 87–97.

[164] S. S. Sastry. *Introductory methods of numerical analysis*. PHI Learning Pvt. Ltd., 2012.

[165] K. Schatten and S. Sofia. “Schwarzschild criterion for convection in the presence of a magnetic field”. In: *Astrophys. Lett.;(United States)* 21 (1981).

[166] E. Schatzman. “The heating of the solar corona and chromosphere”. In: *Annales d’Astrophysique, Vol. 12, p. 203* 12 (1949), p. 203.

[167] J. Schmelz and A. Winebarger. “What can observations tell us about coronal heating?” In: *Philosophical Transactions of the Royal Society A: Mathematical, Physical and Engineering Sciences* 373.2042 (2015), p. 20140257.

[168] M. Schwarzschild. “On Noise Arising from the Solar Granulation.” In: *Astrophysical Journal, vol. 107, p. 1* 107 (1948), p. 1.

[169] S. Shelyag, M. Mathioudakis, and F. P. Keenan. “Mechanisms for MHD poynting flux generation in simulations of solar photospheric magnetoconvection”. In: *The Astrophysical Journal Letters* 753.1 (2012), p. L22.

[170] S. Skirvin, G. Verth, J. J. González-Avilés, S. Shelyag, R. Sharma, F. S. Guzmán, I. Ballai, E. Scullion, S. S. Silva, and V. Fedun. “Small-scale solar jet formation and their associated waves and instabilities”. In: *Advances in Space Research* 71.4 (2023), pp. 1866–1892.

[171] G. A. Sod. “A survey of several finite difference methods for systems of nonlinear hyperbolic conservation laws”. In: *Journal of computational physics* 27.1 (1978), pp. 1–31.

[172] R. Soler, J. Ballester, and T. Zaqarashvili. “Overdamped Alfvén waves due to ion-neutral collisions in the solar chromosphere”. In: *Astronomy & Astrophysics* 573 (2015), A79.

[173] R. Soler and J. L. Ballester. “Theory of fluid instabilities in partially ionized plasmas: an overview”. In: *Frontiers in Astronomy and Space Sciences* 9 (2022), p. 789083.

[174] P. Song, J. Tu, and D. B. Wexler. “Formation of the Transition Region for the Quiet Sun”. In: *The Astrophysical Journal Letters* 948.1 (2023), p. L4.

[175] L. Spitzer. “Physics of fully ionized gases, ed”. In: *Spitzer, L* (1962).

[176] A. H. Squillacote, J. Ahrens, C. Law, B. Geveci, K. Moreland, and B. King. *The paraview guide*. Vol. 366. Kitware Clifton Park, NY, 2007.

[177] A. K. Srivastava, J. L. Ballester, P. S. Cally, M. Carlsson, M. Goossens, D. B. Jess, E. Khomenko, M. Mathioudakis, K. Murawski, and T. Zaqarashvili. *Chromospheric heating by magnetohydrodynamic waves and instabilities*. 2021.

[178] A. Srivastava, S. Mondal, E. R. Priest, S. K. Mishra, D. I. Pontin, R. Kwon, D. Yuan, K. Murawski, and A. Asai. “Localized Heating and Dynamics of the Solar Corona due to a Symbiosis of Waves and Reconnection”. In: *The Astrophysical Journal* 984.1 (2025), p. 36.

[179] R. Stein and Å. Nordlund. “Simulations of solar granulation. I. General properties”. In: *The Astrophysical Journal* 499.2 (1998), p. 914.

[180] R. F. Stein and J. Leibacher. “Waves in the solar atmosphere”. In: *In: Annual review of astronomy and astrophysics. Volume 12.(A75-13476 03-90) Palo Alto, Calif., Annual Reviews, Inc., 1974, p. 407-435.* 12 (1974), pp. 407–435.

[181] A. C. Sterling, N. K. Panesar, and R. L. Moore. “How small-scale jetlike solar events from miniature flux rope eruptions might produce the solar wind”. In: *The Astrophysical Journal* 963.1 (2024), p. 4.

[182] D. Talpeanu, E. Chané, S. Poedts, E. D'Huys, M. Mierla, I. Roussev, and S. Hosteaux. "Numerical simulations of shear-induced consecutive coronal mass ejections". In: *Astronomy & Astrophysics* 637 (2020), A77.

[183] D. Talpeanu, S. Poedts, E. D'Huys, and M. Mierla. "Study of the propagation, in situ signatures, and geoeffectiveness of shear-induced coronal mass ejections in different solar winds". In: *Astronomy & Astrophysics* 658 (2022), A56.

[184] J. Terradas, J. Andries, and E. Verwichte. "Linear coupling between fast and slow MHD waves due to line-tying effects". In: *Astronomy & Astrophysics* 527 (2011), A132.

[185] H. Tian, L. Harra, D. Baker, D. H. Brooks, and L. Xia. "Upflows in the Upper Solar Atmosphere: Invited Review". In: *Solar Physics* 296 (2021), pp. 1–36.

[186] C. Y. Tu, C. Zhou, E. Marsch, L.-D. Xia, L. Zhao, J.-X. Wang, and K. Wilhelm. "Solar wind origin in coronal funnels". In: *Science* 308.5721 (2005), pp. 519–523.

[187] P. Ulmschneider. "Chromospheric and coronal heating mechanisms". In: *Theoretical and Observational Problems Related to Solar Eclipses*. Springer, 1997, pp. 95–102.

[188] V. M. Uritsky, J. T. Karpen, N. E. Raouafi, P. Kumar, C. R. DeVore, and C. E. Deforest. "Self-similar Outflows at the Source of the Fast Solar Wind: A Smoking Gun of Multiscale Impulsive Reconnection?" In: *The Astrophysical Journal Letters* 955.2 (2023), p. L38.

[189] T. Van Doorsselaere, A. K. Srivastava, P. Antolin, N. Magyar, S. Vasheghani Farahani, H. Tian, D. Kolotkov, L. Ofman, M. Guo, I. Arregui, et al. "Coronal heating by MHD waves". In: *Space Science Reviews* 216 (2020), pp. 1–40.

[190] B. Van Leer. "Towards the ultimate conservative difference scheme. V. A second-order sequel to Godunov's method". In: *Journal of computational Physics* 32.1 (1979), pp. 101–136.

[191] V. Venkatakrishnan. "On the accuracy of limiters and convergence to steady state solutions". In: *31st Aerospace sciences meeting*. 1993, p. 880.

[192] N. Viall, I. De Moortel, C. Downs, J. A. Klimchuk, S. Parenti, and F. Reale. "The heating of the solar corona". In: *Solar Physics and Solar Wind* (2021), pp. 35–82.

[193] S. Von Alfthan, D. Pokhotelov, Y. Kempf, S. Hoilijoki, I. Honkonen, A. Sandroos, and M. Palmroth. "Vlasiator: First global hybrid-Vlasov simulations of Earth's foreshock and magnetosheath". In: *Journal of Atmospheric and Solar-Terrestrial Physics* 120 (2014), pp. 24–35.

[194] J. Vranjes and P. S. Krstic. "Collisions, magnetization, and transport coefficients in the lower solar atmosphere". In: 554, A22 (June 2013), A22.

[195] H. Wang, S. Poedts, A. Lani, M. Brchnelova, T. Baratashvili, L. Linan, F. Zhang, D. Hou, and Y. Zhou. "Efficient magnetohydrodynamic modelling of the time-evolving corona by COCONUT". In: *Astronomy & Astrophysics* 694 (2025), A234.

[196] R. Wang and R. J. Spiteri. "Linear instability of the fifth-order WENO method". In: *SIAM Journal on Numerical Analysis* 45.5 (2007), pp. 1871–1901.

[197] Y. Wang and N. Sheeley Jr. "Solar wind speed and coronal flux-tube expansion". In: *Astrophysical Journal, Part 1 (ISSN 0004-637X), vol. 355, June 1, 1990, p. 726-732. Research supported by the US Navy.* 355 (1990), pp. 726–732.

[198] Y. Wang, T. Yokoyama, and H. Iijima. "Fast magnetic wave could heat the solar low-beta chromosphere". In: *The Astrophysical Journal Letters* 916.2 (2021), p. L10.

[199] S. Wedemeyer, B. Fleck, M. Battaglia, N. Labrosse, G. Fleishman, H. Hudson, P. Antolin, C. Alissandrakis, T. Ayres, J. Ballester, et al. "ALMA Observations of the Sun in Cycle 4 and Beyond". In: *arXiv preprint arXiv:1601.00587* (2016).

[200] D. G. Wentzel. "Wave reflection and wave disorder in the solar transition zone and corona." In: 58.2 (July 1978), pp. 307–318.

[201] Y. Whang. "Attenuation of magnetohydrodynamic waves". In: *The Astrophysical Journal* 485.1 (1997), p. 389.

[202] A. Wiśniewska, Z. Musielak, J. Staiger, and M. Roth. "Observational evidence for variations of the acoustic cutoff frequency with height in the solar atmosphere". In: *The Astrophysical Journal Letters* 819.2 (2016), p. L23.

[203] G. L. Withbroe and R. W. Noyes. "Mass and Energy Flow in the Solar Chromosphere and Corona". In: *Annual Review of Astronomy and Astrophysics* 15.1 (1977), pp. 363–387.

[204] D. Wójcik, B. Kuźma, K. Murawski, and A. Srivastava. "Two-fluid numerical simulations of the origin of the fast solar wind". In: *The Astrophysical Journal* 884.2 (2019), p. 127.

[205] D. Wójcik, K. Murawski, and Z. Musielak. "Acoustic waves in two-fluid solar atmosphere model: cut-off periods, chromospheric cavity, and wave tunnelling". In: *Monthly Notices of the Royal Astronomical Society* 481.1 (2018), pp. 262–267.

[206] D. Wójcik, B. Kuźma, K. Murawski, and Z. Musielak. "Wave heating of the solar atmosphere without shocks". In: *Astronomy & Astrophysics* 635 (2020), A28.

[207] A. N. Wright and T. Elsden. "Simulations of MHD wave propagation and coupling in a 3-D magnetosphere". In: *Journal of Geophysical Research: Space Physics* 125.2 (2020), e2019JA027589.

[208] M. S. Yalim, D. V. Abeele, A. Lani, T. Quintino, and H. Deconinck. "A finite volume implicit time integration method for solving the equations of ideal magnetohydrodynamics for the hyperbolic divergence cleaning approach". In: *Journal of Computational Physics* 230.15 (2011), pp. 6136–6154.

[209] X. Yang, Z. Chen, H. Xu, Y. Ma, G. Zhang, D. Zou, and F. Shao. "Hybrid PIC–fluid simulations for fast electron transport in a silicon target". In: *Matter and Radiation at Extremes* 8.3 (2023).

[210] Z. Yang, C. Bethge, H. Tian, S. Tomczyk, R. Morton, G. Del Zanna, S. W. McIntosh, B. B. Karak, S. Gibson, T. Samanta, et al. "Global maps of the magnetic field in the solar corona". In: *Science* 369.6504 (2020), pp. 694–697.

[211] A. Yeates, D. Mackay, and A. van Ballegooijen. "A Prominence Puzzle Explained?" In: *AIP Conference Proceedings*. Vol. 1094. 1. American Institute of Physics. 2009, pp. 216–221.

[212] T. Zaqarashvili, M. Khodachenko, and H. Rucker. "Magnetohydrodynamic waves in solar partially ionized plasmas: two-fluid approach". In: *A&A* 529 (2011), A82.

[213] E. Zita. "The Physics of Plasmas by TJM Boyd and JJ Sanderson". In: *American journal of Physics* 74.5 (2006), p. 462.